INVESTIGATIONS OF LOW LATITUDE THERMOSPHERE - IONOSPHERE SYSTEM

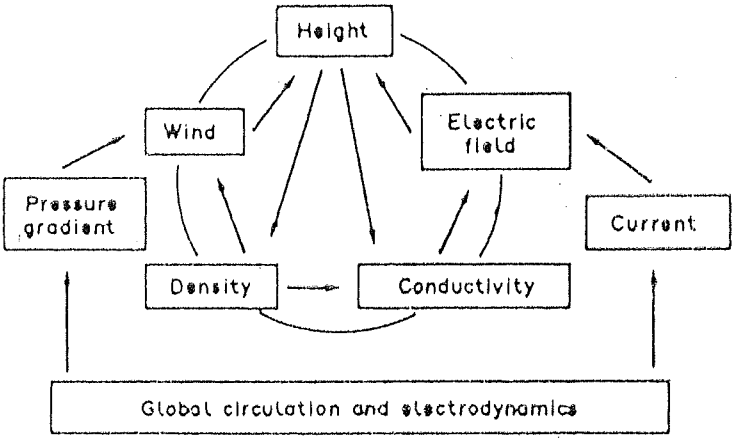

S. GURUBARAN

A THESIS SUBMITTED TO THE
GUJARAT UNIVERSITY
FOR THE DEGREE OF
DOCTOR OF PHILOSOPHY

DEPARTMENT OF PHYSICS
GUJARAT UNIVERSITY

AND

PHYSICAL RESEARCH LABORATORY
AHMEDABAD
INDIA

OCTOBER 1993

CERTIFICATE

I hereby declare that the work contained in this thesis was carried out at the Physical Research Laboratory, Ahmedabad. The results reported herein are original and have not formed the basis for the award of any degree or diploma by any University or Institution.

Author

S. Gurubaran

(S. Gurubaran)

Thesis Supervisor

R. Sridharan

(Prof. R. Sridharan)

Certified by

K. G. Jani

Prof. K. G. Jani
Department of Physics
Gujarat University
Ahmedabad - 380 009
India.

Professor-in-charge
Electronics

PHYSICS DEPARTMENT
GUJARAT UNIVERSITY
Ahmedabad-9

Dedicated to my
parents

Contents

Acknowledgements

To begin with I must express my thanks and gratitude to my Thesis Supervisor Prof. R. Sridharan who was responsible for introducing me to the subject of Upper Atmosphere, in particular, the Optical Aeronomy. Right from the days of coursework, I was always fascinated by his profound depth of understanding on the variety of basic physical and chemical processes of the entire atmosphere. During the course of this work, I have drawn upon both the knowledge and the experience of Prof. R. Sridharan through very many useful discussions. I owe my gratitude to him for having taught me certain basic aspects of life which I found to be very useful in the process of building up my career.

I thank Prof. K. G. Jani for his support and encouragement which enabled me to complete this work. It is my pleasure to thank Prof. R. Raghavarao for his deep concern in the progress of my work. The knowledge I have gathered from him is enormous. I am grateful to him for having spent so much of time during his busy schedule to go through critically my entire thesis and provide valuable suggestions.

I accord my gratitude to Dr. R. Suhasini who introduced me to the art of data analysis. The very many enlightening discussions and arguments I had with Dr. R. Sekar still linger in my mind. It has been a pleasure to know and work with him.

I am grateful to Prof. B. H. Subbaraya for having shown so much of care towards the improvement of my career. His sincere advice on the many facets of life will go a long way. I thank Profs. Harish Chandra and J. N. Desai for their comments and remarks during my assessment reviews. I am grateful for the general encouragement shown to me during my Ph.D. tenure by the Director, Prof. R. K. Verma and Profs. A. C. Das, J. N. Goswami and S. K. Bhattacharya. My interactions at

various stages with Dr. S. A. Haider and with the faculty members of our area, Profs. Vijay Kumar and S. P. Gupta and Drs. G. Subramanian, Shyam Lal, A. Jayaraman, H. S. S. Sinha, D. K. Chakrabarty and K. P. Subramanian, were beneficial and I thank them for the same.

It is a great pleasure to acknowledge my colleagues Mr. N. K. Modi and Mr. R. Narayanan. Their company during our campaigns at Mt. Abu has been quite enjoyable. I have benefited greatly from them on many occasions. My thanks are due to my colleague and friend Pallam Raju for the many long discussions we had on both personal and research activities. I thank Miss Ranna Patel and Mrs. Manisha Pandya for their assistance in the analysis of FPS and ionosonde data. I value the discussions I had with Mr. S. R. Das on the phase path experiment and my thanks are due to him. Mr. Piplapure has been helpful to me in many ways and I owe my thanks to him. I acknowledge the secretarial assistance rendered by Mr. N. R. Pillai.

I would like to thank Prof. T. L. Killeen of Space Physics Research Laboratory, University of Michigan, for kindly sending us the Vector Spherical Harmonic (VSH) model which we found to be valuable for comparing our wind measurements with the model results. I would also like to mention my thanks to Dr. V. V. Somayajulu of Space Physics Laboratory, Vikram Sarabhai Space Centre, Trivandrum, for kindly providing us the data on derived winds for Sriharikota.

I express my thanks to the personnel of the PRL workshop and in particular to Mr. C. L. Gajjar who has entirely devoted himself for the fabrication of the mechanical components of the Fabry Perot Spectrometer. His untiring and sincere work has enabled us on many occasions to get ready for the coordinated campaigns in time. I am grateful to the staff of the Computer Centre and the Library for their cooperation and help. I thank Mr. D. R. Ranpura of the photographic and documentation section for his meticulous work and timely delivery of photographic prints.

I cannot count upon the number of friends in the PRL Hostel who made my stay memorable and refreshing. My batchmates, Ganguly, Krishnan, Supriyo and Seema deserve special mention here. The association and friendship I had with Viju, Jerri, Raju, Subrat, Anjan, Mathew, Sushant, Kishku, Bhushan, Ashwini, Himadri, Debashish and Gopal, are ever to be cherished. I appreciate the help rendered by my friends, Ramani, Manohar Lal, Ramachandran, Pallam Raju, Tarun, Manish Naja and Yags. I thank all other friends in the Hostel and PDF Quarters for their warm and affectionate company.

I would also like to express my thanks to Sam and Abhijit for their company in and out of PRL. The discussions I had with them on varied topics have been invaluable. Jerri was a constant source of inspiration as he made me look into the aspects of interplanetary scintillations and the terrestrial magnetosphere.

I would not have been in this place if not for the constant encouragement provided by my parents right from my childhood. Letters from my mother bathed with full of affection had been inspiring me all through the years. I express my deep sense of gratitude to the families of my Uncles, Mr. V. R. Vedapuri and Mr. V. R. Arumugam, who showered me and my sister the affection and care we badly needed after our mother left this spaceship, earth.

Finally, thanks with love to Devi for her endless letters from so far away that kept me going with renewed vigour and enthusiasm.

Abstract

Optical remote sensing of airglow emissions using a Fabry Perot Spectrometer and radio probing of the ionosphere using a ground-based ionosonde are the means by which investigations of low latitude thermosphere-ionosphere system have been carried out and reported herein. The thesis focuses on the interaction mechanisms governing the neutral-plasma medium of the upper atmosphere and the large scale geophysical processes that drive them.

In recent years, there has been significant activity in developing comprehensive global models that can describe the observed features of the upper atmosphere. However, at low and equatorial latitudes, there has been a grievous lack of data on the basis of which the models have been developed and against which they are tested and validated. The models are capable of predicting only the long term climatological patterns and not the instantaneous 'weather' conditions. Coordinated ground-based measurements of thermospheric and ionospheric parameters are given primary importance in the work presented here which have enabled us to understand the basic interaction mechanisms and identify the role of specific geophysical processes in the behaviour of the thermosphere-ionosphere system. The measurements themselves are expected to serve as inputs to the existing numerical models and can be utilized for the purpose of parameterizing these models in terms of the competing effects of dominant geophysical processes in order to represent the observed features better.

This thesis comprises of seven chapters.

- Chapter 1 provides a background for the thesis. The basic physical and chemical processes that are responsible for the closed cycle of interactions are described. The current understanding on the energetics and dynamics of the upper atmosphere is presented. The efforts made by the various modeling groups are

indicated.

- Chapter 2 describes the experimental methodology, the instrumentation and the method of data analysis adopted for line profile measurements of thermospheric temperatures and line-of-sight winds.

The results are presented in the following four chapters.

- Chapter 3 deals with the variabilities of thermospheric temperatures measured from Mt. Abu, the low latitude observing site, in response to the changing levels of incoming solar flux. The empirical model, MSIS-86, is compared against the direct measurements. The possibility of processes like equatorial spread F, equatorial ionization anomaly and midnight temperature maximum contributing to the energy balance of the thermosphere, has been explored and the importance of each of these processes is discussed.

- It is demonstrated in Chapter 4 that one of the powerful means of investigating the basic coupling processes is the servo model proposed by Rishbeth. The applicability of this model originally formulated for midlatitudes, to low latitudes is critically examined through a simulation exercise that sets up a criterion for the lowest geomagnetic latitude to which the servo model can be applied and tested upon. The measurements of thermospheric temperatures are employed in a case study approach to study the behaviour of the F layer height as predicted by servo model. In the next step, with both temperature and wind measurements being available, a method is described to estimate the peak height of the F_2 layer which is then compared with independent measurements made by the ground-based ionosonde. The thermosphere and the ionosphere are looked upon as a system and several examples are presented that ultimately provide confirmation to the fact that this closed system does behave in accordance with

principles of servo model even over low latitudes. The electrodynamic properties of the system are touched upon by estimating electric fields from the differences between the directly measured and the estimated F layer peak height. The limitations and assumptions involved while adopting the servo model are also discussed in detail in this chapter.

- By making use of the network of ground-based ionosondes located all over the globe, several workers have made use of the servo principles to derive meridional winds. In Chapter 5, the assumptions involved in these methods are discussed and the importance of neutral temperatures in the derivation of meridional winds is demonstrated by specific case studies. The variabilities of meridional winds over the low latitude region around Mt. Abu, are obtained and the relevance of the several geophysical processes in setting up the wind patterns is discussed.

  Having shown their importance in influencing the low latitude thermospheric characteristics in the previous chapters, the geophysical processes, namely, the midnight temperature anomaly, and the equatorial ionization anomaly and its relevance to equatorial spread F, are studied in detail in Chapter 6 with examples drawn from the present work. The potential of newer techniques available now in mapping these large scale features is demonstrated.

- The summary of the results arrived at and suggestions for further work in this direction are given in Chapter 7.

The present investigation has led to the identification of certain aspects of the behaviour of the thermosphere-ionosphere system that need to be explored in detail and whose knowledge is expected to lead to a better and more comprehensive understanding of the system itself.

Chapter 1

Introduction

1.1 Structure of the neutral thermosphere and the ionosphere

The atmosphere is an envelope of gas several hundred kilometres thick surrounding the earth. In the presence of gravity, it is horizontally stratified into different layers or regions. Based on the temperature structure, the atmosphere is classified into *troposphere* (0–15 km), *stratosphere* (15–50 km), *mesosphere* (50–90 km), *thermosphere* (90–400 km) and the *exosphere* higher above (Fig. 1.1a). In the dense lower and middle atmosphere (upto 90 km), large scale macroscopic motions and turbulence lead to mixing of atmospheric gases and the composition remains same at all heights. Owing to large number of collisions, the time constants associated with the vertical separation of individual gases are quite large when compared to those of mixing and this well mixed region is known as the *homosphere*. The sharp upper boundary of the homosphere is called the *turbopause*. Above this altitude, vertical mixing is inhibited since the temperature rises with height making the atmosphere more stable. On the other hand, molecular diffusion dominates in this region aided by less number of collisions and hence each species is distributed on its own according to its molecular

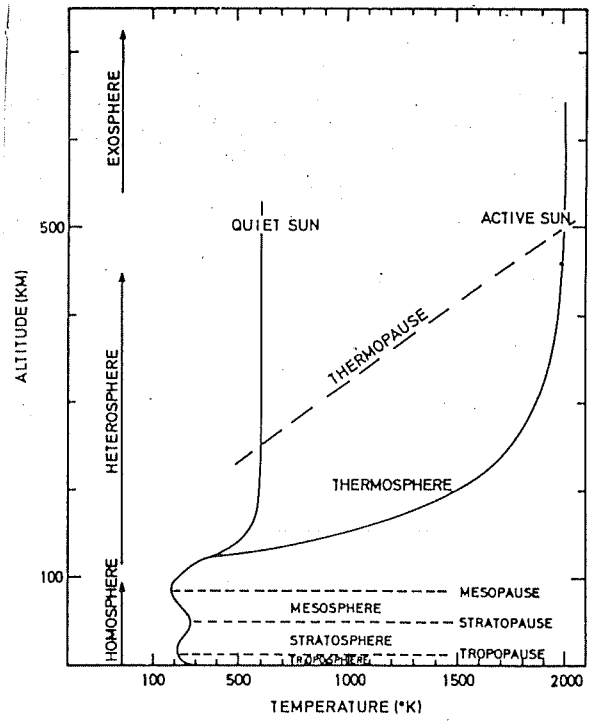

Fig. 1.1a. The different regions of neutral atmosphere based on temperature. The temperature profiles correspond to minimum and maximum solar activity. (after *Banks and Kockarts*, 1973)

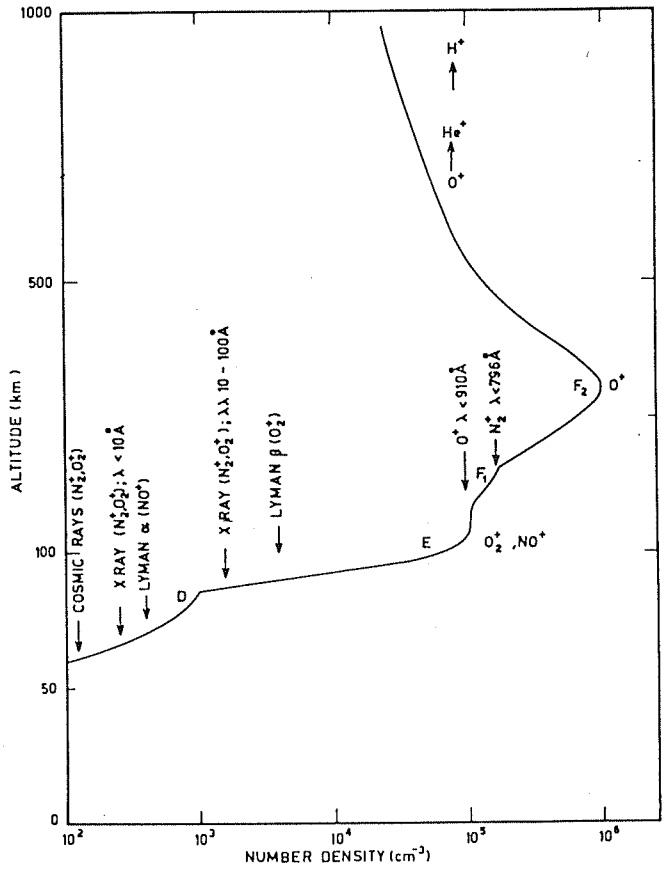

Fig. 1.1b. Average daytime electron density distribution with height. The principal ions in each region and the corresponding ionizing radiation are indicated. (after *Banks and Kockarts*, 1973)

weight. In the absence of chemistry, the gases exist essentially in diffusive equilibrium. Due to its varying composition with height, this region is called the *heterosphere*. Changes in the level of turbopause affect the neutral composition at higher heights with a time constant which depends on the local scale height and the relevant diffusion coefficient.

The region of our interest lies in the upper atmosphere, i.e., the thermosphere, where the temperature starts rising from the base (90 km) to reach a constant value above about 350 km. Its upper boundary is rather ill-defined. Within the thermosphere, the various gases are in thermal equilibrium with each other and fluid dynamic principles are valid. Above 500 km or so, there are very few collisions between gas particles (mean free paths being as large as atmospheric scale height) to have a meaningful concept of temperature and this altitude region can be thought of as the upper boundary of the thermosphere.

The thermosphere is a multi-constituent medium made up of molecular nitrogen (N_2), atomic and molecular oxygen (O, O_2) as major gases and little amounts of argon and helium among other species. Interaction of solar ultraviolet and extreme ultraviolet radiation with the constituents of the thermosphere triggers a host of chemical reactions, producing electron-ion pairs, and causing dissociation of the chemically active molecular oxygen.

Due to the varying chemical composition with altitude, different ionization layers are produced within the thermosphere and the mesosphere, depending on the dominant absorbing species. Thus atomic oxygen, which is more in number than other gases above 150 km produced as a result of photodissociation of O_2, gets ionized and forms the F region. The composition below this region is mainly molecular and the ions such as O_2^+ and NO^+ constitute to form the E region whose base is at 90 km. The ionization below the E region is termed as the D region. At altitudes above 900 km,

hydrogen becomes the dominant ion and this region is called the protonosphere. The ionosphere is thus a plasma with equal numbers of positive ions and electrons, sufficient in number to affect the radio wave propagation. At any instant, chemical loss processes control the ionospheric plasma densities to a large extent. A typical plasma density profile is as shown in Fig. 1.1b, with the various regions identified.

The thermal structure of the neutral upper atmosphere is determined by the absorption of solar UV and EUV radiation by the atmospheric constituents resulting in heating and the downward molecular conduction of heat. The dense lower thermosphere absorbs heat more efficiently giving rise to the sharp gradient in temperature which decreases to zero at the top of the thermosphere, where the thermal conductivity is high and isothermal conditions exist. All the heat absorbed at higher heights are conducted downward and the temperature which has reached an asymptotic value at these heights is called the exospheric temperature (T_∞). The solar heating and its variabilities essentially determine T_∞ which can range from 600 K to 1700 K depending on the solar activity.

The concepts of vertical heat conduction, diffusive equilibrium and turbopause changes described above were initially adopted by many workers in deriving empirical density and temperature models. Neutral air density and temperature structures of the upper atmosphere were inferred from the orbital decay of artificial satellites [*Jacchia*, 1965], which set a background for the present understanding of the more complicated thermospheric dynamics. The importance of dynamics which modifies the composition and temperature characteristics of the thermosphere is well recognized in literature [*Mayr et al.*, 1978].

1.2 The energy balance of the thermosphere

The sun provides the energy in the form of UV and EUV radiation, which are responsible for the large temperatures observed in the thermosphere. Photochemical processes are the means by which this energy is transferred to the various atmospheric gases. At high latitudes, Joule dissipation of electric currents driven by electric fields of magnetospheric origin, and energetic particle precipitation, especially during a geomagnetic storm, also contribute to the heating of the thermosphere. On a global basis, heating by various sources is essentially balanced by the downward thermal conduction and the radiative cooling by species such as nitric oxide, and results in the observed thermal structure.

The interaction of solar radiation with thermospheric species leads to various paths by which the energy is channelled into heating. Exhaustive studies have been conducted by various workers to identify the processes responsible for the channeling of energy and to determine the neutral gas heating rate and the efficiencies of various agencies [*Stolarski et al.*, 1975; *Torr et al.*, 1980 a,b]. The ejected primary photoelectron after a photoionization event carries the excess energy, and undergoes Coulomb collisions with the ambient electrons and ions, and inelastic collisions with the neutrals. Most of the photoelectron energy is lost to space by means of airglow emissions that result from excitation of neutrals. The remaining goes to heat the neutral gas with an efficiency of about 5 %. A chain of exothermic chemical reactions result in the channeling of the chemical energy stored in ions to the neutrals. The combined neutral gas heating efficiency for both ion and photoelectron channels is estimated to be in the 30–40 % range [*Stolarski et al.*, 1975].

Above 300 km, the neutral gas is heated primarily by collisions with the hot electrons and ions. Below this altitude upto $\sim$ 170 km, the thermal energy is provided

by photoelectrons and exothermic chemical reactions. Photodissociation of O_2 by the Schumann-Runge continuum (1250–1750 Å) of solar radiation is the dominant heat source below 170 km with an efficiency of about 30 %. Fig. 1.2 shows the paths along which the solar EUV energy gets channelled to ultimately heat the neutral thermosphere.

The non-uniform absorption of solar energy over different regions of the atmosphere generates pressure gradients on a global scale that drive neutral air circulation. The neutral winds are responsible for the redistribution of heat, transferring energy from the warmer dayside toward the cooler nightside of the thermosphere. Further, inhomogeneities in ionization densities produce drag effects on the neutral air motion that may lead to localized heating and associated circulation [*Dickinson et al.*, 1971].

During geomagnetic storms, one of the possible direct sources of heating for the equatorial region is provided by precipitation of energetic neutrals produced through charge-exchange reactions with the ring current ions [*Tinsley*, 1981]. However, the heating of the thermosphere due to this source is yet to be quantified. At times of enhanced geomagnetic activity, energy is transferred from high latitudes towards equatorial and low latitude regions by means of dynamic processes [*Prölss et al.*, 1988].

Upward propagation of tides and gravity waves generated in the lower and middle atmosphere is also important in the global energy budget since their dissipation due to molecular viscosity, thermal conduction and frictional interactions with ions yields significant energy [*Hines*, 1965; *Chapman and Lindzen*, 1970; *Richmond*, 1979; *Cole and Hickey*, 1981]. An excellent and more recent review on the global energy balance of the thermosphere taking into account the various sources and sinks, exists in the literature [*Killeen*, 1987].

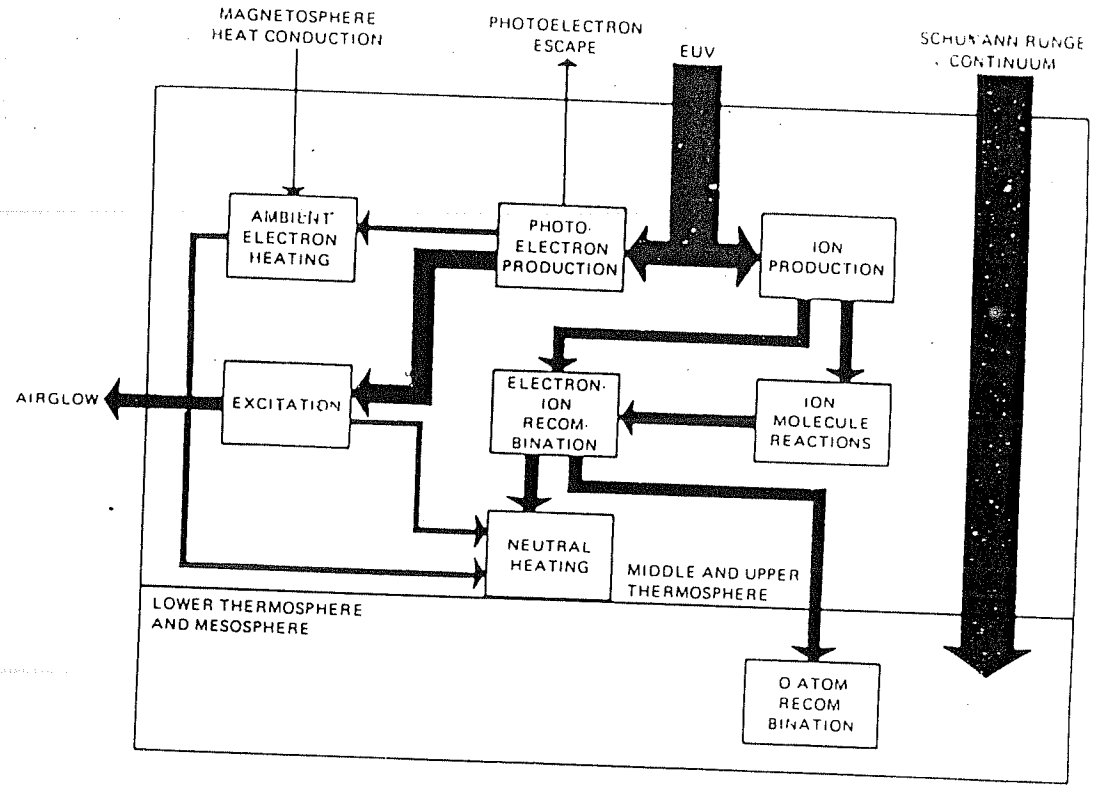

Fig. 1.2. Energy flow diagram of the processes that lead to the conversion of absorbed solar EUV radiation into local thermal energy of the neutral gas. The width of the arrow indicates the relative energy in each process. (after *Stolarski et al.*, 1975)

1.3 Coupling processes of the thermosphere - ionosphere system

The interaction of the thermosphere and the ionosphere within, and these two with the adjoining regions are many (Fig. 1.3) [*Mayr et al.*, 1978]. There exists a variety of physical and chemical processes which couple the neutral and the ionized species, and hence they are treated as constituents of a closely coupled system, namely, the thermosphere-ionosphere system. Worldwide programmes such as Solar Terrestrial Energy Programme (STEP), World Ionosphere Thermosphere Study (WITS) and Coupling Energetics and Dynamics of Atmospheric Regions (CEDAR) have been initiated to understand the various complex processes, all of which finally end up in the transfer of energy and momentum to and between the ions and neutrals. Studies have also been initiated to understand the mechanisms that couple the thermosphere-ionosphere sytem to the mesosphere below and to the magnetosphere above. Few dedicated satellite missions like the Orbiting Geophysical Observatory series, Atmosphere Explorer series and Dynamics Explorer series have also been conducted and these have considerably increased our understanding of the variety of physical, chemical and dynamical processes pertaining to the upper atmosphere.

The coupling of the thermosphere and the ionosphere is associated with the chemical, fluid dynamical and electrodynamical properties of the system. The basic interaction mechanisms are as follows.

(1) **Chemistry** : In spite of the peak production of ionization being located below 200 km, the plasma density continues to increase with altitude due to the role of ion chemistry. The dominant O^+ ion is neutralised either by means of radiative recombination with the ambient electrons or by means of charge exchange reactions with the molecular species which eventually dissociatively recombine with the ambient

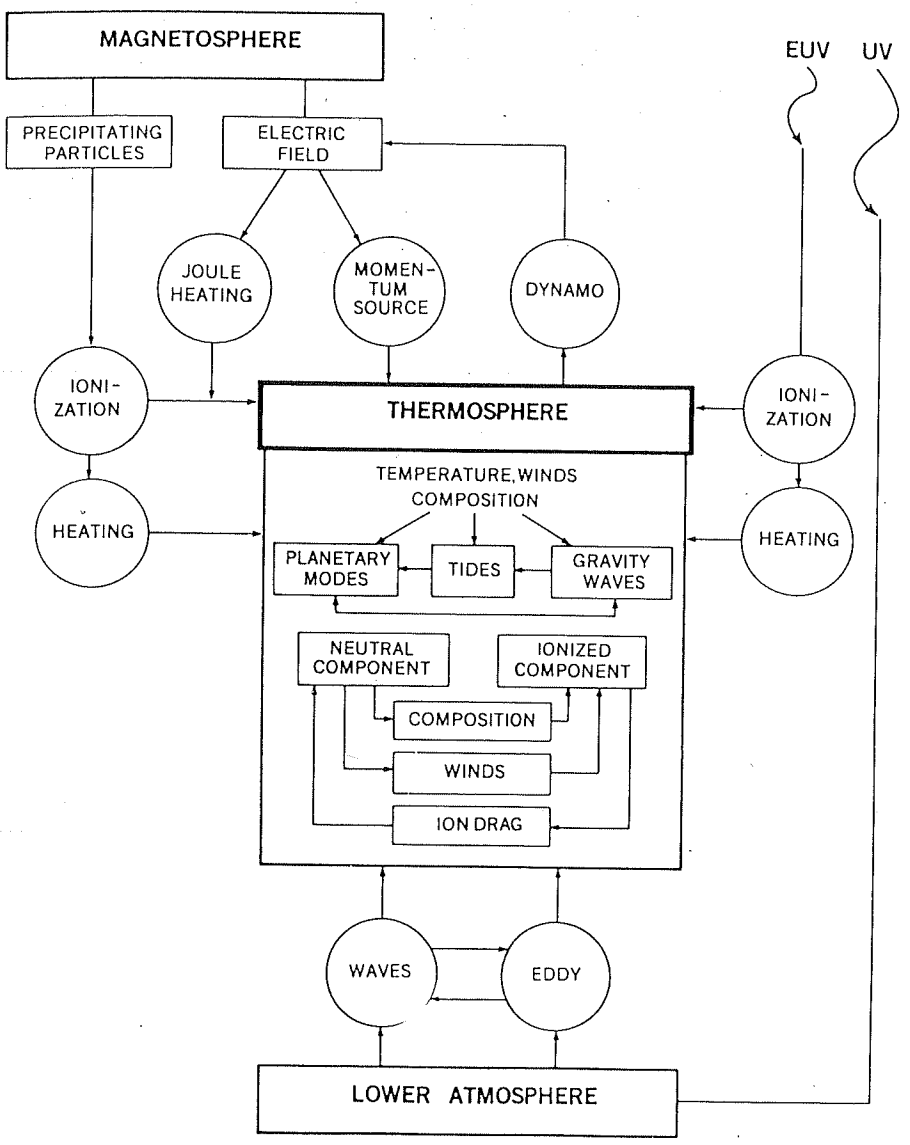

Fig. 1.3. Schematic diagram illustrating the important coupling processes between the regions of terrestrial environment. The interaction mechanisms that couple the neutral and the ionized species, which are of interest to our study, are illustrated within the block labeled 'thermosphere'. (after *Mayr et al.*, 1978)

electrons. The former is an extremely slow process with reaction rate of 10^{-12} cm^3 s^{-1} [*Banks and Kockarts*, 1973] at least two orders of magnitude slower than the latter reactions. With increasing altitude, due to the steep decrease in the molecular concentration, the life time of the dominant O^+ ion continues to increase until it is checked by the plasma diffusion along the geomagnetic field lines. As a consequence, the plasma density in the F region shows a peak at an altitude much higher than the altitude of peak production. The dominant loss processes in the F region are

$$O^+ + O_2 \xrightarrow{\gamma} O_2^+ + O$$

$$O^+ + N_2 \xrightarrow{\gamma} NO^+ + N$$

$$O_2^+ + e \xrightarrow{\alpha} O + O$$

$$NO^+ + e \xrightarrow{\alpha} N + O$$

γ and α are typically of the order of 10^{-10} cm^3 s^{-1} and 10^{-7} cm^3 s^{-1} [*Banks and Kockarts*, 1973]. Under equilibrium conditions, the production rate q is given by

$$\frac{1}{q} = \frac{1}{\alpha N^2} + \frac{1}{\beta N}$$

where $\beta = \gamma[M]$, $[M]$ being the molecular concentration, and N the electron density which is equal to the sum of all atomic and molecular ions: $\sum N_i = N_A^+ + N_M^+ = N$

Therefore in the limits, q becomes

$$q = \alpha N^2 \qquad \text{if} \qquad \beta >> \alpha N$$

$$q = \beta N \qquad \text{if} \qquad \beta << \alpha N$$

In the E and lower F regions, the rate of electron loss is determined by the dissociative recombination reaction and the formula $q = \alpha N^2$ holds. The linear

relation $q = \beta N$ applies to the upper F region where the charge exchange reaction limits the loss rate of electrons. The transition region where both the processes are operative, is around 160 to 200 km. When this region happens to coincide with the level at which the F region ion production rate is the greatest (typically around local noon hours), splitting of the F region into F_1 and F_2 layers occurs. However, these layers merge into a single layer during nighttime.

As mentioned earlier, the loss coefficient β in the F region is a function of the concentration of molecules which participate in the ion-atom interchange reaction, and hence decreases exponentially with altitude. β^{-1} can be considered to be a measure of the average lifetime of individual ions. At 100 km, the lifetime of O^+ is about a few seconds which increases to the order of days in the upper ionosphere. After sunset, in the absence of any further production, the E region where molecular ions dominate, disappears mainly due to the faster recombination process. However, the ionization in the F region is retained all through the night due to the longlived atomic ions O^+. In this region, transport processes, namely, diffusion and plasma drifts compete with the loss process to take control of the behaviour of the entire F layer.

A change in the loss coefficient is effected by several ways [*Rishbeth*, 1986], changes in the ratio of molecular to atomic concentration of neutral air being one of them. Further, the loss coefficient is a sensitive parameter to neutral temperature and its changes through the temperature dependence of the reaction rate coefficients and the molecular concentration.

(2) Diffusion: The vertical diffusion of plasma through the ambient neutral atmosphere depends on the ion-neutral collision frequency and it is expected to control the behaviour of the ionospheric layer at very high altitudes. The diffusion is of ambipolar type, i.e., the ions and electrons diffuse together, and any separation between

them is nullified by the presence of an electric field which results in movements of both ions and electrons. The diffusion of ions and electrons varies with the dip angle since their motion is governed by the geomagnetic field and its configuration. In the F region, they are constrained to move only along the magnetic field lines as their gyrofrequencies are much higher than their collision frequencies with neutrals. The vertical diffusion coefficient, in terms of the dip angle I, is $D \sin^2 I$. Since the magnetic field lines are horizontal in the north-south direction, over the dip equator, the process of vertical diffusion of ions and electrons thus becomes unimportant. The diffusion coefficient D depends on neutral atmospheric densities through its dependence on ion-neutral collision frequency.

The behaviour of the F layer is governed by the competing roles played by the above two processes, namely, chemistry and transport due to diffusion. The concentration of ions and electrons varies as [O]/[M], ([M] being the molecular concentration) and does not rise indefinitely with altitude. As the loss coefficient decreases with height, above a certain altitude, there is sufficient time for the plasma to get redistributed by diffusion, i.e., the characteristic diffusion time becomes shorter than the plasma lifetime $1/\beta$. The F_2 peak lies at the transition height below which the plasma is in chemical equilibrium, and above which diffusion dominates. At the F_2 peak itself, the production and loss are approximately equal.

The dynamic F region is thus controlled by the interplay of the chemical and plasma diffusion processes. The F_2 layer can be moved by external forcings such as winds or electric fields to altitudes where the recombination and diffusion coefficients are different, and the plasma density distribution would vary accordingly. The F_2 layer on its downward motion enters regions of enhanced loss and the peak density $N_{\rm m}F_2$ decreases and the reverse is true when the F region moves upward. This mechanism was proposed initially for midlatitudes where the large dip angle of the

magnetic field lines aids diffusion in the vertical direction [*Rishbeth*, 1967, *Rishbeth et al.*, 1978], which essentially formed the basis of the 'servo principle' of the F region.

(3) Winds: The diurnal heating and cooling of the thermosphere generate horizontal gradients in pressure which drive neutral air circulation. The effects of winds on the ionosphere are many. A component of neutral wind in the north-south meridian plane is capable of inducing vertical motions to the F layer along the magnetic field lines. The vertical plasma velocity is given by $v_z = U \sin I \cos I$. An equatorward wind will push the plasma upward while a poleward wind can force it downward. The zonal motion of ions across the magnetic field produced by the zonal component of neutral winds leads to the generation of dynamo in the E and F regions. It is recognized now that some of the most important parameters of the ionosphere such as plasma drifts, electric fields, as well as the height distribution of plasma density, are governed to a large extent by the magnitude and direction of neutral winds.

(4) Ion-drag: The resistive force on the neutral winds arises through collisions with the ambient ions which, in the F region, are constrained to move only along the geomagnetic field lines. Thus the ions act as a brake on the winds and wave propagation. For the thermally driven wind systems, the ion-drag is the major force that limits the wind velocity and sets the neutral motion across the isobars. *Geisler* [1967] first derived a thermospheric wind system allowing for the decrease of ionization and hence the ion-drag from day to night. The equatorward motion at night was found to be stronger than the daytime poleward motion, suggesting the day-to-night variation of ion-drag. *Rishbeth* [1979] examined the effects of ion-drag on the neutral atmosphere and its motion in the equatorial region.

Ion-drag is important in providing momentum coupling to large scale oscillations and in exciting thermospheric tides [*Forbes*, 1982]. One of the phenomena, namely, the midnight temperature maximum (MTM) observed near the equator, is

believed to be an outcome of interaction between the tidal modes and the ion density variation [*Mayr et al.*, 1979]. At F layer heights, the ion-drag presents an additional interactive mechanism for the coupling of meridional and zonal components of neutral winds. Meridional winds transport ionization vertically along the magnetic field lines thus varying the resistance offered by the plasma to zonal flow. As an example, a poleward wind brings the F layer down enhancing the ion-drag force and the zonal component of the wind gets reduced in magnitude. This mechanism is shown to be effective during nighttime when the F layer is relatively thin compared to that during daytime. The neutral winds thus become sensitive to the vertical movement of the F layer [*Forbes and Roble*, 1990].

(5) Electric fields:

In the presence of an eastward electric field, the plasma in the F region undergoes an $\mathbf{E} \times \mathbf{B}$ drift. Near the magnetic equator, the presence of strong electric fields leads to the fountain effect that is responsible for the equatorial ionization anomaly [*Hanson and Moffett*, 1966]. Further, the electric field is one of the factors that is important in triggering plasma instabilities in the nighttime equatorial F region that culminates in the generation of a wide spectrum of irregularities referred to as equatorial spread F (ESF) [*Fejer and Kelley*, 1980; *Hanson et al.*, 1986]. Thus it could be seen that electrodynamic processes have a significant say in the processes of the equatorial/low latitude ionosphere.

To summarise, the chemical, fluid dynamical and electrodynamical properties of the thermosphere-ionosphere system are coupled. The height of the F region affects the plasma density through chemistry and the electrical conductivity through the ion-neutral collision frequency. The conductivity varies with electron density. The electric field is influenced by the conductivity through the Ohm's law. The neutral winds are affected by the ion-density through ion-drag. Both winds and electric fields, however,

control the ionospheric layer height, thereby closing the cycle of interactions. On a global scale, the horizontal gradient in pressure and the electric current density influence the wind and the electric field respectively thus initiating the complex web of interactions that occur in the upper atmosphere [*Walker*, 1988].

1.4 Dynamics of the upper atmosphere

The differential heating of the upper atmosphere by solar UV and EUV radiation sets in a variety of transport processes the complete understanding of which is necessary for the study of structure, energetics and dynamics of the atmosphere. The name 'tide' is given to the variation of a physical observable such as temperature and winds, in response to the absorption of solar radiation, and can be described in terms of integral multiples of the forcing parameter. In the upper thermosphere, the tides that are generated *in situ*, are basically diurnal in nature. The maximum in neutral temperature occurs at a local time of about 1600 h [*Hedin*, 1987]. Use of empirical models reveals a flow out from the high pressure bulge near the subsolar point and across the terminator into the low pressure region near the anti-solar point. Resolving the resultant motion into components in the latitude-longitude plane, at equinoxes, the motion is westward in the morning and eastward in the evening, and shows poleward motion during the day and equatorward at night [*Dickinson et al.*, 1975].

Fig. 1.4a illustrates the diurnal tide that occurs in the upper atmosphere. The result of transport processes is also depicted in the figure. The neutral gas temperature (T_g) exhibits a bulge on the sunward side (continuous curves) and a dip on the night side. Since the effect of the transport process is to redistribute energy by means of winds, the temperature at the subsolar point is expected to be slightly less and the temperature on the nightside is expected to be slightly more when dynamics is included. Heavier species show a bulge in their densities and lighter species show a

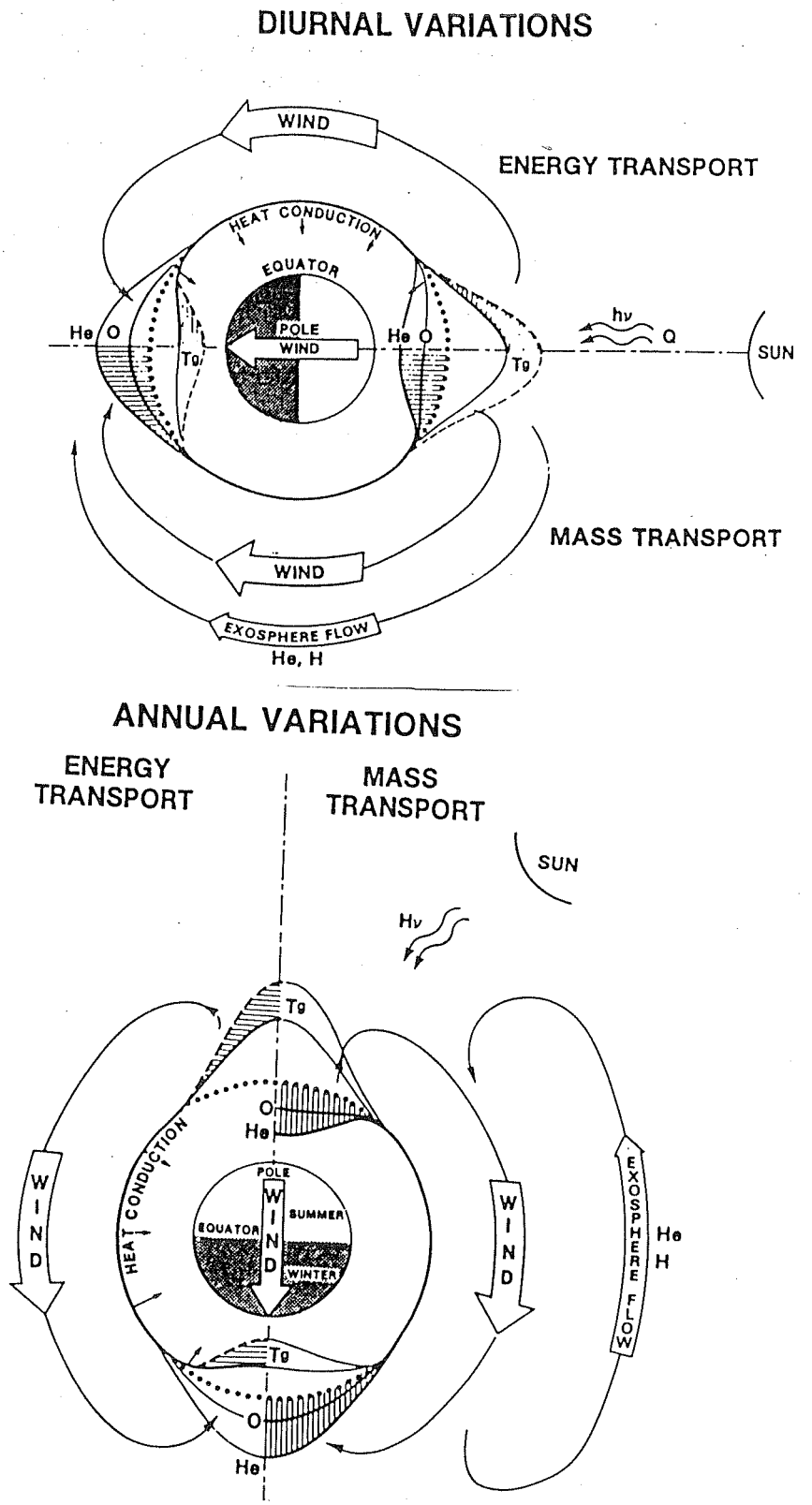

Fig. 1.4a,b. Schematic illustration of diurnal (top) and annual (bottom) tides. The variations in neutral gas temperature T_g, with (——) and without (- - -) dynamics, and the efffect of transport processes on O and He are depicted. (after *Mayr et al.*, 1978)

depletion on the dayside while the opposite effect is observed on the nightside. This mass transport has been discussed by *Mayr et al.* [1978] in the context of 'wind-induced diffusion'.

Apart from the diurnal variations in temperature and density, owing to the inclination of the sun, one of the hemispheres of the earth is heated preferentially in turn leading to the annual tide. Fig. 1.4b illustrates such a situation. A transequatorial wind ($\sim$ 40 m/s) blows from the summer to the winter hemisphere. Adiabatic heat transfer sets in to reduce the temperature contrast analogous to its role in the diurnal tide. Wind-induced diffusion accounts for depletion of oxygen and helium in summer and enhancements in winter. One of the F_2 region features, namely, the winter anomaly (larger ionization density during winter) has been thought of arising due to the increases of O in winter due to interhemispheric transport [*King*, 1964].

This qualitative picture of diurnal and annual variations of atmospheric parameters gets significantly modified during geomagnetic storms, to be discussed in the next section. Further, near the equator, the atmospheric structure and dynamics are much more complicated. *Hedin and Mayr* [1973], from the OGO 6 satellite data, presented latitudinal and longitudinal variations of N_2 density that revealed features which appeared to be controlled by the configuration of the geomagnetic field. Fig. 1.5 shows one of the examples of what is now called the 'neutral anomaly'. It can be seen that the late afternoon minima and the morning maxima tend to follow the magnetic equator. The geophysical process that is responsible for this observed feature is the equatorial ionization anomaly (EIA). The latter refers to the anomalous double-humped structure in the latitudinal distribution of F region ionization densities with crests (at $\pm$ 16° dip latitudes) on either side of the dip equator and a trough centered right on the dip equator [*Rastogi*, 1959]. This anomalous distribution in electron density arises due to the upward lifting of ionization during daytime in

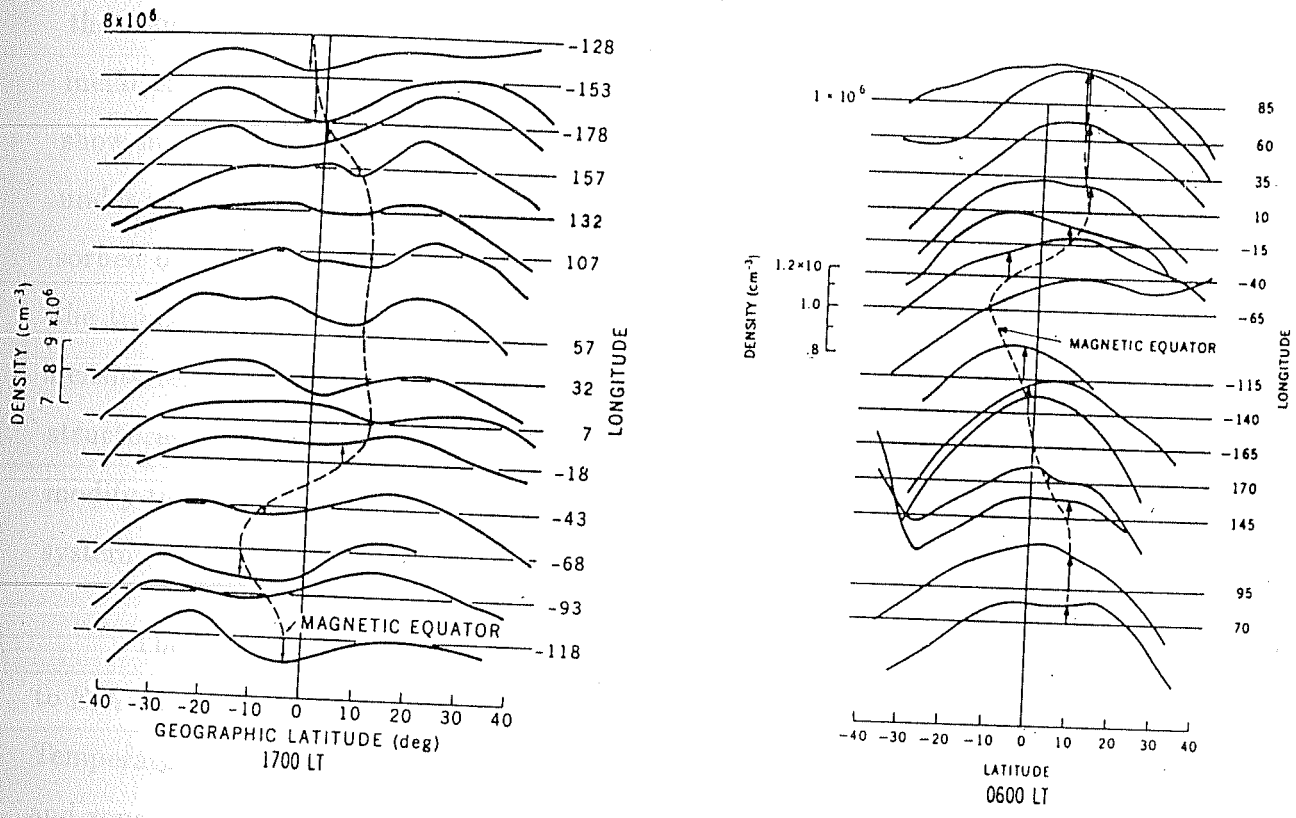

Fig. 1.5. An example of neutral anomaly during evening (22 September 1969) (left panel) and morning (16 March 1970) (right panel) periods over the equatorial region. The geomagnetic control of the latitudinal distribution of neutral densities ($[N_2]$ extrapolated to 450 km) is clearly evident. (after *Hedin and Mayr*, 1973)

the presence of crossed electric and magnetic fields over the equator and its subsequent diffusion along the magnetic field lines. *Hedin and Mayr* [1973] proposed a mechanism and formulated a model that showed the interactive nature of the neutral flow and the ionization anomaly. The winds that advect energy from the dayside toward the nightside get impeded in the presence of enhanced ionization density and become inefficient in transporting energy. Hence the temperature and density are expected to show increases at these locations. At the trough, the winds move past the longitude under consideration coasting towards the nightside and redistributing the energy absorbed on the dayside. The temperature and the density would show a minimum at the trough of the ionization anomaly. Thus the latitudinal distribution of electron density resulting from the EIA affects considerably the density and the temperature structures of the upper atmosphere. During this process, the EIA is expected to modify the neutral wind fields and the energy budget of the thermosphere-ionosphere system.

The first direct evidence on the anomaly in neutral temperature and winds due to EIA was provided by *Raghavarao et al.* [1991] who analysed the WATS (Wind And Temperature Spectrometer) data obtained by the DE 2 satellite. The temperature and zonal winds revealed features as proposed by *Hedin and Mayr* [1973]. The possibility of neutral air circulation that is forced by anomalies in ionization was explored earlier by *Dickinson et al.* [1971]. Using a two-dimensional steady state model, they have shown that for a large horizontal scale (anomalies of the order of a few thousand kilometres), the momentum coupling due to ion-drag produces significant perturbations in the horizontal velocity, vertical motion and the temperature field. Recently, the focus has been on the possibility of a wind system arising out of the temperature anomaly associated with EIA [*Raghavarao et al.*, 1993]. It has been shown that strong pressure ridges are collocated with the crests of the temperature anomaly when the zonal winds flow freely past between them. These pressure ridges near the crests of

EIA act as sources of vertical winds that transfer heat adiabatically.

An additional source of energy and momentum to the thermosphere lies in the tidal waves propagating from lower atmosphere. The forcing that gives rise to tides is of solar or lunar origin, arising from gravitational attraction or heating. It has been agreed that the lunar tidal component is only about 20 % of the magnitude of the solar component [*Forbes*, 1982]. The solar component is driven by diurnally varying insolation absorption, in particular, by water vapour in the troposphere and lower stratosphere, by ozone in the mesosphere and by all atmospheric constituents in the thermosphere. The amplitude of the waves that originate in the lower and middle atmosphere, increases as they propagate vertically upward, due to conservation of wave energy, until the wave breaks or is dissipated by viscosity, thermal conduction or ion-drag, in the thermosphere. The upward propagating diurnal waves are strongly absorbed near 105–110 km and are not expected to have a say on the thermospheric dynamics and energetics. The other components of the tides generated below the thermosphere, especially the semi-diurnal tides, play significant role in coupling various atmospheric regions. Efforts have been made by various workers in order to understand the processes that couple atmospheric regions and develop numerical tidal models [*Miyahara*, 1978; *Forbes*, 1982; *Vial*, 1986; *Forbes and Hagan*, 1988]. Recently, the three-dimensional thermospheric-ionospheric general circulation model [*Roble et al.*, 1988] is used to describe the diurnal and semi-diurnal tides by calculating the global velocity and temperature fields set up in response to various tidal components [*Fesen et al.*, 1986; *Fesen et al.*, 1991a,b; *Burrage et al.*, 1991]. These results suggest that the upward propagating tides significantly affect upper thermospheric temperature and dynamics particularly during solar minimum conditions. However, for a realistic weather prediction of upper atmosphere, the TIGCM results need to be tested against several available data sets on temperature and winds, as was done by *Burrage et al.* [1991] recently.

An example of the presence of semi-diurnal tides in the thermosphere at F region heights is the generation of a secondary maximum of exospheric temperature near midnight hours in the equatorial zone [*Spencer et al.*, 1979; *Mayr et al.*, 1979]. The midnight temperature maximum (MTM) arises mainly due to the momentum coupling of the diurnal tide and the diurnally varying ion-drag. The propagating tides (> 1) provide further momentum coupling that leads to the lability and the complexity of the MTM [*Herrero and Spencer*, 1982]. The wind fields get significantly modified in this process, with abatement of equatorward wind before midnight and reversal to poleward after midnight [*Herrero et al.*, 1988].

The thermosphere-ionosphere system is also perturbed by acoustic gravity waves (AGW) as they propagate through it. At high latitudes, the source of AGW lies in the auroral processes. Gravity waves originating in the lower atmosphere and propagating upwards, do contribute to the dynamics of the upper atmosphere, since they carry both energy and momentum [*Liu*, 1992] and provide a means of downward coupling between the magnetosphere and the ionosphere, upward coupling between the middle atmosphere and the ionosphere and the parallel coupling between the thermosphere and the ionosphere. Several review articles that discuss about the propagation characteristics of the acoustic gravity waves are available in the literature [*Hines*, 1960; *Hooke*, 1968; *Yeh and Liu*, 1974; *Francis*, 1975; *Richmond*, 1978; *Yeh et al.*, 1979; *Hunsucker*, 1982].

1.5 Physical processes associated with geomagnetic storms

In addition to its response to solar UV and EUV radiation, the upper atmosphere receives energy and momentum from the solar wind through the magnetosphere, in the form of precipitating particles and electric fields. During geomagnetic storms when

the solar wind-magnetosphere interaction is enhanced, large scale dynamic processes are driven due to heating at high latitudes. It was *Jacchia* [1959] who first inferred this heating from the orbital decay analysis of satellite data. In spite of lot of efforts that subsequently followed, many effects of the geomagnetic activity are not fully understood [*Prölss et al.*, 1988 and the references therein].

The thermospheric and ionospheric storms are consequences of an increased level of geomagnetic activity. The general features of ionospheric storms, in particular, F region storms, have been reviewed by *Rishbeth et al.* [1987]. It is now well recognized that the ionospheric storm at low and middle latitudes is a manifestation of the changes occurring in the composition and dynamics of the thermosphere during a geomagnetic disturbance. However, during certain times, the contributions due to protonospheric fluxes and electric fields are also important, for example, during the initial stage of a storm when magnetospheric electric fields penetrate to middle and low latitudes.

The overall response of the thermosphere to a geomagnetic storm is as follows. The dissipation of solar wind energy at high latitudes causes a temperature increase which in turn leads to an expansion of atmospheric gases. This expansion produces vertical winds and these winds transport mass and energy to higher altitudes. A bulge in the density and temperature occurs above the region where the energy was initially deposited, and sets up pressure gradients. Both mass and energy are transported by advection towards lower latitudes by means of horizontal winds. A return flow exists in the lower regions to complete the ciculation [*Prölss*, 1983]. The upwelling of air tends to decrease the ratio of light gas to heavy gas concentrations and the downwelling to increase it. Thus the observed composition changes have been thought of arising due to the large scale circulation [*Rishbeth*, 1975]. It has also been suggested that composition changes at midlatitudes might be caused

by propagation of waves such as planetary scale waves, long-period gravity waves or convective travelling disturbances [*Rishbeth et al.*, 1987].

A significant progress in our understanding on the magnetic storm associated changes in the neutral composition has been made due to a number of neutral mass spectrometers on board satellites like OGO 6, Esro 4, Aeros A and B, AE-C, D and E and DE 2. Fig. 1.6 illustrates the basic latitudinal structure of a thermospheric storm obtained by *Prölss* [1980]. He has made use of the Esro 4 satellite data on neutral composition. The top panel shows the development of the magnetic activity during the event and indicates the times at which the measurements were made. The lower panel depicts the storm associated changes in the exospheric temperature (T_∞), in argon (Ar), molecular nitrogen (N_2), atomic oxygen (O) and helium (He) densities, in the molecular nitrogen to oxygen density ratio ($[N_2]/[O_2]$) and in the total mass density (ρ). The extension of storm-effects to lower latitudes is clearly seen in this figure. The transition from intense to moderate activity effect appears to be around $\pm$ 35° magnetic latitude.

Most previous studies of geomagnetic activity effects in the neutral thermosphere have been concentrated on either high latitude or midlatitude regions. The focus has been on the understanding of the response of the high latitude thermosphere to a sharply time-varying forcing. Concerted efforts on the response of the equatorial thermosphere to geomagnetic storms have come about only recently [*Burnside et al.*, 1991; *Burrage et al.*, 1992; *Burns and Killeen*, 1992]. *Burrage et al.* [1992] have made use of the AE-E observations that demonstrated the extension of magnetic storm induced perturbations of $[N_2]$ and [O] in the upper thermosphere into the equatorial zone, but their results were mainly restricted to the midnight/early morning sector. They have pointed out the limitations in both MSIS and TIGCM models in reproducing the observed features. *Burns and Killeen* [1992] making use of

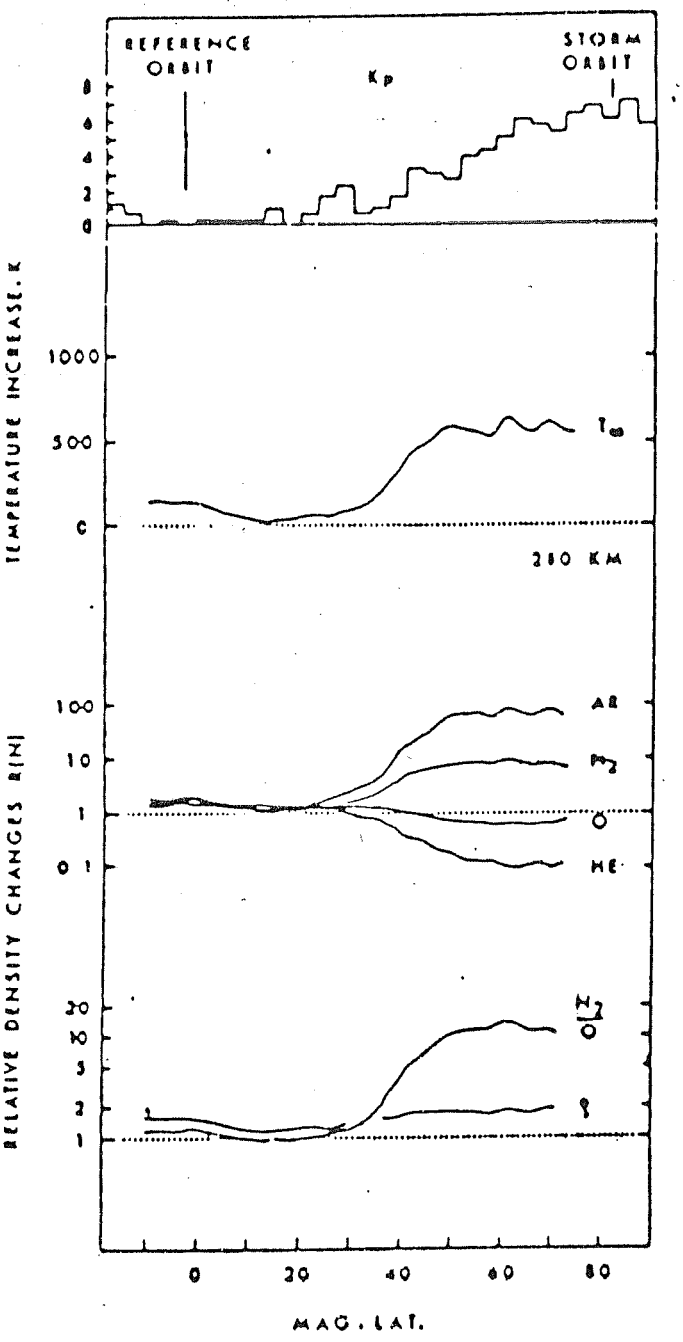

Fig. 1.6. Geomagnetic storm effects on the thermosphere as revealed by Esro 4 satellite data. The measurements were made when the planetary index K_p undergoes variation during the event as depicted in the top panel. The remaining panels illustrate the effects on neutral temperature, densities of Ar, N_2, O_2 and He, the ratio of N_2 to O_2 densities ($[N_2]/[O_2]$) and the total mass density (ρ) plotted with respect to geomagnetic latitude (after *Prölss*, 1980).

the DE 2 data on density and temperature have observed different morphological features of the changes in these measurements in the evening (1800–2000 h LST) and early morning (0400–0600 h LST) sectors. *Burnside et al.* [1991] have demonstrated the storm associated changes in wind fields over Arecibo, Puerto Rico, a low latitude station. Their ground-based Fabry Perot measurements show that the normal nighttime eastward flow of the neutral wind had reversed and that the meridional winds had shown very less equatorward velocities or at times very less poleward velocities. They have compared these observations with TIGCM predictions for Arecibo and demonstrated that after midnight on a storm day, the agreement has been rather poor. The inferred atomic oxygen densities from the incoherent scatter radar and Fabry Perot measurements were about twice as large as on other quiet nights. These observed features indicate that major storm effects in thermospheric winds and composition do propagate to low latitudes. Large increases in electron densities observed further show that these disturbances affect considerably the ionospheric structure over Arecibo.

1.6 Modeling studies

1. Thermospheric modeling:

Several models have been developed in recent times to predict both climatological patterns and instantaneous weather conditions of the upper atmosphere. They range from simple empirical specifications of a few selected parameters to highly complex three-dimensional numerical models.

The empirical models provide the average behaviour of the atmosphere under specified conditions. They are based on data sets collected over a long period by means of remote and *in situ*techniques. The data sets are synthesized, binned with

the aid of appropriate indices and then fitted with simple analytical expressions. The era of empirical and semi-empirical models began with the development of the Jacchia 1965 model, which was based on total densities of the atmosphere as determined from measurements of air-drag on satellites. This model was subsequently modified which culminated in Jacchia 1977, by including to some degree, the results of *in situ* composition measurements. The OGO 6 model [*Hedin et al.*, 1974] has been developed after the realization that the mass spectrometer measurements of densities of individual species were different from those expected from the Jacchia 1965 and 1971 models. The OGO 6 model has been subsequently modified that had led to the MSIS-77 model [*Hedin et al.*, 1977 a,b]. Temperature data from three incoherent scatter radars have been incorporated in this version. Making use of a wider data base, this model has been revised twice to represent better the seasonal differences in composition and temperature and magnetic storm variations [*Hedin*, 1983, 1987]. MSIS-86 model has been adopted as the new COSPAR International Reference Atmosphere (CIRA) empirical model which is now available in computer compatible form.

An empirical global model on thermospheric winds (HWM-87) is also available now [*Hedin et al.*, 1988] and is based on the wind data obtained from AE-E and DE 2 satellites. The limitations of this model are that it yields neither the altitude variations nor the solar cycle variations of horizontal winds, due to lack of data coverage. This model has been revised subsequently incorporating ground-based data from several incoherent scatter radar and Fabry Perot interferometers extending the data coverage in both solar activity and altitudes [*Hedin et al.*, 1991].

The global empirical and semi-empirical models represent the variations of a thermospheric parameter by an expansion in vector spherical harmonics with each expansion coefficient represented by a Fourier series. The input parameters they need are the solar decimetric flux index ($F_{10.7}$), the geomagnetic activity index (A_p), the

local time and the geographic coordinates. These models are readily accessible, easy to use, and represent well the average geophysical conditions of the thermosphere. The limitations of these models when used for a case study approach are many and are discussed later in this dissertation.

The other currently used thermospheric models include analytical and simple numerical models and thermospheric general circulation models. The MVH (Mayr, Volland and Harris) model of *Mayr et al.* [1978] makes use of a semi-analytical approach in which physical parameters are described in an expansion of spherical and Fourier harmonics by applying linear perturbation theory. Advection of both mass and momentum as well as the several dissipative processes are included in their approach. They have neglected mode coupling on the basis of the assumption that the most fundamental properties of thermospheric dynamics are of a linear nature.

The thermospheric general circulation models (TGCM) of both University College London (UCL) and National Centre for Atmospheric Research (NCAR) groups have been formulated primarily to study the global circulation, temperature and compositional structure of the thermosphere. They involve numerical solution of the primitive equations of energy and momentum with appropriate boundary conditions [*Fuller-Rowell and Rees*, 1980; *Dickinson et al.*, 1981]. With realistic specifications of energetic input from the UV and EUV components of solar radiation as well as due to solar wind-magnetosphere interaction and an appropriate global ionospheric model to compute ion-neutral coupling, these models are capable of generating a distribution of density, temperature and wind velocities in the low and middle latitude thermosphere. Though the predictive capability of the TGCM's is becoming more and more realistic, these models are much more complex to use, and the phenomenal computing resources are not readily accessible and available with many users.

2. Ionospheric modeling:

The wide range of ionospheric models include (i) empirical models based on extensive world-wide data sets, (ii) simple analytical models for a restricted number of ionospheric parameters, (iii) comprehensive, three-dimensional time-dependent models, (iv) spherical harmonic models and (v) models driven by real-time magnetospheric inputs [*Schunk and Sojka*, 1992; *Stening*, 1992].

The most comprehensive empirical model is the International Reference Ionosphere (IRI) that provides information on the global distribution of electron density, ion composition and electron and ion temperatures [*Rawer and Bilitza*, 1989]. The altitude variations of these parameters are described in terms of mathematical functions, while the variations with respect to latitude and longitude are described by orthogonal polynomials. The coefficients of the functions and the polynomials are adjusted so that the model agrees with the measurements. The IRI is ideally suited to midlatitude F region because of adequate data coverage.

The physical models of the ionosphere solve the continuity, momentum and energy equations for the electrons and ions either as a function of altitude or along curved geomagnetic field lines. These models have evolved from regional (an example being a model for the equatorial ionosphere developed by *Anderson* [1981]) to fully global ionospheric models [*Sojka and Schunk*, 1985]. In this case also, complex numerical methods and supercomputers are generally required to obtain the solution. Recently, realizing that the ion-neutral coupling is equally important for a realistic simulation of both thermospheric and ionospheric parameters, fully coupled self-consistent thermospheric-ionospheric general circulation models have been developed both by UCL and NCAR groups [*Fuller-Rowell et al.*, 1987; *Roble et al.*, 1988]. Fig. 1.7 illustrates TIGCM simulations of thermospheric temperatures and winds obtained by *Roble et al.* [1988].

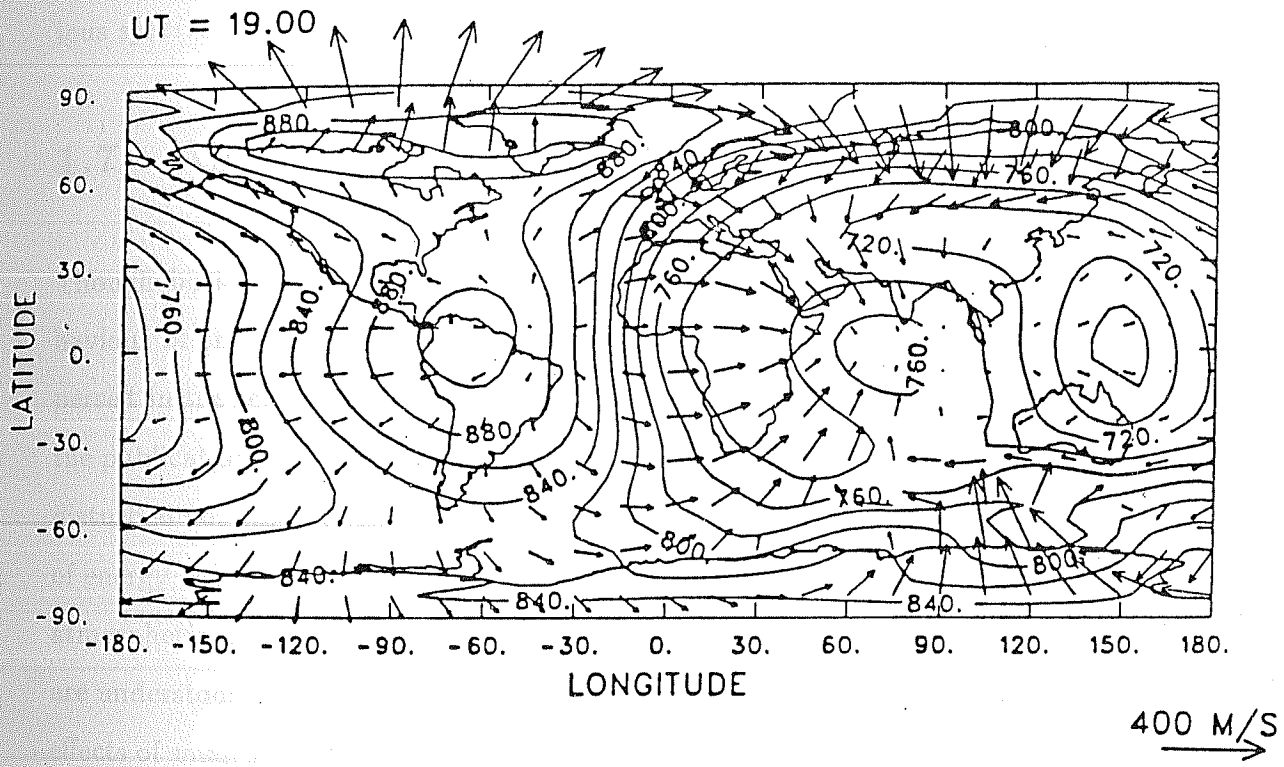

Fig. 1.7. Theoretical simulation of global thermospheric temperatures and winds for solar minimum March equinox conditions at 1900 UT on a constant pressure surface with a mean altitude of 286 km. The subsolar point is at the equator corresponding to 105°W longitude (after *Roble et al.*, 1988).

For an easy accessibility to common users, a new set of analytical models has recently been developed. The Fully Analytical Ionospheric Model (FAIM) of *Anderson et al.* [1989] is based on harmonic fits to the output from the Semi-empirical Low latitude Ionospheric Model (SLIM) developed by them earlier [*Anderson et al.*, 1987]. The FAIM is computationally efficient and provides electron density profiles for various spatial locations and times.

1.7 Aim of the present investigation

Though both the thermospheric and ionospheric models provide a reasonable behaviour of the respective regions, they do not represent the actual conditions that persist in the real neutral-plasma medium. As quoted by Rees in his introduction to the publication on CIRA models [1988], we have a non-linear medium that is strongly disturbed not only by changes in solar input and by a continuing, fluctuating, transfer of energy and momentum from the magnetosphere, but also by the lower and middle atmospheric inputs. The effects of the perturbations due to these external sources are understood only in a 'climatological sense'. Further, complexities arise due to the effects of small scale and rapidly fluctuating magnetospheric inputs and the propagating planetary, tidal and gravity waves. The future challenge relies on the continuous monitoring of the various inputs as well as a better parameterization of the existing models in terms of these inputs.

Apart from the disturbances of external origin, many of the features of the thermosphere-ionosphere system within, are not properly explained. The configuration of the geomagnetic field near the dip equator makes it unique in that some of the basic principles that are applicable to midlatitudes may not be valid at all in this region. The coupling processes of the thermosphere-ionosphere system play a different role in the equatorial and low latitude regions that had not been explored

till recently. The effects of electrodynamic processes on the neutral atmosphere and the resultant interactions in these regions have not been properly understood either.

The limitations in our understanding of the many physical processes of the low latitude thermosphere-ionosphere system have been due to the non-availability of data for various geophysical and geomagnetic conditions. Except for a few measurements scattered over the globe, the data base in the near equatorial zone is sparse, presenting difficulties in determining the variabilities of several geophysical parameters in response to the various inputs mentioned earlier. These aspects have led to the initiation of a comprehensive, coordinated thermospheric and ionospheric measurements and the results have formed a base for the present thesis.

Chapter 2

Instrumentation and data analysis

2.1 Basic requirements

The importance of airglow emission spectroscopy in monitoring the upper atmospheric parameters has been well recognized, since the early work of *Babcock* [1923]. The various emission lines and their relative intensities are well documented in the literature [*Chamberlain*, 1961]. The spectroscopic temperatures determined from line profile analysis are being used as measures of the kinetic temperature and its variations and as indicators of excitation mechanisms leading to airglow emissions. A knowledge of the rotational structure of molecules leads to determination of rotational temperatures. Several naturally occurring lines such as O_2 Atmospheric 0–1 band at 8645 Å, O_2 Herzberg bands and OH Meinel bands are being routinely studied to obtain rotational temperatures of the upper atmosphere. At heights where the atomic species dominates, the profile of an emission line is usually governed only by the motions of the atoms, and by the associated Doppler effect. This line-broadening serves well to define a Doppler temperature representing the region of emission. In the presence of neutral air motions, the whole profile gets shifted in wavelength due to Doppler

effect and the magnitude of this shift yields the value of line-of-sight wind. Measurements of Doppler parameters have been made on the atomic oxygen green (5577 Å) and red (6300 Å) lines by several workers [*Babcock*, 1923; *Armstrong*, 1953; *Bens et al.*, 1965; *Biondi and Feibelman*, 1968; *Shepherd*, 1969; *Hernandez*, 1977; *Sipler and Biondi*, 1978; *Hernandez and Roble*, 1979; *Rajaraman et al.*, 1979; *Burnside et al.*, 1981; *Meriwether et al.*, 1983; *Yagi and Dyson*, 1985; *Cogger et al.*, 1985; *Sridharan et al.*, 1991].

Following *Babcock* [1923] who demonstrated the use of interferometric techniques to detect the night airglow emissions, several studies have been made to evaluate the spectrometers used for such purpose [*Chabbal*, 1953; *Jacquinot*, 1954; *Connes*, 1956; *Meaburn*, 1976; *Desai*, 1984; *Hernandez*, 1986]. After making a comparative study of different instruments, namely, prism, grating and an interferometer like Fabry Perot etalon, *Jacquinot* [1954] concluded that for a given spectral resolution, the Fabry Perot interferometer has the highest luminosity of all these dispersing devices. The arguments forwarded by him in comparing the Fabry Perot with prism and grating spectrometers are discussed in detail by *Hernandez* [1986]. It is recognized now that the high resolution Fabry Perot Spectrometer is an ideal choice for line profile measurements of natural airglow emissions.

In the present study in which neutral temperatures and winds at F region heights are desired, a central aperture-scanned high resolution Fabry Perot Spectrometer is most suited for measurements of O I 6300 Å red line emissions emanating from an altitude of above about 250 km during nighttime. The Fabry Perot system is required to operate from Mt. Abu (24.6°N, 72.7°E geographic; 20°N dip latitude), a station located under the crest of equatorial ionization anomaly. As catalogued in the book on aurora and airglow by *Chamberlain* [1961], the red line is expected to have a pronounced post-twilight decrease and on some occasions a pre-dawn rise, the

intensity in the middle of the night averaging around 50 to 100 Rayleighs (1 Rayleigh = 10^6 photons/cm^2/s). The low intensities of O I 6300 Å red line at a low latitude station like Mt. Abu, pose stringent requirements on the stability and the flux gathering power of the instrument. During solar maximum period, due to the passage of crests of equatorial plasma fountain, the red line exhibits significant variations in its intensity calling for careful analysis of line profiles.

The basic design of the Fabry Perot Spectrometer selected for the present study is described following a brief discussion on the theory pertaining to such devices. The choice of various instrument parameters is argued upon, in the next section. The optimum operating conditions for its use are discussed next. A new data analysis procedure to recover Doppler parameters from the observed fringes is described in one of the sections to follow. The errors induced upon the retrieved parameters due to various reasons are elaborately examined and a criterion is set to select line profiles for analysis. Finally, the use of such a Fabry Perot in its applications to upper atmospheric studies is critically studied.

2.2 Theory of Fabry Perot Spectrometer

A complete mathematical treatment of Fabry Perot interferometers is described by *Hernandez* [1986]. In this section, only the important points are highlighted.

A Fabry Perot etalon is made up of a two high quality fused silica plates arranged perfectly parallel with a spacing t between them. On incidence at an angle θ to the normal, the light of wavelength λ undergoes multiple reflections and the transmitted and reflected rays interfere to form circular fringes. Constructive interference takes place for the transmitted light beam, when the path difference between rays is

an integral multiple of wavelength satisfying the following relation:

$$2\mu t \cos\theta = n\lambda \tag{2.1}$$

where n is the order and μ is the refractive index. The resultant reflected and transmitted beams can be collected by two separate lenses. It is seen that for a fixed wavelength λ, a change in optical spacing μt, forces λ to appear at any arbitrary angle θ, actually a set of θ's. This change can be accomplished by either changing the value of t or μ. If both μ and t are fixed, the necessary change in wavelength to vary the order by one unit is called the free spectral range (FSR) and is given by

$$\Delta\lambda = \frac{\lambda^2}{2\mu t} \tag{2.2}$$

The name, free spectral range, arises due to the fact that the separation between two lines is free of ambiguity over the wavelength interval defined by one order.

The behaviour of an ideal etalon of reflectivity and absorption coefficients being R and A respectively, is expressed as follows:

$$Y_t(\delta) = \left[1 - A(1-R)^{-1}\right]^2 (1-R)(1+R)^{-1}\left[1 + 2\sum_{m=1}^{\infty} R^m \cos(m\delta)\right] \tag{2.3}$$

[*Hernandez*, 1986]

where Y_t is the intensity of the transmitted beam and δ is the phase. Thus a strictly monochromatic beam undergoes broadening on passage through a Fabry Perot (FP) etalon. The spread of the resultant profile defines the instrument function of the FP etalon. The full width at half maximum (FWHM) ($\delta\lambda$) of the output profile is related to FSR through the instrument finesse N_R:

$$N_R = \frac{\Delta\lambda}{\delta\lambda} = \frac{\pi\sqrt{R}}{1-R} \tag{2.4}$$

This is called the reflective finesse. Since two lines cannot be resolved unless their wavelengths differ by $\delta\lambda$, the FP should have a limit of resolution of at least $\delta\lambda$. This

implies that the resolving power of the instrument is proportional to N_R. The finesse can be interpreted as the effective number of interfering beams which increases rapidly with R. With the advent of multi-layer dielectric coatings which eventually replaced metallic coatings, a value of N_R upto 300 can be achieved. Though such high values of reflectivity can be achieved, the finesse, in practice, is limited by plate defects of the etalon. Since the Fabry Perot plates are neither flat nor perfectly parallel, small deviations in both these quantities will broaden the output profile.

The effect of defects may be quantified by attributing a defect finesse to the interferometer [*Atherton et al.*, 1981]:

(1) Spherical defect: When the plates are spherically bowed with a maximum deviation δt_s from the plane surface, then the associated finesse is given by

$$N_{DS} = \frac{\lambda}{2\delta t_s} = \frac{k_s}{2} \qquad (\delta t_s = \lambda/k_s)$$

(2) Roughness defect: If the plate is not perfectly smooth and the root mean square deviation of surface irregularities appearing in the plate is given by $\sqrt{\delta t_G{}^2}$, then

$$N_{DG} = \frac{K_G}{4.7}$$

(3) Parallelism: The finesse associated with the departure from parallelism of the plates is given by

$$N_{DP} = \frac{K_p}{\sqrt{3}}$$

An overall instrument finesse is then written as

$$\frac{1}{N^2} = \frac{1}{N_R^2} + \frac{1}{N_D^2} \qquad \left(\frac{1}{N_D^2} = \frac{1}{N_{DS}^2} + \frac{1}{N_{DG}^2} + \frac{1}{N_{DP}^2}\right) \qquad (2.5)$$

Thus as the reflectivity of the coating is increased, the half width of the output profile reaches a lower limit determined by the overall defect finesse N_D.

An aperture is used normally to collect the flux over a solid angle. Since the signal transmitted by the etalon is integrated over this finite angular spread, further broadening of the resultant profile is effected by this process. The finesse due to the aperture-broadening is given by

$$N_{AP} = \frac{\Delta\lambda}{\delta\lambda_{AP}} = \Delta\lambda \left[\frac{\lambda d^2}{8 f_L^2}\right]^{-1}$$

where d is the diameter of the aperture, and f_L is the focal length of the lens used to focus the transmitted beams on to the aperture. For a fixed f_L, more and more flux can be collected by increasing the aperture size d as the finesse goes down.

Taking all the broadening factors into account, it is seen that the output profile of a Fabry Perot Spectrometer is a distortion of the original source profile. The broadening depends on the reflectivity, the quality and the surface defects of the etalon plates, the parallelism maintained between them and the aperture used.

2.3 Selection of instrument parameters

The foremost requirement of any high resolution optical instrument meant for the detection of faint line emission, is the aperture of the spectral device to be as large as possible. For nightglow measurements when detection of low emission rates (< 100 R) is desired, the Fabry Perot etalon is required to have an aperture of at least 125 mm [*Hernandez and Mills*, 1973] with good stability. Owing to limitations imposed by cost and other factors, an etalon of 100 mm usable aperture has been selected for the present study. The resolution of the instrument is determined by the order of interference selected, which can be made high by choosing a high value of the etalon spacing. A gap of 1 cm between the etalon plates with reflectivity of 85 %, yields a resolving power of 6×10^5 which is most suited for high resolution measurements. An air-gap etalon with optically contacted plates has been purchased from IC Opticals,

UK. The substrates that support the etalon plates are made of Spectrosil B of 30 mm thickness. The spacers use Zerodur as basic material because of its extremely low thermal coefficient of expansion. The flatness and the parallelism at wavelengths close to red region of the electromagnetic spectrum, have been specified to be $\lambda/100$ and $\lambda/20$ respectively. To measure a line profile, a change in the refractive index is effected by changing the pressure of the air between the etalon plates.

Following the description of the spectrometer described by *Jacquinot and Dufour* [1948], we use an annulus of zero inside diameter, i.e., a circular aperture, following the etalon. This aperture will receive radiation which passes through the etalon between angles 0 and θ, i.e., a cone of angle 2θ is subtended at the position of the aperture. Thus the field of view of the instrument becomes 2θ. If the size of the aperture f is expressed in orders, say, then

$$\cos\theta = 1 - f/n_0 \tag{2.6}$$

where n_0 is the central order [*Hernandez*, 1986]. Using the definition of half width ($\delta\lambda_{AP}$) of the profile due to aperture broadening given in the last section, the relation between f and $\delta\lambda_{AP}$ is

$$f = \frac{\delta\lambda_{AP}}{\Delta\lambda}$$

f being a fraction of the free spectral range.

For an ideal etalon with high reflectivity, the resolving power $R_0 = n_0/f$ and hence the solid angle $\Omega = 2\pi f/n_0$ becomes $\Omega = 2\pi/R_0$ which is the result arrived at by *Jacquinot* [1954]. Thus the product of the solid angle of acceptance and resolving power is fixed and is equal to 2π. The resolving power R of the instrument examining a line source of finite width, however, is less than R_0, since the resultant width becomes greater than f [*Hernandez*, 1986].

In the literature, two methods of selecting the optimum aperture size have

been discussed [*Chabbal*, 1953; *Hernandez*, 1979]. *Chabbal* [1953] made use of the requirement that the product of flux received by the optical device and the resolving power is greatest, what is called later an LRP criterion. This was found to occur when the ratio of the FWHM of the aperture f to the FWHM of the etalon-source combination is near unity. He plotted the ratio of the ideal etalon width to the resultant width and the ratio of the flux transmitted by the aperture to that flux transmitted over one free spectral range, as a function of the ratio of aperture width to etalon width (f/a). When the product of the former two ratios is plotted against f/a, there exists a maximum value of intensity for which f/a is 1.15. In practice, there exists a range of values of f/a ($0.9 < f/a < 1.5$) when the intensity for a given resolution is constant and maximum (Fig. 2.1). Thus using the LRP criterion, a compromise between instrumental broadening and luminous flux can be made.

Hernandez [1979] has discussed the limitations of this method for the optimum choice of resolution of the instrument. The LRP criterion is strictly applicable only when the recorded line is well separated from other wavelengths prominently placed in the spectrum. This may not hold when the emission line is contaminated by a continuous background and when noise inherent in the signal reduces the precision with which the Doppler parameters are retrieved using this criterion. *Hernandez* [1979, 1986] has derived the optimum conditions for operating a Fabry Perot Spectrometer taking into account all these factors. For minimum uncertainty in the retrieved parameters, he has obtained a set of values for a, f and dg, the widths corresponding to an ideal etalon, the aperture and the Gaussian line source. Near the optimum points of operation, the effects due to surface and curvature defects of the etalon are negligible [*Hernandez*, 1982a]. Least minimum uncertainty in the Doppler temperature occurs when a, f and dg take values of 0.07, 0.13 and 0.22, normalized with respect to free spectral range. Similarly, for the wind determination, he has obtained values of 0.14, 0.256 and 0.28. He has suggested that when simultaneous wind and

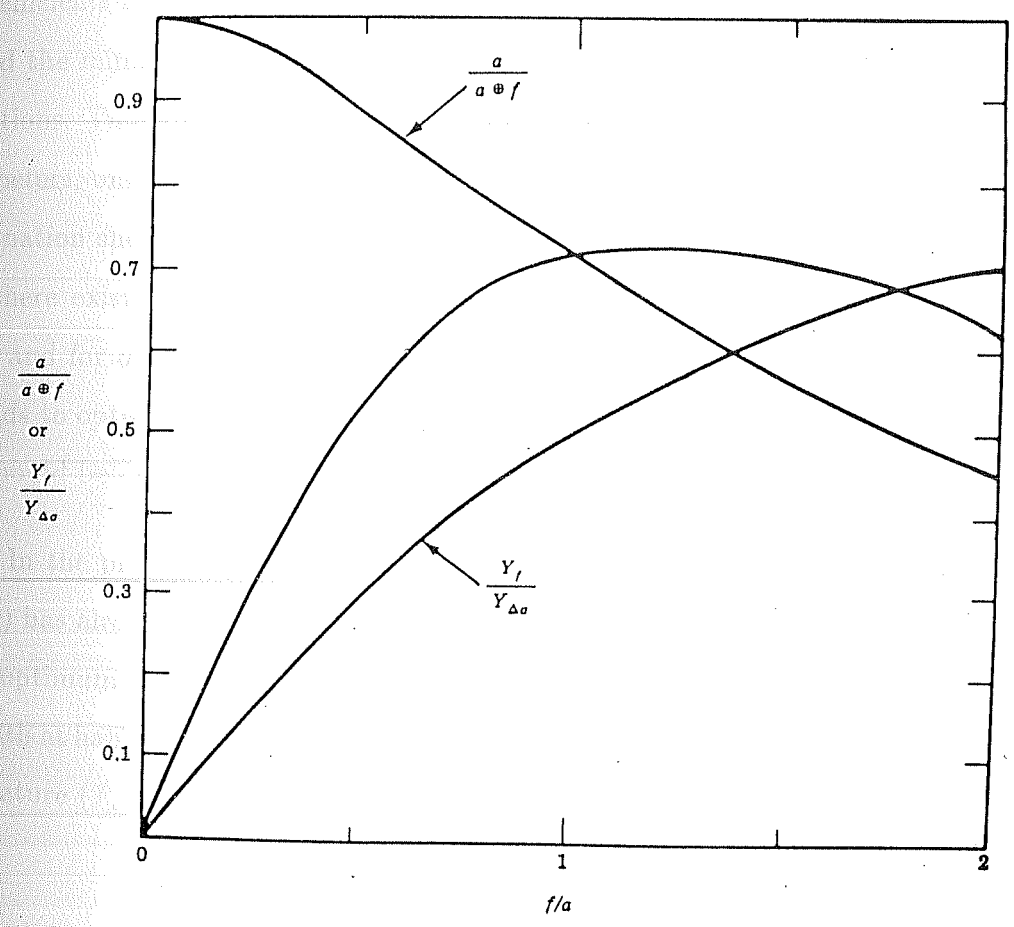

Fig. 2.1. Optimum range of operation of a Fabry Perot Spectrometer. The curves plotted are (1) the ratio of ideal etalon width to resultant width (convolution of ideal etalon function with the aperture broadening function), $a/(a \otimes f)$, versus ratio of aperture width to etalon width (f/a) and (2) the ratio of flux transmitted by the aperture to that flux transmitted over one free spectral range, $Y_f/Y_{\Delta\sigma}$, versus f/a. The product $a/(a \otimes f)$ and $Y_f/Y_{\Delta\sigma}$ is shown as the unlabeled curve. The optimum range of operation corresponds to the broad maximum. (after *Hernandez*, 1986)

temperature measurements are desired, it is necessary to use the parameters obtained from minimum uncertainty in temperature. Since the response of a Fabry Perot Spectrometer can be expressed in terms of a Fourier series, the minimum number of coefficients necessary to unambiguously describe a measurement becomes equal to 7, and the minimum number of samples to be taken is twice this number, for these conditions. Though the LRP criterion does not demand any preference for the above parameters, only that the ratio of the scanning aperture to the etalon-source width combination should be nearly unity. However, the results by *Hernandez* [1979] show that there exists a set of parameters for the least uncertainty in temperature and winds and for other values, the uncertainties are more. Thus use of these different methods to optimize the instrument, yields different results for the set of parameters that should be used.

In the present study, since a, the normalized FWHM of the etalon (without defects) has already been fixed (= 0.0519, for a reflectivity of 0.85), it is desirable to use an optimum value for the scanning aperture. The relation between the normalized full width at half maximum of an emission line of central wavelength λ and the Doppler temperature (T_n) is given by

$$dg = 7.16 \times 10^{-7} \lambda (T_n/M)^{1/2} / \Delta\lambda$$

where M is the molecular weight of the emitting atom. For a temperature of 1000 K and when the emitting atom is oxygen, $dg = 0.1797$ at $\lambda = 6300$ Å. This width varies from a value of 0.127 for $T_n = 500$ K to a value of 0.22 for $T_n = 1500$ K. We have adopted the LRP criterion of *Chabbal* [1953] to determine the resolution of the instrument for maximum luminosity. It is seen later that as the selected parameters are not too far from the best set of parameters arrived at by *Hernandez* [1979], the increase in standard deviation of Doppler parameters for the selected set is small.

The following calculations were made to arrive at the optimum value of f,

given all the etalon parameters. We shall consider an emission profile of Gaussian shape with a Doppler temperature of 800 K. This yields the source width $s = 0.1607$ (normalized with respect to free spectral range).

With the given etalon parameters, the contribution of the etalon to the broadening of a monochromatic line is given by $e = 0.1162$ (corresponding to an etalon finesse of 8.6). A source of width s will get broadened by the etalon and the resultant width is a convoluted product of e and s. This turns out be 0.1983 for the above selected value of s. Use of the LRP criterion that $f/e \otimes s$ should vary between 0.9 and 1.5 implies a value of aperture diameter in the range 3.3 mm to 4.3 mm, using the basic definitions presented in last section. We have chosen a value of 3 mm for the size of the aperture for which the luminosity should be very close to its maximum. An aperture of 3 mm diameter leads to a width $f = 0.1428$. Using equation (2.6), this corresponds to a field of view of 0.34° for the instrument.

It is interesting to compare the set of parameters arrived at with that recommended by *Hernandez* [1986] for least uncertainty in the retrieved Doppler parameters. The above value of f is different only by 9 %. For the extreme conditions of $T_n = 700$ K and $T_n = 1500$ K, the selected value of s deviates by 30 % for the lower limit and approaches that obtained by the least uncertainty criterion of Hernandez as the temperature reaches its upper limit of 1500 K. However, the present value of the ideal etalon width is 70 % of that using the least uncertainty criterion. Since the derived and the available parameters, f, a and s, are close to their optimum values determined by least uncertainty criterion, the minimum uncertainties of determination are expected to be only slightly larger than what have been arrived at by *Hernandez* [1979].

2.4 Experimental details of the Fabry Perot Spectrometer

The optical lay-out of the high resolution Fabry Perot Spectrometer used in the present investigation for upper atmospheric studies is depicted in Fig. 2.2. This FPS system is being operated from Mt. Abu since the winter months of 1985. The position of the instrument within the observatory is such that detection of light from only two, namely, south and east, out of the four cardinal directions is possible. The lowest elevation chosen for the measurements of the horizontal component of neutral wind, has been 20°. Because of the increased emission column, the apparent emission rate of the natural airglow increases by a factor of almost 2 relative to that for the overhead sky (Van Rhijn advantage). It becomes necessary to gather light from a low elevation sky, especially during solar minimum period, when the 6300 Å line intensity decreases continuously throughout the night, with occasional recovery around midnight. Since the large scale geophysical processes of interest like equatorial ionization anomaly and equatorial spread F depend on the configuration of the magnetic field and originate over the dip equator, observations are confined to emissions originating from magnetic south. For wind measurements to be discussed later, the reference wavelength is obtained from the measurements made overhead (zenith), with the assumption that the Doppler shifts in the vertical direction are negligible.

Front silvered mirrors are used to direct light from the sky to the FPS. The optically contacted etalon is sealed inside a housing with an optical window in the front end and a lens (L_1) in the rear end. The beam of light after multiple reflections is projected onto the scanning aperture by means of the lens L_1 of focal length 50 cm. The beam is collimated before getting directed into a narrow band (3 Å) interference filter which selects the wavelength of interest and the resultant beam is focused onto the photocathode of an EMI 9863 A photomultiplier tube with a cathode sensitivity

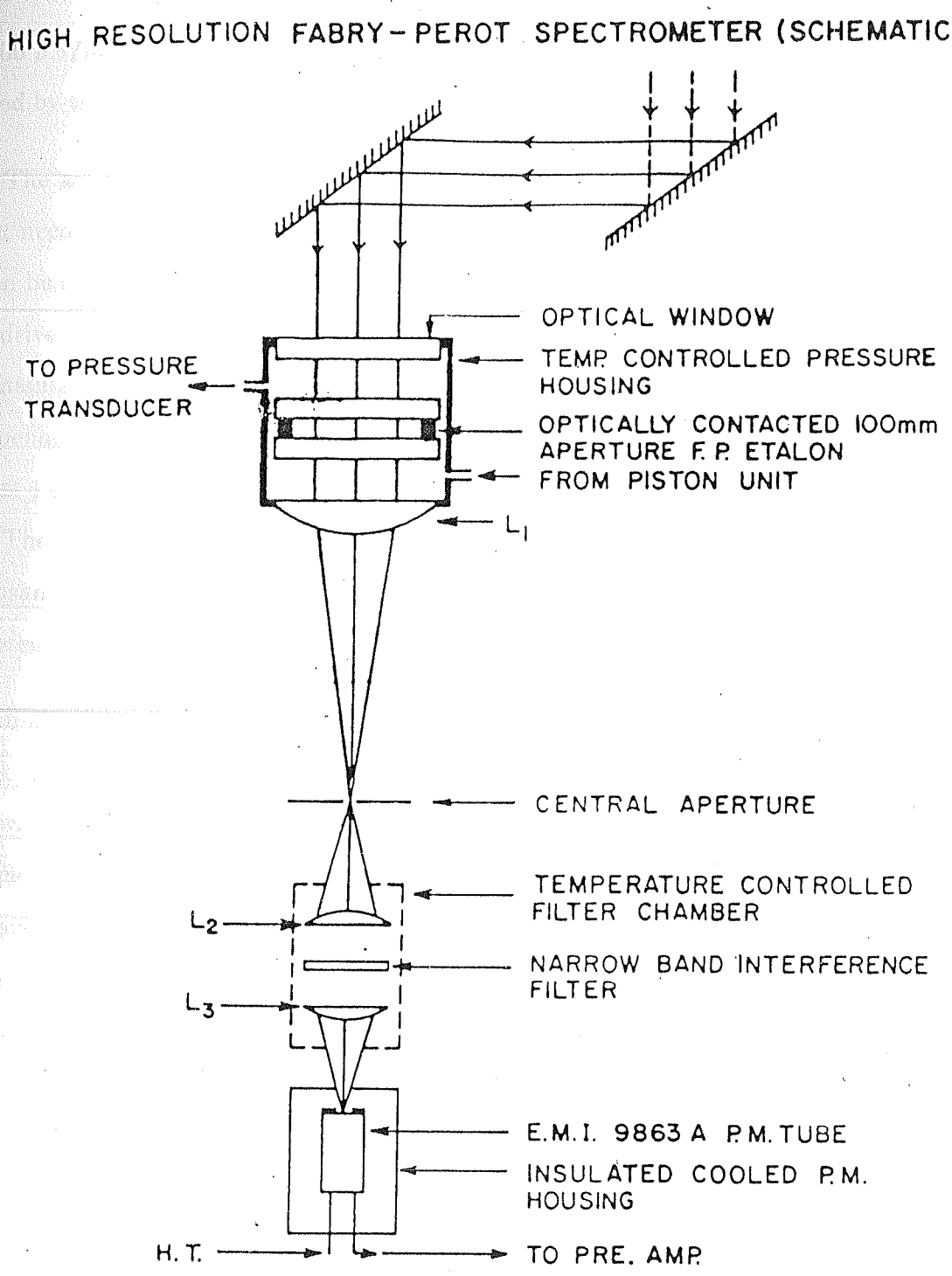

Fig. 2.2. Schematic diagram of the high resolution Fabry Perot Spectrometer (central-aperture pressure-scanned).

of ~ 200 μA/lumen. The data acquisition system employed for counting the photons collected by the etalon and integrated over the area of the aperture, is described later.

The air between the plates of the etalon acts as a medium whose refractive index μ needs to be changed to get the spectral distribution of incident radiation. This can be achieved by changing the pressure of the air. A stepper motor controlled piston drive unit serves this purpose. The limitations of using pressure scanning are in maintaining the linearity of the change in μ with pressure, and the temperature dependence of μ. With air as the medium, a pressure change of about 90 torr (1 torr $\equiv$ 1 mm Hg) results in one order change (FSR = 0.1985 Å) for a 1 cm gap etalon. The change in μ for this pressure change is non-linear to only about 1 part per thousand [*Hernandez*, 1986] and hence can be assumed to be negligible for the work presented here.

An absolute temperature-controlled pressure transducer (type 590, Datametrics Inc.) is used to monitor the pressure. This has a Barocel pressure sensing element which acts as a high precision stable capacitive potentiometer in which the variable element is a thin highly prestressed metal diaphragm. Positioned between fixed capacitor plates, the diaphragm forms the separation between the two gas tight enclosures. A difference in total pressure within enclosures produces a force which deflects the diaphragm and varies the relative capacitance of the diaphragm and the fixed capacitor plates. The capacitance variations are converted into voltage whose amplitude is proportional to applied pressure. The prescribed accuracy of pressure reading is $\pm$ 0.05 %. The etalon housing has two external ports, one connected by a rubber tube to the piston drive unit for changing the pressure and the other for monitoring the pressure through the pressure transducer.

Since the refractive index μ also depends on the temperature, the thermal stability of the etalon is important, especially when the measurements of neutral

winds are desired. It is necessary to maintain the temperature of the etalon to better than 0.1° C (corresponding to a shift of 0.0002 Å which is equal to a wind of 10 m/s). Typically the winds in the upper atmosphere are of the order of 50 to 100 m/s. The thermal stability is achieved by means of a dual heating enclosure. The gap between the etalon chamber and the outside jacket kept close to each other, is maintained at a constant temperature by an on-off type temperature controller. The resistive heating element wound on the etalon chamber is used as a part of a linear-proportional temperature controller. This dual heating system is found necessary in order to encounter the variation in room temperature at Mt. Abu, which becomes pronounced during winter.

Coming to the separation of the selected wavelength λ, the lens L_2 is used to collimate the beam for normal incidence to fall on the narrow band interference filter (3 Å bandwidth; 35 % peak transmission at 6300 Å). The interference filter makes use of the same principle as that of Fabry Perot etalon but with a spacing of a few thousand angstroms thickness. The reflectivity of the filter is greatly increased by the use of a multi-layer dielectric coating. Each layer has a thickness of $\lambda/4$ with a refractive index either higher or lower than the layer adjacent to it.

The filter is tuned to the wavelength λ of interest (i.e., 6300 Å) by changing μ of the coatings. In this case, the temperature is varied till the peak transmission of the filter reaches λ. The characteristics of the filter have been studied and calibration curves for different temperatures obtained for the actual experimental set-up. This method is adopted to circumvent the shift in the peak transmission towards lower wavelength side due to the filter getting tilted unwantedly at the time of integration. The temperature control of the filter is maintained to better than 0.5^0 C, and is achieved by using Peltier elements and a bipolar temperature controller. Since the ambient temperature condition over Mt. Abu has a wide fluctuation seasonally, Peltier

elements are used in heat/cool mode. The filter along with the collimating and the camera lenses is sealed in an assembly and is attached to the earlier optics.

The filtered beam collected by a focusing lens L_3 is then projected onto the photocathode of 9 mm effective diameter, of an EMI 9863 A photomultiplier tube. The photocathode material is of S-20 type (Na_2KCsSb material) with a quantum efficiency of 6 % at red wavelengths. The gain of the PMT is about 3×10^7 and the rise time of the output pulse is typically 2.5 ns. A thermoelectrically cooled housing is made use of, for cooling the PMT to less than about - 15° C, to bring down the thermal noise. The PMT is operated at a high optimum voltage of 1650 V. The voltage level is such that the mean signal pulse height is well above the pulse height of the noise which results from thermionic emission from the photocathode as well as other sources such as preamplifier noise and electromagnetic interference pickup. An EMI pulse amplifier/discriminator is being used to amplify the signal and to select signal pulses by setting the discriminator at a proper level. The resulting pulses are transferred to counter 'A' of SR400 gated photon counter (Stanford Research Systems Inc.). The latter measures the intensity of the signal by counting the number of photons which are detected by the PMT in a given time interval decided by the stepper motor piston drive (operator selectable). The pressure information which is available in analogue form from the pressure transducer is passed through a precision voltage-to-frequency converter and fed as input to counter 'B' of SR400 gated photon counter.

The schematic of the complete data acquisition system for the Fabry Perot Spectrometer is shown in Fig. 2.3. The two channels available within the gated photon counter are made use of for the pressure and intensity information which at each step of the spectral scan, is transferred to an IBM PC for on-line plotting and to be stored in floppy diskettes after the completion of the scan. The movement of

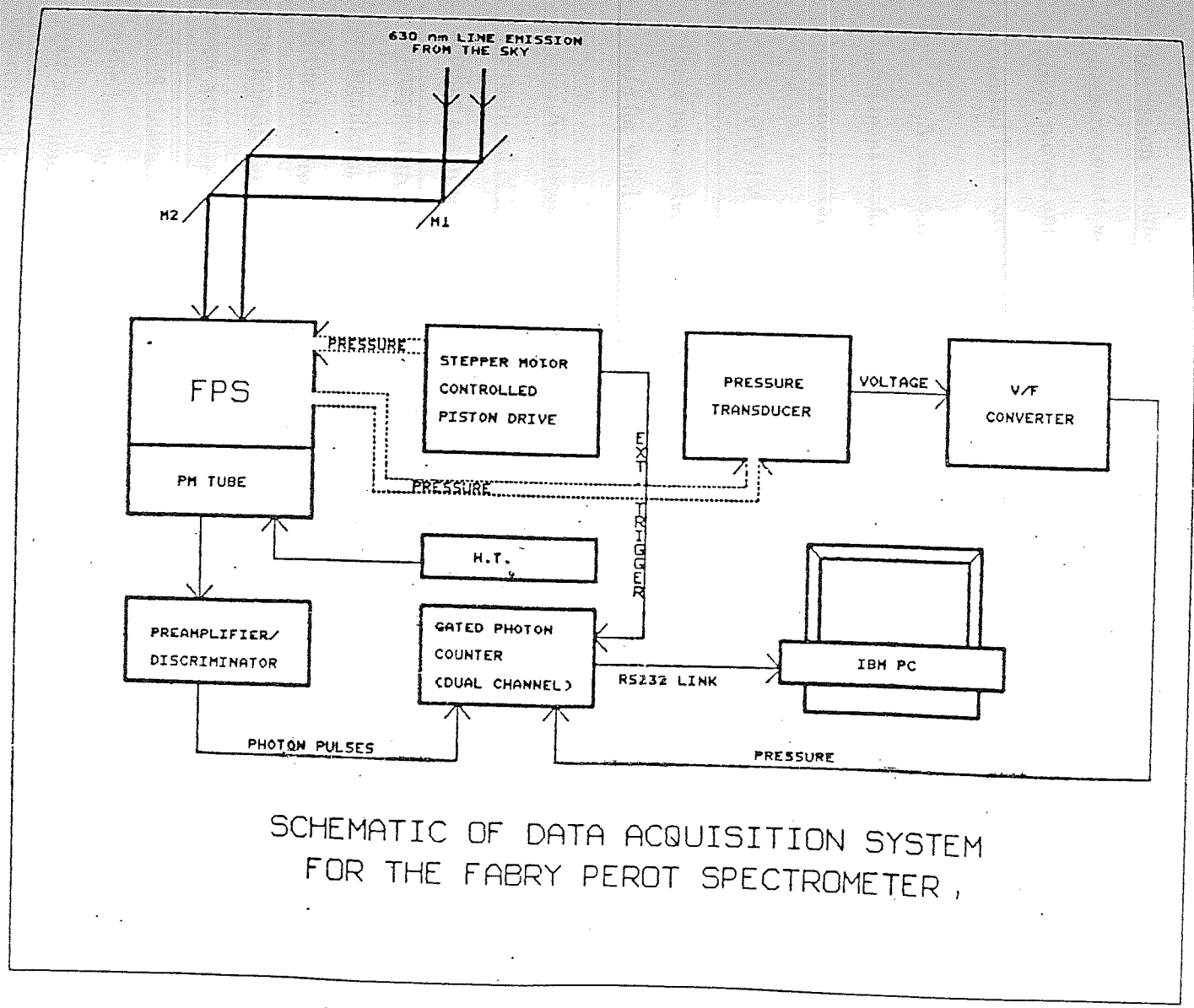

Fig. 2.3. Block diagram of the complete data acquisition system for the Fabry Perot Spectrometer.

the piston by the stepper motor is synchronized to the data acquisition. After every movement of the piston which changes the pressure by $\sim$ 1 torr, the pressure inside the etalon chamber is allowed to stabilize. The respective counters for photon and pressure counts are enabled, the counts accumulated for a preset integration time, the piston moved and the cycle repeated. At each pressure step, the airglow photons are counted for 8 seconds and a spectral scan covering 1 order lasts for about 18 minutes.

A single mode helium-neon laser operating at 6328 Å is used to obtain the instrument profile at the beginning of observations on each night. The representative instrument parameters observed on 13 February, 1991 are as follows:

FWHM = 12.46 torr; FSR = 91.061 torr; Contrast = 15

These parameters yield an overall instrument finesse of 7.3 which is considered adequate for wind and temperature measurements.

As discussed in the next section, the measured instrument profile is used for the retrieval of Doppler width. For the pressure-scanned Fabry Perot Spectrometer, it is being assumed that the variation in the refractive index (μ) with respect to changes in temperature between the etalon plates, is either negligible or small. If the changes are significant upto, say 0.1°C, then the magnitude of the drifts in the peak position of the line profile due to changes in temperature, need to be known beforehand for the line-of-sight wind measurements. An AD-590 precision temperature sensor has been attached to the body of the etalon to continuously monitor the temperature of the etalon chamber. Making use of the convenience of setting the temperature of the heating system used for the thermal stability of the etalon to our choice, the peak positions of the highly stable, single mode, 6328 Å He-Ne laser profile were determined for various chamber temperature settings after allowing sufficient time to lapse for the etalon chamber to get stabilized. Fig. 2.4 is a result of such an exercise.

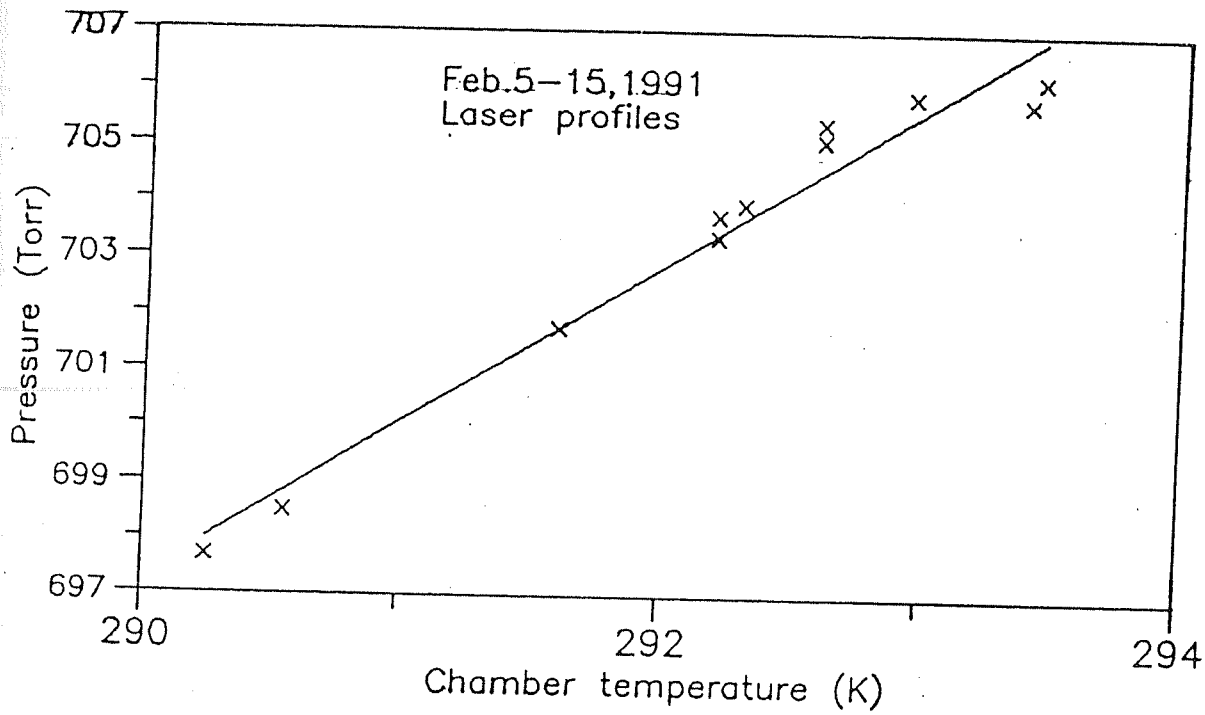

Fig. 2.4. Drifts (measured in pressure units, i.e., torr) in peak position of Fabry Perot fringes obtained using a highly stable He-Ne laser with respect to changes in temperature between the etalon plates. The slope of the best fit curve has a value of 2.77 torr/K.

The instrument profiles obtained on each of the nights during the February, 1991 campaign were made use of, for this purpose. The linear increase in pressure corresponding to the peak position, with chamber temperature, when the latter varies by 4 K, is to be noted. The best fit line yielded a slope of 2.77 torr/K, which has been incorporated as a correction for determining Doppler shifts.

2.5 A method to retrieve Doppler parameters from observed fringes

The output profile of the Fabry Perot Spectrometer is essentially a distortion of the source profile due to the various broadening factors discussed in section (2.2). The instrument acts as a window over which each spectral element of the source function is integrated. In other words, the expected output profile $\phi(x)$ is a resultant of the convolution of the source function $S(x)$ and the instrument broadening function $I(x)$ and can be expressed as

$$\phi(x) = \int I(x - x')\, S(x')\, dx' \tag{2.7}$$

In practice, the observed profile is contaminated by noise inherent in the detected signal, the background continuum and the contribution due to neighbouring sources, if present. If $O(x)$ represents the observed profile, $\epsilon(x)$ the noise and other extraneous factors and B the background continuum, then

$$O(x) = \phi(x) + \epsilon(x) + B$$

The problem is to solve for $S(x)$, the source function under consideration given $O(x)$ and $I(x)$ and then retrieve the Doppler parameters of interest from $S(x)$. There are two ways of doing this.

(1) Assuming that the noise and the background are insignificant, express each of the functions in (2.7) in terms of their Fourier transforms. In the Fourier domain,

the convolution becomes simple multiplication of the Fourier transforms of the two functions. The deconvolution then can be easily performed since the problem reduces to a simple division. The solution is obtained by taking the inverse Fourier transform of the resultant function. However, this method becomes useless when the noise inherent in $\phi(x)$ and to a lesser extent in $I(x)$ gets amplified in the deconvolution process [*Anandarao and Suhasini*, 1986]. *Cooper* [1977] expresses this important fact in the following way:

'All too often deconvolution procedures are applied blindly to ailing data with the expectation of a miraculous recovery of information. However, the hallucinatory side effects of this particular course of treatment can be more damaging than the original illness !'

(2) The second approach is to take into consideration the noise $\epsilon(x)$ in the observed profile $O(x)$, which can be effectively filtered out by applying one of the smoothing procedures to the acquired data before the Doppler parameters are determined. The noise-free data can then be subjected to an appropriate statistical optimization method to arrive at the solution, i.e., to retrieve the source profile $S(x)$ under consideration. Several workers have followed the general non-linear least squares approach to estimate the best solution for the Doppler parameters of $S(x)$ [*Hays and Roble*, 1971; *Hernandez*, 1986; *Meriwether et al.*, 1986; *Okano and Kim*, 1986; *Sahai et al.*, 1992b].

We have developed a new method entirely suited to the quality and the amount of data that are being collected. Though the approach is based on the general non-linear minimization principle, the method at each step takes care of the practical problems we faced during observations and enables us to examine and overcome the limitations imposed by various factors in retrieving the Doppler parameters. The method of line profile analysis is as follows.

It can be assumed that the line source associated with the optical observation of this kind is described by a function $S(x)$ that is of Gaussian shape.

$$S(\lambda) = \frac{S_0}{d\lambda} \exp\left[-\frac{(\lambda - \lambda_o)^2}{(d\lambda)^2}\right] \tag{2.8}$$

S_0 is the intensity of the line whose center wavelength is λ_0 and $d\lambda$ is the Doppler width of the emission profile and is related to the full width at half maximum ($\delta\lambda$) by $\delta\lambda = 2\ (\ln 2)^{1/2} d\lambda$ and to the kinetic temperature (T_n) by

$$\delta\lambda = 7.16\times10^{-7}\lambda_0(T_n/M)^{1/2}$$

where M is the molecular weight of the emitting species in amu.

In its discrete form, the convolution integral can be written as

$$\phi(x_i; p_j) = \sum_{k=1}^{n} I(x_i; x_k)\ S(x_k; p_j) \tag{2.9}$$

Here p_j's (j = 1,2,3) represent the parameters of the Doppler profile to be determined. n is the number of data points. In terms of p_j's, $S(x)$ becomes

$$S(x_k; p_j) = \frac{p_1}{p_3} \exp\left[-\frac{(x_k - p_2)^2}{p_3^2}\right]$$

p_1 being the peak line intensity, p_2 the line centre and p_3 the line width. x_i is a variable that describes the scan of the device. In our experiment, it represents the value of the pressure at a particular step i. The summation of (2.9) is over one free spectral range, and if there are n steps to cover this, then we have n equations for $\phi(x_i; p_j)$.

The criterion for estimating p_j's is minimization of the sum of squares of deviation ($[\chi(p_j)]^2$) between the observed and the expected profiles at each step i which would then lead to a best set of estimates of p_j's.

$$\text{If} \qquad [\chi(p_j)]^2 = \sum_{i=1}^{n} [O(x_i) - \phi(x_i; p_j)] = \sum_{i=1}^{n} [\epsilon(x_i)]^2 \tag{2.10}$$

then minimization of $[\chi(p_j)]^2$ implies

$$\frac{\partial}{\partial p_j}[\chi(p_j)]^2 = \frac{\partial}{\partial p_j}\sum_{i=1}^{n}\left[w_i\,[O(x_i) - \phi(x_i;p_j)]^2\right] = 0$$

that can be solved for p_j's.

There are several methods available for searching parameter space for a minimum of $[\chi(p_j)]^2$ [*Bevington*, 1969]. An alternative to such methods and a simpler approach would be to linearize the fitting function $\phi(x_i;p_j)$ in the neighbourhood of optimum values of p_j's [*Guest*, 1961; *Draper and Smith*, 1966; *Bevington*, 1969]. Since the form of the expected profile $\phi(x_i;p_j)$ is known (equation 2.9) (a convolution of the instrument and source profiles), this method is adopted for the determination of p_j's.

Hays and Roble [1971] have adopted an analytical expression for the behaviour of the instrument by expressing its response in terms of a Fourier series. The overall instrument function is expressed as a convolution of all known broadening functions described in section (2.2). For the instrument employed in the present work, difficulties were experienced in describing analytically the behaviour of the instrument with the available etalon parameters. This could be due to our limited knowledge on the possible errors present in the optical system. Though the observed contrast is in the range 10–15, the contrast deduced from an analytical expression representing the instrument function is as high as 50. However, the widths do not differ much. Further, it is not possible to incorporate any asymmetry in the observed instrument profile if present, in the analytical expression. Thus since the theoretical profile evaluated from Fourier series analysis of etalon parameters does not represent the actual instrument performance, the observed instrument profile measured on each night is made use of for deconvolution, in the present analysis.

The detector attached to the Fabry Perot Spectrometer yields photon counts

per unit time interval. The properties of the photon field are that it is fluctuating and is discontinuous, and follows a Poisson distribution [*Bevington*, 1969; *Hernandez*, 1986]. If the detector yields N photons for a given time, then the variance is N for the same time. *Hernandez*, in a series of papers [1978, 1979, 1982a, 1985], has highlighted and quantified the uncertainties caused by inherently noisy measurements. *Hays and Roble* [1971] have shown that the high frequency components associated with the fluctuating photon field can be effectively filtered by considering only the first five Fourier coefficients when the observed profile is expressed in terms of a Fourier series. The other approach would be to employ cubic smooth spline functions with appropriate weighing factors in order to minimize the random errors present in the data [*Sridharan et al.*, 1991]. We have used both the methods and the results agreed well within the statistical uncertainties in the retrieved parameters. However, we adopt the Fourier decomposition method described below to minimize the random errors associated with the photon noise, since this is computationally faster.

If $Y(p_i)$ represents the observed count at a pressure p_i of the medium between the etalon plates and Δp is the free spectral range expressed in pressure units, then the cosine and sine transforms are written as

$$\tilde{Y}_{cm} = \frac{1}{\pi m} \sum_{i=1}^{n} Y(p_i) \left[2 \sin \left(2\pi m \frac{p_i}{\Delta p}\right) \sin^2 \left(\pi m \frac{\delta p_i}{\Delta p}\right) \right.$$

$$\left. + \cos \left(2\pi m \frac{p_i}{\Delta p}\right) \sin \left(2\pi m \frac{\delta p_i}{\Delta p}\right) \right] \qquad (2.11)$$

and

$$\tilde{Y}_{sm} = -\frac{1}{\pi m} \sum_{i=1}^{n} Y(p_i) \left[2 \cos \left(2\pi m \frac{p_i}{\Delta p}\right) \sin^2 \left(\pi m \frac{\delta p_i}{\Delta p}\right) \right.$$

$$\left. - \sin \left(2\pi m \frac{p_i}{\Delta p}\right) \sin \left(2\pi m \frac{\delta p_i}{\Delta p}\right) \right] \qquad (2.12)$$

Theoretically, the fringe profile can then expressed in terms of the Fourier series:

$$Y_s(x) = \frac{\tilde{Y}_{co}}{2} + \sum_{m=1}^{\infty} \tilde{Y}_m \cos(mx + \alpha) \qquad (2.13)$$

where $\tilde{Y}_m = (\tilde{Y}_{cm}^2 + \tilde{Y}_{sm}^2)^{1/2}$ and $\alpha = \tan^{-1}(\tilde{Y}_{sm}/\tilde{Y}_{cm})$. $\tilde{Y}_{co}$ is the zero order transform of the data. Using the above equations and with m = 4 (first four coefficients), the random noise in the observed data appearing as higher order coefficients in (2.13), is filtered out leaving the data free of fluctuations associated with these components.

Hays and Roble [1971] have solved equation (2.10) in terms of Fourier transforms and the coefficients. They have used a parabolic least squares technique to determine the minimum values of the sum squares of deviations between the observed data and the analytical profile calculated using the instrument coefficients and a Gaussian profile of a given temperature T_n. Three arbitrary temperatures are assumed to begin with, and a search is made for a minimum in deviations. The constants which are made use of to fit a parabola to the deviations, are solved to yield T_n. However, this method is computationally intensive and the solution will not converge if the selected initial values are too far from the minimum and if the curvature of the deviations calculated happen to be of wrong sign such that the minimum is never approached [*Bevington*, 1969; *Killeen and Hays*, 1984].

We adopt the linearization method mentioned earlier to retrieve the Doppler parameters in our data reduction procedure in which the first step would be to assume that the background is zero. In order to estimate the best set of estimates p_j's, the generalized Newton-Raphson method is used which is an iterative procedure based on a Taylor series expansion about the current approximation to the required solution.

The linearization method uses the results of linear least squares in a succession of stages. The function, $\phi(x_i; p_j)$ is first expanded in a Taylor series about p_j^0's (a set

of initial values):

$$\phi(x_i; p_j) = \phi(x_i; p_j^0) + \sum_{j=1}^{3} \left(\frac{\partial \phi^0}{\partial p_j}\right)_i p_j' \tag{2.14}$$

where $p_j' = p_j - p_j^0$ and $\phi^0 = \phi(x_i; p_j^0)$, p_j^0 being an approximation to p_j. Higher order terms in p_j' are neglected. The parameters corresponding to the observed profile $O(x_i)$, are taken to be the initial values p_j^o's assuming that $O(x_i)$ follows a Gaussian distribution. If

$$v_i' = O(x_i) - \phi(x_i; p_j^0) \qquad \text{and} \qquad x_{ji}' = \left(\frac{\partial \phi^0}{\partial p_j}\right)_i$$

then χ^2, the sum of squares of deviation is given by

$$\chi^2 = \sum_{i=1}^{n} w_i \, v_i^2 = \sum_{i=1}^{n} w_i \left[v_i' - \sum_{j=1}^{3} p_j' x_{ji}'\right]^2$$

Minimization of χ^2 leads to the normal equations

$$\sum_{i=1}^{n} w_i \, (v_i' - \sum_{j=1}^{3} p_j' x_{ji}') \, x_{mi}' = 0 \tag{2.15}$$

which can be solved for p_j' and hence the estimates of the parameters will be $p_j = p_j^0 + p_j'$.

Writing out the functional form of $\phi(x_i; p_j)$, in the case of a Doppler-broadened profile,

$$\phi(x_i; p_j) = \sum_{k=1}^{n} \frac{p_1}{p_3} \exp\left[-(x_k - p_2)^2/p_3^2\right] \, I(x_i - x_k)$$

The derivatives are

$$\frac{\partial \phi}{\partial p_1} = \frac{\phi}{p_1}$$

$$\frac{\partial \phi}{\partial p_2} = \frac{2(x_k - p_2)}{p_3^2} \, \phi$$

$$\frac{\partial \phi}{\partial p_3} = \left[\frac{2(x_k - p_2)}{p_3^2} - \frac{1}{p_3}\right] \phi$$

Since the derivatives of the sum squares of deviations with respect of p'_j are zero,

$$\frac{\partial}{\partial p'_m}\left[\sum_{i=1}^{n} w_i \left[O(x_i) - \phi(x_i; p_j^0) - \sum_{j=1}^{3}\left(\frac{\partial \phi^0}{\partial p_j}\right)_i p'_j\right]^2\right] = 0$$

which becomes

$$2\sum_{i=1}^{n} w_i \left[O(x_i) - \phi(x_i; p_j^0) - \sum_{j=1}^{3}\left(\frac{\partial \phi^0}{\partial p_j}\right)_i p'_j\right]\left(\frac{\partial \phi^0}{\partial p'_m}\right)_i = 0$$

neglecting the second derivative terms.

The normal equations are therefore

$$\sum_{i=1}^{n} w_i\, O(x_i)\left(\frac{\partial \phi^0}{\partial p_m}\right)_i - \sum_{i=1}^{n} w_i\, \phi^0 \left(\frac{\partial \phi^0}{\partial p_m}\right)_i$$

$$- \sum_{i=1}^{n} w_i \sum_{j=1}^{3}\left(\frac{\partial \phi^0}{\partial p_j}\right)_i \left(\frac{\partial \phi^0}{\partial p_m}\right)_i p'_j = 0 \qquad (2.16)$$

$(m = 1, 2, 3)$

Let $O(x_i) - \phi^0 = R_i$ and $B_m = \sum_{i=1}^{n} w_i R_i \left(\frac{\partial \phi^0}{\partial p_m}\right)_i$. Then (2.16) reduces to

$$B_m - \sum_{i=1}^{n} w_i \left[\sum_{j=1}^{3}\left(\frac{\partial \phi^0}{\partial p_j}\right)_i \left(\frac{\partial \phi^0}{\partial p_m}\right)_i p'_j\right] = 0 \qquad (2.17)$$

Writing in matrix form

$$\mathbf{B} = \mathbf{A}\,\mathbf{P}' \qquad \text{or} \qquad \mathbf{P}' = \mathbf{A}^{-1}\,\mathbf{B} \qquad (2.18)$$

$\mathbf{P}'$ are obtained by solving (2.18) by one of the standard elimination methods and retaining the elements of $\mathbf{A}^{-1}$ also at every step.

Since p_j^0's have been the rough estimates of the original parameters, they can be improved upon by successive iteration. p_j's will then play the same role as p_j^0's and

the whole procedure is repeated till the solution converges. The rate of convergence of this method varies with the quality of the data and the initial values selected. The second step of the data reduction procedure would be to estimate the background count for these estimated values of p_j's.

Evaluation of background for the estimated p_j's

The response of a Fabry Perot etalon to a broadened source profile has been considered by *Chabbal* [1953]. The transmission of the instrument is a product of the contributions due to (i) absorption by reflecting layers of the etalon (these are extremely small in the case of the dielectric coatings), (ii) surface defects of the etalon, (iii) the scanning function f, and (iv) the source not being monochromatic. Except the source itself having a finite width, all the other factors are inherent in the measured instrument profile. Thus the former needs to be estimated for an accurate determination of the source width. The actual contrast of the airglow profile is always less than the instrument contrast as determined using a laser due to the finite width of the source function and is related to the product of the instrument contrast and the transmission of the etalon for the Doppler-broadened source. Due to the presence of unwanted background radiation in the signal, the observed contrast (I_{max}/I_{min}) is slightly less than the actual contrast C_{act}. Hence the contribution due to the background needs to be subtracted from the observed profile. The actual contrast is then

$$C_{act} = \frac{I_{max} - BG}{I_{min} - BG} \tag{2.19}$$

where I_{max}, I_{min} and BG represent the maxmimum and minimum intensities and the background level respectively. *Chabbal* [1953] has studied the variation of the transmission factor of the instrument in response to various source-instrument width combination.

In order to evaluate the performance of our instrument in response to a Doppler-broadened source, a method was developed which also yields the background level. The instrument coefficients (a_n) are first evaluated using the Fourier decomposition technique described earlier. The expected airglow profile for a temperature T_n is then given by

$$A(x) = I_{max} \left[a_0 + \sum_{m=1}^{M} a_m \, e^{-m^2 \gamma T_n / 4} \cos \left(\frac{2\pi x_i m}{\Delta x} \right) \right] \qquad (2.20)$$

where γ is a constant (= 0.000458), Δx is the free spectral range and I_{max} is the intensity at the peak position [*Hays and Roble*, 1971]. a_0 is the zero order coefficient ($= 1/2\pi$). If C is the resultant contrast for a zero width source, i.e., a monochromatic line, the transmission in response to a finite width source is written as

$$\tau_B = C_{act}/C$$

where C_{act} is the contrast for the assumed source width (= C if the line width is zero for which $\tau_B = 1$). The ratio of the source width s to the etalon width e is increased in discrete steps and the transmission is evaluated using the above expression. Fig. 2.5 shows the response curve of the instrument which is compared with the theoretical curve given by *Chabbal* [1953]. The deviation of the actual response curve from that obtained by Chabbal is due to the fact that the instrument broadening has a functional form between a Gaussian and an Airy type whereas the theoretical curve ($G \otimes F$) has a functional form when the etalon function E is of a rectangular type. Similar result with regard to the spectrometer behaviour has also been obtained earlier by *Rajaraman* [1982].

Using the transmission curve and the formulation given above, the background can be evaluated for any value of source width under consideration. The background thus determined is then subtracted from the observed profile. The first step of the method is once again applied to this new profile for the determination of a new set

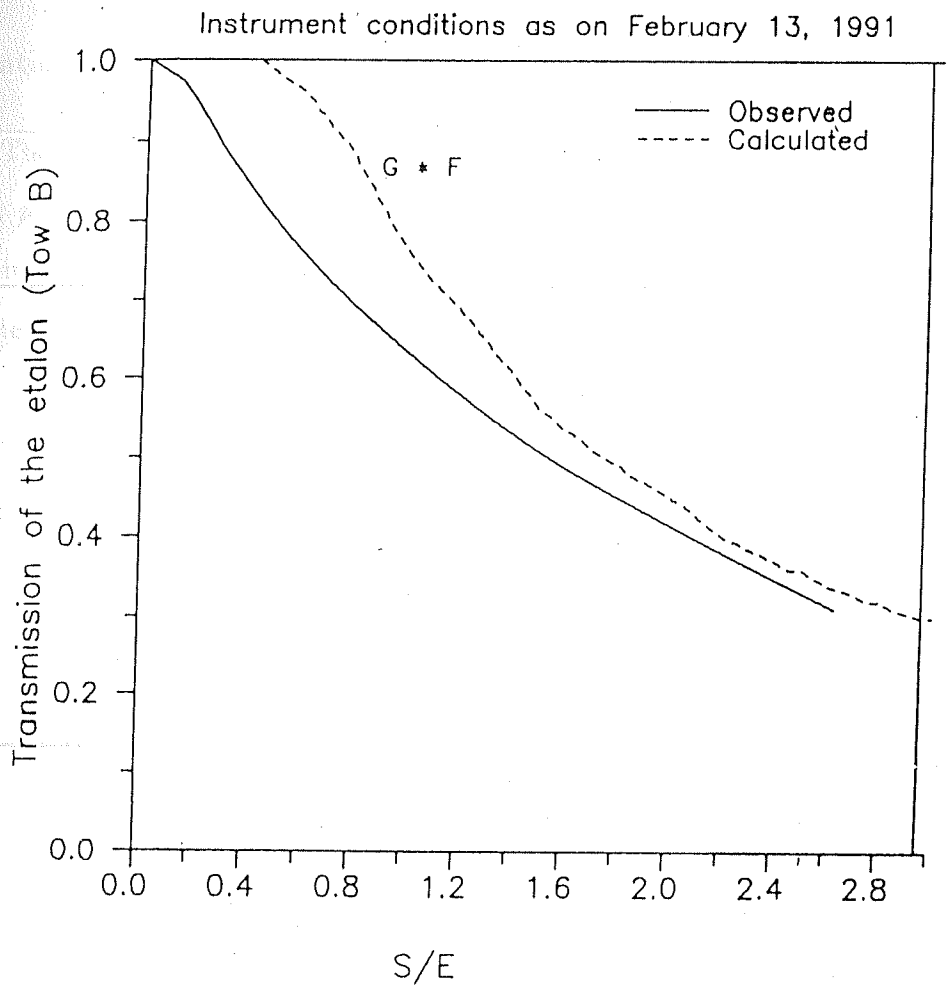

Fig. 2.5. The response of the instrument to various source widths. The dashed curve represents the result of theoretical calculation done by *Chabbal* [1953] and the continuous curve represents the result based on observed data from the instrument.

of p_j values and the whole process is repeated until the difference in the estimated temperatures between two successive iterations is less than 10 K.

Estimation of errors

The standard deviation σ_{p_j} for the uncertainty of determination of any parameter p_j is the root sum square of the products of the standard deviation of each data point σ_i multiplied by the effect that data point has on the determination of the parameter p_j [*Bevington*, 1969].

$$\sigma_{p_j}^2 = \sum_{i=1}^{n} \left[\sigma_i^2 \left(\frac{\partial p_j}{\partial O(x_i)} \right)^2 \right] \tag{2.21}$$

Since the fluctuations in our measurements are statistical, the standard deviation corresponding to each observation can be estimated analytically. It is known that the observed counts follow a Poisson distribution. With the usual assumptions and approximations owing to the difficulties in solving equations associated with a Poisson distribution, the uncertainties σ_i are reasonably approximated by $\sigma_i^2 = O(x_i)$ which is the observation corresponding to the independent variable x_i [*Hernandez*, 1978].

From the normal equations,

$$p_j = \sum_{m=1}^{3} \epsilon_{jm} \left[\sum_{i=1}^{n} w_i \left[O(x_i - \phi^0 \right] X_m(x_i) \right] \tag{2.22}$$

where ϵ_{jm} are the elements of the inverse matrix $\mathbf{A}^{-1}$ and

$$\left(\frac{\partial \phi^0}{\partial p_j} \right)_i = X_j(x_i)$$

The remaining factor on the right hand side of (2.22) is the same as the matrix **B** defined earlier.

For determining the uncertainty in each parameter p_j, the derivative of p_j with respect to the observation $O(x_i)$ is to be calculated.

$$\frac{\partial p_j}{\partial O(x_i)} = \frac{\partial}{\partial O(x_i)} \left[\sum_{m=1}^{3} \epsilon_{jm} \left[\sum_{i=1}^{n} w_i \left[O(x_i) - \phi^0 \right] X_m(x_i) \right] \right]$$

Therefore

$$\left[\frac{\partial p_j}{\partial O(x_i)}\right]^2 = \left[\sum_{i=1}^{n} w_i \, \epsilon_{jm} \, X_m(x_i)\right]^2$$

(2.21) becomes

$$\sigma_{p_j}{}^2 = \sum_{m=1}^{3} \sum_{l=1}^{3} \epsilon_{jm} \, \epsilon_{jl} \sum_{i=1}^{n} [w_i X_m(x_i) X_l(x_i)]$$

$$= \sum_{m=1}^{3} \sum_{l=1}^{3} (\epsilon_{jm} \, \epsilon_{jl} \, \epsilon_{ml}) = \epsilon_{jj} \qquad (j = 1, 2, 3) \qquad (2.23)$$

The result of this calculation is that the diagonal elements of the error matrix ϵ which is the inverse of the matrix **A** defined earlier, are the uncertainties of the parameters p_j's.

To have a check on the temperature determined using this method, a fringe profile is constructed using equation (2.20) with this temperature and the available instrument coefficients and is compared with the observed profile. An example is depicted in Fig. 2.6 and the agreement is indeed very good. Using this powerful technique to determine Doppler parameters, useful results have been obtained on the dynamics of the thermosphere-ionosphere system [*Sridharan et al.*, 1991; *Gurubaran and Sridharan*, 1993].

2.6 Line profile measurements of O I 6300 Å emissions

Though the method developed for the deconvolution of a source profile can be applied to any optical observation, its application to airglow O I 6300 Å emission is critically examined in this section. This follows from our basic necessity of obtaining thermospheric parameters for which the present investigation was initiated. The properties

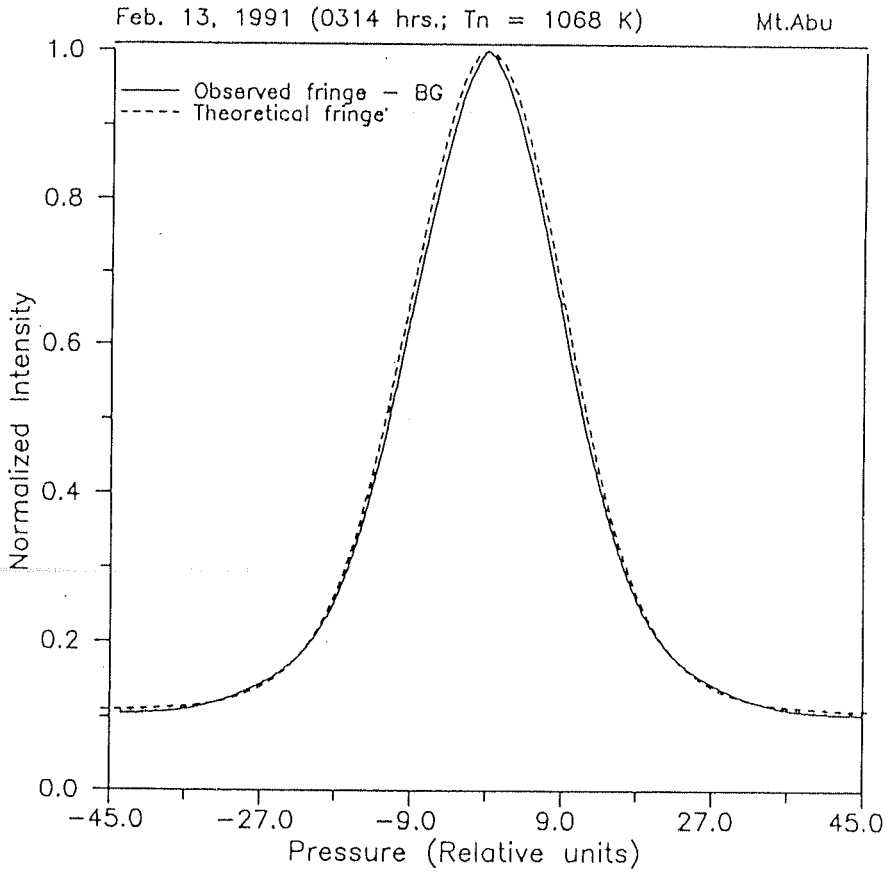

Fig. 2.6. An observed airglow fringe (—-) after filtering out the random noise present in the data by applying Fourier decomposition and after due correction for the background, and the theoretical fringe (- - -) determined for the measured temperature from the former.

of the ^1D to ^3P transition of excited atomic oxygen giving rise to 6300 Å emission are well known [*Chamberlain*, 1961]. The emission line strictly follows the shape of a Doppler-broadened profile and can be expressed by a Gaussian function [*Biondi and Feibelman*, 1968]. The factors which limit the precision of the parameters of the line profile retrieved using the method described in the last section, are as follows: (1) Tilt and/or smear in the aperture used, (2) Thermal stability of the etalon, (3) Low intensity level of the emission, (4) Fast intensity variations, (5) Shears present in the wind systems of the emitting region and (6) Contamination of 6300 Å due to OH molecular band. These aspects and the methods adopted to overcome/minimize the effects are briefly discussed below.

(1) One of the effects which causes an asymmetry in the measured profile is due to the tilt of the aperture plate with respect to the normal to the optical axis and possible smear in the aperture (due to improper machining). A careful examination of the fringe pattern as the spectral scan is made, will show that as the pressure of the air between the etalon plates is increased, a bright spot first appears at the centre of the aperture which subsequently evolves into a fringe. At a particular value of pressure, it completely fills the aperture and then moves away from the centre, leading to the original 'darkening' of the aperture. Similarly, the reverse happens if the pressure is varied in the opposite direction, i.e., when it is decreased. The left half of the scanned profile gets developed during the period when the bright spot first appears at the centre, evolves and completely fills the aperture (during forward scan). The right half corresponds to the fringe 'leaving' the centre. A simple reasoning suggests that, in the absence of other factors, any asymmetry in the measured profile arises either due to the aperture not being exactly circular or it is not concentrically aligned and/or the aperture plate has a tilt with respect to the optical axis. Under such circumstances, once the fringe maximum is reached, the light will not be uniformly cut as the scan progresses, and hence would lead to an asymmetry. Due to the

reasons mentioned above, the left half of the airglow profile is reflected to the right thus eliminating the asymmetry and broadening, and the resultant profile is analysed using the method described in the previous section.

(2) If the etalon chamber temperature and hence the temperature of the air enclosed changes during a scan, the profile is likely to get distorted. This is mainly due to the refractive index being dependent on temperature. This effect becomes significant for wind determination and not so much for temperature estimates. However, since the thermal stability of the etalon is maintained to better than 0.1° C by a dual heating enclosure and by housing it in a chamber having large thermal capacity (section (2.4)), the instrument profile is not expected to drift in wavelength due to the variations in μ arising purely out of changes in etalon temperature. This eliminates the possibility of the distortion of the observed profile due to changes in μ associated with temperature alone, during a spectral scan.

(3) Earlier workers have stressed the need for an adequate signal to noise ratio to obtain accurate Doppler temperatures [*Hays and Roble*, 1971; *Hernandez and Roble*, 1976; *Hernandez*, 1978; *Hernandez et al.*, 1984].

The emission profiles and the corresponding retrieved temperatures obtained during the coordinated campaign in the month of February, 1991, are scrutinized and a plot of the peak intensity (in counts) versus the standard deviation in retrieved temperature (the third diagonal element of the error matrix ϵ; see last section) is shown in Fig. 2.7. The peak intensity level measured is in the range of 100–1400 counts. The precision with which the temperature is determined, is seen to fall sharply as the count level reaches below 200. Owing to a large error present (> 200 K), profiles with peak intensity below 100 counts, which is rather frequent at our

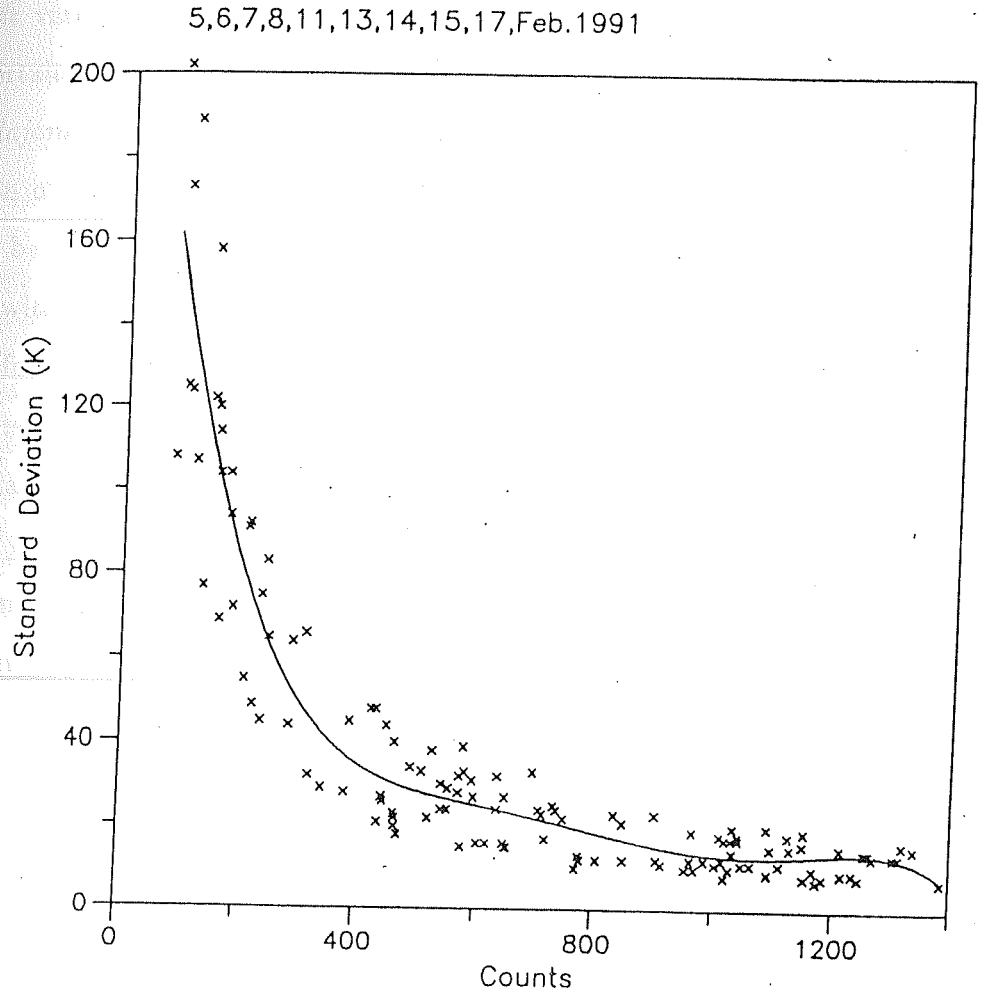

Fig. 2.7. Standard deviation in the temperature determination versus peak intensity (in counts) of airglow fringe profiles for February 1991. The best fit curve using polynomial approximation is also plotted.

latitudes, are not considered for analysis. This sets a criterion for the rejection of line profiles.

(4) Fast variations in line intensity distort the profile shape and width, and lead to uncertainties in the retrieved parameters [*Hernandez et al.*, 1975; *Hays and Roble*, 1971; *Rajaraman*, 1982]. It was suggested by *Hernandez et al.* [1975] that an intensity variation of more than about 20 % leads to a greater uncertainty and such profiles need to be rejected. This suggestion is seriously considered in the present work and profiles with large variation in intensity (peak to peak of sequentially observed fringes) are carefully analysed. As the intensity of the line increases, during a forward scan, the left half of the profile is expected to have a larger contrast (maximum to minimum ratio) than that of the right half and the reverse holds when the scan is made in the opposite direction. Similar effects would be seen when the intensity decreases. Such distortions in the profile are expected to affect the temperature measurements often manifesting as higher temperatures. In spite of these expectations, on many occasions, when the intensity changes were by more than 25 %, the temperatures obtained are not very different and the profiles are still neat and clean. However, variations on a much larger scale do contribute to significant changes in temperatures, and profiles with such variations are duly rejected.

(5) *Biondi and Feibelman* [1968] pointed out the possibility of a line profile distortion due to gross motions of the thermosphere. Within the emitting layer of thickness in the range of 50 km, a shear or velocity gradient in the neutral atmospheric motion is expected to lead to a slightly non-Gaussian line with a skew about the line centre. During their observations from Laurel Mountain, Pennsylvania, *Biondi and Feibelman* [1968] have observed a few profiles of marked asymmetry and attributed them to a sharp gradient in wind velocity within the emitting region. However, in the Indian zone, *in situ* measurements by means of release of vapour clouds by rockets, revealed

that there were no shear or changes in the wind velocity in the altitude region of emission [*Sridharan et al.*, 1989] thus suggesting that such occurrences may not be common. Hence their possible effect is not considered in the line profile analysis.

(6) The presence of emission lines of the OH molecule (6287.5 Å, 6297.9 Å and 6307 Å) near the O I 6300 Å emission line has been well recognized for more than three decades [*Chamberlain*, 1961; *Hernandez*, 1974]. *Hernandez* [1974], in an important work, has investigated the effects of OH contamination of the 6300 Å line and found them to be significant at certain times. As the emission rate of atomic oxygen line decreased below 20 R, the OH contribution has been observed to be significant. In the present work, a narrow band interference filter (3 Å bandwidth) tuned to 6301 Å is expected to filter out all the other lines of the OH emission band except 6297.9 Å. Though the 6297.9 Å component of the OH band is close to 6300 Å, it lies at the rapidly falling edge of the filter transmission curve and secondly the gap between the Fabry Perot etalon plates (1 cm gap) is so chosen as to make this emission feature appear in the middle of two 6300 Å profiles corresponding to adjacent orders. Hence it is not expected to contaminate the observations even when the emission rate of 6300 Å falls low, except on occasions when the molecular emission intensity is unusually high.

The results obtained on temperatures and winds from the low latitude station are presented and discussed in the chapters to follow.

Chapter 3

Measurements of thermospheric temperatures from low latitudes

3.1 Thermal structure of the neutral upper atmosphere

The temperature structure of the upper atmosphere is formed in response to heating and cooling processes, as well as to transport of mass, momentum and energy. The most important heat source of the thermosphere is the extreme ultra violet radiation from the sun, which is highly dependent on solar activity, varying by a factor of 2 between extremes of a solar cycle. Though the total amount of energy available from this source is small compared to that from the ultraviolet and visible radiation of the solar spectrum, considering the rarified absorbing medium, the specific heat input due to the EUV source is very large accounting for the large temperatures observed in the thermosphere.

There are several reasons for the sharp temperature increase in the lower thermosphere. There exist sinks of energy near the mesopause region due to the infrared radiative cooling of excited species such as nitric oxide and carbon dioxide, which have

their own height distribution. In the event of decrease of densities of such species above the mesopause, the temperature starts building up due to EUV absorption. However, there occurs another physical process in the real atmosphere which tends to counteract the temperature increase. Though the radiative cooling of the excited minor species acts as a principal energy loss process, conduction of heat helps to remove the amount of energy absorbed at higher levels. The coefficient of heat conduction though independent of the ambient gas density, rises with temperature like $T^{1/2}$. The rapid rise in temperature in the lower thermosphere assists heat conduction, which in turn, acts as an efficient means of temperature equalization in the upper atmosphere. This simple physical reasoning in conjunction with the diffusive equilibrium of all species that prevails above about 120 km, had led to the development of static diffusion models [*Jacchia*, 1965, 1971].

The regular daily variation in temperature produced by the sun's transit across the sky amounts to about 30 %; the minimum nighttime value (T_∞) occurs at about 0400 h local time in near-equatorial latitudes and the maximum value occurs at about 1600 h local time usually near the equator. During sunspot minimum, T_∞ is near 600 K and on a night during a typical sunspot maximum, T_∞ is about 900 K.

Fig. 3.1 shows vertical distributions of the major neutral species in the upper atmosphere, corresponding to minimum and maximum solar activity levels. Extreme cold (corresponding to late night conditions at low latitudes) and extreme hot (corresponding to low latitude afternoon conditions with additional heating associated with strong geomagnetic activity) thermospheric temperature profiles were made use of to obtain the altitude distribution of these species [*US Standard Atmosphere*, 1976]. Below 100 km, the major constituents are molecular nitrogen, molecular oxygen and argon, with respective densities of about 2×10^{19} cm^{-3}, 5×10^{18} cm^{-3} and 2×10^{17} cm^{-3} at sea level decreasing exponentially with increasing height to the values

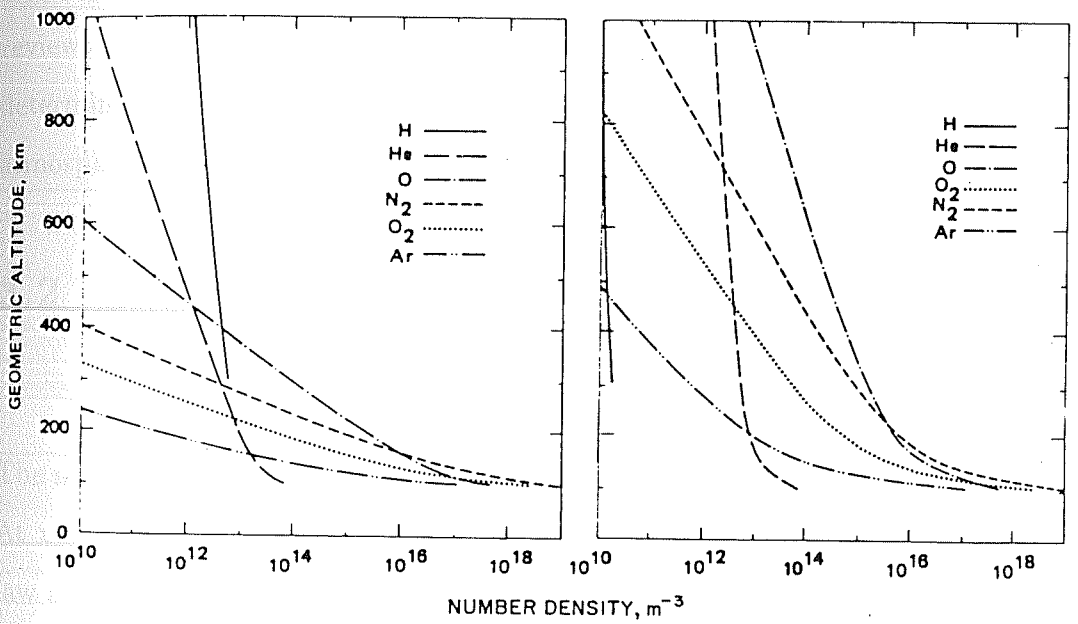

Fig. 3.1. Vertical distribution of major neutral species in the upper atmosphere for solar minimum and solar maximum periods [*US standard Atmosphere*, 1976]. The density profiles in the left panel are for low latitude nighttime conditions (coldest) and those in the right panel are for low latitude afternoon conditions superposed on the geomagnetic activity associated heating (hottest).

shown in the figure at 100 km. As it is apparent in Fig. 3.1, the thermosphere expands as the temperature increases in response to solar activity. The density at 500 km can vary by almost three orders of magnitude and has been having an important influence on the satellite orbits when it increases to its highest value.

In addition to solar EUV source, there are other sources such as magnetospheric particle precipitation and joule dissipation of ionospheric electric currents, which are important at high latitudes. Non-local processes such as transport of mass, momentum and energy due to winds and wave motions significantly alter the above simple physical picture that had evolved before satellites were flown into space. Many reviews exist in the literature that discuss these dynamic processes, which ultimately determine the compositional, dynamical and thermodynamical state of the upper atmosphere [*Dickinson*, 1975; *Mayr et al.*, 1978; *Killeen*, 1987; *Crowley*, 1991].

3.2 Neutral temperature as a measurable parameter in the thermosphere

The neutral temperature is one of the observable parameters of the upper atmosphere. At any height, the temperature is related to pressure and density by the ideal gas law and hence the changes in neutral density follow the changes in temperature. As a certain region of the atmosphere is heated, it expands and the cell of gas above it is raised to an increased height, thereby replacing a less dense cell. The result is, at a fixed altitude, the density increases with increase in temperature above the mesopause level (Fig. 3.1). Making use of the exponential decrease of pressure with height, it is useful to express the various atmospheric parameters such as neutral and ion densities in terms of fixed pressure levels. Since the weight of air overlying any cell of air at a given pressure level does not change during heating, the result of an increase in temperature is the expansion of the pressure levels while the density

within the cell decreases [*Garriott and Rishbeth*, 1963].

Given the temperature profile, the height distribution of the neutral atmospheric density can be determined, provided the density at some lower boundary is known. Analysis of satellite drag data showed that the temperature is characterized by a single value referred to as the exospheric temperature (T_∞), and prevails in the height region of about 400 km and above. Empirical models of Jacchia made use of this finding and in order to run such models, it is sufficient to know the exospheric temperature.

The thermospheric temperature is an indicator of a variety of photochemical reactions that lead to conversion of solar energy to the kinetic energy of the atmospheric gases. Our knowledge of the global scale sources and sinks can be tested by modeling the thermospheric mean temperature profile. Several chemical reactions are temperature dependent and the composition of the neutral and the ionized species are thus influenced by the thermal structure of the atmosphere. Several transport coefficients such as those of diffusion, viscosity and conductivity, that appear in the conservation equations of mass, momentum and energy, depend on an accurate knowledge of temperature.

The neutral temperature is one of the parameters that couples energetics and dynamics. The adiabatic heating and cooling that result from a large scale neutral air circulation associated with a global scale pressure gradient, is an example of this coupling. A net result of this process, in the case of diurnal heating and cooling by solar radiation, is that, energy is literally taken out of the dayside and transported towards the nightside. Transport of mass, also referred to as wind-induced diffusion, results in net accumulation of a minor species such as helium in one of the hemispheres and a net depletion in the other [*King*, 1964; *Mayr et al.*, 1978]. An expansion of the atmosphere due to heating brings in molecular enriched air from lower heights thereby

altering the atomic to molecular concentration ratio. This has been invoked to explain the seasonal and storm-time behaviour of F region electron densities [*Shimazaki*, 1972; *Rishbeth*, 1975]. These examples illustrate the importance of thermospheric temperature whose knowledge is essential in understanding many of the underlying physical processes.

3.3 Techniques available to measure neutral temperature

The techniques that are available to measure upper atmospheric temperatures can be broadly classified into (1) the *in situ* measurements by means of rockets and satellites including drag measurements, (2) optical remote sensing of airglow emissions, both by ground-based and space-borne measurements, and (3) inferences from remote sensing measurements of the ionosphere by incoherent scatter radar.

With the launching of satellites in 1950's, a new method had evolved to infer thermospheric temperature from the orbital drag data acquired. Since the deceleration of the satellite is a direct function of atmospheric density, neutral temperatures were determined using simple physical formulation [*Jacchia*, 1971; *Jacchia*, 1977]. These static diffusion models were soon outclassed by the more appropriate Mass Spectrometer and Incoherent Scatter (MSIS) models.

Mass spectrometers for the *in situ* measurements of neutral temperature have been flown on several rockets as well as on Atmosphere Explorer and Dynamics Explorer satellites. The temperature of the ambient gas at the location of the satellite is determined by measuring the velocity distribution of the dominant species. This principle has been used in the Neutral Atmosphere Temperature Experiment (NATE) on AE-C, D and E and the Wind and Temperature Spectrometer (WATS) on DE 2.

A significant contribution from AE mission to low latitude zone is the observation of midnight temperature maximum in the equatorial thermosphere [*Spencer et al.*, 1979; *Mayr et al.*, 1979]. With the useful data from this mission, in conjunction with incoherent scatter measurements, *Hedin et al.* [1977a,b] developed a global thermospheric model known as the Mass Spectrometer and Incoherent Scatter (MSIS) model. This model has been subsequently revised twice as more information on the thermospheric variability is being gathered [*Hedin*, 1983; *Hedin*, 1987]. A recent result from the WATS data on DE mission has been the discovery of an Equatorial Temperature and Wind Anomaly [*Raghavarao et al.*, 1991].

Release of vapour clouds such as sodium and trimethyl aluminium in the upper atmosphere by means of rockets and measurements of the expansion rate of clouds yield diffusion coefficient from which neutral temperatures are inferred. A series of such experiments have been conducted in the past and have given good results [*Golomb et al.*, 1968; *Rees et al.*, 1972; *Desai and Narayanan*, 1970; *Ranjan Gupta et al.*, 1986].

Though an incoherent scatter radar (ISR) measures charged particle characteristics, a method was developed to determine thermospheric temperatures with these data [*Nisbet*, 1967]. The close coupling between the ions and neutrals has led to most of the thermospheric information from the incoherent scatter radars [*Oliver et al.*, 1988]. Using the equations of collisional heat transfer among the neutral and the ionized species, the neutral temperatures are calculated from the measured ion and electron temperatures and densities. An exclusive review on the contributions of ISR to the development of global thermospheric models exists in the literature [*Oliver et al.*, 1988].

Spectroscopic determination of thermospheric temperature by means of optical remote sensing of airglow emissions is one of the direct methods that are available

now. A high resolution Fabry Perot Spectrometer is most suited for this purpose [*Hernandez*, 1986 and the references cited therein]. Optical remote sensing devices have been flown on spacecraft such as OGO 6 and DE 2 to monitor the upper atmospheric parameters [*Blamont and Luton*, 1972; *Hays et al.*, 1981]. The review by *Hernandez and Killeen* [1988] deals with the type of instruments that have been used for this purpose. The data from OGO 6 spacecraft were used to generate an empirical model of thermosphere [*Thuillier et al.*, 1977], which turned out to be the only model that has been derived from direct measurements of kinetic temperature. The results from FPI data on DE 2 satellite have been reviewed by *Hernandez and Killeen* [1988].

Continuous ground-based observations of airglow emissions using Fabry Perot Spectrometer are being made since *Armstrong* [1953] who revived the utility of the instrument for upper atmospheric temperature measurements.

3.4 Results of previous optical measurements on neutral temperatures

Since *Hernandez* [1972] who demonstrated the use of Fabry Perot Spectrometer in studying specific geophysical processes (stable auroral red arcs in his study), there have been many other workers who have effectively employed this instrument to measure thermospheric parameters for a considerable amount of time [*Sipler and Biondi*, 1978; *Rajaraman et al.*, 1979; *Burnside et al.*, 1981; *Hernandez*, 1982b; *Yagi and Dyson*, 1985; *Sahai et al.*, 1992a,b]. Data from equatorial and low latitudes are rather sparse. Considerable effort has been made to understand the response of the midlatitude thermosphere to geomagnetic storms and the consequent auroral heating processes. Whereas indirect methods are available for the determination of meridional winds based on ionospheric data, no such methods are available for the estimation of neutral temperatures (except for incoherent scatter radars at Jicamarca and to some

extent, Arecibo in the low latitude sector). In this section, the results pertaining to low and equatorial latitudes that have been obtained by previous workers using ground-based Fabry Perot technique are briefly reviewed.

Hernandez et al. [1975] reported the measurements from the equatorial station, Jicamarca (11.95°S, 76.87°W, geographic; 1°N dip latitude), obtained by a pressure-scanned Fabry Perot Spectrometer on six nights and he compared them with the temperatures inferred from the incoherent scatter radar. There was overall agreement between the two but for a slight difference. His results supported the conclusions arrived at by earlier comparisons [*Hays et al.*, 1970; *Cogger et al.*, 1970]. *Sipler et al.* [1983] presented observations of winds and temperatures from Kwajalein Atoll, Marshall Islands (9.4°N, 167.5°E, geographic; 8.6°N dip latitude). The temperatures, on the average, were higher by 330 K than the MSIS model predictions. *Biondi and Meriwether* [1985] studied the response of the equatorial thermospheric temperatures to various geomagnetic activity levels and solar flux changes. They had carried out measurements from Arequipa (16.4°S, 71.5°W, geographic; 4.4°S dip latitude), Peru, during 1983 and had compared the nocturnal variation of temperature with MSIS model. On an average, during quiet times, the neutral temperature exceeded the model values by 180 K. They had discussed the possible causes which could probably give rise to detection of such large temperatures, significantly higher (100 to 500 K) than the predicted values and categorized such observations as 'unexplained'. During increased geomagnetic activity, rapid rise in temperature has been observed. The failure of the semi-empirical models such as those of Jacchia and MSIS to predict such fast response of the thermosphere to sudden changes in geomagnetic activity, is due to the fact that the models describe atmospheric conditions based on geomagnetic and solar activity indices which are time-averaged over a longer period [*Biondi and Meriwether*, 1985; *Biondi and Sipler*, 1985].

As a part of the Brazil Ionospheric Modification Experiment (BIME), *Biondi and Sipler* [1985] carried out measurements of neutral temperature from Natal (5.9°S, 35.2°W, geographic; 6.4°S dip latitude) for 15 nights during August–September, 1982. Though the measured temperatures showed good agreement with the MSIS model in the early part of the night, there has been a post-midnight increase of 250 K observed on some nights, and this is substantially higher than those reported from satellite measurements [*Spencer et al.*, 1979]. An important observation of *Biondi and Sipler* [1985] has been the significant vertical flows and the associated neutral temperature increase in response to persistent convergence in the horizontal flow.

In contrast to the large temperature deviations from models observed by the above workers, *Sahai et al.* [1992b] have reported observations which are in agreement with the MSIS-86 model predictions. They have reported Fabry Perot measurements from Brazilian latitudes (23°S geographic) for equinoctial and winter seasons. They have claimed the midnight temperature increases seen in the average pattern to be the ones that are consistent with the midnight temperature maximum (MTM) observed in the satellite measurements [*Spencer et al.*, 1979]. Though the equinoctial mean temperature in their data did show an increase at midnight, the rise had been small ($\sim$ 50 K) when compared to the standard deviation in their measurements ($\sim$ 150 K).

Hernandez [1982b] described the long term behaviour of the observed neutral temperatures of the midlatitude thermosphere in terms of four parameters, namely, the $F_{10.7}$ radio flux, the A_p index of geomagnetic activity, the annual and semi-annual variations. Having shown that most of the presently available empirical models do not represent the observed response of the thermosphere to changing levels of solar flux, he obtained a better fit to the observed data from midlatitudes (Fritz peak observatory, 39.89°N, 105.5°W, geographic) after parameterization in terms of the known variabilities. A fit with each of the empirical models revealed a correlation

coefficient ranging from 0.81 to 0.86 while a description of the data in terms of these parameters revealed a correlation coefficient of 0.9.

In the following section, an attempt is made to depict the variabilities of neutral temperature with respect to changes in the incoming solar radiation at a low latitude station, Mt. Abu (24.6°N, 72.7°E, geographic; 20°N dip latitude). The first attempt to obtain neutral temperatures from Mt. Abu was made by *Rajaraman* [1982] which paved the way for a more systematic investigation presented in this dissertation. The earlier work was more of an exploratory nature, confining to a particular period of solar activity, with a limited number of observations mostly confined to pre-midnight hours. The experimental set-up and method of analysis have been drastically changed and completely redone during the course of the present investigation. The results from the observations carried out using the Fabry Perot Spectrometer described in Chapter 2, are presented below.

3.5 Neutral temperatures from low latitudes

The purpose of this chapter is to describe the response of thermospheric temperatures to changing levels of solar flux and several other geophysical processes that occur near the equatorial region. The neutral temperature is a sensitive indicator of the interaction of the solar radiation with the thermosphere-ionosphere system and therefore its variabilities need to be studied in detail. Though the empirical models are based on a large body of data acquired by different techniques, they do not explain in detail, the observed behaviour of the thermosphere event by event. As noted in the earlier section, the models employ certain indices representative of solar flux and the geomagnetic activity effects averaged over a long period. In this regard, it is useful to carry out individual case studies that may lead to the identification of specific geophysical processes that are responsible for the observed variabilities.

The central-aperture Fabry Perot Spectrometer is being operated from Mt. Abu since 1985 during the winter and equinoctial periods (October to May), when the sky over Mt. Abu remains clear. The data base covers almost 3/4 of a solar cycle. The solar minimum occurred during September–December 1986, while the maximum decimetric solar flux ($F_{10.7}$) of 359 was observed on 30 January, 1991 [*World Data Center A, Solar-Geophysical Data prompt reports*, 1991].

A large number of measurements is available for the periods October 1986 to March 1987 and November 1990 to April 1991, the data being sparse and scattered for other periods due to technical problems. During solar minimum, the airglow intensity decayed fast from its twilight value, occasionally recovering to some extent around midnight.

A total of 57 nights of observations is available for the period October 1986 to March 1988 out of which 20 nights were selected with a good number of data points for the case studies. This being a solar minimum period, the intensity at a later time depended on its twilight value which varied from day to day. For the years 1990–1992, the bulk of data comes from observations made in the months of February and April, 1991. The geomagnetic activity was low (A_p less than 20) on all the nights under study. The number of nights selected for the present study during the peak of the solar activity and during its minimum amounts to 41, with individual measurements running upto about 500. This may be a meagre amount when compared to a large data set (about 15000 measurements) utilized by *Hernandez* [1982b] in his midlatitude study, nevertheless it will be shown later that these measurements have played an important role in the understanding of the behaviour of the low latitude thermosphere-ionosphere system.

Figs. 3.2a, 3.2b and 3.2c depict the variation of neutral temperature (T_n) representing the months of October, November and December, 1986, and January

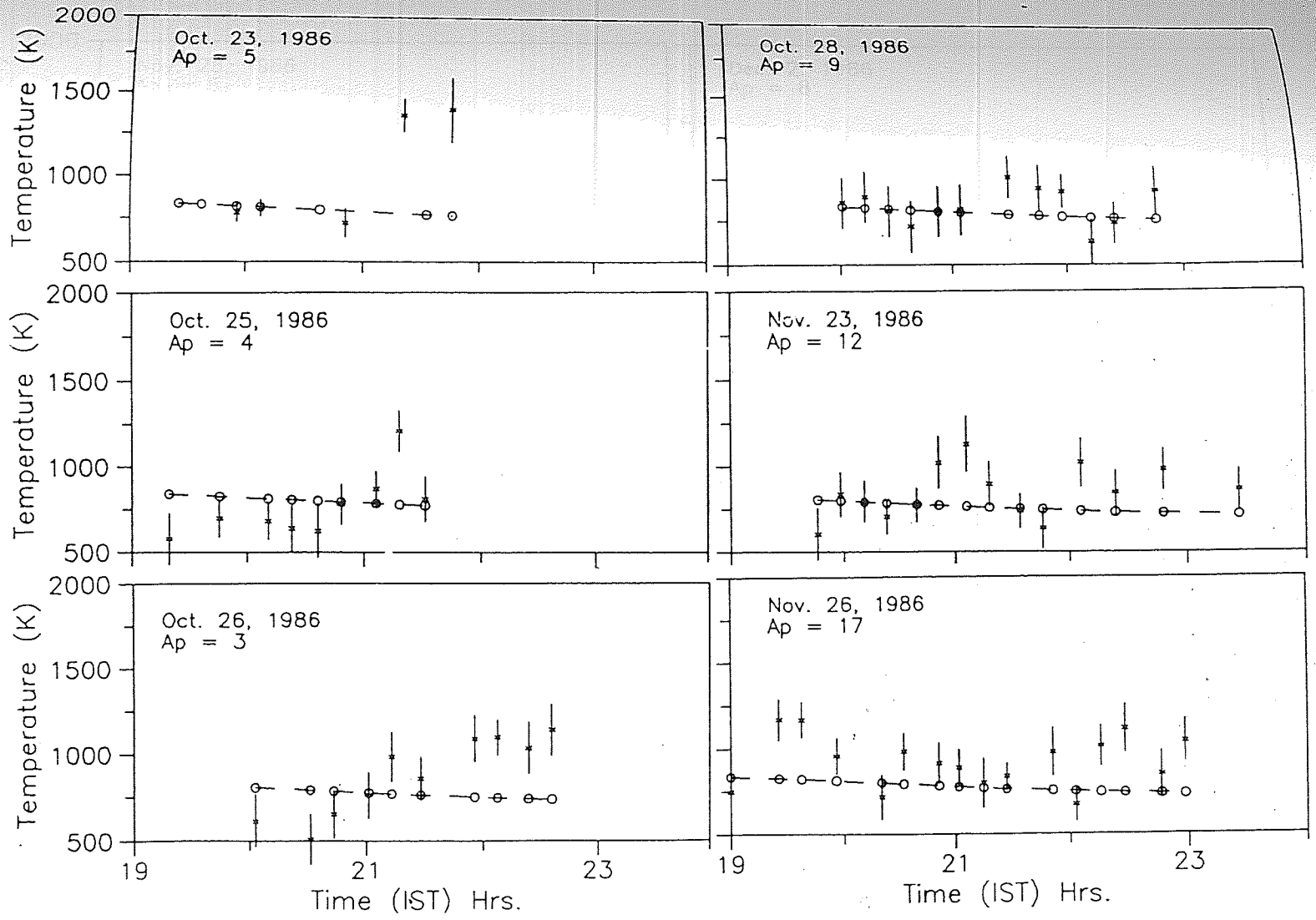

Fig. 3.2a. Temporal variation of spectroscopically measured thermospheric temperatures from Mt. Abu (stars with error bars) along with MSIS-86 model predictions (dashed curve joining circles) for the period October 1986 to March 1987 shown for individual nights.

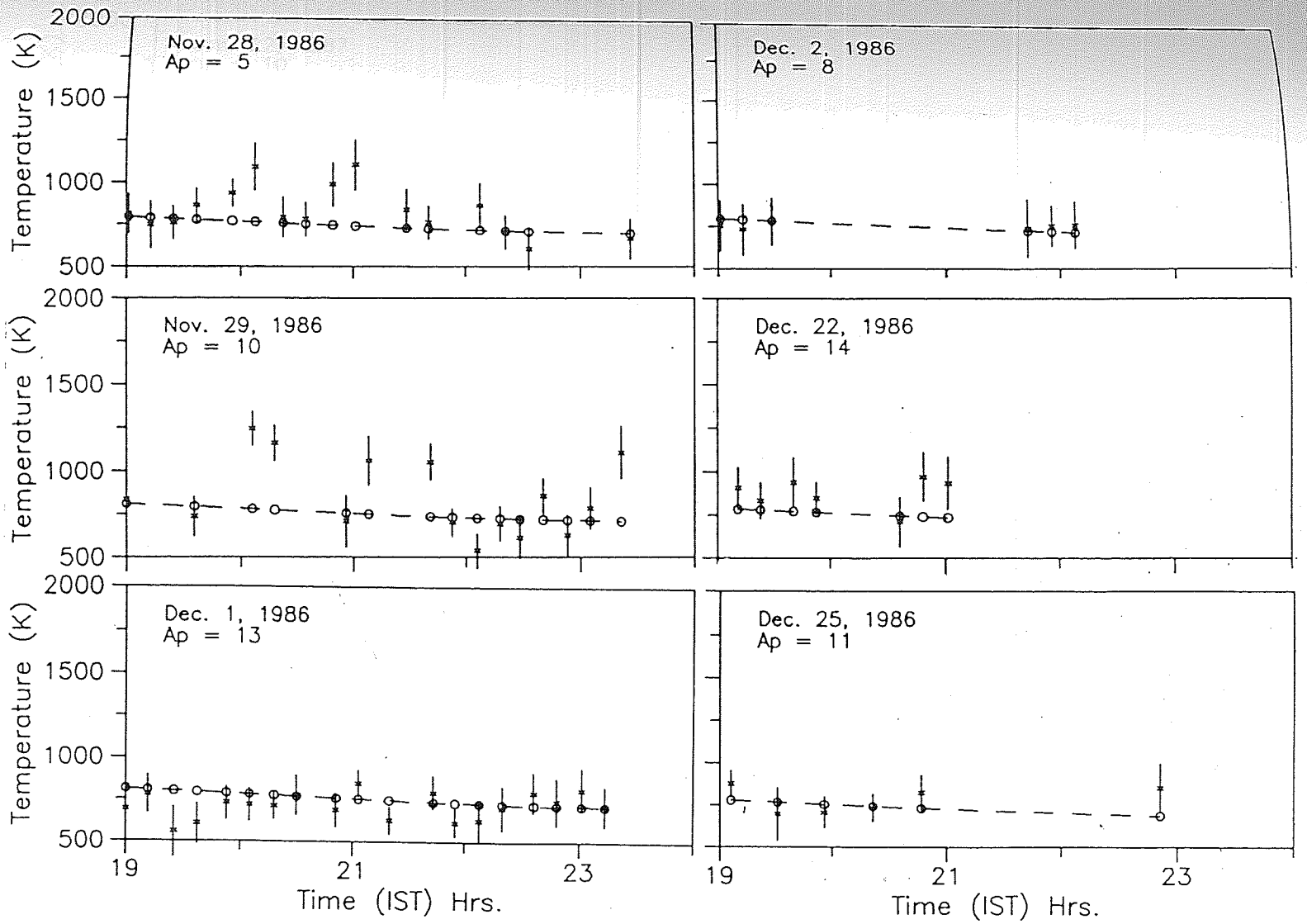

Fig. 3.2b. Same as in Fig. 3.2a.

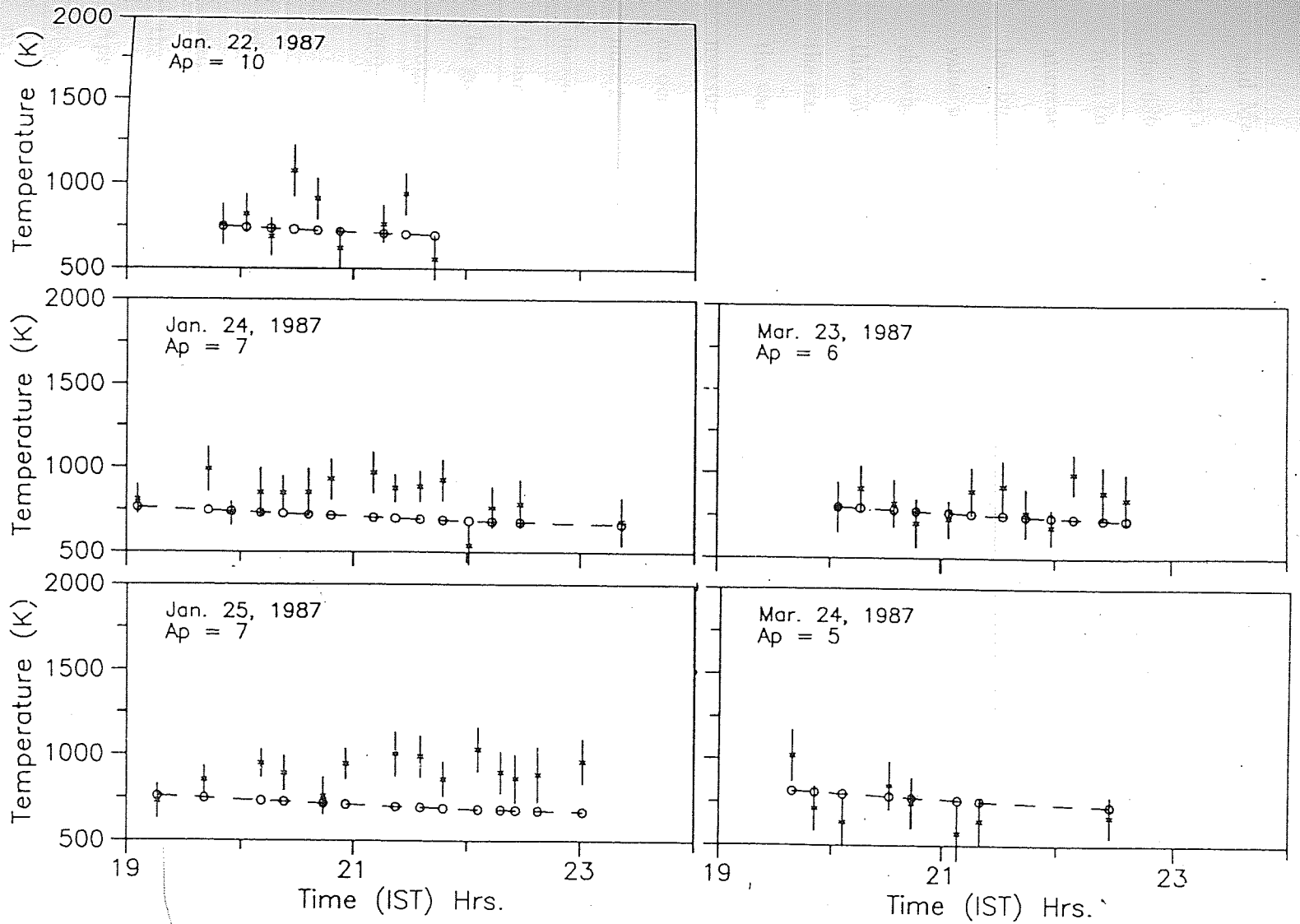

Fig. 3.2c. Same as in Fig. 3.2a.

and March, 1987. Dashed lines joining circles represent the prediction of MSIS-86 model for the days depicted. Observations are limited upto midnight, beyond which the 6300 Å intensity was too low rendering it difficult to recover useful information from the observed fringes. On most of the nights, there is an enhancement in temperature seen after 2100 h Indian Standard Time (IST). On 23 October, the temperature has built up to about 1250 K and a deviation of more than 500 K from the model value is evident. Since the intensity was decreasing slowly with time and as has been shown in the last chapter, the possibility of the line profiles getting distorted due to this, showing up as enhanced temperatures, does not exist. On 25 and 26, October, the model has overestimated the temperatures at least upto 2045 h. If we go through the variation depicted in Figs. 3.2a to 3.2c for different nights, it may be noticed that measured temperatures are in excess as compared to the model predictions except on occasions like for instance, during the month of December. It is interesting to note that on 1 December, the average MSIS-86 model value is 756 K and the average measured value is 712 K, the difference being only 44 K. Also on 2 and 25, December, though the number of data points is less, the agreement with the model seems to be good. A temperature bulge is clearly seen on 24 and 25, January 1987, centered around 2100 and 2200 h respectively, the magnitude of the bulge being as large as 300 K.

Figs. 3.3a and 3.3b show the variation of T_n during February and April months of 1991, representing high solar activity period. A close examination of them indicates significant deviation of the measurements from the model predictions on most of the occasions. The temperature deviations are larger in February months than in April months. The enhancements are seen to occur during pre-midnight (5 and 7, February), midnight (11 and 13, February) and both, showing some sort of a wavy structure (14 and 17, February) thus depicting high variability. On the other hand, the agreement with model has been fairly good on 9, 10 and 14, April. Wavy patterns

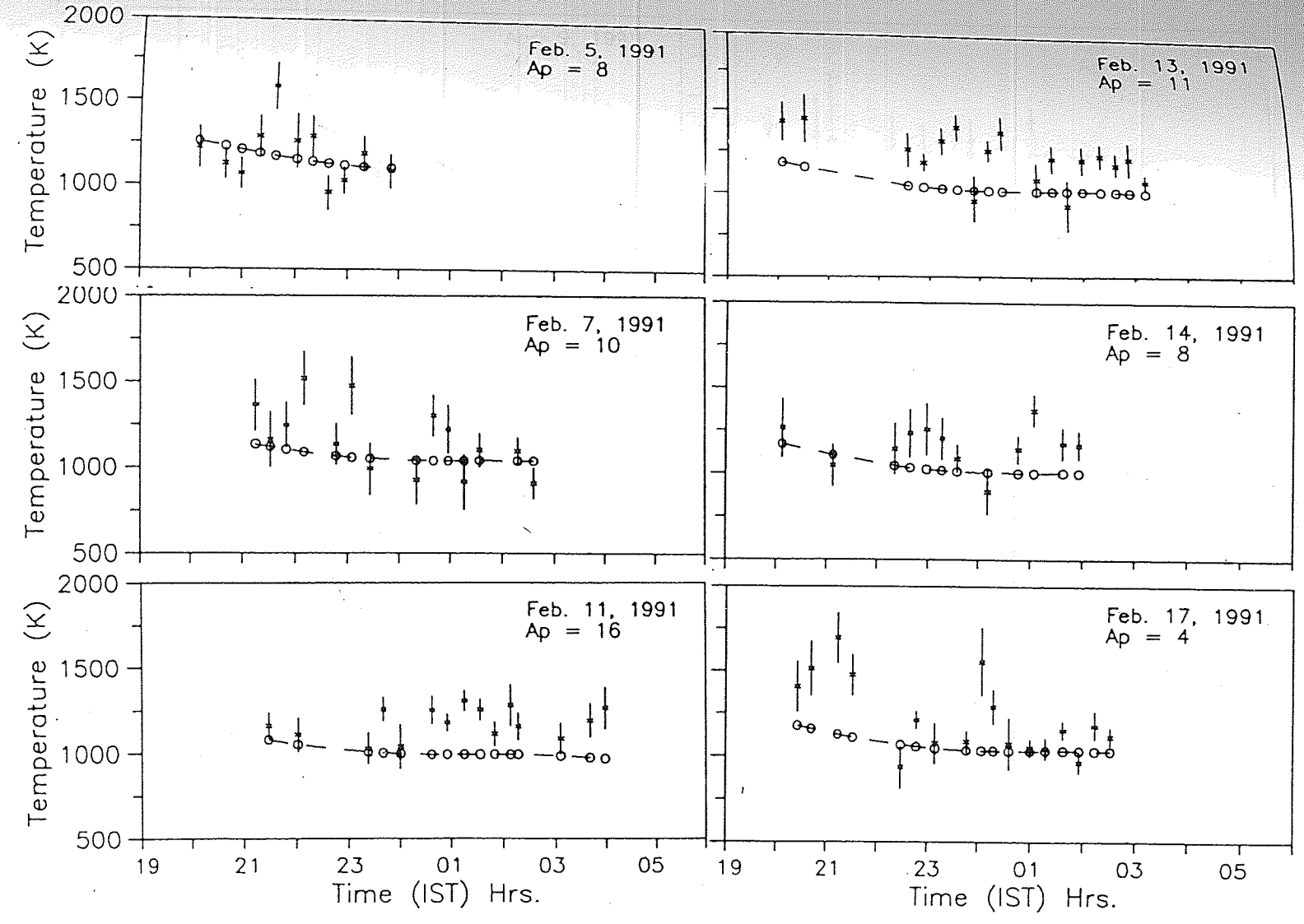

Fig. 3.3a. Same as in Fig. 3.2a but for February 1991.

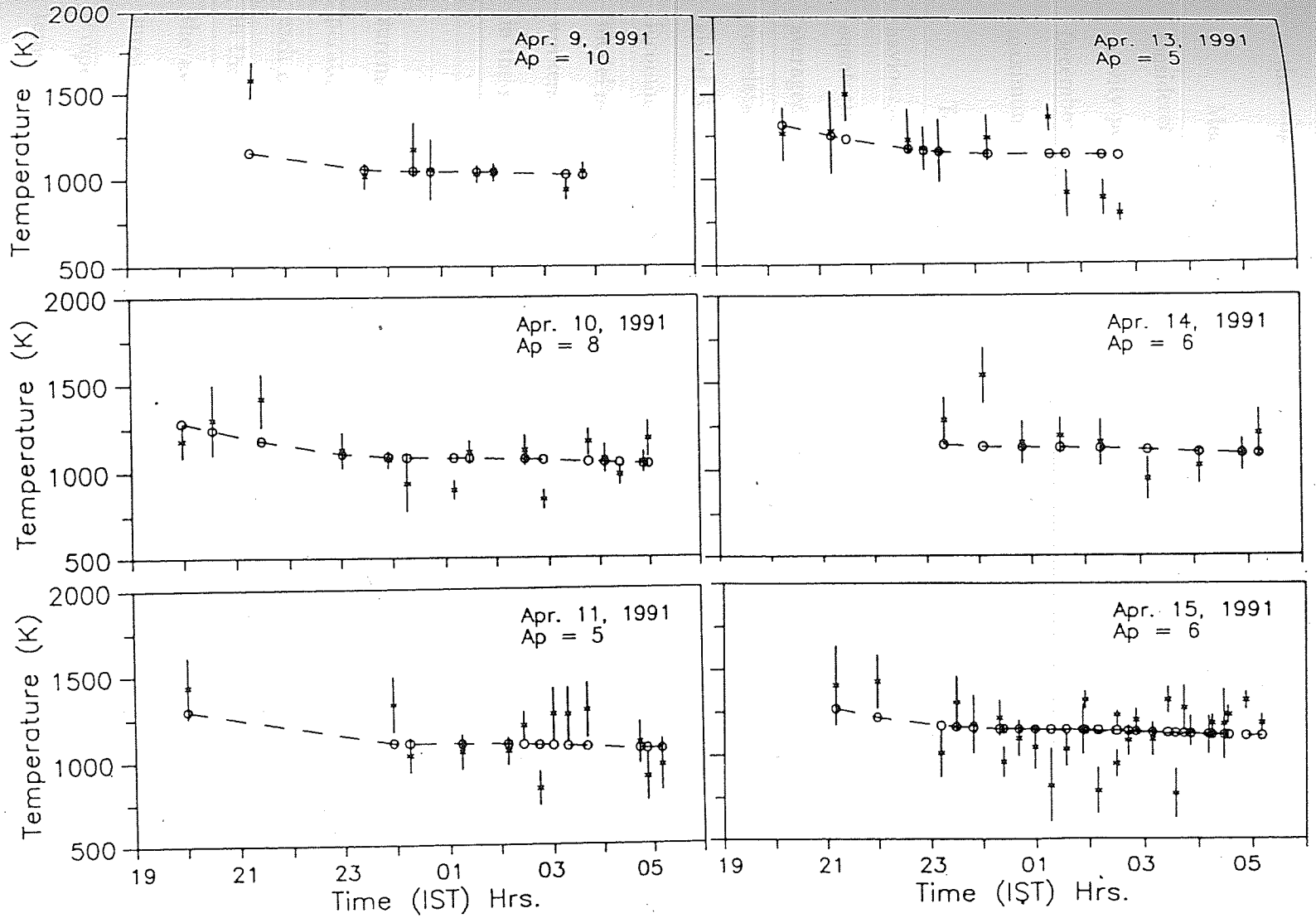

Fig. 3.3b. Same as in Fig. 3.2a but for April 1991.

in the range of 4 to 5 hours) are seen on 11, 13 and 15, April.

Measurements of thermospheric temperature for the 41 nights of observations considered here are plotted in Fig. 3.4. The two groups correspond to the low solar activity period of October 1986 to March 1987 and the high solar activity period of December 1990 to April 1991. The scatter in the plot is slightly more during solar maximum than during solar minimum.

To see how good the neutral atmospheric model represents the overall behaviour of the thermosphere in order to improve the model represent the low and equatorial latitudes reasonably well, the measurements on each of the 41 nights are averaged and are plotted in Fig. 3.5 along with model mean values. Though the correlation coefficient is high of the order of 0.8 (implying that the model can explain about 65 % of variation in neutral temperature ascribing it only to changes in the incoming solar radiation), most of the mean values of observations are higher than model mean values. This observation agrees with the conclusions arrived at by earlier workers and indicates that there exist additional factors that need to be incorporated in the models.

Fig. 3.6 depicts the variation of mean nighttime temperatures, both from measurements and model predictions, for the three periods considered. The average temperatures are computed by sorting out the measurements into different time slots, each of 30 minute duration. The vertical bars indicate the night-to-night variation in the mean temperature at each time. For the 1986–1987 plot (top panel), though the evening mean temperature value was close to the model prediction, the measured temperatures do not show the fall observed in model variation. Instead the temperature fluctuated about a mean value of about 850 K while the model shows a temperature drop of 100 K from the evening average value of 800 K.

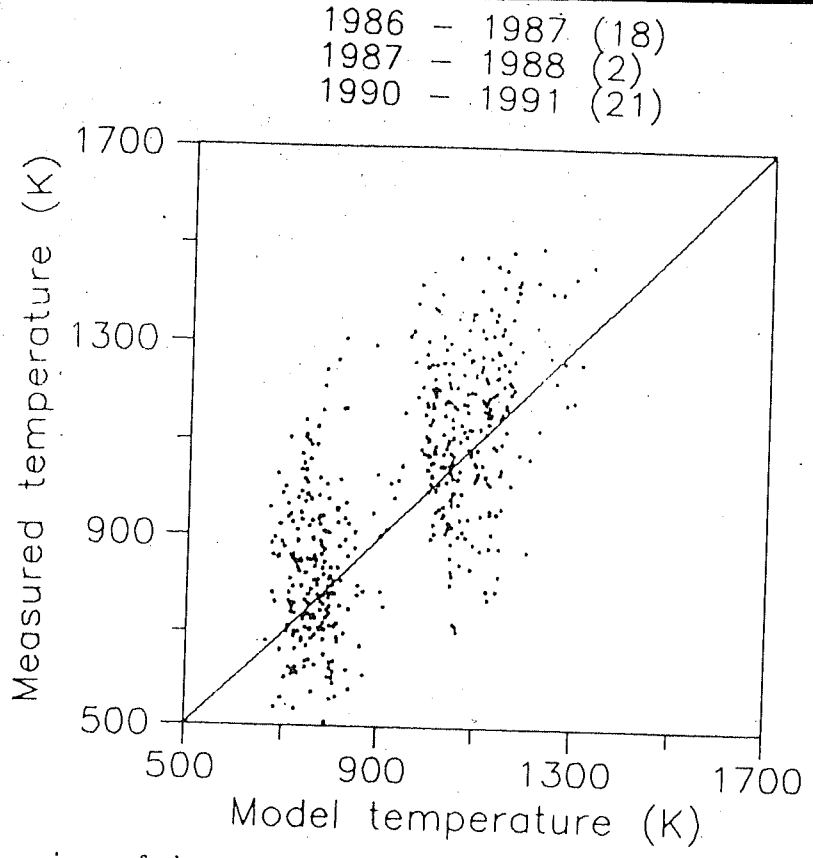

Fig. 3.4. Comparison of the measured thermospheric temperatures with MSIS-86 model predictions for the three periods under study. Individual line profile measurements are plotted against the model values at respective times.

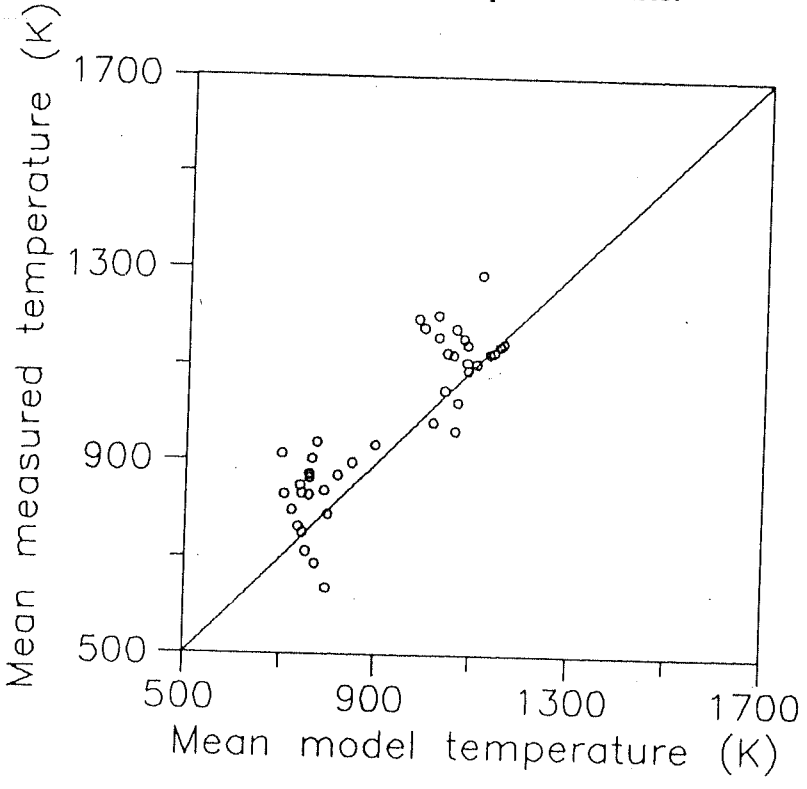

Fig. 3.5. Average thermospneric temperatures for each night of observations made under the present study. The measured and the model average values are compared.

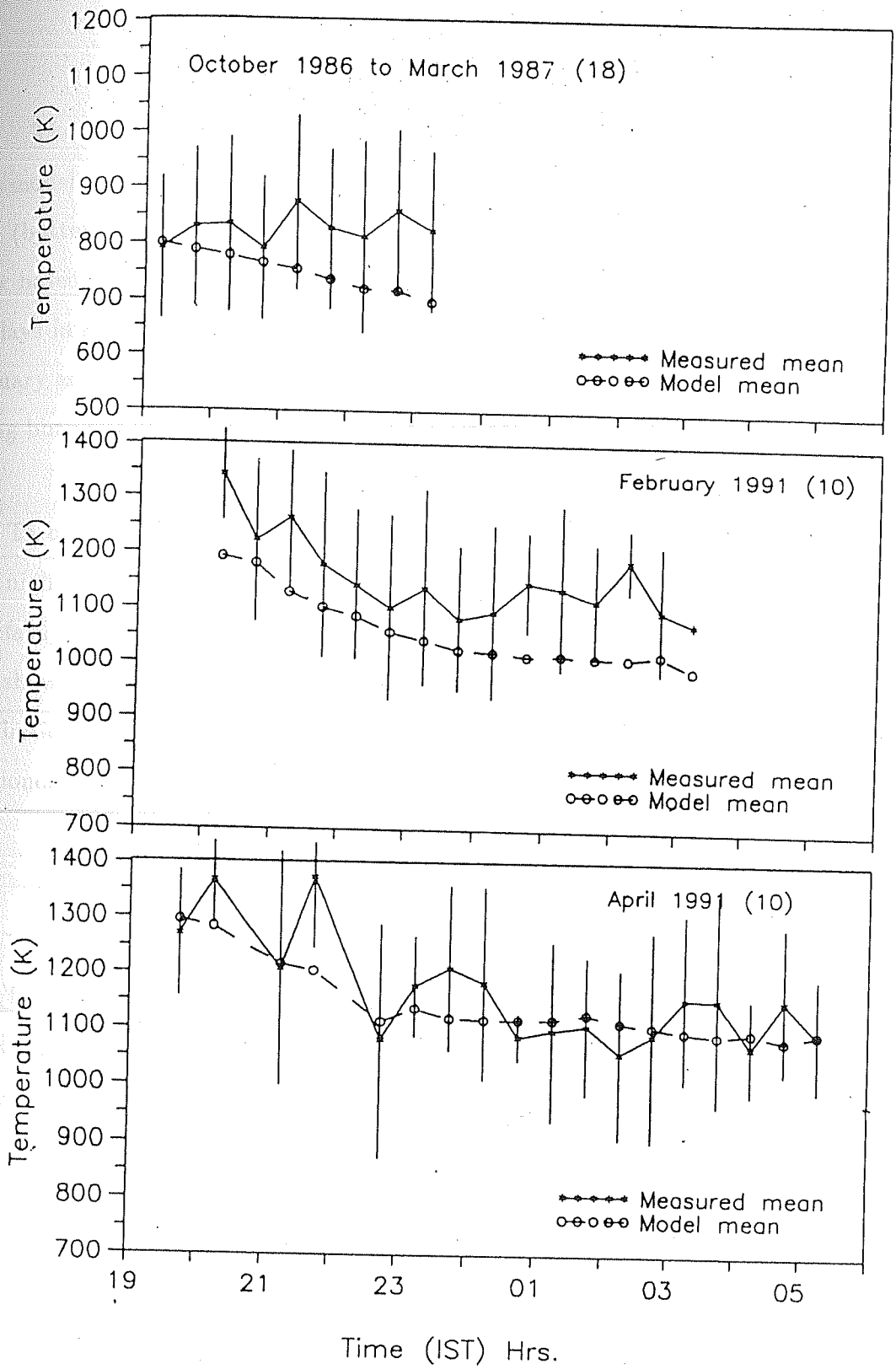

Fig. 3.6. Temporal variation of average thermospheric temperatures for each period under study. The vertical bars denote the night-to-night variation of measured temperatures.

The average temperatures for February 1991 (middle panel), are always higher than model values, the maximum being 150 K after midnight, while those during April 1991 (bottom panel), followed the variation predicted by the model. The solar flux index based on 10.7 cm flux, i.e., $F_{10.7}$, had average values of about 190 and 240 for the days in February and April respectively. Thus the average temperatures during February are expected to be less than those during April. However, the temperatures during both the months fluctuated about 1120 K.

- To conclude, though the semi-empirical model MSIS-86, predicts the average nighttime temperature in response to the changing levels of the solar radiation fairly well (Fig. 3.5), there are occasions on which the observed temperature shows significant deviations from the model, which indicate possible contribution of other physical processes that occur in the nighttime thermosphere-ionosphere system.

3.6 Possible sources of additional energy inputs

Apart from its response to solar radiation, the thermosphere-ionosphere system is perturbed by various other sources like the ones listed below. The study of energetics as it pertains to low latitude and equatorial regions has taken shape only after identification of some of these processes. However, since many of these processes can operate simultaneously and their mutual interaction is largely unknown, it is not possible to associate, say, any heating event as revealed by large rise in temperature, with any of these processes directly. Coordinated measurements from many locations are needed to delineate their physical significance and quantify their role in the overall energy budget of the thermosphere-ionosphere system.

Some of the physical processes that are known to cause enhancements in neutral temperature are

(1) Joule heating associated with the fluctuating electric fields of equatorial spread F (ESF) irregularities

(2) The equatorial temeprature and wind anomaly (ETWA) associated with equatorial ionization anomaly (EIA)

(3) Midnight temperature maximum

(4) Heating associated with high latitude geomagnetic disturbances and associated particle precipitation.

Since a detailed description of each of these processes ((1) to (3)) is given in chapter 6, in this section, we state only their relevance to the energetics of the low latitude thermosphere. Since we do not have results for temperature measurements during a storm period, we shall not consider the effects of a magnetic storm.

(1) ESF associated heating

A strong association of electrostatic turbulence with spread F has been established by an early work of *Kelley* [1972]. The vertical drift velocities of the spread F irregularities were often observed to be three to four times greater than the drift velocity of the normal undisturbed ionosphere. The main observed feature has been the turbulent nature of the velocity pattern which gave rise to the view that the electrostatic turbulence and the spread F are related [*McClure and Woodman*, 1972]. *Balsley et al.* [1972] have observed large spread F drift velocities ($\sim$ 400 m/s) using a 50 MHz coherent radar located over the dip equator, at Thumba, India. This implied that spread F is associated with a mechanism capable of producing a turbulent electric field having rms values several times the magnitude of the normal dynamo electric

field of the undisturbed ionosphere [*McClure and Woodman*, 1972]. *Cole* [1974] made use of this view to suggest dissipation of these electric fields and possible subsequent heating of the neutral atmosphere at F region heights. A brief account of his theory of spread F associated heating of the upper atmosphere follows.

By moving charged particles, an electric field does mechanical work which then appears as heat due to collisions within the conducting medium (Joule's law). The rate of frictional heating of species 1 due to collision with species 2 is

$$Q_{12} = \frac{m_1 m_2}{m_1 + m_2} n_1 (v_1 - v_2)^2 \nu_{12} \tag{3.1}$$

where m_1, m_2 and v_1, v_2 are the masses and drift velocities of the gases 1 and 2 respectively. ν_{12} is the collision frequency of gas 1 with gas 2. From this expression, it becomes clear that for an ion-neutral gas medium, neglecting the drift velocity of neutral species, and since the drift velocity of the ions is proportional to the applied electric field E, the corresponding heat input Q varies as E^2. The amount of heat appearing in the ion gas due to the presence of an electric field can then be estimated.

The heating rate of the ion gas is given by

$$Q = \frac{1}{2} n_i m_i \left(\frac{E}{B}\right)^2 \nu_i \tag{3.2}$$

(from equation 3.1)

Assuming that the energy loss of the ions is mainly due to the elastic collisions with neutrals responsible for frictional heating, a simple relationship can be established between the temperature difference of ions and neutrals and their relative velocity. The rate of energy exchange (cooling rate) between the ion and the neutral gases is given by

$$L = -\frac{3}{2} n_i k (T_i - T_n) \nu_i \tag{3.3}$$

[*Banks and Kockarts*, 1973]

Equating the heat input to the heat loss (energy balance considerations) leads to the result

$$T_i - T_n = \frac{m_i}{3k}\left(\frac{E}{B}\right)^2 \tag{3.4}$$

This expression shows that the temperature difference depends neither on particle concentration nor on collision frequencies but varies as the square of the drift velocity of the ion gas. For a drift velocity of 400 m/s which has been detected by *Balsley et al.* [1972], the temperature difference is as high as 100 K. The dissipation rate can be calculated from equation (3.2) with $n_i = 10^{12}$ /m^3, $\nu_i = 0.2$ /s and is approximately 0.03 mW/m^2 which is comparable to that provided by the solar EUV flux [*Roble and Dickinson*, 1973]. If we use the expression for the temperature gradient with height,

$$\frac{\partial T}{\partial h} = \frac{1}{AT^{1/2}} \int Q \, dh \tag{3.5}$$

[*Rishbeth and Garriott*, 1969]

it leads to a rise in neutral temperature of about 1 K per km, which is significantly higher than what has been arrived at by model atmospheres in use.

The above theory of *Cole* [1974] suggests that significant amount of energy is consumed if the fluctuating electric fields and drift velocities associated with spread F as reported by *Balsley et al.* [1972] exist. Spread F associated ionospheric irregularities that are known to be magnetic field aligned, are often observed upto $\pm$ 20° north and south of the magnetic equator, [*Weber et al.*, 1983]. In such a case, the heating may be inferred to occur all along the flux tubes in which spread F occurs. Since the ion-neutral collision frequency is much larger at lower altitudes in the magnetic conjugate regions, Cole expects a higher flux tube integrated heat input at the two farther ends of the flux tubes.

In the early work by *Rajaraman et al.* [1979] and *Rajaraman* [1982], using the temperature measurements from Mt. Abu, a statistical analysis of the behaviour of the neutral temperatures was done and it was found that on 35 % of the occasions, they were in excess of more than 50 K when compared to the Jacchia model predictions. The large increases in measured temperature were interpreted as possibly due to the equatorial spread F associated heating. A height region of 250–300 km over Mt. Abu gets connected magnetically to a height of about 700 km over the magnetic equator. The spread F information over the magnetic equator has been made use of in their study. Though a good correlation between the spread F occurrence over the magnetic equator and the enhanced temperature over Mt. Abu has been observed, it is to be noted that on all the seven nights presented and discussed by them, spread F did not occur at Ahmedabad (two degrees south of Mt. Abu) as evidenced by the ionosonde located here. This is an important point to be noted, as according to Cole's theory, the presence of spread F irregularities and fluctuating electric fields are a must along the flux tubes, for enhancing the neutral temperature.

This is further strengthened by the results obtained from the present work. For the temperature measurements available for 17 nights in February and April months of 1991 (out of which twelve were presented in the last section), spread F over Ahmedabad occurred on only three nights (5 and 11, February and 12 April) and temperature enhancements were indeed seen at these times. However, increases in temperature were seen on other nights also while spread F did not occur. Similarly during the years 1986–1987, on most of the nights, there is no indication for spread F occurrence over Ahmedabad, and we do not have information about the occurrence on remaining nights at this low latitude station due to paucity of simultaneous ionospheric data.

In this regard, it is useful to look into the evolution of equatorial spread F irregularities. They occur at regions of steep electron density gradients associated with plasma depletion in the equatorial ionosphere, which is generated by a Rayleigh-Taylor instability mechanism. It has been established that, after sunset, the irregularity regions develop from the bottom side of the ionosphere, and cause a plasma depletion or a plasma bubble which rises into region above the peak of the F_2 layer moving up to well over 1000 km in altitude. Under the influence of magnetic field, the irregularities extend in latitude along the magnetic meridian and give rise to spread F echoes in the ionograms when they reach the bottomside of the low latitude ionospheric regions [*Huang et al.*, 1987]. In the event of the irregularities not being generated locally over Ahmedabad/Mt. Abu, the occurrence of spread F in this region then depends on the intensity of development of spread F (range or frequency type) over the magnetic equator and the magnitude of the drift velocities of the irregularities.

- Since on most of the occasions, simultaneous ionospheric - thermospheric data when available, do not show simultaneous occurrence of spread F both over the equator and at Ahmedabad, the important conclusion that one arrives at is that the observed enhancement in neutral temperatures cannot be ascribed to spread F associated processes alone. Coordinated measurements of thermospheric and ionospheric parameters from two or three stations in the equatorial and low latitude zone are needed to provide conclusive evidence for the heating associated with spread F irregularities as proposed by *Cole* [1974].

(2) Equatorial temperature and wind anomaly (ETWA)

The ionosphere near the magnetic equator exhibits an anomaly in the ionization distribution with magnetic latitude (equatorial ionization anomaly (EIA)).

During daytime, the plasma drifts are upward over the equator from where they diffuse along the geomagnetic field lines analogous to a plasma fountain, to latitudes away from the equator. This leads to formation of enhanced plasma densities at latitudes $\sim \pm 16^{\circ}$ north and south of the dip equator. The plasma drifts turn downward during the night and a reverse plasma fountain takes place when the crests of ionization move back towards the equator. The flow of air past an anomaly in ion density and the resulting circulation have been first described by *Dickinson et al.* [1971]. The role of a dense region of ionization is to limit the speed of neutral air flow through frictional interaction (ion-drag). Thus a zonal wind gets impeded in its flow past an enhanced ion density. The wind driven by the global scale differences in pressure, acts as a carrier of energy which is to be distributed everywhere in order to reduce the differences in temperature and hence pressure. When the ion-drag is operative in the region of ionization anomaly, the wind dissipates its momentum and energy at these locations [*Anderson and Roble*, 1974]. The temperature builds up in this region accompanied by increases in neutral density [*Hedin and Mayr*, 1973]. The EIA, as expected, gives rise to anomalies in neutral temperature and zonal winds.

Raghavarao et al. [1991] have reported this anomaly (ETWA) using the simultaneously obtained neutral atmospheric and ionospheric data from the DE 2 satellite. Recently, an evidence for the presence of vertical winds of significant magnitude in the equatorial thermosphere have also been shown by *Raghavarao et al.* [1993]. They have also shown the existence of pressure ridges which are collocated with temperature crests. A new wind system has been proposed by them with rising motion at the location of the crests and sinking motion near the magnetic equator.

Fig. 3.7 depicts the DE 2 measurements of electron density, neutral temperature and zonal wind as reported by *Raghavarao et al.* [1991]. The enhancements in neutral temperature to the tune of a few hundred degrees are very well collocated

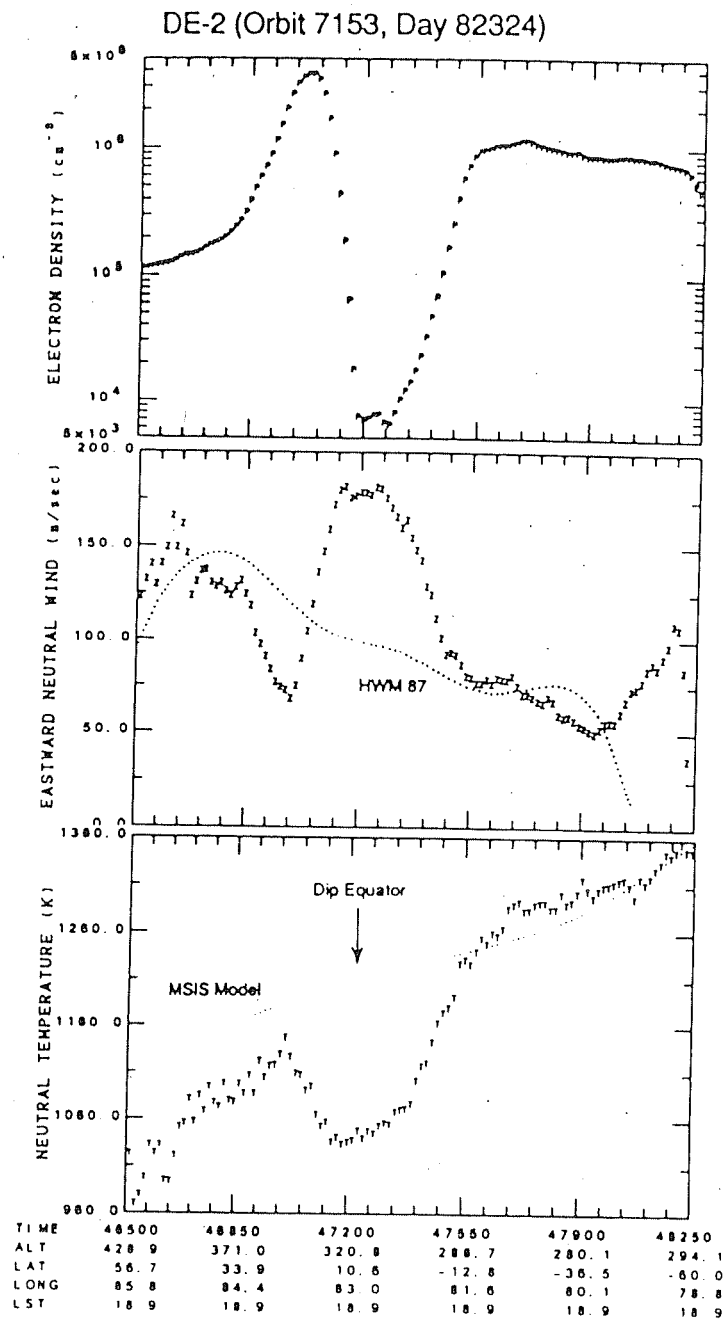

Fig. 3.7. The equatorial anomaly observed in neutral temperature and zonal winds (ETWA) shown for comparison with the anomaly in electron density (equatorial ionization anomaly) based on the DE 2 satellite mission. (after *Raghavarao et al.*, 1991)

with the crests of equatorial ionization anomaly. The expected variation in zonal wind magnitude with dip latitude is also seen.

With the observational evidence for temperature build-up at the location of the crests of EIA having been shown, we look into this mechanism as a possible source of temperature increases observed from Mt. Abu. It is to be noted that this possible source has relevance only during solar maximum period. A renewal of fountain effect due to prereversal enhancement of the electric field in the evening hours over the equator, strengthens the anomaly crest and the reverse fountain prolongs well beyond midnight hours during solar maximum whereas during solar minimum period, the reverse fountain starts in the evening hours and the crests of ionization disappear by midnight [*Sastri*, 1990]. We expect that the ETWA would not be significantly affected during solar minimum.

- The results presented in last section showed that though the average nighttime temperature is fairly well correlated with changes in solar flux, on certain occasions, the thermospheric temperatures do not respond to such changes. The measured temperatures in the month of February, 1991, are higher (average of $\sim$ 150 K) than the MSIS-86 model predictions while the agreement has been fairly good for the measurements during April, 1991. This indicates a source of energy during the February months which becomes less significant during April months. It is suggested here that localized processes like EIA associated processes, i.e., the ETWA, might play a role in causing enhancements in neutral temperatures in excess of model predictions.

(3) Midnight temperature maximum

Using the NATE (neutral atmosphere temperature experiment) instrument on AE-E satellite, *Spencer et al.* [1979] have obtained direct *in situ* measurements of the

diurnal variation of exospheric temperature. They have observed that in the equatorial region, the diurnal temperature variation exhibits pronounced secondary maxima at about midnight, sometimes larger than the primary maxima in the afternoon hours. In association with these maxima in temperature, a large poleward wind ($\sim$ 100 m/s) has been observed which is superposed over the nighttime equatorward component of the meridional wind. A careful analysis of the nature of the wind system reveals that winds converge towards the equator during pre-midnight hours and diverge afterwards. The convergence and the associated pressure build-up would result in the adiabatic heating and a consequent temperature rise [*Harper*, 1973; *Spencer et al.*, 1979]. *Mayr et al.* [1979] attributed this feature to a complex interaction between the semi-diurnal tide generated in the lower atmosphere and ion-neutral momentum coupling associated with the diurnal variation of the ion density, which in turn also generates higher order tidal modes.

It is difficult to infer the latitudinal extent of the midnight temperature maximum from the AE-E satellite measurements. The AE-E satellite was flown near the equatorial region during solar maximum period, with an orbit inclination of 19°. Within the latitudinal belt of 19° north and south of the equator, the temperature maxima have been observed. These observations reveal no apparent dependence on longitude or the local magnetic field and this feature is present about one-half the time of the total measurements.

From the observations within a zone where equatorial ionization anomaly has its influence, like for instance, from Mt. Abu and Ahmedabad, it is not possible to decipher the feature associated with midnight temperature maximum. Before the direct measurements from AE-E data were available, increases in temperature near midnight have been predicted by the OGO 6 model atmosphere [*Hedin et al.*, 1974] and these were also inferred from the measurements of Jicamarca radar [*Hernandez*

et al., 1973]. *Anderson and Roble* [1974] have attempted to invoke the neutral atmospheric response to the changing ion densities at a particular height due to the $\mathbf{E} \times \mathbf{B}$ drifts, in order to explain the observed temperature rise near midnight. The interaction mechanism was similar to what has been proposed earlier by *Dickinson et al.* [1971]. The rapid uplift of ionization due to the pre-reversal enhancement in electric field in the evening hours offers a reduced ion-drag near the equator. The resulting renewed fountain effect pumps the ionization to locations away from the equator where the ion-drag starts showing its effect of impeding the zonal winds. The deposition of momentum and energy by the zonal winds could give rise to a temperature increase at these locations similar to the one observed by *Raghavarao et al.* [1991] using the DE 2 measurements.

- With the two different mechanisms incorporated to explain the temperature increase observed near midnight sector of equatorial region (though both are based on ion density variations), coordinated ground based measurements from at least two stations are needed to quantify the relative role played by them in governing thermospheric dynamics and energetics.

Chapter 4

Servo model and its applicability to low latitudes

4.1 Introduction

The location of peak electron density well above the peak of ion production was an enigma to the ionospheric physicists in the late 1940's and 1950's. Whereas the lower regions (E and F_1) conform closely to the Chapman's theory of layer formation, the ionization distribution in the F_2 region differs considerably from the expected morphology. It was recognized by then that the behaviour of the F_2 layer is complex and inexplicable in terms of solar ionizing radiation and chemical recombination alone. It was *Mitra* [1946] who first realized the importance of motions of plasma along the magnetic field lines at heights where the plasma-neutral collision frequencies are small, and hence the geomagnetic control of ions and electrons in the F_2 region of the ionosphere. *Martyn* [1956] showed that, under the forces of gravity and of its own partial pressure gradient, diffusion of ionization along the magnetic field lines in the vertical direction would considerably affect the shape and height of the F_2 region. Further, he demonstrated that the ionospheric layer with any initial height distribution of electron density, would approach the Chapman form. He was the

first to realise that the morphology of the F_2 layer might be explained with the inclusion of electrodynamic drifts of ionospheric plasma. *Duncan* [1956] extended the conclusions reached by Martyn and showed that a uniform vertical drift would alter the equilibrium height of the F_2 layer.

With the plasma diffusion in the upper atmosphere becoming important, *Shimazaki* [1957] derived expressions for the contribution of diffusion to overall motion of F_2 layer plasma. *Yonezawa* [1958] solved the relevant equations for a particular model atmosphere to arrive at appropriate analytic functions which revealed the formation of the F_2 peak by the action of diffusion. Following this, *Rishbeth and Barron* [1960] in an important work, arrived at general relationships between the parameters, namely, the diffusion and recombination rates, which determine the position and magnitude of the F_2 peak for equilibrium conditions. They showed that above the peak electron density, i.e., $N_m F_2$, diffusive equilibrium gets established in a time of order $1/d(z)$ where $d(z) = D(z)/H^2$, $D(z)$ being the diffusion coefficient at the level z and H the scale height of the ionizable gas. At the peak, the time taken for equilibrium is slower, being of the order $1/d_m$ $(=1/\beta_m)$.

Briggs and Rishbeth [1961] obtained an analogue solution to the continuity equation for F region electron density by considering an equivalent electrical network with a series of condensers and resistors. The charge on a condenser represented the electron density at a certain height, and the value of a resistor which provided a path for the leakage of this charge, represented the loss and diffusion coefficients. The continuity equation was first transformed into a type similar to that for the voltage on each condenser. Operation of the electric circuit with the inclusion of a potentiometer representing the diurnally varying ionizing solar radiation, yielded useful outputs which were analogous to the actual ionospheric behaviour. The advantage of analogue method was that any desired height variation of temperature, loss coefficient, etc.,

could be incorporated with ease. It further demonstrated the validity of the concepts about the F region which were originally developed for more restricted models. In spite of the drifts due to electromagnetic forces and the diurnal temperature variation of the atmosphere not being taken into account, this analogue method showed how the F region would behave if controlled by the three basic processes of production, loss and diffusion [*Rishbeth*, 1963]. By developing a time-varying model, *Rishbeth* [1964] examined the processes governing the behaviour of the F layer. However, because of the complexity of the problem, it had been difficult to develop a basic theory to account for the major features of the F layer.

One of the intriguing features of the F layer is the large variabilities it exhibits in its vertical motion. It was recognized by *Martyn* [1956] that the processes responsible for the vertical motion of the F_2 layer are the drifts imposed by electrodynamic forces and the winds associated with the ionospheric electric current systems which are manifested as the daily magnetic variations at the ground. The effects of atmospheric heating, and the temperature dependence of reaction rate and the diffusion coefficients, on the equilibrium height distribution of electron density were estimated by *Garriott and Rishbeth* [1963]. The interest in the wind systems set up by the diurnal heating and cooling of the thermosphere had begun when they were shown to have significant speeds of the order of 100 m/s to be effective at F region heights [*King and Kohl*, 1965; *Geisler*, 1966]. These winds were invoked to explain the large vertical displacements the F_2 layer showed at midlatitudes, as they are capable of driving the plasma along the geomagnetic lines of force thereby altering the plasma density distribution. *Rishbeth* [1967] developed an approximate method to compute the theoretical diurnal variation of the peak electron density in the midlatitude ionosphere. Observing that external forces such as winds perturb the equilibrium distribution, the F_2 layer was envisaged as behaving like a servo mechanism. The effect of winds on both 'day equilibrium layer' and 'night stationary layer' was investigated by him. It

became clear from his studies that the day-to-night changes of the height of the peak electron density, $h_m F_2$, at midlatitudes, are caused largely by the action of winds on the F_2 layer.

The servo model of *Rishbeth et al.* [1978] provides a means of investigating the basic interactive nature of the thermosphere-ionosphere system. With reasonable assumptions, it offers possibilities of examining the behaviour of the F_2 peak, given the information on thermospheric parameters and the F_2 layer peak height. The limitations of the servo model as pointed out by *Rishbeth et al.* [1978], are its limited accuracy and the fact that it treats the F_2 layer as a unit, and therefore can give no information about height variations within the layer. In spite of this limitation, the servo model is being adopted by various workers to understand and determine the nature and magnitude of the driving forces on the midlatitude F region and the variabilities associated with them [*Yagi and Dyson*, 1985; *Miller et al.*, 1986; *Buonsanto et al.*, 1989; *Forbes and Roble*, 1990].

It is to be noted that the behaviour of the thermosphere-ionosphere system as a servo system at a particular location on the globe needs a large magnetic dip angle in order to aid the diffusion of ionization along the magnetic field lines in the vertical direction. In a region where the magnetic dip is I, the vertical velocity is reduced (from a value for the case $I = 90°$) by $\sin^2 I$. It was the fact that the vertical diffusion gets inhibited over the magnetic equator that allowed earlier workers such as *Martyn* [1956] to confirm the importance of diffusion at midlatitudes. *Martyn* [1956] showed that the absence of vertical diffusion at the equator is responsible for the observed large variations in the F region height, and the same diffusion would prevent the F_2 region from being elevated above about 400 km in moderate to high latitudes and even this height should seldom be attained. With the absence of vertical diffusion at the magnetic equator, electrodynamical processes control the F region and its

variabilities.

At low latitudes, where the dip angle is non-zero, it is not known whether the F layer behaves as expected by the servo model. Therefore it became necessary to investigate the basic processes of low latitude thermosphere-ionosphere system, which close the cycle of interactions illustrated in Chapter 1. The behaviour of the low latitude region is complicated by large scale processes such as equatorial ionization anomaly [*Moffett*, 1969], neutral density anomaly [*Hedin and Mayr*, 1973], equatorial temperature and wind anomaly [*Raghavarao et al.*, 1991], equatorial spread F [*Fejer and Kelley*, 1980] and midnight temperature maximum [*Spencer et al.*, 1979], whose role in the energetics and dynamics of the upper atmosphere is largely unknown.

The present investigation was initiated in order to understand the basic interaction mechanisms which play a significant role in the wake of the presence of such large scale processes. In doing so, coordinated measurements of thermospheric parameters, namely, neutral temperature and meridional winds, and ionospheric parameters, namely, the F layer peak height, deduced from the existing ground-based ionosonde, during nighttime, are made use of, along with the servo model concept proposed by Rishbeth as a tool. *Rishbeth* [1986] in his paper on the F_2 layer continuity equation has discussed the possible ways of altering the loss coefficient β and also the contributions of various other parameters to the transport term. As suggested by him, it becomes easier and rewarding to interpret the F_2 layer processes by means of a term-by-term examination of the continuity equation. In the following section, the significance of the transport parameter in the overall behaviour of the F_2 layer is discussed by means of the continuity equation. This is followed by a brief description of the principles underlying the servo model leading to the discussion on 'night stationary layer'. The results providing the first experimental evidence for the validity of servo model at low latitudes is presented next. The effects of neutral temperatures on

the F layer height are determined quantitatively. A new method is being adopted to estimate the F layer peak height i.e., $h_m F_2$, with the available data on winds and temperatures. The estimated heights are compared with observed heights deduced from ground-based ionograms and the factors, namely, electric fields, which contribute to the deviations between the observed and the estimated heights are determined.

4.2 The F_2 layer continuity equation

The effects of transport processes on the electron density N at any height become evident through the continuity equation for the F_2 layer which is given by

$$\frac{\partial N}{\partial t} = q - L(N) - \mathrm{div}(N\mathbf{v}) \tag{4.1}$$

where q is the rate of production of plasma, L the rate of loss which takes the linear form βN in the F_2 layer and $\mathbf{v}$ the drift velocity of the electrons whose divergence represents the transport of ionization.

The importance of each of the terms in (4.1) is well documented in the literature [*Rishbeth and Garriott*, 1969; *Rishbeth*, 1986]. Below the peak of electron density and during the day, photochemical equilibrium prevails, with $q \sim \beta N$. Above the peak, where the production of ionization becomes unimportant, the transport term dominates and governs the dynamics of the F_2 layer. During most of the day, the F_2 peak is in a state of quasi-equilibrium in which the production, loss and transport terms are comparable in magnitude and are much larger than $\partial N/\partial t$. This state is established within a time of the order of $1/\beta$ ($\sim$ 1.5 h by day). During nighttime, when the average life time of the plasma becomes larger (thrice during solar maximum period) than that during daytime, the layer could be perturbed easily and therefore the term $\partial N/\partial t$ becomes significant. This typically happens during sunrise and sunset times and during when plasma irregularities are generated over short time

and small spatial scales.

The important contributions to the transport term are as follows.

(i) The plasma diffusion velocity, in the absence of thermal diffusion, is given by

$$-v_D = D(h)\left[\frac{1}{N}\frac{\partial N}{\partial h} + \frac{1}{T}\frac{\partial T}{\partial h} + \frac{\mu}{H}\right]\sin^2 I \tag{4.2}$$

[*Shimazaki*, 1957; *Rishbeth and Barron*, 1960]

$D(h)$ denotes the ambipolar diffusion coefficient at a height h, T the temperature, H the scale height of the ionizable gas and μ the ratio of mean molecular weights of the plasma and the ionized gas which takes the value $1/2$, if the two are chemically the same.

The diffusion velocity can also be derived with a simple physical reasoning as was done by *Martyn* [1956]. If a particle of mass m, making an average of ν collisions per second with the surrounding gas, is influenced by a force F, it will drift through the gas with the velocity $v = F/m\nu$. The vertical gravitational force on an ion pair is $\sim m_i g$. In the presence of a pressure gradient, the vertical force per unit volume on the ionization is $-\partial(p_i + p_e)/\partial h$, where $p_i = p_e = NKT$, K being the Boltzmann's constant. Thus this force is $-2KT\partial N/N\partial h$ per ion pair.

The transport velocity due to gravity and pressure gradient is therefore

$$v_D = -\frac{m_i g_i}{m_i \nu_i} - \frac{2KT}{N m_i \nu_i}\frac{\partial N}{\partial h}$$

$$= -\frac{g}{\nu_i}\left[1 + \frac{2H}{N}\frac{\partial N}{\partial h}\right]$$

For ionization transport along the magnetic field lines with a dip angle I, this becomes

$$v_D = -\frac{g}{\nu_i}\left[1 + \frac{2H}{N}\frac{\partial N}{\partial h}\right]\sin^2 I \tag{4.3}$$

(4.2) and (4.3) are equivalent if D takes the form $2gH/\nu_i$ and the gradient of temperature with height is neglected.

At the peak, the diffusion velocity becomes

$$v_{D_m} = -\frac{D_m}{2H} \sin^2 I \tag{4.4}$$

(ii) A neutral wind $\mathbf{U}$ is capable of moving the plasma along the magnetic field lines, at a speed equal to its component in that direction. The resulting drift velocity is given by

$$\mathbf{v}_w = (\mathbf{U}.\mathbf{B})\ \mathbf{B}/B^2 = \mathbf{U} \sin I \cos I \tag{4.5}$$

At latitudes away from the equator, an equatorward wind can push the plasma upward and a poleward wind can bring it down. By moving the layer vertically, the wind thus alters the balance between the production and loss, increasing $N_m F_2$ if it is equatorward and decreasing $N_m F_2$ if it is poleward.

(iii) The electromagnetic forces in the presence of an electric field $\mathbf{E}$ and the magnetic field $\mathbf{B}$ produce an $\mathbf{E} \times \mathbf{B}$ drift, given by the well known formula

$$\mathbf{v}_E = \frac{\mathbf{E} \times \mathbf{B}}{B^2} \tag{4.6}$$

This can be derived by considering the equation of motion of a charged particle under the influence of electric and magnetic fields [*Chen*, 1974]:

$$m\frac{d\mathbf{v}}{dt} = q\,[\mathbf{E} + \mathbf{v} \times \mathbf{B}]$$

$m\ d\mathbf{v}/dt$ represents the circular motion of frequency ω_c $(= qB/m)$. Omitting this term, the above equation becomes

$$\mathbf{E} + \mathbf{v} \times \mathbf{B} = 0$$

Taking the cross product with $\mathbf{B}$,

$$\mathbf{E} \times \mathbf{B} = \mathbf{B} \times (\mathrm{v} \times \mathbf{B}) = \mathrm{v}B^2 - \mathbf{B}\,(\mathrm{v}.\mathbf{B})$$

The transverse components (perpendicular to $\mathbf{B}$) of this equation are $\mathrm{v}_\perp = \mathrm{v}_E = \mathbf{E} \times \mathbf{B}/\mathrm{B}^2$. v_E is the electromagnetic drift of the charged particle and is independent of its charge and mass. Thus ions and electrons in the F region of the ionosphere drift together in the presence of electric and magnetic fields, producing no net current. The collisions of neutrals with ions, namely, the ion-drag, reduce the drift term by a small magnitude.

(iv) The effects of thermal expansion and contraction of the atmosphere on the electron density profile in the F_2 layer were first discussed by *Garriott and Rishbeth* [1963]. It was shown by them that, if the electron density profile is expressed in terms of reduced height z, rather than the real height h, the temperature dependence of the diffusion and the recombination coefficients can be accounted for. The reduced height z then corresponds to a fixed pressure level. Changes in temperature lead to changes in the height of the pressure levels. The plasma takes part in the thermal expansion and contraction. The continuity equation can be solved in terms of fixed pressure levels thereby properly accounting for the temperature dependence of the coefficients D and β [*Rishbeth*, 1986].

Returning to the continuity equation, an expansion of the transport term leads to

$$\frac{\partial N}{\partial t} = q - \beta N - N \,\mathrm{div}\, \mathbf{v} - \mathbf{v} \,.\, \mathrm{grad}\, N \qquad (4.7)$$

In the F region, the divergence of velocity is often small. The last term $(v\partial N/\partial h)$ on the right hand side represents the effect of moving a density gradient across the point of observation. For upward drifts, this term leads to an increase

of N on the topside ($\partial N/\partial h$ is negative) and a decrease on the bottomside ($\partial N/\partial h$ is positive) and vice versa. The result of the action of an imposed vertical drift is thus the motion of the whole F layer with velocity v_z. Since q and β vary with height, the density distribution in the translated layer at and below the peak, then adjusts itself within a time of the order of $1/\beta$ to the altered values. Above the peak, the redistribution of ionization occurs at the rate of diffusion. For small displacements, the peak electron density (given by q_m/β_m) remains unaltered. To have a significant effect, a drift has to move the plasma through a vertical distance (say one scale height) within its lifetime, which in turn, requires the drift velocity $v_z \sim \beta H$.

Fig. 4.1 shows the equilibrium behaviour of the F region following the ionospheric model for Arecibo ($I = 50°$) developed by Walker and his colleagues [*Walker*, 1988]. When the F layer is displaced upward by forcings such as winds and electric fields, the downward diffusion increases and opposes further upward motion of the layer. For downward drifts, increased recombination rate opposes further lowering of the layer-maximum. Under equilibrium conditions, the imposed vertical drift is balanced by diffusion if the layer is displaced upward and by recombination if the layer is displaced downward. This is illustrated by the top panel. The bottom panel shows how the equilibrium height of the F_2 peak responds to the imposed vertical drift.

In what follows, the servo equation for the behaviour of the F_2 peak in the absence of applied drifts, is derived from the first principles using the continuity equation.

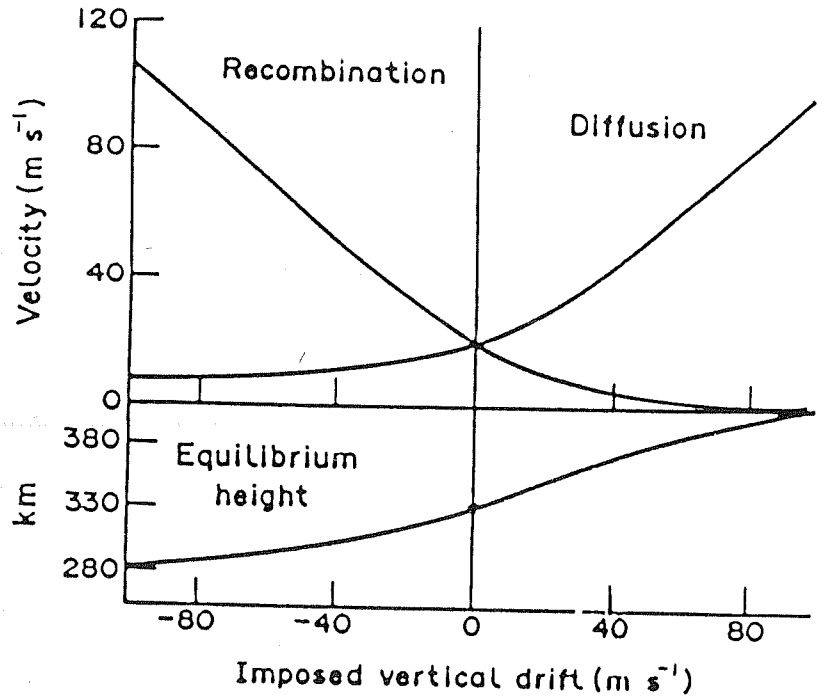

Fig. 4.1. Response of the F region to changes in imposed vertical drift. The top panel illustrates the roles played by chemical recombination and plasma diffusion in altering the equilibrium height of the F_2 peak. The equilibrium height is depicted in the bottom panel. (after *Walker*, 1988)

4.3 The night stationary layer (Rishbeth's servo model)

The F_2 layer behaves like a servo system obeying the following laws [*Rishbeth*, 1967; *Rishbeth et al.*, 1978]:

(a) In the absence of applied vertical drift, the F_2 peak lies at a balance height determined by diffusion and loss.

(b) Vertical drift due to changes in neutral temperature, meridional winds or electric fields, displaces the equilibrium position of the peak to a new level, which is time-varying if the drift is time-varying.

(c) At any instant, the actual height of the peak approaches its equilibrium value at a rate determined by diffusion and loss.

(d) The rate of change of peak electron density is determined by local values of the production rate and loss coefficient.

Expressing the electron density profile in terms of the reduced height z, the continuity equation (4.1) is rewritten as

$$\frac{\partial N}{\partial t} = q - \beta N - \frac{1}{H}\frac{\partial}{\partial z}(N v_z) \tag{4.8}$$

where H is the scale height of the ionizable gas related to z by

$$z = \int_{h_0}^{h} \frac{dh}{H(h)}$$

where h_0 is the balance height in the absence of applied drifts. The suffix 'm' is used to represent the quantities at the level of the peak electron density $N_m F_2$. v_z in (4.8) represents the vertical plasma velocity. In the continuity equation, the contribution to the transport term is assumed to arise largely in the vertical direction.

Integrating (4.8) from $z = z_m$ to $z = \infty$,

$$\frac{\partial}{\partial t}\int_{z_m}^{\infty} N dz \;=\; H\int_{z_m}^{\infty}(q-\beta N)dz - \Phi_\infty + N v_z|_{z_m}$$

The relative vertical velocity of the plasma and the peak is $(v_{z_m} - H dz_m/dt)$. The above equation then becomes

$$\frac{\partial}{\partial t}\int_{z_m}^{\infty} N dz \;=\; H\int_{z_m}^{\infty}(q-\beta N)dz - \Phi_\infty + N_m\left(v_{z_m} - H\frac{dz_m}{dt}\right) \qquad (4.9)$$

Φ_∞ corresponds to the plasma flux flowing outward along the magnetic field lines at the top of the ionosphere. This outward flux is insignificant over low and equatorial latitudes. However, redistribution of F region plasma due to processes like the equatorial ionization anomaly and transport due to transequatorial winds would contribute significantly to Φ_∞.

The following assumptions are made in order to arrive at an expression for the rate of change of layer height, dz_m/dt, i.e., the servo equation:

(i) The topside of the F layer maintains a constant shape. If a is the layer shape factor, then the integrated ion content is aHN_m. The equilibrium distribution of the F_2 region takes a Chapman form for which $a = 2.82$. Indeed it was shown by *Duncan* [1956] that a Chapman layer irrespective of its height, maintains a constant shape.

(ii) The F_2 peak is well above the peak of ion production so that $q \propto e^{-z}$.

(iii) The dominant ion is O^+ and decays by reacting with neutral N_2, for which $\beta \propto e^{-kz}$ where k (=1.75) is the ratio of the scale heights of the molecular gas participating in the charge exchange reaction, i.e., N_2 and the ionizable gas, i.e., O.

The validity of these assumptions, when it comes to the expected behaviour of the F layer in accordance with the 'servo' concept, is discussed later.

(4.9) then becomes

$$aH\frac{dN_m}{dt} = q_m H - a'\beta_m N_m H - \Phi_\infty + N_m(v_{z_m} - H\frac{dz_m}{dt}) \qquad (4.10)$$

For $k = 1.75$, the constant a' which comes from the height integral of $\beta_m N$ can be approximated by $1/k = 0.57$.

If W is the vertical drift applied to the layer by a wind or electric field, and v_{D_m} the drift due to the diffusion (expressions (4.3) and 4.4)), then the vertical plasma velocity is given by

$$v_{z_m} = W - \frac{g}{\nu_{in}}\sin^2 I = W - \frac{D_m}{2H}\sin^2 I \qquad (4.11)$$

Substituting in (4.10) and dividing by $N_m H$,

$$\frac{dz_m}{dt} = \frac{q_m - \Phi_\infty/H}{N_m} - \frac{a}{N_m}\frac{dN_m}{dt} - \frac{\beta_m}{k} - \frac{D_m \sin^2 I}{2H^2} + \frac{W}{H} \qquad (4.12)$$

Now the total derivative of N_m with time is

$$\frac{dN_m}{dt} = \left(\frac{\partial N}{\partial t} + \frac{\partial N}{\partial z}\frac{\partial z}{\partial t}\right)_{z_m}$$

$$= q_m - \beta_m N_m - \frac{v_z}{H}\frac{\partial N_m}{\partial z} - \frac{N_m}{H}\frac{\partial v_z}{\partial z} \qquad (4.13)$$

The term corresponding to $\partial N_m/\partial z$ vanishes at the peak.

Including the flux Φ_∞ uniformly distributed over the 'equivalent thickness' aH, of the layer and combining the effects of diffusion and the transport processes at the peak by introducing a constant c, (4.13) becomes

$$\frac{dN_m}{dt} = q_m - c\beta_m N_m - \frac{\Phi_\infty}{aH} \qquad (4.14)$$

The constant c has been estimated to be 1.6 by *Rishbeth* [1967] from idealized solutions of the full diffusion equation. He has ignored the effect of vertical drifts on c.

Combining this expression with (4.12),

$$\frac{dz_m}{dt} = (1-a)\frac{q_m}{N_m} + \frac{kac-1}{k}\beta_m - \frac{D_m \sin^2 I}{2H^2} + \frac{W}{H} \tag{4.15}$$

During nighttime, $q_m = 0$, and in the absence of the applied vertical drift W, and for equilibrium conditions $dz_m/dt = 0$, (4.15) reduces to

$$\beta_s = \frac{kD_s \sin^2 I}{2H^2(kac-1)} \tag{4.16}$$

and if z_m is measured from this level, the servo equation is

$$\frac{dz_m}{dt} = \frac{D_m \sin^2 I}{2H^2}\left[e^{-kz_m} - e^{z_m}\right] + \frac{W}{H} \tag{4.17}$$

wherein the exponential variation of β and D with height are made use of.

Further, the whole ionospheric layer, during nighttime, decays with an effective loss coefficient β_e at the F_2 peak given by

$$N_e = N_{e_0}\, e^{-\beta_e t}$$

With $q_m = 0$, it decays continually unless maintained by a downward flux of ionization. However, if the height of the F layer is altered due to external forces, it would have a significant influence on the rate of decay. Fig. 4.2a shows typical variations of peak electron density after sunset, in the pre-midnight hours on 23 and 24 October, 1986, at a low latitude station, Ahmedabad. Fig. 4.2b shows the plot of $\log_e(N_{max})$ with time for the two days. The slope of the curves yields β, the recombination coefficient, which turns out to be $\sim 2.0 \times 10^{-4}$ s^{-1} during the pre-midnight hours. On 23 October, the layer was pushed upward to higher heights after 2100 h (probably due to increase in neutral temperature as can be seen in Section 4.5) and the decay turned out to be very slow. On the next day, i.e., 24 October, the effect which caused the upward motion of the F layer occurred at a later time after 2230 h, after N_{max}

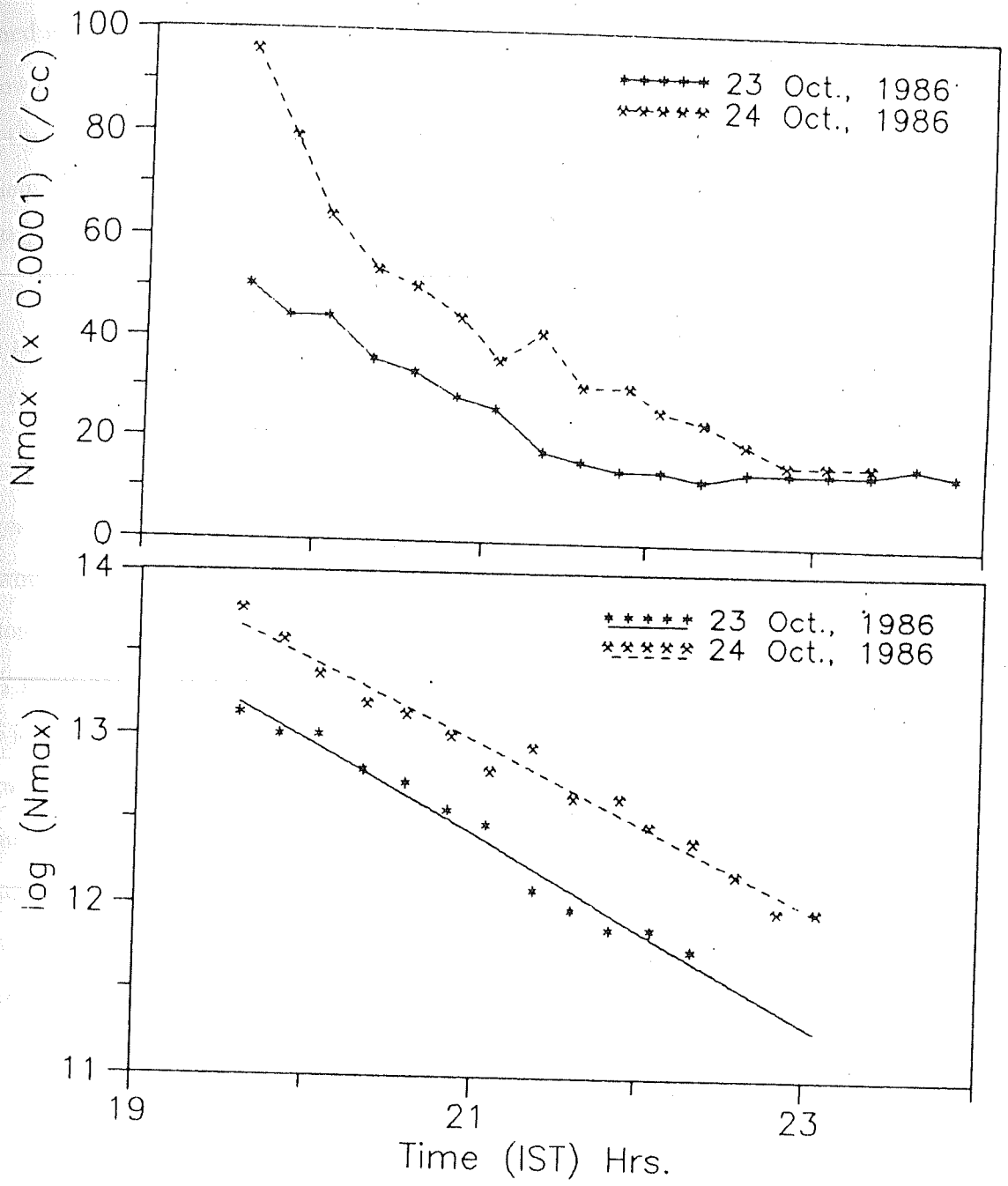

Figs. 4.2a,b. Temporal variation of the peak electron density, N_{max}, and $\log_e(N_{max})$ over Ahmedabad for the two nights of October 1986. The top panel depicts the decay of peak electron density with time. A measure of β ($\sim 2 \times 10^{-4} s^{-1}$) is obtained from the slope of the best fit line shown in the bottom panel.

attained low values ($\sim 1.6 \times 10^5$ cm^{-3}). From these examples, it becomes clear that at a low latitude station, in the absence of any sources of ionization, i.e., during nighttime, the external forces can move the layer to very large heights thereby decreasing β and help to sustain the layer without further decay. Indeed it was shown by *Hanson and Patterson* [1964] that if the F_2 peak height is raised by vertical drift, the net effect is to decrease the rate of decay of the layer. They suggested that this appeared to be an attractive alternative for the maintenance of the midlatitude F region at night rather than the protonosphere providing a supply of ionization.

The F_2 peak would be formed at a level where equation (4.16) holds. Local changes in neutral temperature cause changes in the neutral composition, which in turn would alter the height where the peak ionization density of the F_2 layer occurs. The contribution from the neutral temperature in inducing changes in the height of the F_2 peak can be estimated by studying the response of the latter to the changes in the former. Since β and D vary with height, the expression (4.16) can be used for determining the layer height directly. The other method would be to use an iteration technique to find the height where the balance occurs. An initial height, say, 200 km is assumed to begin with, and the servo expression is worked out for this height to determine the deviation between the terms corresponding to β and D. The height is incremented in steps of 1 km and this procedure is repeated till the deviation is minimized and the solution converges towards the height where the balance occurs. We have used both the methods to determine the balance height and examined the effects of changes in neutral temperature on the peak level. The following values are adopted to solve (4.16) for h_s, the 'night stationary height' of the F_2 peak.

$$\beta = 10^{-18}\,[\mathrm{N_2}] \qquad (\mathrm{s}^{-1})$$

$$[\mathrm{N_2}] = 3.22 \times 10^{15} \exp[-\frac{k(h_s - 200)}{H}] \qquad (\mathrm{m}^{-3})$$

$$[\mathrm{O}] = 4.07 \times 10^{15} \exp[-\frac{(h_s - 200)}{H}] \qquad (\mathrm{m}^{-3})$$

$$D = \frac{2gH}{\nu} \qquad (\mathrm{m}^2\ \mathrm{s}^{-1})$$

$$\nu = 7.3 \times \left(\frac{T}{1000}\right)^{1/2} [\mathrm{O}] \qquad (\mathrm{s}^{-1})$$

[*Rishbeth et al.*, 1978; *Banks and Kockarts*, 1000 K Thermopause model, 1973; *Dalgarno*, 1964].

A useful approximation for the scale height H in F region is $H_M \simeq 0.93T/M$ [*Rishbeth and Edwards*, 1989], where M is the mean molecular mass, and H_M is expressed in kilometres.

Substituting these values in (4.16), and solving for h_s,

$$h_s = 200 \times 10^3 + 21.23\ T_n \left[1.5\ \ln\ T_n - \ln\ \sin^2 I - 4.85\right] \quad (\mathrm{m}) \quad (4.18)$$

Fig. 4.3 shows the dependence of the F layer displacement Δh_s with dip angle when the exospheric temperature varies from 700 K to 800 K (for solar minimum conditions). From this figure, it is evident that at very low latitudes, the vertical displacements are expected to be significant for 100 K change in T_n. To examine the 'servo' nature of the thermosphere-ionosphere system at low and equatorial latitudes, a theoretical simulation was done and the results are presented below.

Figs. 4.4a to 4.4d show the effect of temperature on the equilibrium height of the F layer at four different latitudes (dip angles of 68°, 33°, 11° and 5° respectively). Each set of curves depicts the balance of diffusion and recombination terms (equation 4.16) with temperature being varied from 600 K to 1400 K. These sets of curves are generated with the MSIS-86 model yielding densities of N_2, O_2 and O, which are then

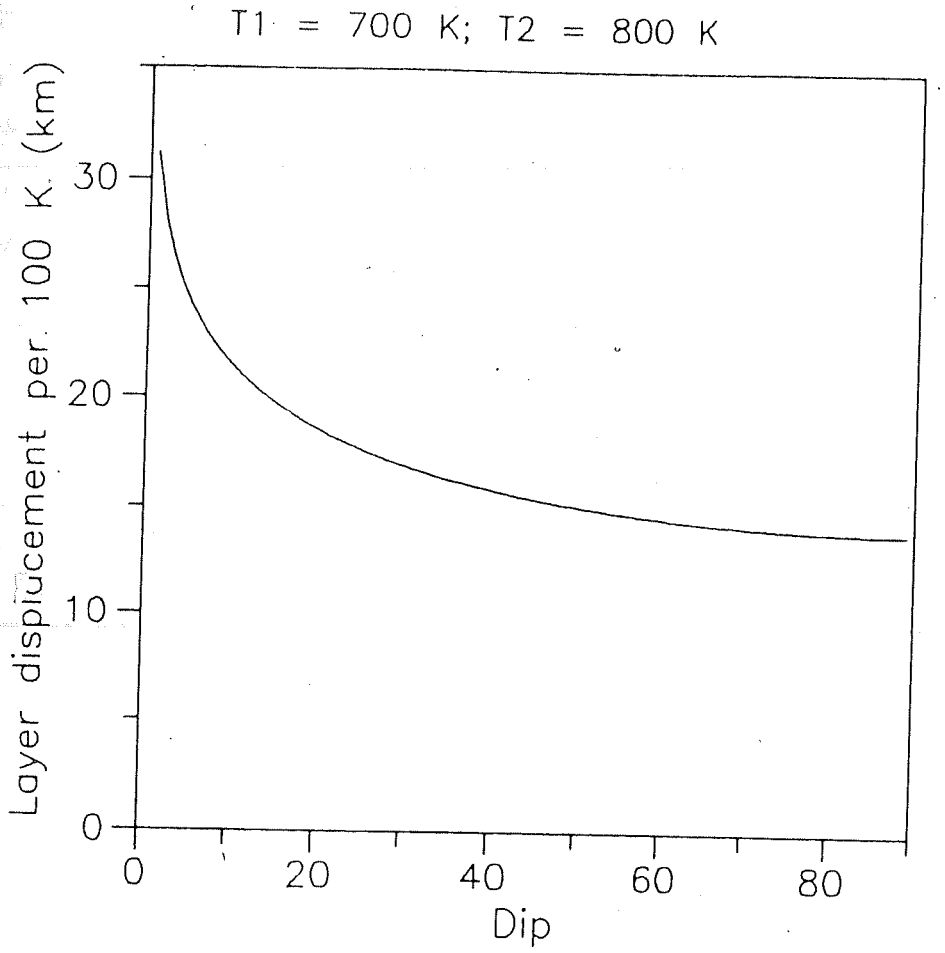

Fig. 4.3. Response of the F region to changes in thermospheric temperature at various dip angles. The $\sin^2 I$ dependence of the layer displacement, Δh_s, is brought out here.

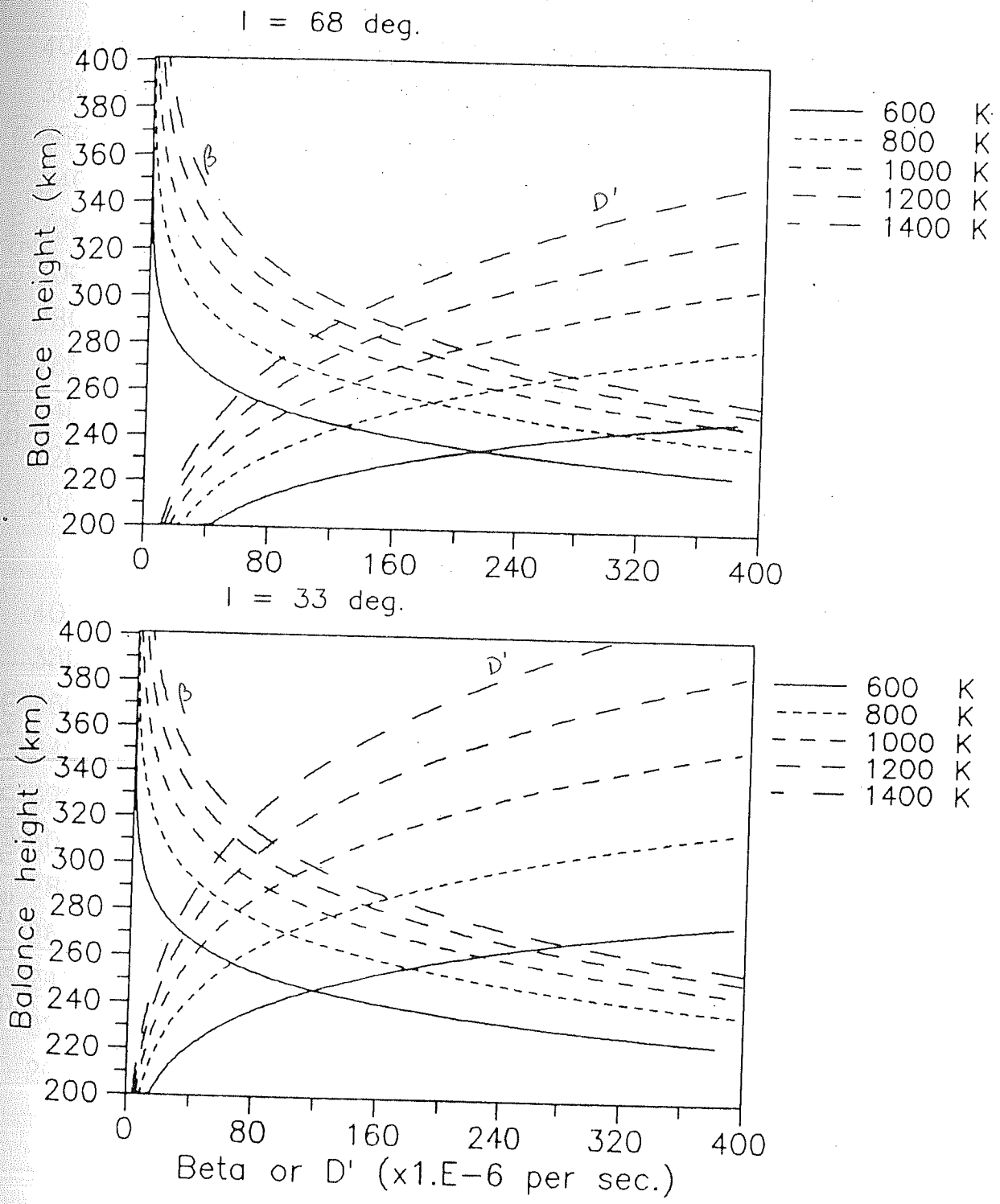

Figs. 4.4a,b. Sets of diffusion and recombination curves for various thermospheric temperatures depicted for dip angles of 68° (top panel) and 33° (bottom panel). The balance height of the F_2 peak occurs at a level where plasma diffusion and chemical recombination are of equal importance. Each set of curves correspond to the balance terms of the servo expression (4.16).

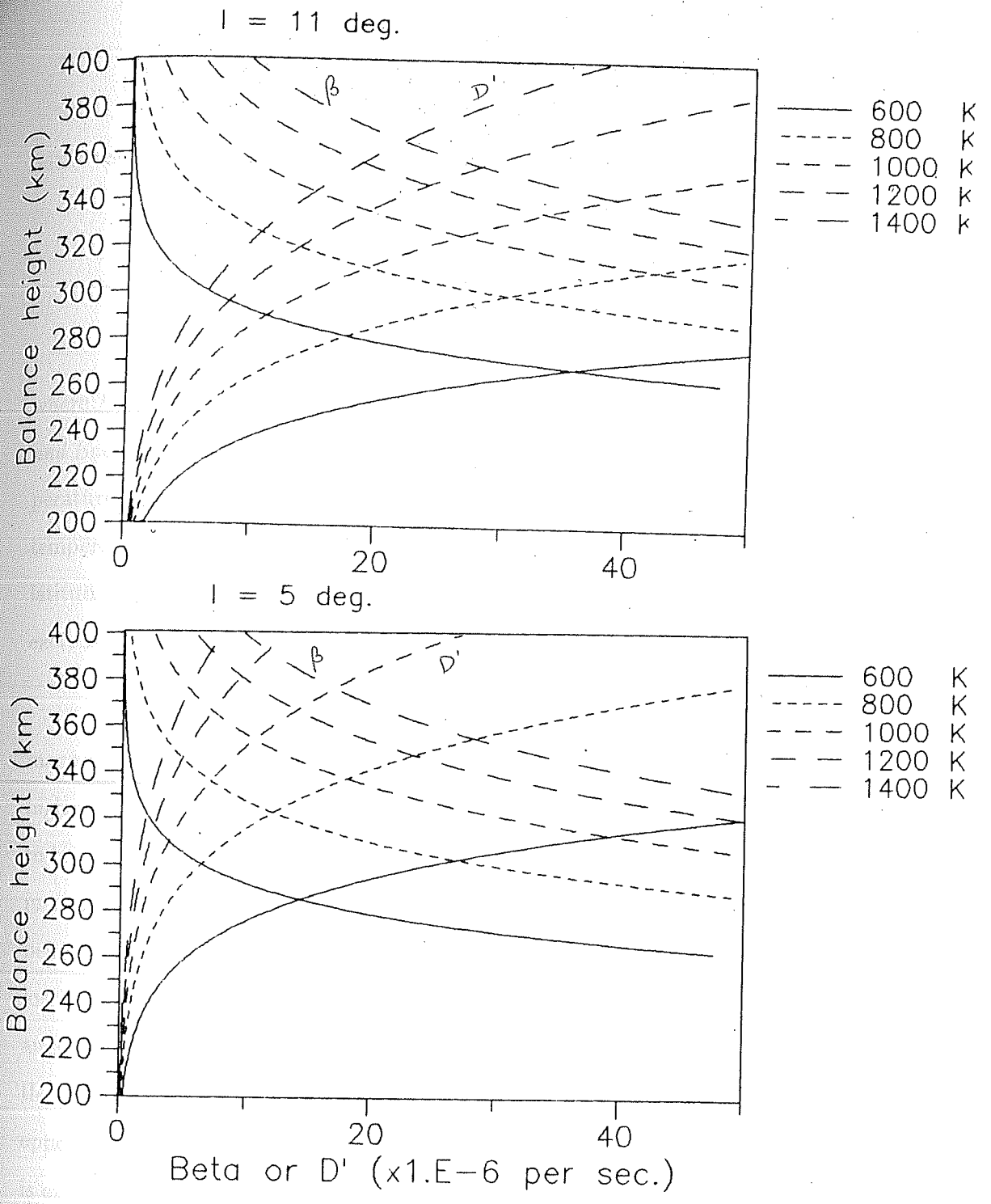

Figs. 4.4c,d. Same as Figs. 4.4a,b but for dip angles, 11° (top panel) and 5° (bottom panel).

made use of in the computation of β_m and D_m as given below.

$$\beta_m = 10^{-17}O_2 + 4 \times 10^{-19}[N_2] \quad (s^{-1}) \tag{4.19}$$

$$D_m = \frac{R(T_i + T_e)}{16[O]K_1 + 28K_2[N_2]} \quad (m^2s^{-1}) \tag{4.20}$$

where $K_1 = 0.93\,(T_n/1000)^{0.37} \times 10^{-16}$ m^3s^{-1} and $K_2 = 3.9 \times 10^{-16}$ m^3s^{-1} [*Rishbeth and Edwards*, 1989]. R is the gas constant and T_i and T_e are the ion and electron temperatures, which are assumed to be equal to T_n during nighttime. Each of the selected temperatures is fed as T_∞, the exospheric temperature, into the MSIS-86 model. The latitudinal dependence of the neutral densities in the model is not considered in this exercise.

Figs. 4.4a to 4.4d show the decreasing importance of diffusion with decreasing magnetic dip angle. The diffusion curves expand out and the balance level occurs at higher and higher height as the magnetic equator is approached. The important point to be noted is that, at low latitudes, the displacement of the layer for a given change in neutral temperature, is inversely proportional to the dip angle, the magnitude being largest near the dip equator. The sharp rise in the curve of Fig. 4.3 at very low latitudes (the layer displacement for 100 K change in T_n is $\sim$ 25 km at a dip angle of 5°) is interpreted to be due to the decreasing influence of plasma diffusion as the geomagnetic field lines become more and more horizontal, which implies reduced opposition on the vertical motion of the layer effected by other applied forcings. This is expected since the F layer response varies as $\sin^2 I$ with dip angle I. This raises a basic question on the validity of servo model at low and equatorial latitudes. In this regard, the assumptions made while deriving the 'servo' expression (4.16), need to be looked into and the validity checked.

In deriving the servo equation (4.17), the shape of the topside of the F_2 layer

is assumed to remain the same. *Harper* [1979] in his paper on the effect of semi-diurnal tides on the F layer over Arecibo, found significant changes in the topside semi-thickness. Such changes in the layer shape will affect plasma diffusion near the peak (through the term $\partial^2 N/\partial h^2$ in the diffusion equation) and this influences the height of the F_2 peak [Ganguly et al., 1980]. Large drifts at very low latitudes due to temperature effects seen in the form of layer movements in Fig. 4.3, could as well give rise to changes in layer shape and hence (4.16) might not represent the actual balance height. At very low latitudes, electrodynamic effects are rather important and the large excursion of F layer observed in the vertical direction is mainly due to the drift associated with electric fields in the equatorial region as was originally shown by *Martyn* [1956]. A detailed study is thus desirable to determine upto what extent the effects of neutral temperature compete with those associated with electrodynamics at and near the magnetic equator.

Another aspect which has not been discussed yet is the dependence of Δh_s on T_n. Equation (4.18) was derived using the density values at a fixed lower boundary (200 km), from the 1000 K thermopause model of *Banks and Kockarts* [1973]. Though the model enabled us to express Δh_s in terms of T_n, the effects of changes in composition associated with the solar activity level, diurnal variation of temperature, etc., are not explicit. Equation (4.18) shows a linear relationship between Δh_s and T_n. However, the simulation study suggests that the recombination curves become narrower at higher temperatures and the displacements are smaller, for identical solar-geophysical conditions.

It follows from this simple theoretical simulation of the 'night stationary balance height' at different latitudes that, the region where the servo model is expected to be applicable may well be upto $\sim 20^\circ$ dip angle ($\sim 10^\circ$ dip latitude) below which the physical picture becomes complicated. The coordinated experiments, the results

of which form a part of the present study, provide confirmation to the applicability of the servo principles to the latitudes of Mt. Abu (24.6°N, 72.7°E geographic; 20.3°N dip latitude) and Ahmedabad (23°N, 72.1°E geographic; 18.4°N dip latitude) and these would be discussed in later sections. As a backdrop to the present study, some of the relevant results from midlatitudes obtained by earlier workers are discussed below.

4.4 Results from midlatitudes

Yagi and Dyson [1985] examined the effects of temperature and meridional winds on the F_2 peak height at midlatitudes using the servo model. They have made use of coordinated measurements of temperatures and winds with a high resolution Fabry Perot spectrometer and the base height of the F layer, $h'F$, from ionosondes located Canberra (35.4°S, 149.2°E, geographic) and Hobart (42.9°S, 147.2°E, geographic) in Australia. Data from 16 nights have been used to examine the behaviour of the F_2 layer in response to changes in neutral temperatures and winds. They found that the 'night stationary level' of the F_2 layer depends on temperature, with the height changing by (13 $\pm$ 6) km per 100 K and concluded that this agreed well with the prediction of the servo model. A brief description of their analysis is given below.

The expression (4.16) relating the plasma diffusion and chemical recombination coefficients has been solved to determine the relation between the F_2 peak height and the neutral temperature. Adopting the 1000 K thermopause model of *Banks and Kockarts* [1973], they solved equation (4.16) for a dip angle $I = 68°$ to obtain an expression for the peak height given by

$$h_s = 5.3 \times 10^{-3}\, T_n\, (5.5 \ln T_n - 19) + 200 \qquad \text{(km)} \qquad (4.21)$$

The virtual heights $h'F$ corresponding to times when the meridional wind was

close to zero were identified, and a plot of $h'F$ and neutral temperatures (T_n) at these times showed good correlation between them. The 'night stationary level' in the absence of wind varied by 13 $\pm$ 6 km for every 100 K change in temperature, which is in accordance with that expected by the servo model.

It is to be noted in this context that there is a discrepancy in the formula relating Δh_s and T_n, derived by *Yagi and Dyson* [1985]. According to equation (4.18), the 'night stationary level' at Beveridge (dip angle of 68°) varies by 15 km for every 100 K change in T_n. While solving the expression (4.18) for this location, it has been found that the source of error in the formula used by Yagi and Dyson appears to lie in the value of g adopted by them for F layer heights.

Fig. 4.5 shows the result obtained by Yagi and Dyson for midlatitudes. The correlation coefficient was 0.76, indicating that almost 60 % of the variation in $h'F$ can be accounted for by the variation in neutral temperature. The two important observations are (i) the scatter in the data points and (ii) the dc shift of $\sim$ 45 km in the theoretical and experimental curves. According to Yagi and Dyson, the latter might be due to the fact that the theoretical curve represented the altitude of maximum electron density, while the experimental curve referred to the base of the F region. The scatter in the data was suggested to be due to the limitations in the model used and the drifts associated with the electric fields not being accounted for and/or due to variations in the parameters like layer shape, time constants of the ionosphere, etc.

A parameter whose effects are most ignored by the current working models on the neutral atmosphere is the turbopause height, the level above the mesopause, above which molecular diffusion is the dominant process, and hence diffusive equilibrium of different atmospheric constituents prevails. It has been shown by earlier workers that the turbopause level has large day-to-day variations [*Pokhunkov et al.*, 1985; *Danilov et al.*, 1979, 1980] and it has an independent control over neutral densities at F region

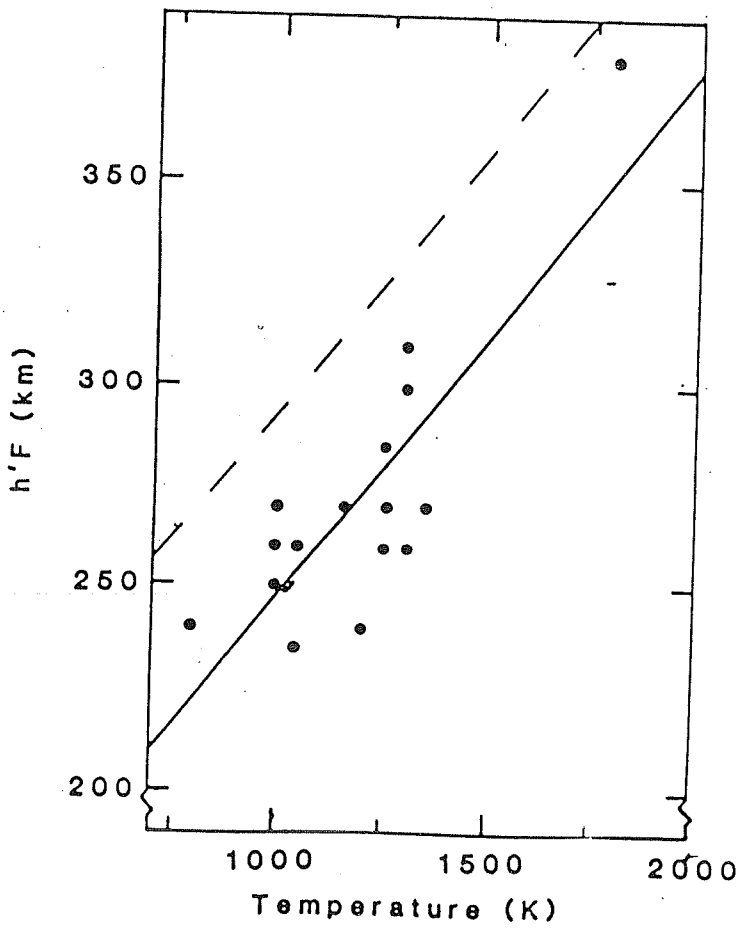

Fig. 4.5. Plot of virtual height $h'F$ and spectroscopically measured temperature at times of zero meridional wind over the midlatitude station, Beveridge (68°S dip). The dashed line corresponds to equation (4.21) in the text. (after *Yagi and Dyson*, 1985)

heights [*Sridharan and Raghavarao*, 1984]. Since both β_m and D_m are strongly dependent on T_n, the neutral composition and the densities, any change in the height of the turbopause would have significant changes in both these parameters, eventually manifesting in the F layer heights. This is an important aspect and might account for the observed scatter in the $h'F$ vs T_n curve obtained by Yagi and Dyson.

4.5 Results from the coordinated measurements from low latitudes

In spite of its limitations and inherent assumptions, it has been demonstrated that the servo model can act as a tool in understanding the nature of the coupling of the thermosphere and the ionosphere [*Ganguly et al.*, 1980; *Yagi and Dyson*, 1985]. The present study was initiated in order to understand this behaviour in low latitude regions.

Coordinated measurements of neutral temperature and meridional winds obtained from Mt. Abu (24.6°N, 72.7°E geographic; 20.3°N dip latitude) and F region parameters such as layer height deduced from the existing ground-based ionosonde at Ahmedabad (23°N, 72.1°E geographic; 18.4°N dip latitude), are made use of, to provide experimental evidence for the applicability of the servo principles. Specific case studies pertaining to magnetically quiet times were made with the existing data base. The data encompass periods from minimum solar activity in the years 1986 and 1987 upto the present level of activity (1992). Since the stability of Fabry Perot etalon to the desired limit of being able to determine the line of sight winds was achieved only in the winter months of 1989, there exist only temperature measurements in the period 1986–1989. Notwithstanding this limitation, individual case studies utilizing the data for the period 1986–1988 provide credence to the concept that the thermosphere and the ionosphere behave like a fairly well coupled servo system at these

latitudes [*Sridharan et al.*, 1991]. The results are presented in this section.

The ionograms obtained by the ionosonde operating from Ahmedabad are reduced to $N - h$ profiles by the standard Budden Matrix method. An electron density (N_e) of 1.2 $\times$ 10^{-5} cm^{-3} is taken as representative of the base of the F region, whose variation (h_{N_e}) is obtained from the reduced $N - h$ profiles.

The two examples presented in Figs. 4.6a and 4.6b show the movement of the F layer as a whole, when there was a simultaneous change in T_n, on the nights of 25 and 26, October 1986. Depiction of the variation of two N_e values indicates that the F_2 layer retains its shape fairly well. The movement is a physical displacement of the layer and not an apparent displacement that would be seen in the event of the plasma getting neutralised at the base of the F region as these measurements are well after sunset. In the examples presented herein, the whole of the F layer is shown to move up and down with a corresponding change in neutral temperature.

These examples clearly show the strong influence of T_n on the F region height. Another effect of the increase in the neutral temperature would be to increase the vibrational temperature of N_2, the dominant neutral species. Due to this, the effective recombination rate of the F region, through the charge exchange reaction of O^+ and N_2, would get enhanced significantly. For a neutral temperature change from 1000 K to 2000 K, the reaction rate of N_2 (vibrational) is known to increase by atleast a factor of 20 [*Banks and Kockarts*, 1973]. This is expected to have significant effect on the electron densities at any height. Though the decrease of N_{max} as shown in Figs. 4.6a and 4.6b is expected on the basis of the 'night stationary decay' as discussed earlier, the role of such large changes in T_n in altering N_{max} densities cannot be ruled out.

The next five diagrams (Figs. 4.6c to 4.6g) depict the behaviour of the thermosphere - ionosphere system on nights of 23, 24 and 27, October 1986, 23 November

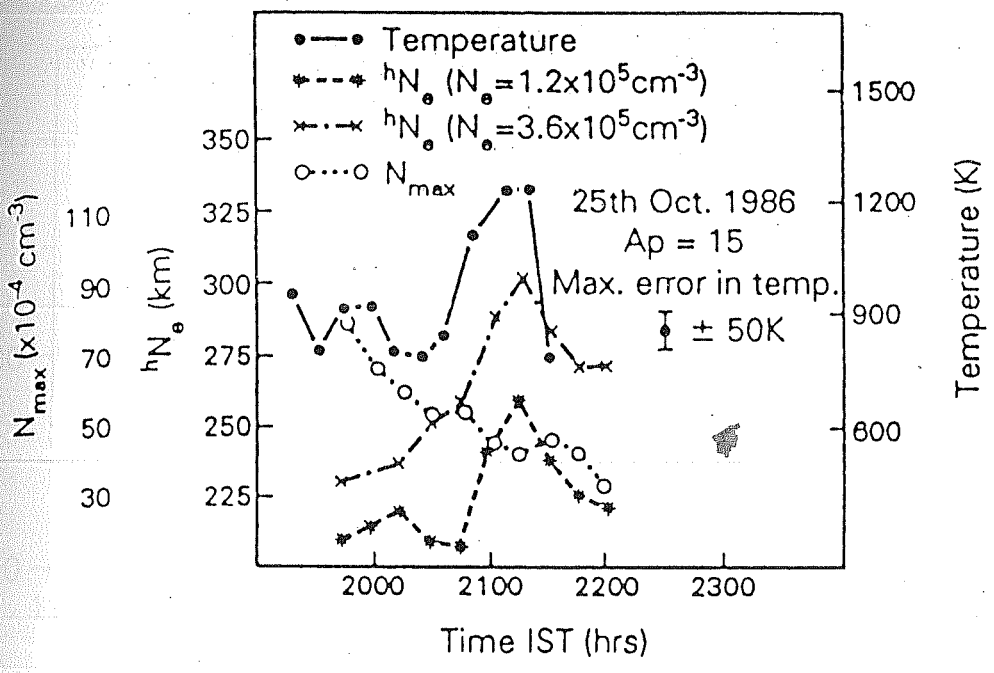

Fig. 4.6a. Spectroscopically measured neutral temperature from Mt. Abu and the corresponding movement of the F layer (representative densities of $1.2 \times 10^5 \mathrm{cm}^{-3}$ and $3.6 \times 10^5 \mathrm{cm}^{-3}$) obtained from the ionograms at Ahmedabad along with the peak electron density, N_{max}, with time for 25 October 1986.

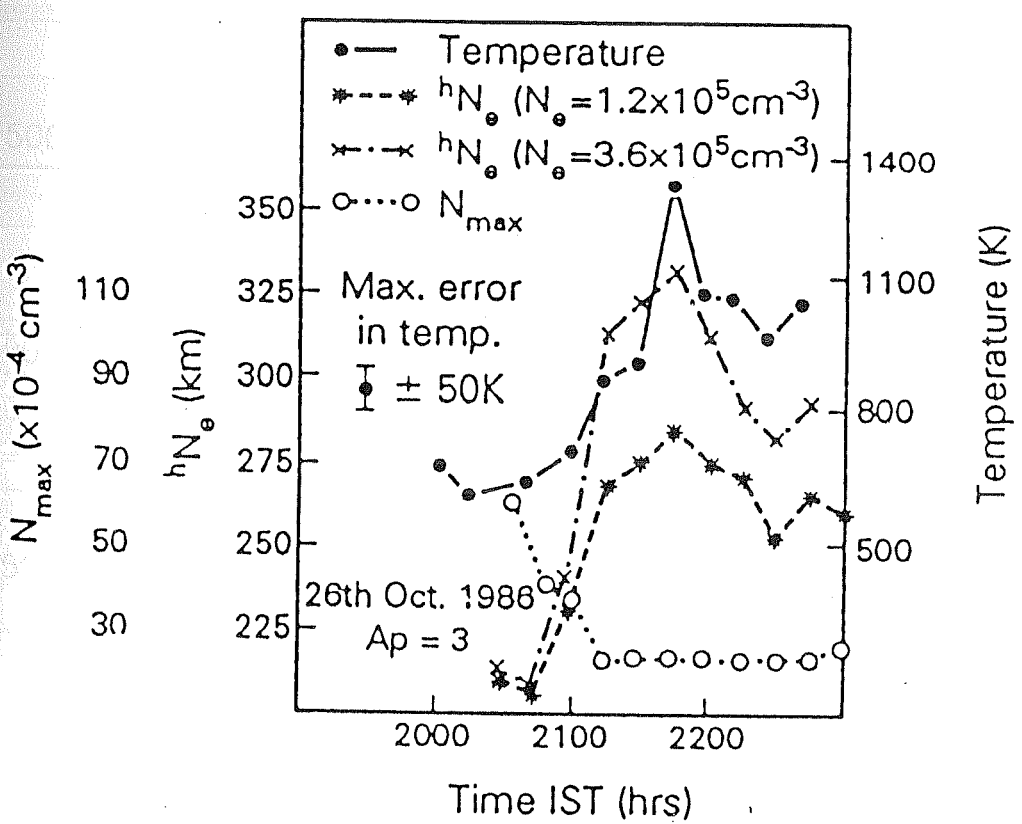

Fig. 4.6b. Same as above but for 26 October 1986.

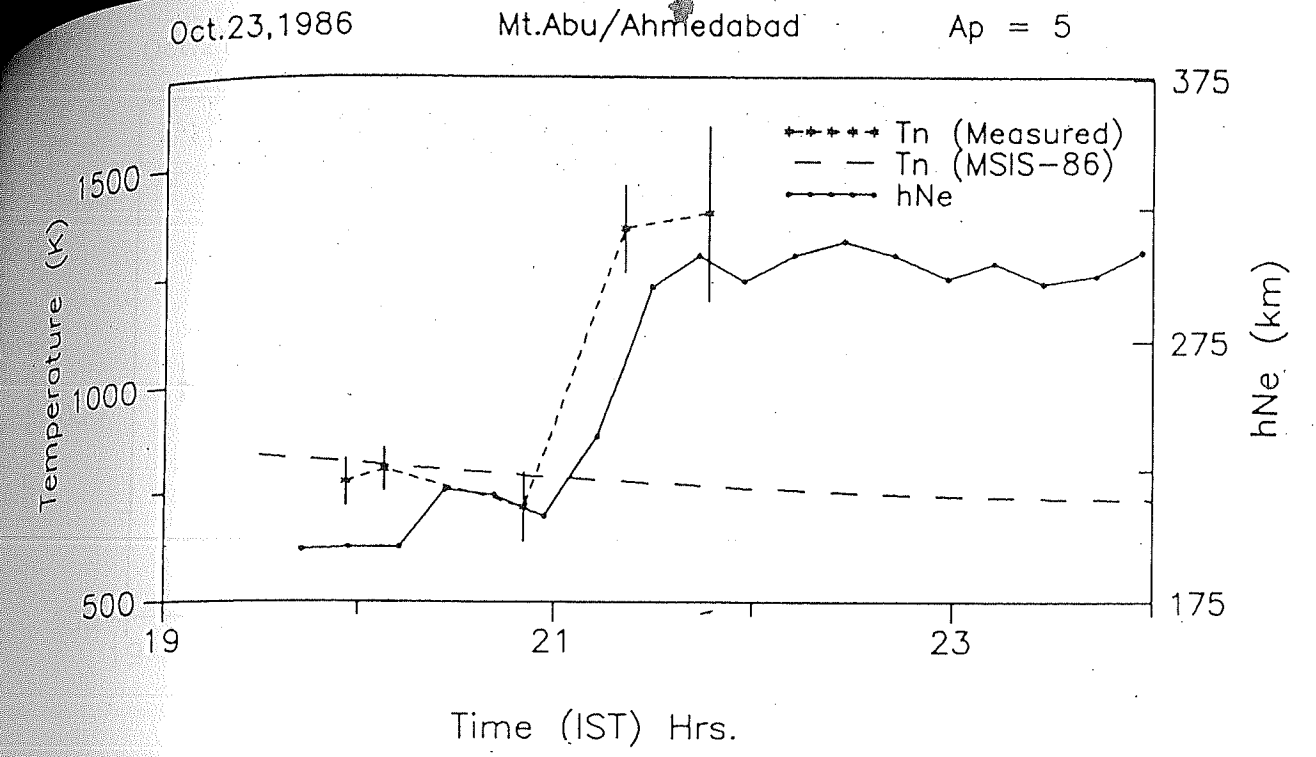

Fig. 4.6c. Neutral temperatures and the F layer base height (corresponding to a density of $1.2 \times 10^5 cm^{-3}$) for the night of 23 October 1986. The MSIS-86 model temperature variation is also shown for comparison with the measurements.

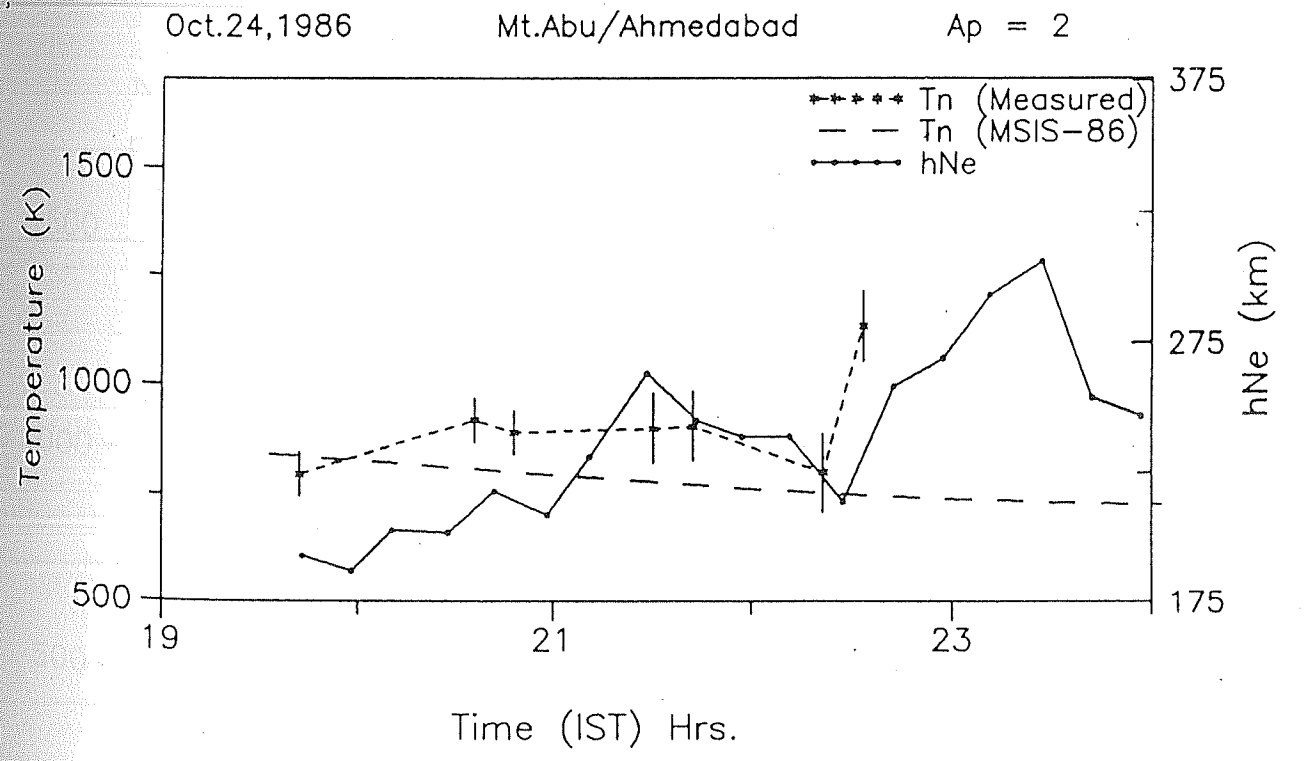

Fig. 4.6d. Same as above but for 24 October 1986.

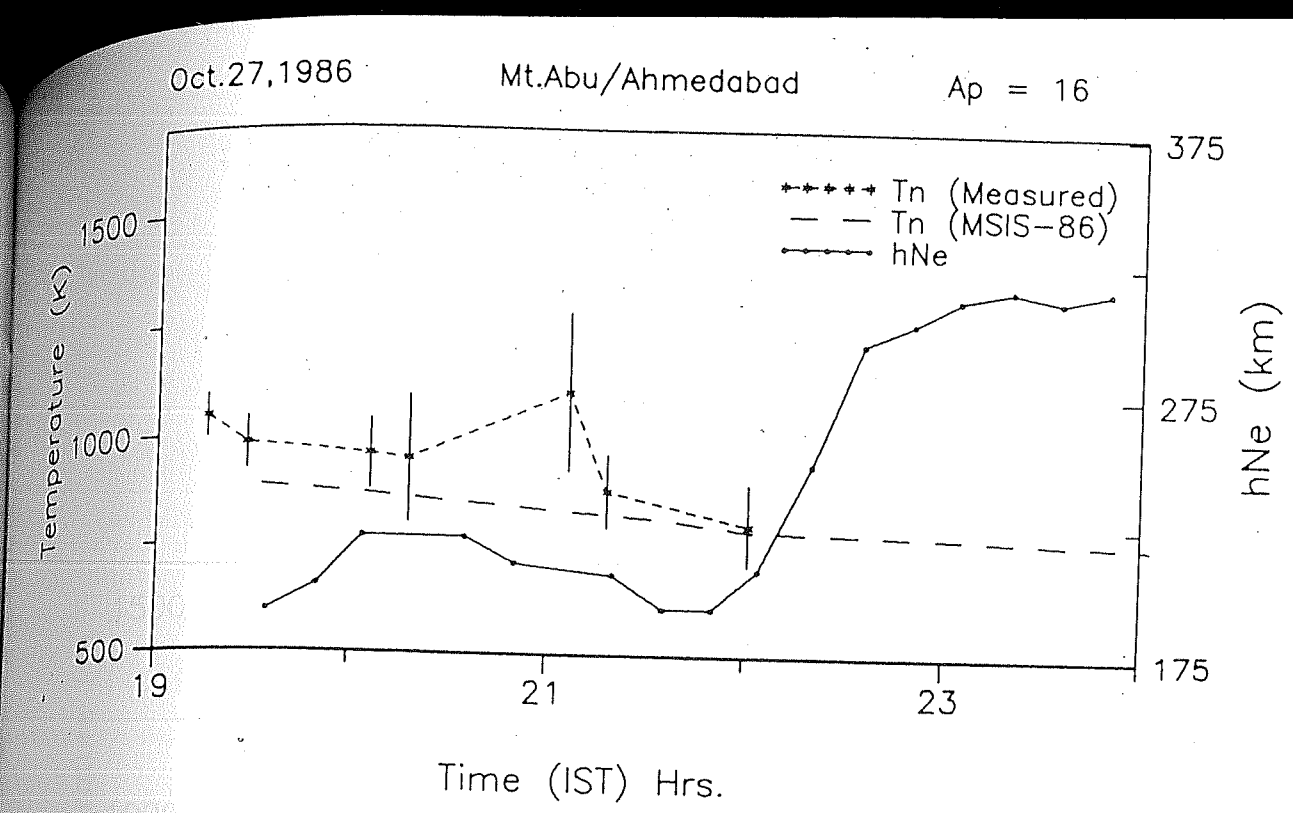

Fig. 4.6e. Same as Fig. 4.6c but for 27 October 1986.

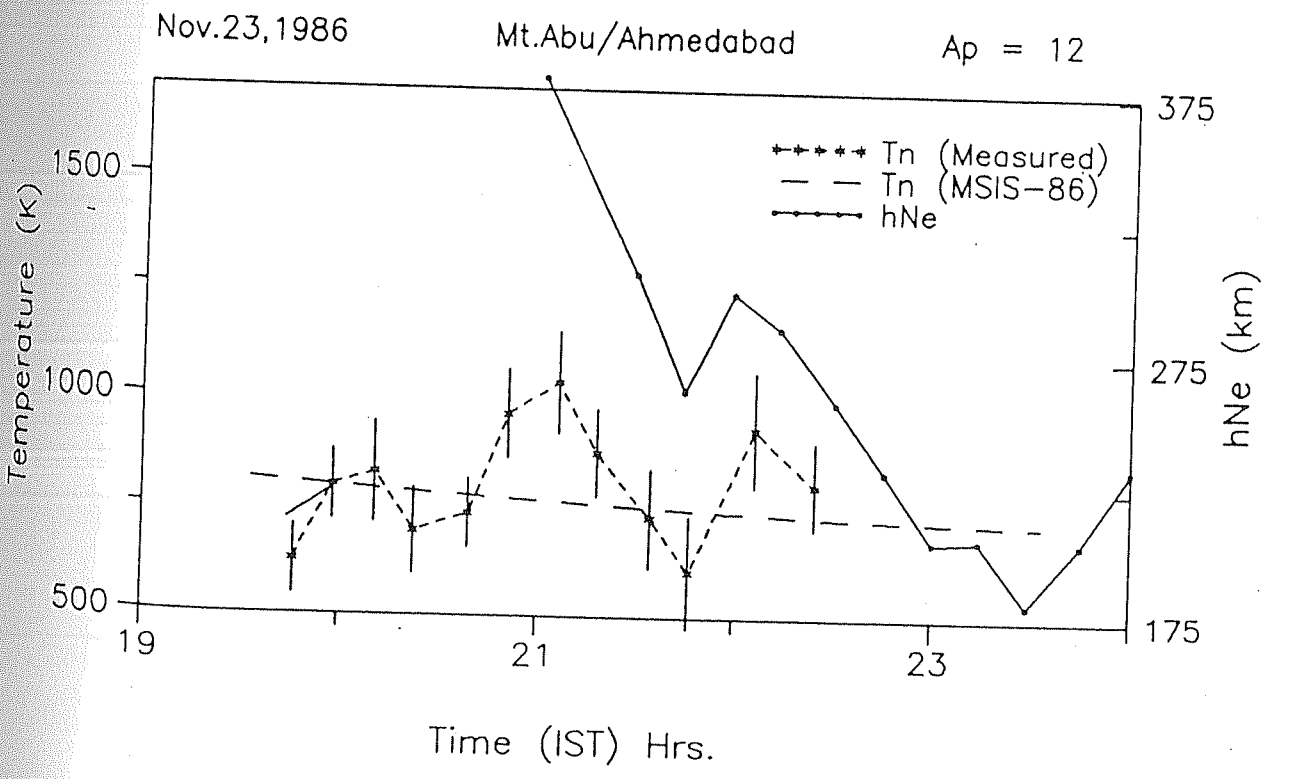

Fig. 4.6f. Same as Fig. 4.6c but for 23 November 1986.

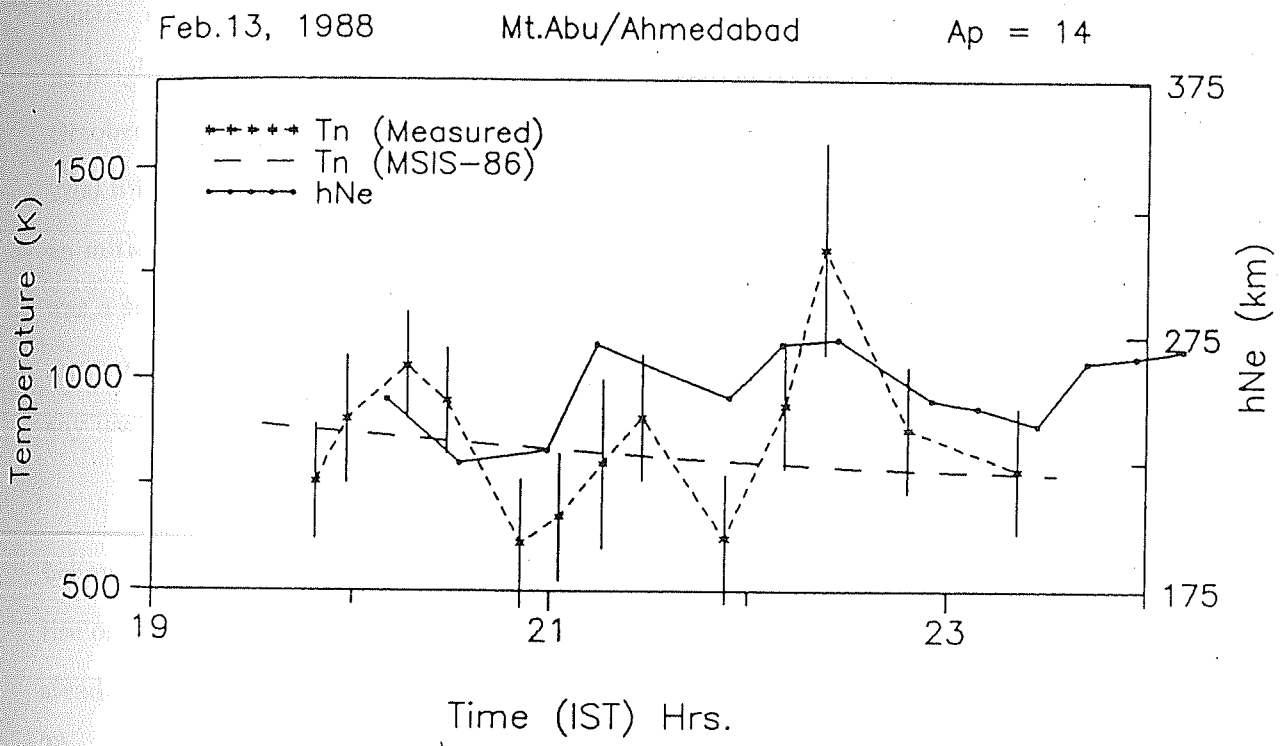

Fig. 4.6g. Same as Fig. 4.6c but for 13 February 1988.

1986 and 13 February 1988 when both thermospheric and ionospheric data are available. For these nights, MSIS-86 model was run to obtain the predicted temperatures for the times when direct measurements are available. The model values are also plotted in these figures. On all the nights in 1986, the F layer showed large rise in its height associated with an increase in temperature but at different times. On 23 October, after a sharp rise at about 2100 h, the layer remained at about 300 km till 2200 h beyond which no temperature data were available. On 24 October, there was an initial rise of 50 km at 2100 h after which the layer started moving down. There was a subsequent increase in its height and the neutral temperature too showed corresponding variations. On both the nights, the airglow intensity was too low to allow any useful data beyond 2230 h.

The examples presented in Figs. 4.6e and 4.6f show contrasting features. The behaviour of the ionosphere on 27 October was similar to that on 23 October but the rise on 27 October was seen only after 2200 h before which the F layer had remained steady. T_n too had shown a nearly steady value except for a singularity at 2100 h. There are no temperature data during the period of steep rise in h_{N_e}. The F layer on 23 November was located beyond 350 km at about 2100 h and it came down to $\sim$ 270 km by 2145 h. The corresponding change in T_n had been only 400 K. Subsequent variations in base height had corresponding variations in T_n. In Fig. 4.6g representing 13 February 1988, the temperature and the F layer height show good correlation. The temperature exhibited a wavy feature which is reflected in the variation of h_{N_e}. On this night, though the T_n shows a large rise of about 650 K between 2200 and 2300 h, the base height of the F layer shows only a marginal increase.

The measurements of T_n and the base height of the F region for the nights of October and November, 1986, are plotted in Fig. 4.7. The line of best fit is also shown and it has a slope corresponding to 11 $\pm$ 2 km per 100 K at 95% confidence

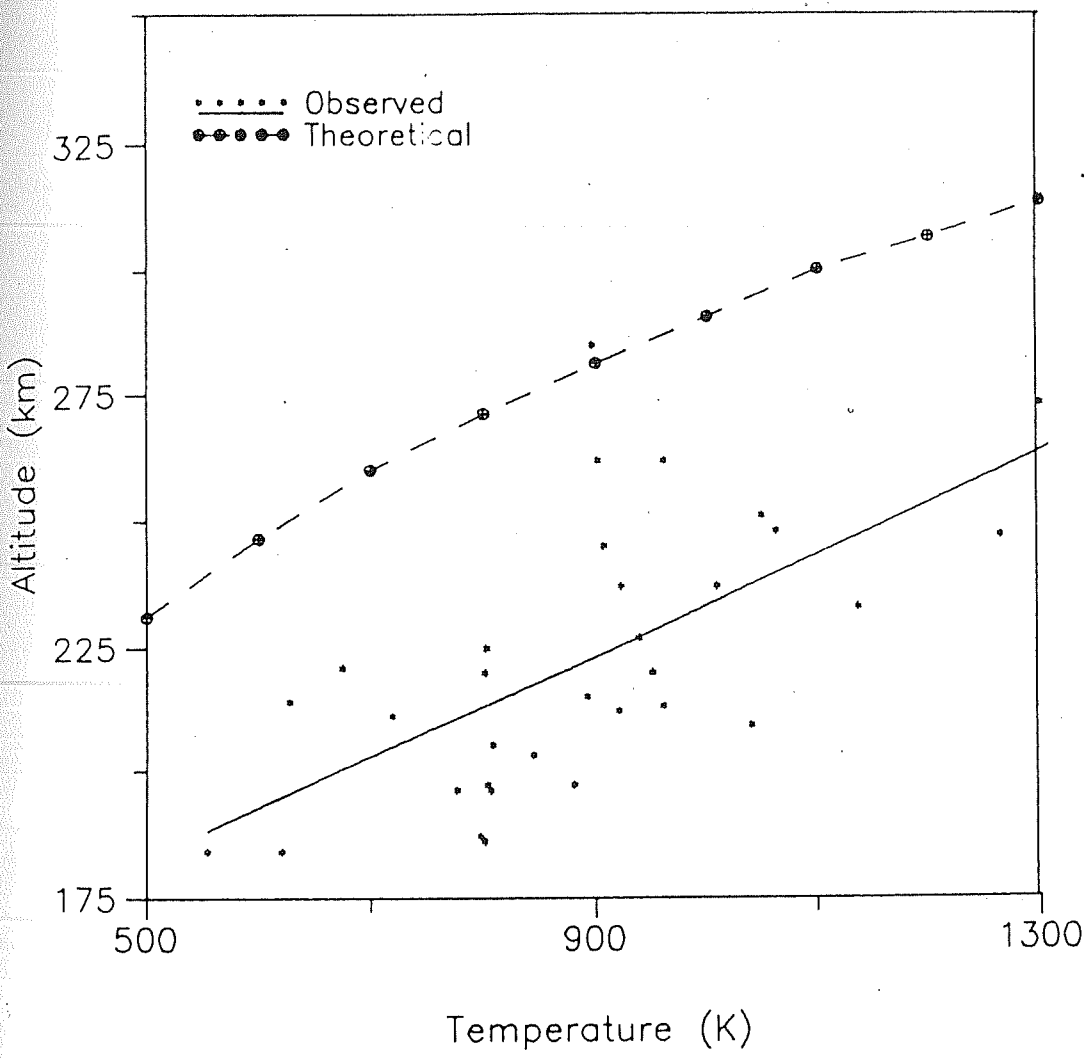

Fig. 4.7. Plot of measured temperatures and the base height of the F layer for different times on the nights covered under study. The slope of the best fit line to the data points has a value of 11 $\pm$ 2 km per 100 K at 95 % confidence limit. The dashed curve shows the result of theoretical calculation carried out using the servo expression (4.16).

level. Using the iteration technique discussed in section (4.3), the balance height for each of the measured temperatures is computed from equation (4.16) and this is also plotted in Fig. 4.7 along with the observations. Since the observed h_{N_e} represents the base height of the F_2 region and not the height of the maximum electron density, the difference in the computed peak heights by $\sim$ 65 km is understood. The line of best fit to the data has a correlation coefficient of 0.74, which implies 55% of the variation in h_{N_e} can be accounted for by the variation in neutral temperature alone. The non-linearity in the response of the F layer height at higher temperatures is clearly evident in the computed peak height.

- In spite of meridional winds and electric fields not being taken into account in determining the peak height of the F layer, the agreement in the slope of the theoretical and experimental curves provides confirmation to the belief that the F layer at low latitudes behaves like a servo system and that the 'night stationary level' of the F_2 peak depends on temperature in the manner predicted by the servo model.

Since we do not have neutral wind measurements for this period, it was not possible to eliminate the effects of winds in determining the balance height. However, this study indicated the need for examining the thermosphere and the ionosphere as a system, incorporating the effects of all known factors.

4.6 The thermosphere-ionosphere system

Having ascertained the role of neutral temperature in determining the height where the F_2 layer is formed, the next step would be to quantify the role played by winds and electric fields in perturbing this 'night stationary level' (h_s). Since the work of *Rishbeth*

and Barron [1960], there were several studies which attempted to deduce the effects induced by these forcings on the F region [*Rishbeth*, 1967; *Rishbeth*, 1972; *Rishbeth et al.*, 1978; *Chandler et al.*, 1983; *Crary and Forbes*, 1986; *Forbes and Roble*, 1990; *Buonsanto*, 1990]. Realising the closed cycle of interdependence of thermospheric and ionospheric parameters, various workers have succeeded in the inverse process of deriving meridional winds by making use of this relationship [*Miller et al.*, 1986; *Miller et al.*, 1987; *Buonsanto et al.*, 1989; *Krishnamurthy et al.*, 1990]. Though extremely useful in studying average, systematic, variations, there are certain limitations in the derivation of neutral atmospheric parameters like meridional winds purely based on ionospheric data and model atmospheric parameters. These are brought out in a later chapter on meridional wind and its variabilities.

The action of external forcings such as winds and electric fields on the F region was described in section (4.2) and depicted in Fig. 4.1. When the applied drifts are upward, increased downward diffusion opposes the upward motion of the plasma and when the drifts are downward, increased recombination, leading to the loss of ionization, opposes further lowering. At any instant, the actual height (h_m) of the F_2 peak approaches the equilibrium level (h_b). If the time required for diffusion at the peak is shorter than time scales over which the largest variations in drifts occur, it can be assumed then that the F_2 peak relaxes to its equilibrium height (h_b) before it is altered further [*Forbes and Roble*, 1990].

If electric fields are small and for small wind speeds, there exists a linear relationship between the wind speed (U_p) and the resulting change in the height of the layer peak [*Rishbeth and Barron*, 1960; *Rishbeth*, 1966; *Buonsanto et al.*, 1989]. In this section, this relationship pertaining to our latitudes (dip angle of 33°) is examined. A new method has been evolved to estimate the height of the F layer peak, h_m, incorporating the effects of both neutral temperatures and meridional winds. This

balance height is then compared with independently measured peak height (h_{max}) deduced from ionograms. It is then shown that the comparison reveals fairly good agreement reproducing most of the observed features and thus providing experimental evidence for the close coupling of the thermosphere and the ionosphere.

Rewriting the servo equation (4.17) and replacing the reduced height z_m by the real height h_m, we get

$$\frac{dh_m}{dt} = \frac{D_m \sin^2 I}{2H}\{\exp[-k(h_m - h_0)/H] - \exp[-(h_m - h_0)/H]\} + W$$

Here W is the vertical drift due to winds and electric fields.

It was shown by *Buonsanto et al.* [1989] that for most conditions in the F region, the effects of both the time rate of change of the layer height and the non-linear term on the right hand side of the above equation are small. The above expression then becomes

$$W = \frac{(k+1)D_m \sin^2 I}{2H^2}(h_m - h_0) \tag{4.22}$$

Combining equations (4.5) and (4.6), the vertical drift of ionization, being the result of a combination of motion along the magnetic field lines due to a meridional wind U_p and an ion drift induced by the east-west electric field E_E, is given by

$$v_z = -U_p \sin I \cos I + \frac{E_E}{B} \cos I \tag{4.23}$$

Equating (4.22) and (4.23) and solving for the layer displacement $(h_0 - h_m)$,

$$(h_0 - h_m) = \alpha \left[U_p - \frac{E_E}{B} \sin I\right] \tag{4.24}$$

where

$$\alpha = \frac{2H^2 \cos I}{(k+1)D_m \sin I}$$

If the electric field is small

$$h_m = h_0 - \alpha U_p \tag{4.25}$$

This yields the new balance height of the F_2 peak in the presence of a meridional wind U_p.

The extent of linearity that holds between the layer displacement (Δh_m) and U_p has been examined for the location ($I = 33°$) under study and it is shown in Chapter 5 (section (5.5)) that the approximation is valid for equatorward wind speeds less than 200 m/s and poleward wind speeds less than 125 m/s. Since the magnitude of the measured meridional wind is less than 150 m/s most of the times, the linear approximation (4.25) to the servo equation is adopted [*Gurubaran and Sridharan*, 1993] and the effects of meridional winds at a low latitude station, Mt. Abu, are examined and discussed below.

Having seen the importance of neutral temperatures in determining the altitude of the F_2 layer peak, the measured temperature and its changes are incorporated in the present analysis. These temperatures obtained from the top of the thermosphere by line profile analysis of 6300 Å emissions, are close to the exospheric temperature (T_∞) itself [*Hays et al.*, 1970; *Hernandez et al.*, 1975]. The minimum uncertainty in the measurements is estimated to be $\sim \pm$ 50 K. Based on the simulation done by *McCormac et al.* [1987], and taking into account the uncertainties in the measurements, the spectroscopically determined T_n would at the most differ from the actual exospheric temperature (T_∞) by 100 K, which would in turn alter the estimated layer height by $\pm$ 10 km and this could be taken as a steady dc value for one night.

In the present exercise, the neutral atmospheric parameters are deduced from the MSIS-86 model by treating the measured temperature as T_∞. The same set of

expressions for β and D (4.19 and 4.20) is made use of in determining the balance height of the F_2 peak by iteration, where equation (4.16) holds. This would represent h_0 for this particular time. The meridional wind component along the geomagnetic field lines would alter h_0 to a new level h_m satisfying equation (4.25). The h_m, i.e., the height of maximum density in the F region, is thus estimated at different times when the T_n and U_p are available in the course of the observations. These estimates are compared with the independently obtained peak height (h_{max}) values from ground-based ionosondes and the results obtained for a few days, indicate fairly good to very good agreement. These are presented below.

The behaviour of the thermosphere-ionosphere system on seven magnetically quiet nights ($A_p < 20$) in the months of February and April, 1991, when we had the complete data on T_n, U_p and h_{max}, is depicted in Figs. 4.8a to 4.8g. The top and middle panels show the variation of spectroscopically determined neutral temperature and meridional wind (poleward treated as positive). The dashed line in the top panel represents the T_∞ estimated using the MSIS-86 model. The measurements correspond to emissions emanating from south (20° elevation) of the sky over Mt. Abu. The ionospheric F_2 peak height is independently determined from the true height reduction of ionograms obtained by the ionosonde at Ahmedabad (2° south of Mt. Abu) and its variation (stars) is depicted in the bottom panel. Also shown is the estimated height (circled crosses) of the F_2 peak. The statistical error of the uncertainty in the estimated height is calculated from (4.25) and is given by

$$\frac{\delta h_m}{h_0 - h_m} = \left[\left(\frac{\delta U_p}{U_p} \right)^2 + \left(\frac{\delta h_0}{h_0 - h_m} \right)^2 + \left(\frac{\delta \alpha}{\alpha} \right)^2 \right]^{1/2} \qquad (4.26)$$

[*Miller et al.*, 1989]

The uncertainties in h_0 and α depend on T_n. δU_p is the uncertainty in the measured U_p and is determined by the spectrometer characteristics. While estimating the balance height h_m, the effect of electric fields is not taken into account. They are

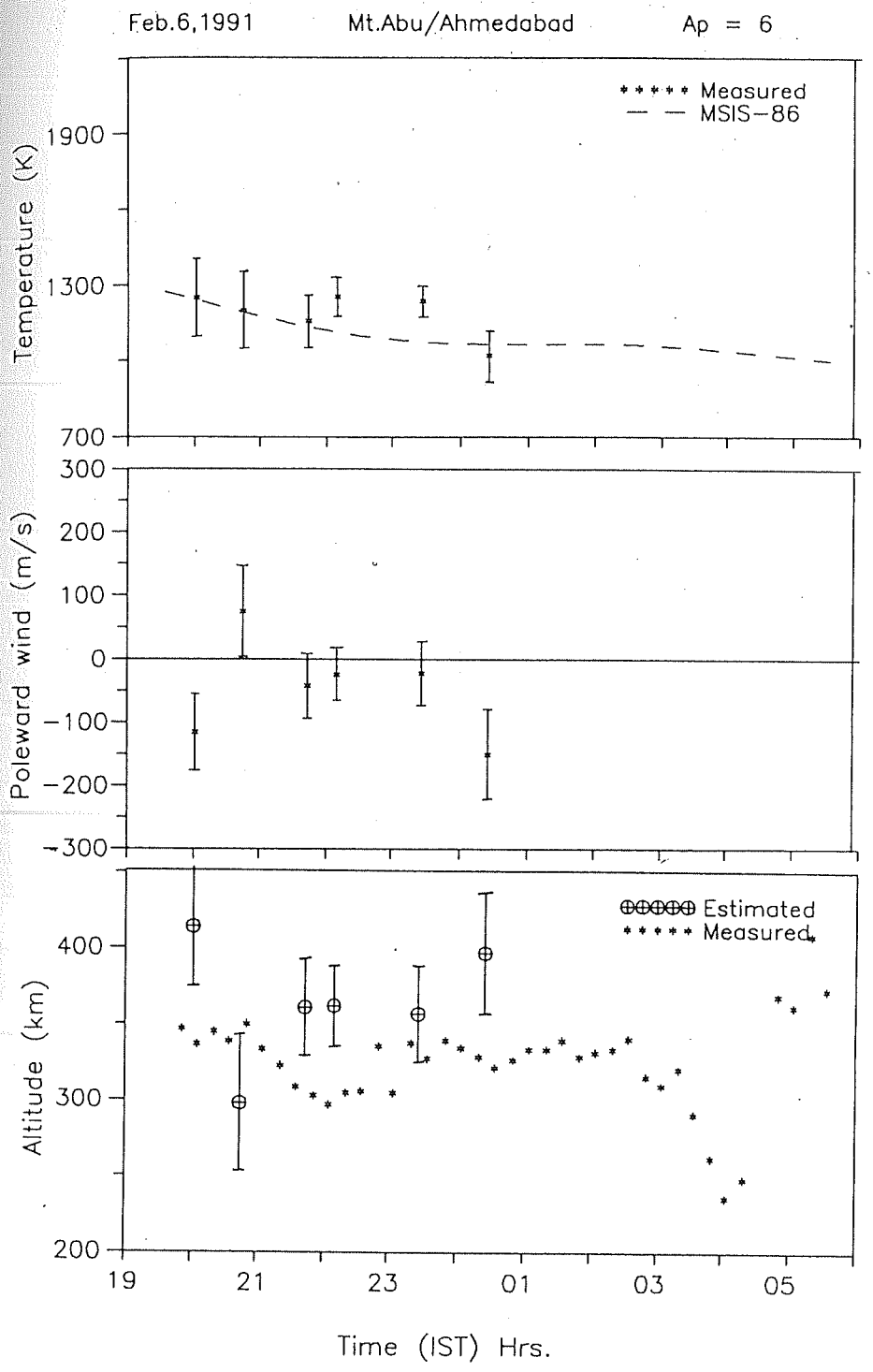

Fig. 4.8a. Spectroscopically measured thermospheric temperatures (T_n) and MSIS-86 model predictions for 6 February 1991 depicted in the top panel. The middle panel depicts the variation of measured meridional wind (U_p) (positive poleward). The theoretical estimated F layer peak height based on servo principles using T_n and U_p along with ionosonde measurements are depicted in the bottom panel.

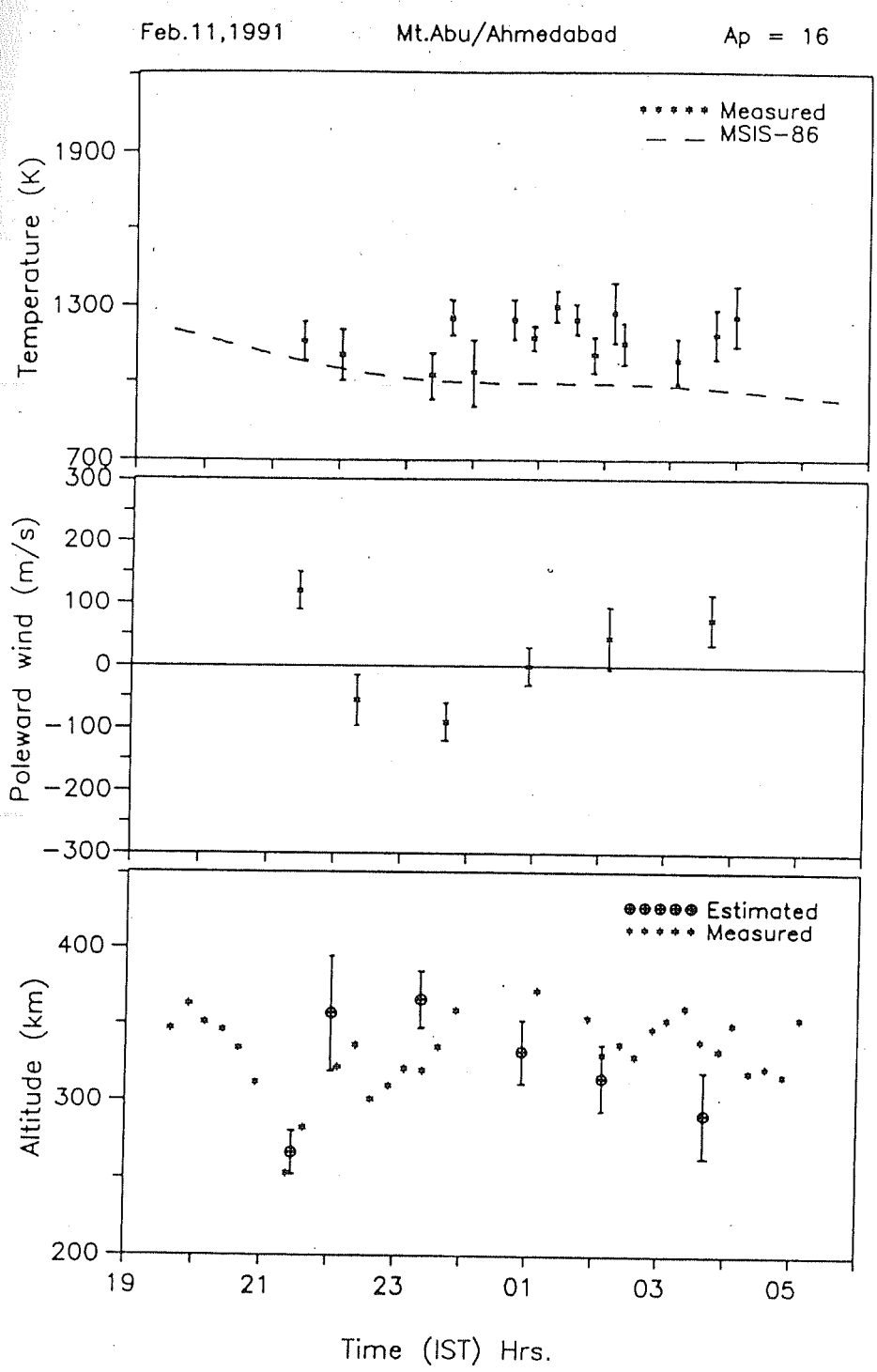

Fig. 4.8b. Same as Fig. 4.8a but for 11 February 1991.

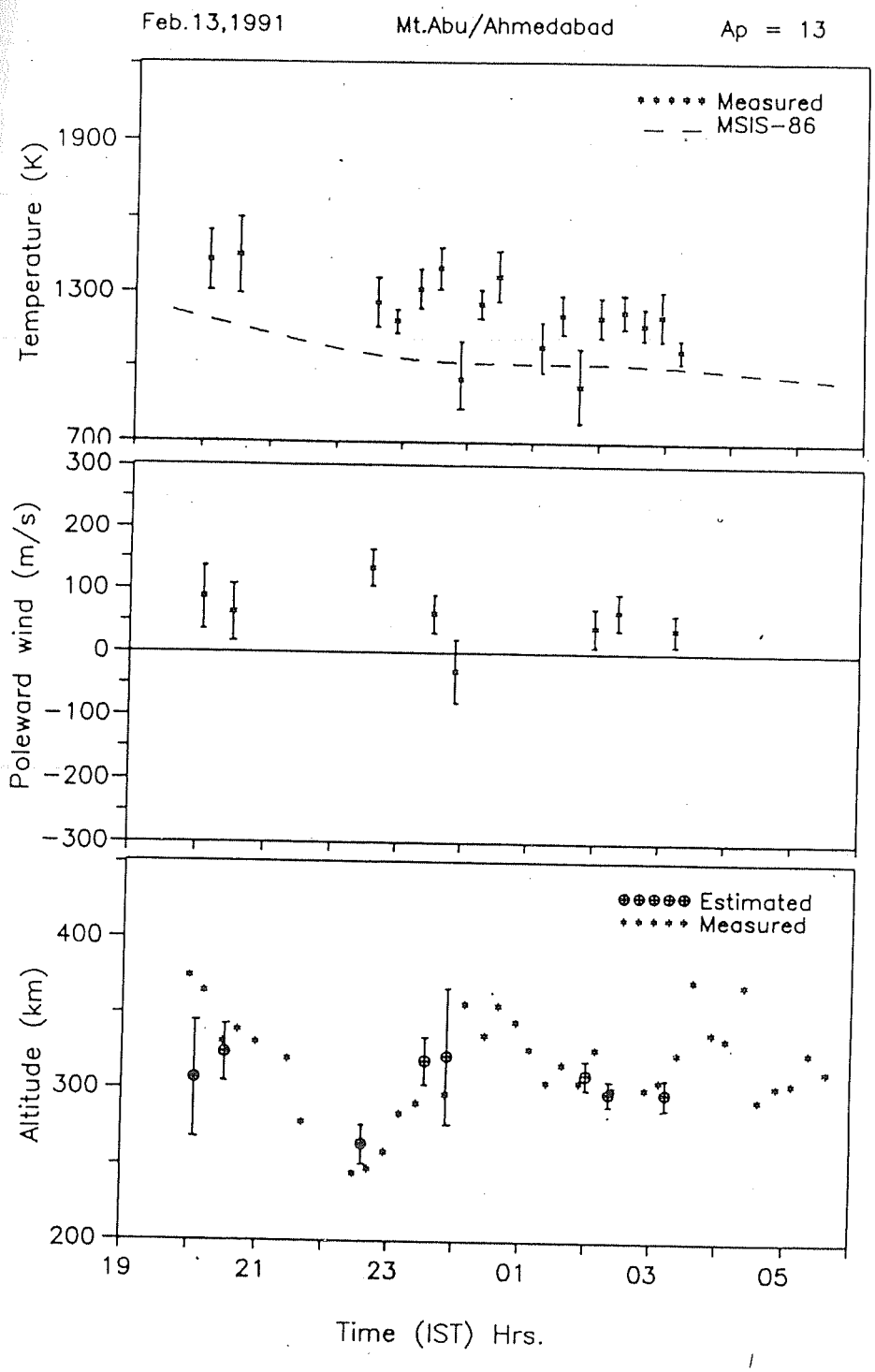

Fig. 4.8c. Same as Fig. 4.8a but for 13 February 1991.

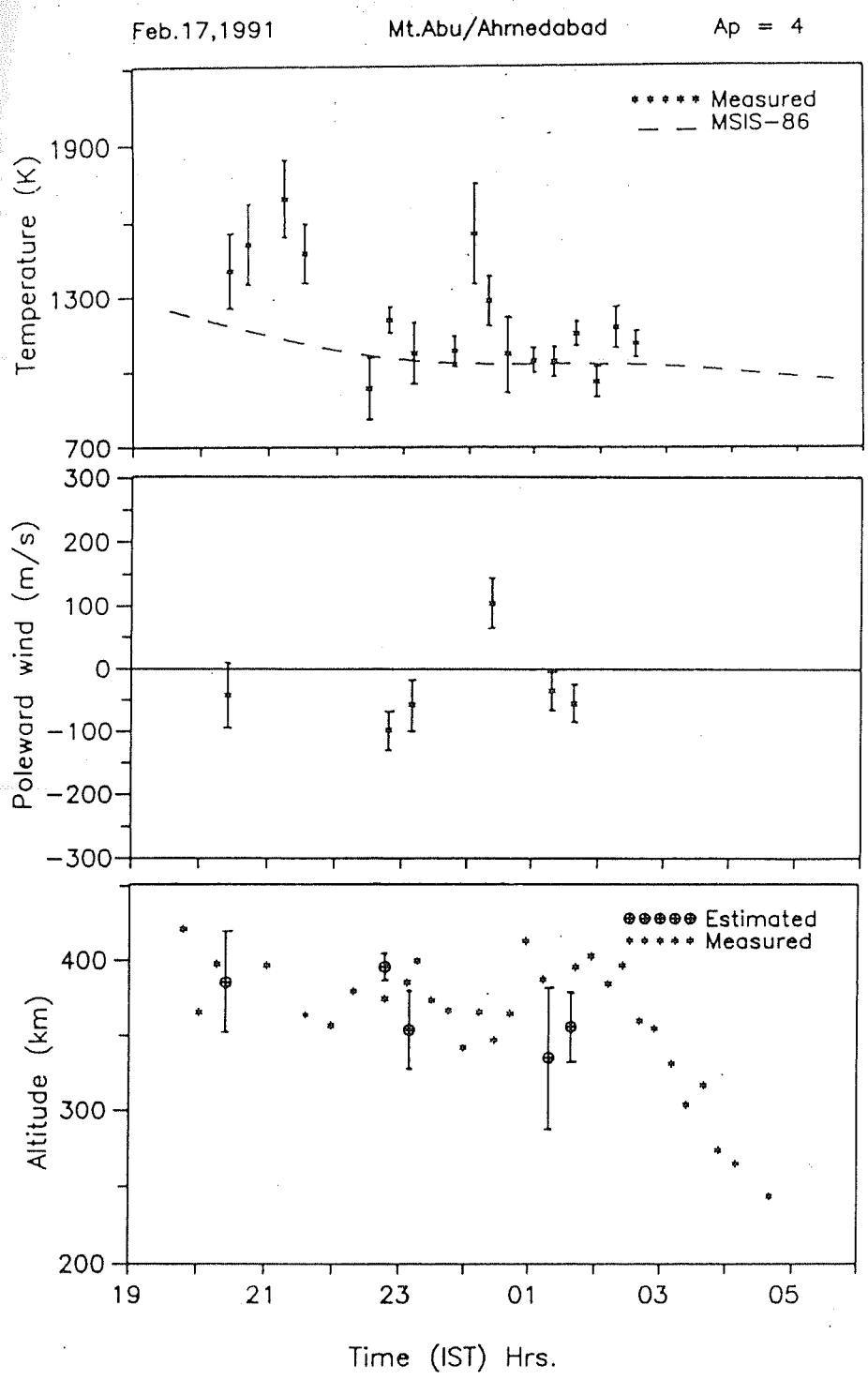

Fig. 4.8d. Same as Fig. 4.8a but for 17 February 1991.

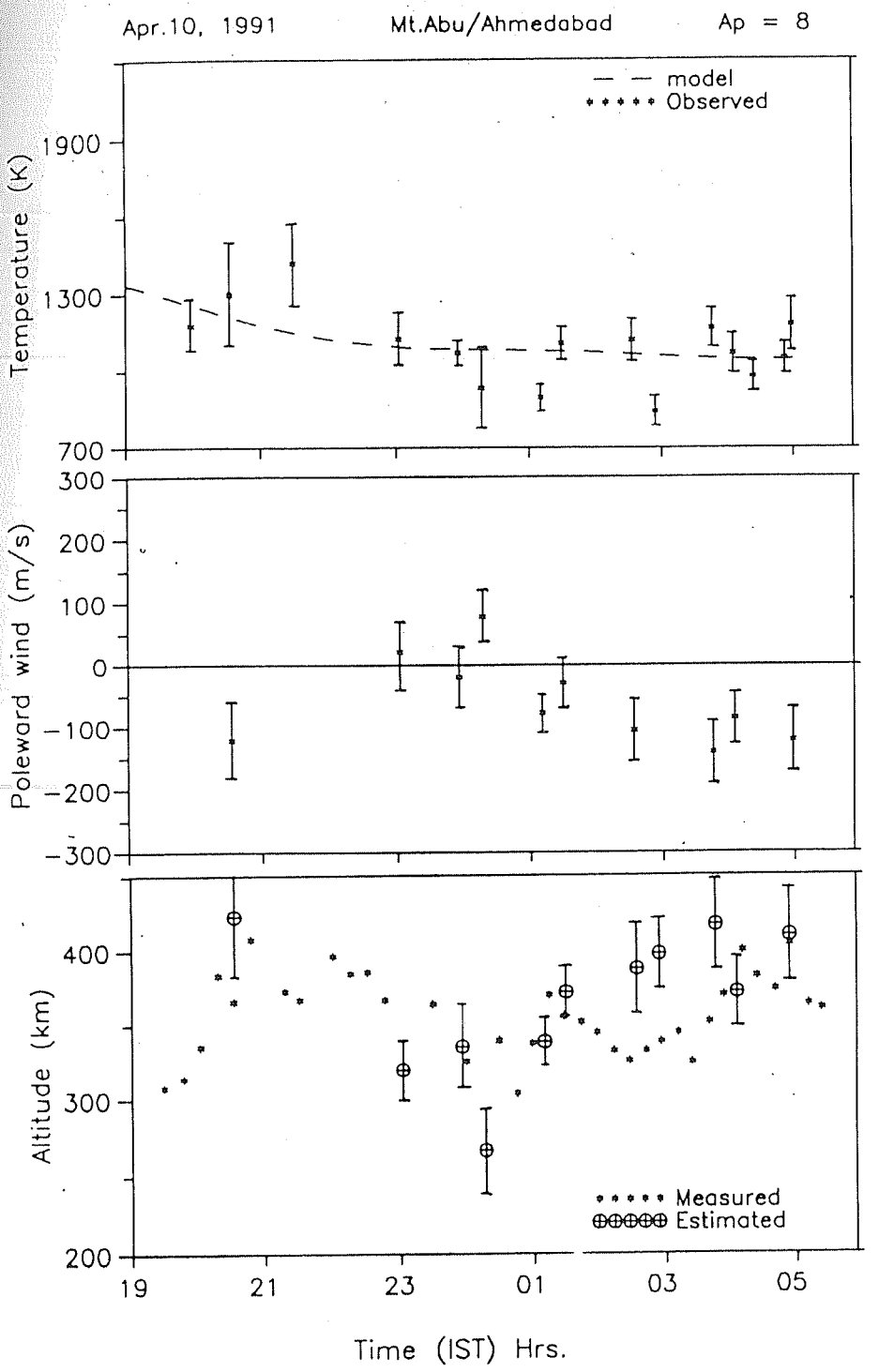

Fig. 4.8e. Same as Fig. 4.8a but for 10 April 1991.

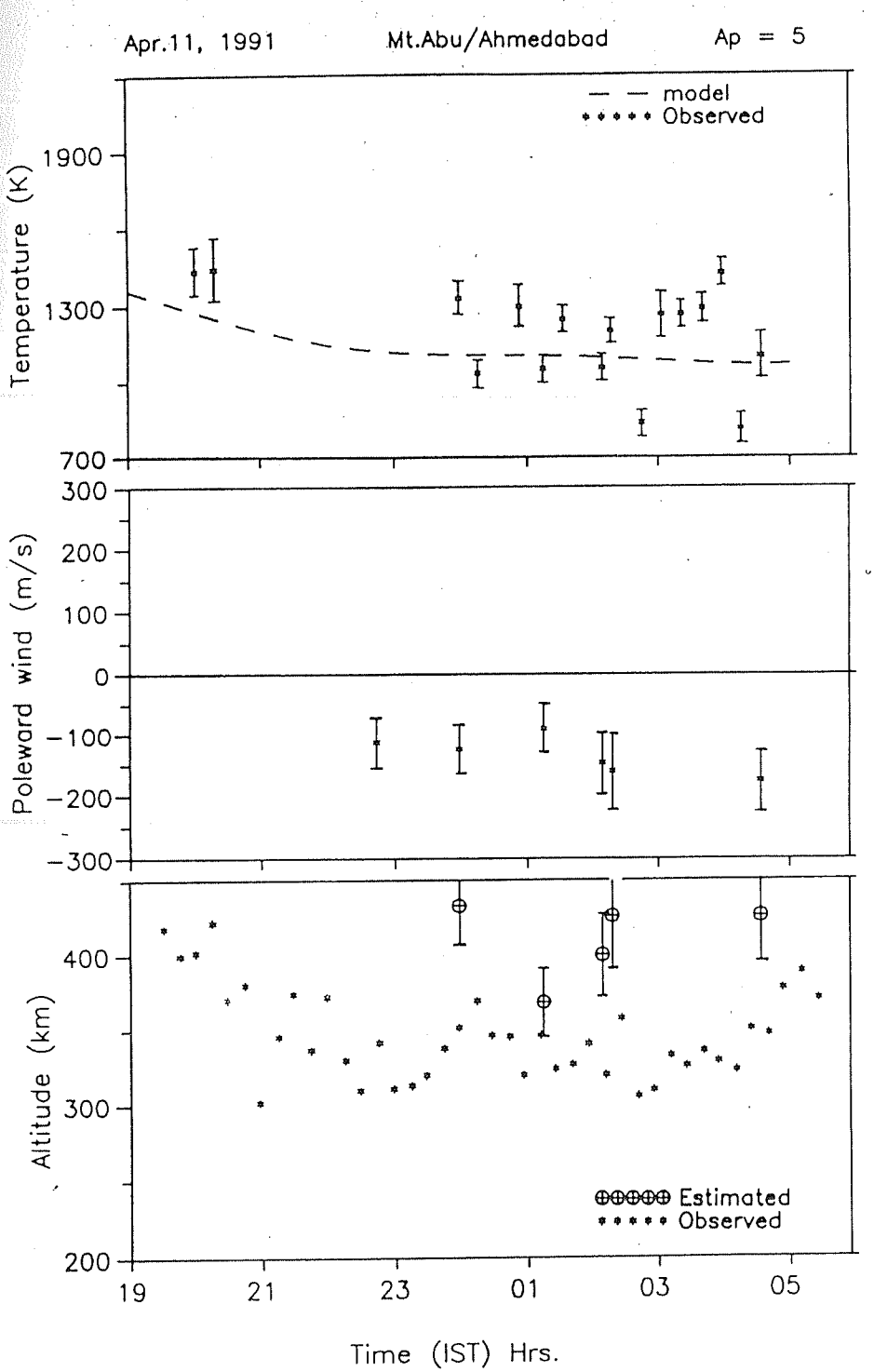

Fig. 4.8f. Same as Fig. 4.8a but for 11 April 1991.

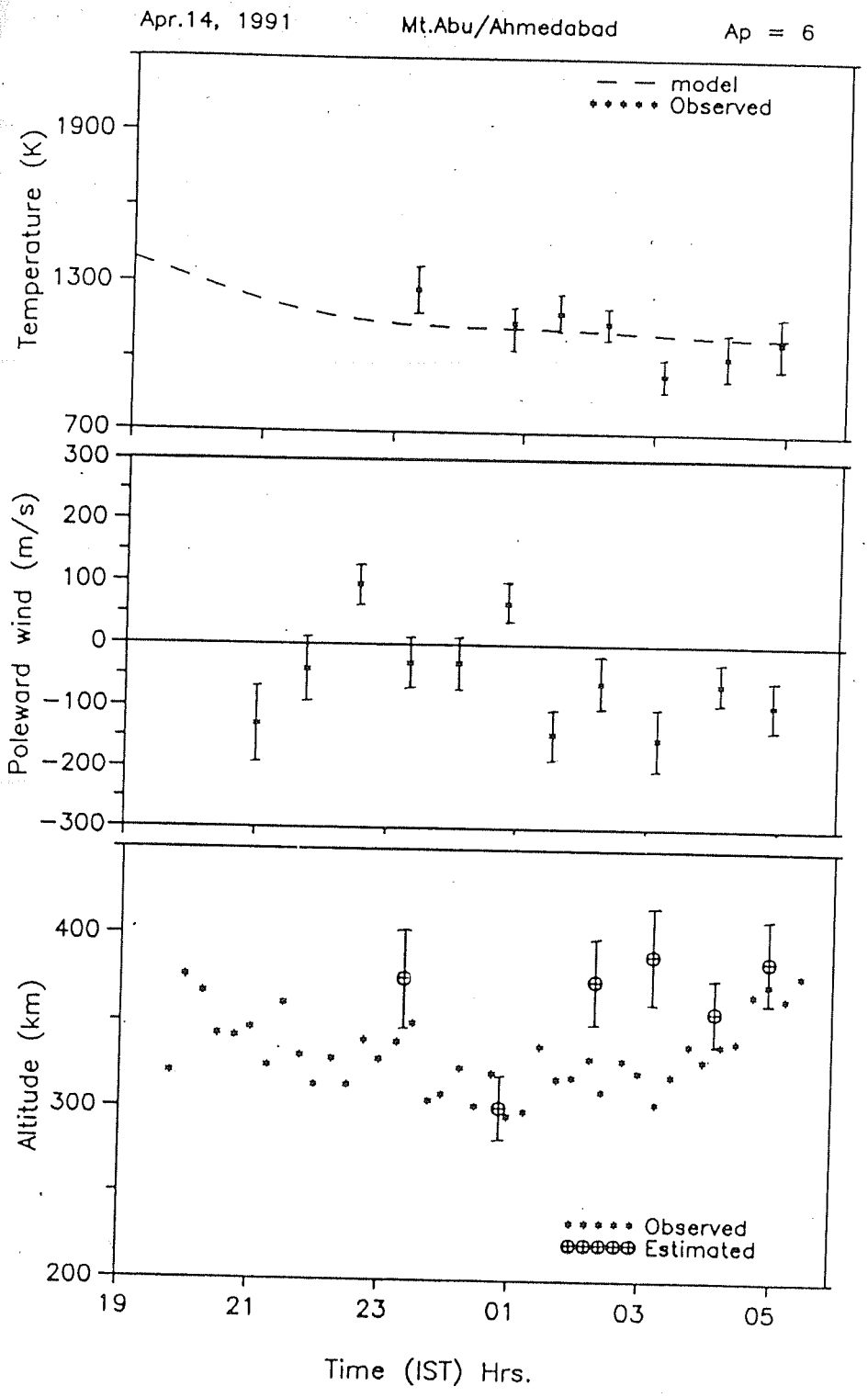

Fig. 4.8g. Same as Fig. 4.8a but for 14 April 1991.

treated as either to be constants or of less significance. The electric fields are estimated separately and the results presented in the next section. In this case study approach, the ionospheric and thermospheric conditions are assumed to be the same over Ahmedabad and the southern sky at Mt. Abu.

Fig. 4.8a shows the results for 6 February, 1991. The measurements are few in number on this night. The neutral temperatures follow closely the model predictions. The wind has remained equatorward all through the observing period. The measured and the estimated F_2 peak heights depicted in the bottom panel differ considerably for this night.

Fig. 4.8b shows the results for 11 February 1991. There is a temperature bulge as revealed by the measurements at about 0100 h. The poleward wind of 100 m/s around 2100 h changes its phase to equatorward around 2200 h reversing back to poleward at 0100 h. The layer reaches its minimum at about 2130 h after which it moves upward. The F_2 peak is at its highest level of about 370 km between 0000 and 0100 h. The vertical motion of the F_2 peak clearly follows the direction of meridional winds. The oscillatory pattern exhibited by the $h_{\max}$ is corroborated well by the meridional wind variation. The estimated and measured heights differ in the range of 30–50 km for this day.

Fig. 4.8c shows the results for 13 February 1991. The measured T_n and the model differ considerably on this day too. The behaviour of the meridional wind has been quite different when compared to that of 11 February. The wind remains mostly poleward except at 2330 h when it either comes down in magnitude close to zero or just has a brief reversal to equatorward. The agreement between the measured and estimated $h_{\max}$ is fairly good. $h_{\max}$ reaches its minimum later at about 2230 h on this night and the poleward wind shows its maximum amplitude at about the same time. The large uncertainty in the estimated layer peak height at 2350 h is due to the large

measurement errors in the spectroscopically determined parameters.

Fig. 4.8d represents the outcome of a similar exercise for 17 February 1991. The neutral temperatures show considerable deviation from those expected by the model at $\sim$ 2100 h and also during midnight. The meridional wind remains equatorward most of the time and the layer is at a higher height when compared to that on previous days. The F layer seems to behave differently between 0100 and 0200 h. Its peak reaches 400 km whereas the temperature deviated from the model only slightly ($\sim$ 150 K) and the equatorward wind speeds were of the order of 50 m/s. The agreement between the measured and estimated heights of the F_2 peak is reasonably good on this day. The deviation in the expected and the measured heights could be due to the electric fields not being accounted for.

The results from a similar analysis for three nights of data belonging to the coordinated measurements for the month of April 1991, are depicted in the Figs. 4.8e, 4.8f and 4.8g. The measured temperatures on 10 April, agreed with the model. The equatorward wind shows large amplitude at about 2030 h and in the early morning hours. The meridional wind has small speed ($\sim$ 50 m/s) in the poleward direction which has resulted in the lowering of the peak height at and immediately after midnight. There is a reasonable agreement between the estimated and measured peak heights for this night.

Coming to the measurements on the night of 11 April, the measured temperatures shown in the top panel of Fig. 4.8f exhibit a peculiar oscillatory feature, fluctuating about the model values, not seen on any of the other nights. The wind has remained steady and equatorward and leads to high estimated F_2 peak heights (between 375 and 425 km). The estimated and the measured $h_{\max}$ differ by at least 30 km. Such deviations might result from the presence of strong electric fields which will be discussed in the next section.

The results on 14 April are depicted in Fig. 4.8g. The measured neutral temperature closely follows the model values. Because of the rapid intensity changes during the early part of the night, the uncertainties in temperature were very large leading to the rejection of such measurements. The meridional wind shows a tendency of reversing to poleward during the middle of the night, which is well corroborated by the lowering of the F layer to about 300 km. After midnight, the measured height does not show the rapid increase as expected by the 'servo' action of thermosphere-ionosphere system due to the changing meridional wind.

- The case study pertaining to the application of servo model through the seven examples presented, clearly provides experimental evidence for the existence and also the extent of the close coupling that prevails in the low latitude thermosphere-ionosphere system.

4.7 Estimation of electric fields

As had been mentioned earlier, the role of electric fields is not considered in the case study approach presented in the last section, for want of electric field data. However, if the differences in the estimated and actually measured $h_{\max}$ are only due to electric fields, using (4.24), the electric fields could be inferred for the days under discussion. From (4.24), the electric field (positive eastward) and its uncertainty are given by

$$E_{\mathrm{E}} = \frac{B}{\sin I}\left[U_{\mathrm{p}} - \frac{h_0 - h_{\mathrm{m}}}{\alpha}\right] \tag{4.27}$$

$$\delta E = \frac{B \sin I}{\alpha}\left[\alpha^2(\delta U)^2 + (\delta h_{\mathrm{o}})^2 + (\delta h_{\max})^2 + ((h_{\mathrm{o}} - h_{\max})\delta\alpha/\alpha)^2\right]^{1/2} \tag{4.28}$$

[*Gurubaran and Sridharan*, 1993]

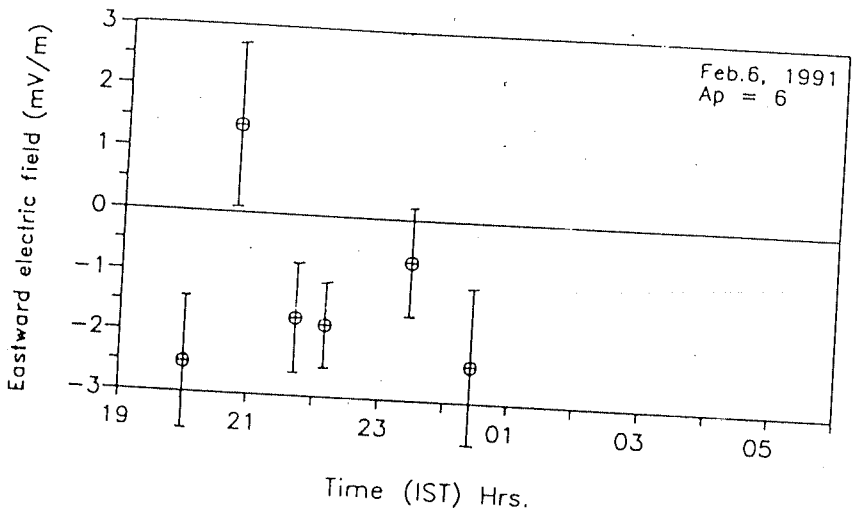

Fig. 4.9a. Electric fields calculated from the differences between the estimated (h_{m}) and the measured (h_{max}) peak heights of the F layer for 6 February 1991.

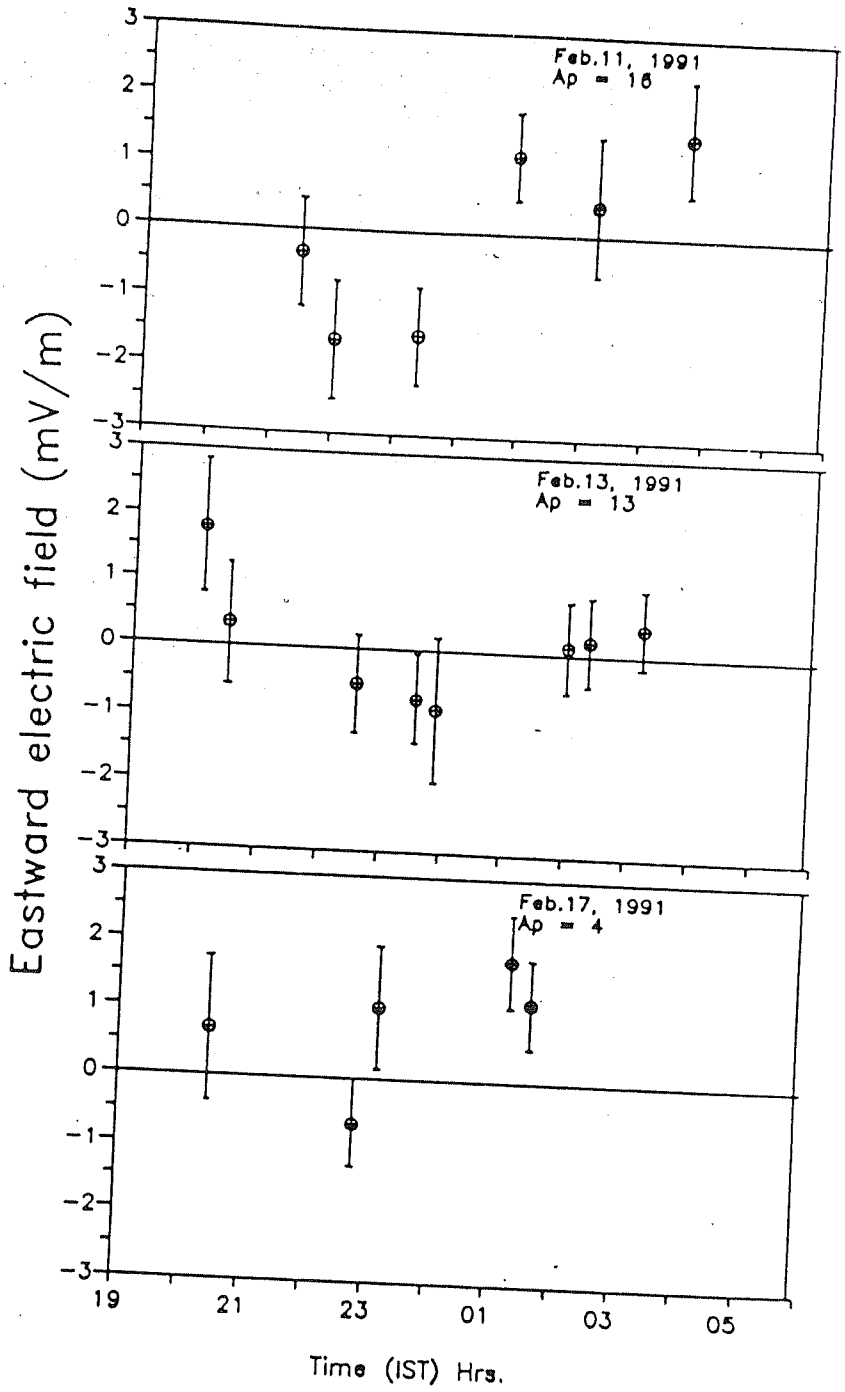

Figs. 4.9b,c,d. Same as Fig. 4.9a but for 11 (top), 13 (middle) and 17 (bottom), February 1991.

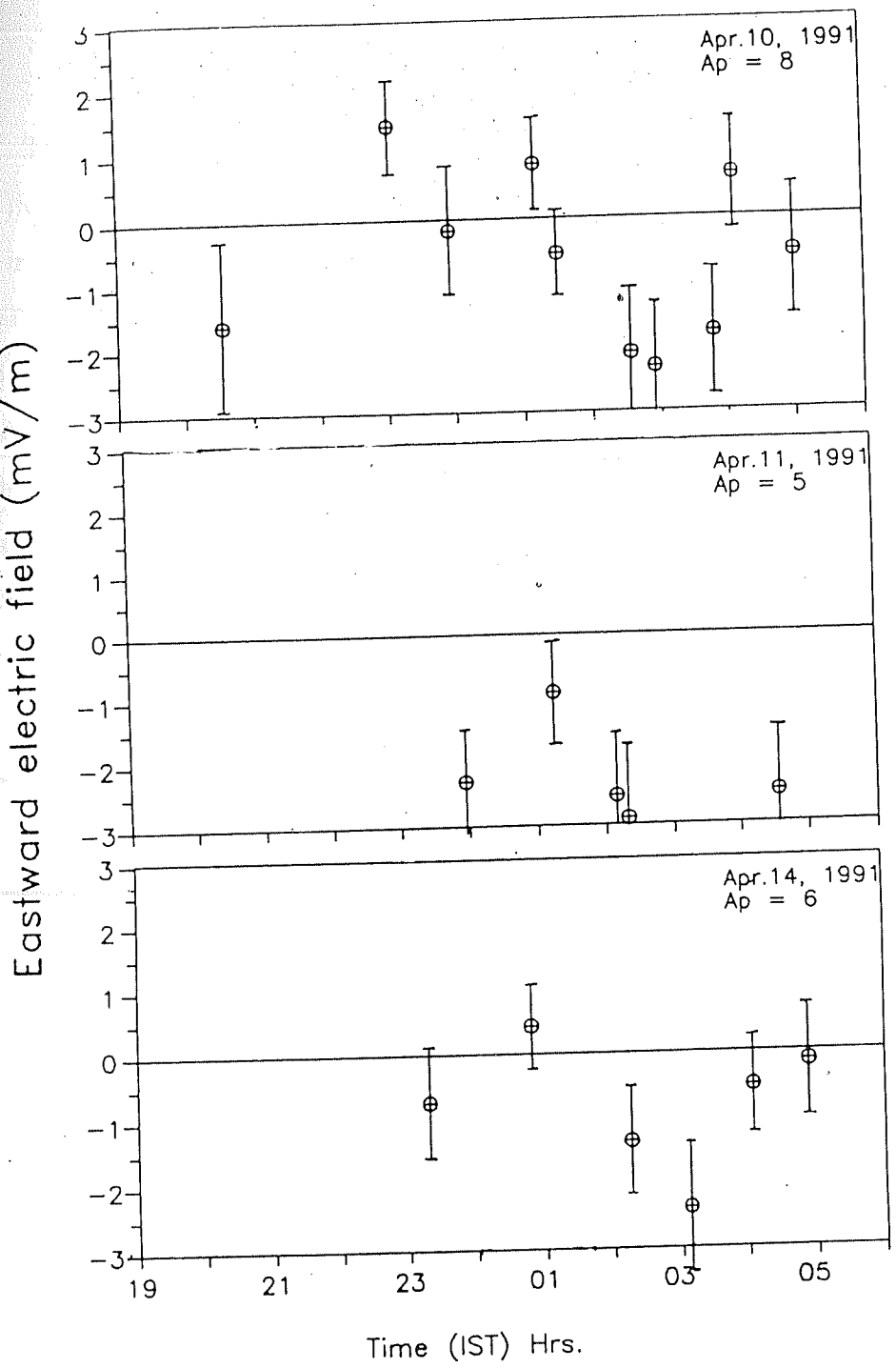

Figs. 4.9e,f,g. Same as Fig. 4.9a but for 10 (top), 11 (middle) and 14 (bottom), April 1991.

Thus evaluated electric fields for the nights belonging to February and April (1991) are depicted in Figs. 4.9a to 4.9g. It is seen in these figures that the electric fields in the month of February are eastward after sunset (at least on 13 and 17 February) and become westward at about 2100 h. They change their direction again near midnight and except on 6 February, continue to be eastward till the end of the observing period. This might represent the winter months. The results shown in Figs. 4.9e to 4.9g suggest that the electric fields in equinoctial months (April) however reveal a different picture altogether. They reach maximum westward amplitude at $\sim$ 0300 h to subsequently become eastward just before sunrise. On 10 and 14 April, there appeared to be a transition from eastward to westward field at about 0100 h. A wavy pattern in the electric field variation is clearly seen on 11 and 13, February, and 10 and 14, April, with periodicities in the range 4 to 6 hours. Variations of such periods are also noticed in the measured temperatures (Chapter 3, section (3.5)) and meridional winds (Chapter 5, section (5.7))from the same location. The assumptions/limitations involved in the estimation of electric fields are discussed below.

A first look at the electric fields calculated from the differences between the estimated and measured $h_{\max}$ reveals that the values are large when compared to the value in the range of 0.5 to 1 mV/ m reported for equatorial region [*Woodman*, 1970; *Namboothiri et al.*, 1989]. We would rather expect that the electric field at the magnetic equator gets mapped along the field lines towards low latitudes. The fact that estimated electric fields are large, warrants close examination at the physical processes that occur in the low latitude F region.

One of the factors that causes uncertainties in the estimates of electric fields is the explicit assumption of steady state in the servo model. At each instant of time, the F layer has been assumed to be in chemical equilibrium, and the effect of meridional winds was then superposed to find the new balance height. As mentioned

earlier, the diffusion time at the F_2 peak height is assumed to be fast enough that the layer soon reaches a balance level before the drift due to a subsequent change in wind can be applied. The assumption of steady state may not be valid for large applied vertical drifts (say, more than 100 m/s), since the height of the ionosphere does not react immediately to wind changes as it has a finite time constant. Thus the electric fields are overestimated for drifts producing large changes in heights by the simplistic servo model approach adopted herein. It becomes necessary that the time delay in the response of the ionosphere needs to be taken into account in this regard.

The physical process which is of relevance to the uncertainties of the electric field estimates over low latitudes, is the equatorial ionization anomaly. The renewal of equatorial fountain resulting from the evening pre-reversal enhancement of upward plasma drifts [*Rishbeth*, 1971b; *Heelis et al.*, 1974], is known to provide an additional supply of ionization to the nighttime low latitude F region [*Sastri*, 1982]. *Buonsanto* [1987, 1988] investigated the behaviour of the F layer at the crest of the equatorial ionization anomaly (Tahiti (17.7°S geographic; 16.6°S dip latitude) in South Pacific Ocean) in the evening and pre-midnight hours. The place of our observations is located under the crest of the equatorial ionization anomaly. The relevance of the fountain effect to the low latitude F region is discussed elaborately in Chapter 6 (section (6.2)). It is suffice to note here that the movement of the crests of the anomaly across the low latitude observing stations, Mt. Abu/Ahmedabad, and the consequent ionization density variation, might have a partial role in inducing vertical motions of the ionization layer and it is possible that the electric fields are slightly overestimated. These are some of the aspects that have not been accounted for in the present study.

- In spite of the coordinated measurements being limited, the case study based on individual nights of observations suggests that there seems to be a distinct phase

difference in the variation of electric field from winter to equinoctial months. The geophysical processes like EIA associated with the electrodynamic properties of the low latitude and equatorial thermosphere-ionosphere system could possibly be the cause for the variabilities exhibited by the electric field.

These aspects need further investigation.

Chapter 5

Measured and derived meridional winds and their variabilities

5.1 Introduction

In his paper to Nature, *Jacchia* [1959] first pointed out the possibility of a difference in density of the upper atmosphere between the bright and dark hemispheres of the earth, which had led to the orbital decay of artificial satellites. It was recognized by then that the variations in air density are primarily due to heating by solar EUV radiation. The existence of a diurnal bulge of atmospheric density above about 200 km was attributed to the thermal expansion of the atmosphere at heights above 100 km in response to the large diurnal variation of temperature in this region. This 'bulging' of the atmosphere was shown to be responsible for the horizontal gradients of air pressure which would then drive horizontal winds [*King and Kohl*, 1965; *Geisler*, 1966]. *Kohl and King* [1967] showed the existence of a global wind system at F region heights through calculations using data from Jacchia's model atmosphere. They demonstrated the importance of ion-drag as a force determining the form of the atmospheric wind system.

Rishbeth [1972] in his review, examined the various properties of the wind system and the effects of the winds on the ionospheric F_2 layer. Experimental and theoretical results have suggested that the large scale dynamics arising out of such wind systems, would in turn, influence the temperature and composition of the thermosphere [*Shimazaki*, 1972; *Mayr et al.*, 1978].

Apart from the role of meridional winds in moving the ionization along the magnetic field lines thereby altering the plasma density distribution, the neutral wind has many other effects on the equatorial and low latitude F region. The winds are responsible for the global dynamo action leading to the generation of electric fields. The thermospheric zonal winds act as a primary driving force for the F region dynamo, which gives rise to the enhancement of the post-sunset equatorial electric field [*Rishbeth*, 1971a,b; *Heelis et al.*, 1974]. A transequatorial wind would transport ionization from one hemisphere to the other, thereby making the distribution of ionization asymmetrical about the equator [*Bramley and Young*, 1968]. It thereby aids the renewed fountain action in one of the hemispheres in the evening hours and enhances the crest of ionization. This feature has been shown to result in increase in peak electron density at a low latitude station, Tahiti, [*Buonsanto*, 1988]. Another effect of the transequatorial wind is to suppress the generation of ESF irregularities by enhancing the E region Pedersen conductivity in one of the hemispheres and shortcircuiting the polarization electric field [*Mendillo et al.*, 1992]. Recently, it has been shown that the vertical winds at the equator have significant role in enabling/inhibiting the Rayleigh-Taylor instability which is responsible for the generation of irregularities in electron and ion densities (Equatorial Spread F(ESF)) [*Raghavarao et al.*, 1987, 1992; *Sekar and Raghavarao*, 1987].

An outcome of the interaction of the global scale wind with anomalies in ionization distribution is a circulation associated with the temperature and pressure

perturbation [*Dickinson et al.*, 1971]. The horizontal convergence (divergence) of the neutral wind forces a downward (upward) vertical wind in the immediate region of the ionization anomaly. Such motions would lead to adiabatic heating and cooling within the location of anomaly. Recently, *Raghavarao et al.* [1991] have reported an Equatorial Temperature and Wind Anomaly (ETWA) at thermospheric altitudes characterized by the formation of two regions of enhanced temperature on either side of a prominent trough over the magnetic equator. The zonal winds were shown to reach their maximum near the magnetic equator with two minima on either side of it. The trough in temperature and the maximum in zonal winds were seen to be collocated with the trough of the equatorial ionization anomaly. In a more recent paper, *Raghavarao et al.* [1993] proposed two whorls of meridional winds at each of the temperature (and pressure) crests. These winds are superposed on the planetary scale meridional winds due to diurnal tide. Thus the importance of measuring neutral winds and their variation with time in the low latitude region can hardly be over-emphasized.

In the following section (5.2), the various techniques available for wind measurements are discussed. In section (5.3), a brief review on the results obtained by several workers from ground-based optical studies for low and equatorial latitudes is given. This is followed by a discussion on a few indirect methods available to infer neutral winds (section (5.4)). For the low latitude stations, Mt. Abu/Ahmedabad, under the present study, we utilize direct measurements of meridional winds with the Fabry Perot Spectrometer, and the meridional winds derived using ionospheric data, for a detailed study on their (meridional winds) behaviour and their interaction with the ionospheric F region. The results are presented in sections (5.6) and (5.7). The method adopted for deriving meridional winds from the ionospheric data is described in section (5.5). The variation in neutral temperature is shown to be important in the procedure of deriving meridional winds, more so when specific events are studied

(section (5.6)). However, for gross, average, features, use of the model temperature itself is adequate. This conclusion has been arrived at from a critical study to be discussed here (section (5.7)). The seasonal dependence of the magnitude and direction of meridional winds (both inferred and directly measured) is presented in section (5.7).

5.2 Sources of experimental data on neutral winds

One of the oldest methods to measure neutral winds in the upper atmosphere is by releasing vapour clouds from a rocket, as was first suggested by *Bates* [1950] and had thus proved to be the most fruitful method at height range of 120–200 km. The vapours most often used were sodium and trimethyl aluminium. Few of the limitations of the vapour trail method are that observations from at least two locations are required in order to determine, by triangulation, the position of an identifiable point in the release, and releases like that of sodium are confined to twilight periods only. It further requires cloud-free skies over a large area during the experiment. In spite of these stringent requirements, many series of observations have been successfully completed and yielded good results [*Jarrett et al.*, 1963; *Bhavsar et al.*, 1969; *Bedinger*, 1972; *Desai et al.*, 1975; *Raghavarao et al.*, 1984, 1987, to state a few].

With the advent of satellites, a series of experiments was conducted to obtain *in situ* measurements of neutral atmospheric parameters using omegatron instruments on San Marco 3 and 4 and quadrupole mass spectrometers on Aeros A and B, Atmosphere Explorer C, D and E and Dynamics Explorer 2 [*Spencer et al.*, 1981 and references cited therein]. In the later version of quadrupole mass spectrometers, measurements of the neutral winds were made through interpretation of the modulation of the particle stream entering the mass spectrometer, using the baffle technique. The accuracy of measuring neutral winds by this technique, i.e., with the Wind and

Temperature Spectrometer (WATS) on board the DE 2 satellite was estimated to be 10–20 m/s at 650 km altitude. Subsequently, *Raghavarao et al.* [1991, 1993] have shown that the error is only 2 m/s at 300 km as it is inversely proportional to the square root of the gas density. The scientific results arrived at and important contributions made by the DE 2 mission have been reviewed by *Killeen and Roble* [1988]. The measurement concept of obtaining the neutral atmospheric parameters using mass spectrometers has been discussed by *Spencer and Carignan* [1988].

Line profile measurements of natural airglow emissions using Fabry Perot Spectrometer (FPS) have been yielding thermospheric temperatures and winds for more than four decades, starting from the pioneering work by *Armstrong* [1953]. The Fabry Perot interferometers have also been flown on satellites such as Dynamics Explorer 2 and have yielded good data [*Killeen and Roble*, 1988]. In their review article, *Hernandez and Killeen* [1988] have given the historical development of optical remote sensing with FPS as a tool and discussed the scientific progress made from the data base collected at various observing stations round the globe. As pointed out by them, although the Doppler measurements of winds and temperatures provide continuously a synoptic picture of dynamic and thermodynamic behaviour of the upper atmosphere, they (the measurements) assume utmost importance when interpreted in conjunction with a global circulation model.

5.3 Results from previous ground-based optical studies from low and equatorial latitudes

The ground-based measurements from the near equatorial zone are not many, when compared to those in high and midlatitudes. The only measurements reported in the literature in recent times are enumerated below. The results obtained by them are briefly reviewed.

Sipler and Biondi [1978] and *Sipler et al.* [1983] have made measurements over a span of several years at sites such as Kwajalein Atoll in the Marshall Islands (9.4°N, 167.5°E, geographic; 8.6°N dip latitude). They showed that the winds in the equatorial region are strongly influenced by variations of ion-drag due to the variations in the ion densities effected by $\mathbf{E} \times \mathbf{B}$ drifts, upward propagating tides from the lower atmosphere and also by high latitude magnetospheric convection. They have made this suggestion after comparing their results with the NCAR thermospheric general circulation model (TGCM) predictions.

Some useful results have been obtained on the equatorial thermospheric dynamics by measurements carried out by *Biondi and Sipler* [1985] as a part of the Brazil Ionospheric Modification Experiment (BIME) from Natal (5.9°S, 35.2°W, geographic; 6.4°S dip latitude), Brazil. They observed new effects such as (a) significant vertical flows and neutral temperature increases in response to persistent convergence in horizontal flows and (b) gravity wave modulation of thermospheric flow. These results, although of a single night measurements, are considered to be extremely important.

Meriwether et al. [1986] have obtained nighttime measurements of horizontal winds at Arequipa (16.5°S, 71.4°W, geographic; 3.5°S dip latitude), Peru, on 62 nights. Comparison with the predictions of NCAR TGCM model for equinoctial and solstice conditions showed good agreement. In their earlier study on O I 6300 Å nightglow brightness at Arequipa [*Meriwether et al.*, 1985], they have examined the effect of a prolonged equatorward wind ($\sim$ 100 m/s) on the equatorial ionosphere. They have observed widespread areas of airglow depletion, with reduction in intensity as large as factors of 3 or 4. Ruling out the possibility of association of these depletions with equatorial plasma depletion events, they have invoked the presence of an equatorward neutral wind which would drive the F region plasma up the magnetic field lines sufficiently to account for the intensity depletions.

As part of the CEDAR (Coupling, Energetics and Dynamics of Atmospheric Regions) program, *Biondi et al.* [1988] have carried out coordinated measurements of the dynamical behaviour of the upper atmosphere and the ionosphere at the magnetic equator, using a Fabry Perot interferometer from Arequipa and the incoherent scatter radar from Jicamarca. Motions between the zonal neutral wind and the zonal drift velocity of the F region plasma were compared. The operation of F region dynamo in conjunction with the decrease in E region Pedersen conductivity was invoked to account for the correlated motions of the neutral and plasma in the zonal direction during late night hours. During daytime, however, the F region dynamo field is shorted by the higher conductivity in E region accounting for the uncorrelated motions.

Continuous nighttime FPI measurements on the 6300 Å emission line from Arequipa have yielded a data base covering 2/3 of a solar cycle. *Biondi et al.* [1990, 1991] have reported monthly average variations in the meridional and zonal components of neutral wind, displaying seasonal changes in wind patterns. The measured seasonal variations in the wind patterns are more pronounced than the solar cycle variations, which are expected in terms of the underlying forcing and damping processes. At the winter solstice, they have observed a weak ($\sim$ 100 m/s) transequatorial flow in the earlier and late part of the night, with essentially zero velocities in between. At equinoxes, there is an early night poleward flow during solar minimum, which becomes equatorward during solar maximum. The zonal winds were observed to be predominantly eastward throughout the night, except during solar minimum equinoxes when there is a brief westward flow in the early and late part of the night. *Biondi et al.* [1990] have compared their results with the horizontal wind model (HWM-87) of *Hedin et al.* [1988] and the vector spherical harmonic model (VSH) of *Killeen et al.* [1987] and found a general agreement. Comparison has also been

made with the winds measured at Arecibo (18°N, 67°W, geographic; 30°N dip latitude) [*Burnside and Tepley*, 1989], the geographic 'mirror twin' of Arequipa. With the solar EUV source acting as the principal driving force, the expected oppositely directed meridional flows and similar eastward zonal flows at the two locations have been reported by them.

Contradicting the conclusion arrived at by *Burnside and Tepley* [1989] that nocturnal and seasonal variations in the neutral wind field are remarkably unaffected by changes in the solar cycle, *Biondi et al.* [1991] demonstrated significant differences in both meridional and zonal wind patterns at different seasons as the solar cycle progressed. As pointed out by them, this is expected since the increase in pressure gradients from solar minimum to solar maximum would produce higher wind speeds near the subsolar point at locations such as Arequipa. However, the increase in the zonal wind has been observed to be moderate suggesting the opposing role played by ion-drag which would reduce the effect of the stronger pressure gradients. It is to be noted that the meridional wind speeds at Arequipa are small throughout the solar cycle, the wind flows near the subsolar point being dominantly in the zonal direction. Also at times during magnetic disturbances arising out from the auroral regions, the meridional flows would tend to cancel near the magnetic equator.

Though the ionosphere over Arecibo in Puerto Rico has midlatitude characteristics (dip angle I = 51°), the thermospheric dynamics in this region exhibits features characteristic of low latitude behaviour. Optical observations at Arecibo have yielded very useful results supporting the conclusions arrived at by satellite measurements. Burnside and his coworkers [*Burnside et al.*, 1981; *Burnside et al.*, 1983; *Burnside*, 1984; *Burnside and Tepley*, 1989] have been reporting optical observations of nighttime thermospheric winds carried out from Arecibo since 1980. Apart from their conclusion that the thermospheric wind fields at Arecibo do not appear to show any

solar cycle dependence, they have reported nighttime wind patterns controlled by the disturbance associated with midnight pressure bulge. The zonal winds are eastward throughout the night in winter. A reversal to westward flow is usually observed after local midnight in summer months. The meridional flows are largest in summer, while a reduction or sometimes reversal occurs after midnight. The data from the incoherent scatter radar have been used along with optical observations to infer the occurrence of midnight pressure bulge [*Burnside et al.*, 1983]. A feature which is associated with the reversal of equatorward wind near midnight, is the meridional intensity gradient (MIG) in 6300 Å emission [*Herrero and Meriwether*, 1980; *Friedman and Herrero*, 1982]. The interaction of the disturbance originating in polar region and moving towards the equator, with the poleward winds associated with the midnight pressure bulge, leads to a transition region where large horizontal gradients in wind velocity and in the airglow intensity have been observed.

Sahai et al. [1992a] have reported thermospheric neutral wind measurements by observing O I 6300 Å nightglow emission at Brazilian locations, Sao Jose dos Campos (23.2°S, 45.9°W, geographic) and Cachoeira Paulista (22.7°S, 45°W, geographic) during 1988–1989. The dip latitude was about 16°S for these stations. These measurements turned out to be the first ever reported from a location near the crest of the equatorial ionization anomaly. *Sahai et al.* have displayed graphically the average nocturnal variations of both meridional and zonal winds during all seasons and compared their results with HWM-87 and HWM-90 models. On comparison, they have reported some discrepancies both in the absolute magnitudes and in details of nocturnal variations. The overall wind patterns were similar to those reported from Arequipa. Fig. 5.1 shows their results on seasonal variabilities of meridional winds over Cachoeira Paulista and the comparison with the models.

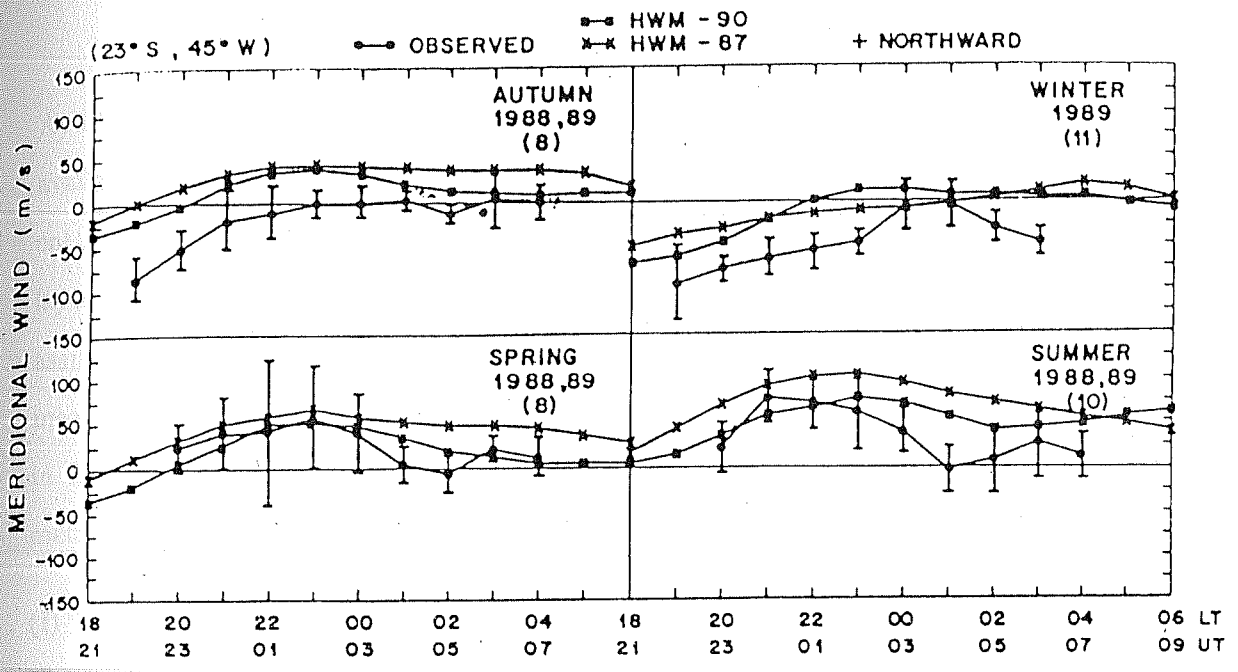

Fig. 5.1. Temporal variation of the measured meridional winds for different seasons over the Brazilian latitudes (23°S, 45°, geographic; 16°S dip latitude) (after *Sahai et al.*, 1992a).

5.4 Indirect methods available to infer neutral winds

Apart from the direct ground-based optical techniques, several other methods are available to determine neutral winds; from (i) ion velocity measurements of incoherent scatter radars, (ii) satellite measurements of O I 6300 Å emission, and (iii) F layer height and its variation deduced by ground-based ionograms. There are several assumptions and limitations in each of these methods. With more data on direct measurements of winds being accumulated, these methods are refined and they help in further advancement of our knowledge on the thermospheric dynamics. These methods are briefly reviewed below.

(i) Neutral winds deduced from incoherent scatter radar (ISR) observations

The method of employing F region ion drift measurements obtained by incoherent scatter radar (ISR) to determine the meridional component of the neutral wind was originally suggested by *Vasseur* [1969] and has been applied widely to the study of thermospheric dynamics at various radar locations, namely, Millstone Hill, Sondrestrom, Arecibo, EISCAT (Scandinavia) and Saint Santin. The technique involves determination of the ion velocity parallel to the magnetic field at a particular height from field aligned radar Doppler measurements. The drift velocity of the ions is due to the combined action of neutral winds, plasma diffusion and electric fields. With the measurements made simultaneously on F region plasma parameters, subtraction of the diffusion velocity component from the observed drift velocity and projection of the residual velocity in the horizontal plane yield a measure of the meridional wind.

The major source of uncertainty in this method comes from limited knowledge on the ion-neutral collision frequency which determines the diffusion coefficient. The

statistical errors due to the measurement of the various parameters lead to an error estimate of 20–30 m/s in the neutral wind at F region heights [*Oliver and Salah*, 1988]. During disturbed periods, the uncertainty may be as high as 100 m/s. Such large uncertainties lie in the neutral composition being used to compute diffusion velocity.

Contributions from the ISR at Arecibo, Puerto Rico, to the thermospheric dynamics are many. *Nelson and Cogger* [1971] first made use of the data on ion velocity and observed a large drop in the height of the F layer, at Arecibo, after midnight. With the technique of determining meridional winds from ISR data being well established, *Behnke and Harper* [1973] began the study of ion-neutral interactions and examined the morphological features of the dynamic F layer over Arecibo. *Harper* [1973] in his pioneering work, inferred large equatorward meridional wind speeds in the 2100–2400 h sector, which decreased rapidly after midnight and reversed sometimes near 0200–0300 h sector. This led *Behnke and Kohl* [1974] to conclude that the midnight collapse of F region observed at Arecibo, is caused by the post-midnight poleward winds dragging the F layer ions down the magnetic field lines. This picture evolved slowly with measurements from other techniques rapidly coming up, and has proved to be important in maintaining or depleting the nighttime ionosphere, particularly at magnetic midlatitudes, by the meridional winds. To a lesser extent, these winds influence the F layer densities at low latitudes as well.

(ii) Inferences from satellite measurements of airglow emissions

Utilizing the greater spatial coverage by a satellite, *Bittencourt et al.* [1976] used the OGO 4 tropical nightglow data on 1356 Å and 6300 Å atomic oxygen airglow to infer meridional wind velocities. They have made use of the fact that the morphology of the tropical emissions is associated with processes such as Appleton

anomaly which cause the F layer to be situated at different heights and with different values of electron density in different locations. From the latitudinal asymmetry present in the tropical emissions, they have deduced meridional wind patterns over low latitudes. The difference in the height of the F layer at northern and southern conjugate points is directly related to the sum of the components of wind velocity in the magnetic meridian at the conjugate points. In a subsequent study, *Bittencourt and Tinsley* [1977] have analyzed simultaneous measurements of the electron density, O_2^+ density and zenith 6300 Å column emission rate obtained from the AE-C satellite, to infer meridional wind speeds. Their results agreed with the models of the global thermospheric wind system. The number of inferences made in this method is limited because of the requirement that there exist asymmetries about the magnetic equator in the ionospheric plasma parameters.

The other work reported in the literature concerns the AE-E measurements of 6300 Å emission by *Burrage et al.* [1990]. The satellite brightness measurements of 6300 Å emission are first subjected to a two-dimensional inversion technique to obtain altitude profiles of the volume emission rate. The volume emission rates are then converted to electron density profiles, which provide estimates of the F_2 layer height. In conjunction with MSIS-86 model to obtain neutral atmospheric densities, the layer peak heights are used to derive meridional winds. They have taken into account the effect of zonal electric field by incorporating typical values obtained by the ISR at the equatorial station, Jicamarca. They have thus demonstrated the utility of the AE-E 6300 Å data base for the investigation of the tropical neutral wind pattern as a function of latitude, longitude, local time and season. The main results arrived at by them are as follows.

In the Indian sector, the derived winds are almost exclusively northward over the entire latitude and local time range, indicating a clear summer to winter flow. A

distinct abatement of northward wind in the midnight sector is observed during this summer season in the southern hemisphere. The results obtained by them compare reasonably well with both HWM-87 and TGCM models, which however, do not predict the midnight abatement feature observed both in Indian and Pacific sectors. The main limitation in this method is the inability to derive meridional winds very close to the magnetic equator. Since the layer displacements due to meridional winds are very small near the equator, large uncertainties arise in the derived winds.

(iii) Meridional winds derived from ground-based ionosondes

This is the third method which is widely used by various workers and is based on the servo model concept of *Rishbeth* [1967]. Since the work of *Ganguly et al.* [1980] who showed that the servo model method can be successfully exploited to understand the ionosphere over Arecibo, and demonstrated its behaviour to be in accordance with the model prediction, various workers have attempted to determine the meridional wind field from the vast amount of ionospheric data regularly archived in the existing ground-based ionosondes [*Buonsanto*, 1986; *Miller et al.*, 1986; *Forbes et al.*, 1988; *Krishnamurthy et al.*, 1990]. These workers have proved on and often that besides complementing the capabilities and shortcomings of other methods of determining neutral atmospheric parameters, ionosondes can provide data to validate and cross-check with their own, the outputs available from various numerical models.

The use of ionosonde data to infer meridional winds has attracted attention because of the recognition that the F layer peak height $h_{\max}$, which is determined by diffusion and chemistry, and is dependent on magnetic latitude (Chapter 4, section (4.3)), undergoes displacement ($\Delta h_{\max}$), which is nearly linearly proportional to the meridional component (U) of the neutral wind [*Rishbeth and Barron*, 1960; *Hanson and Patterson*, 1964; *Rishbeth et al.*, 1978]. If the balance height can be computed from a numerical model with realistic specifications of photochemistry and diffusion,

and with the assumption that the effects of electric fields are unimportant, then this method allows one to estimate meridional winds. This approach has been adopted by *Miller et al.* [1986], who found reasonable agreement of their estimates with other independent measurements available.

The method of *Miller et al.* [1986] involves the use of an ionospheric model to develop a relationship between the meridional wind and $h_{\max}$. This is done by modeling the F layer at a few wind speeds. The meridional wind is then derived by a comparison of the modeled and measured layer heights. They have obtained better values of α, the constant of proportionality, from the ionospheric model at various neutral winds by a linear regression through values of $h_{\max}$. Fig. 5.2 shows the comparison of their model results for Arecibo with Fabry Perot measurements and those calculated from ion diffusion velocities obtained by the incoherent scatter radar at Arecibo. The three results show agreement to about $\sim$ 30 m/s all through the night. However, as seen in the figure, the difference between their results and those derived from ISR data is about 50 m/s at midnight when the wind speed is rapidly decreasing.

Forbes et al. [1988] gave a parameterization of the linear dependence that exists between $\Delta h_{\max}$ and $U_{\rm p}$. This study was taken up by them as part of an attempt to delineate the effects of latitudinal penetration of ionospheric storms. *Buonsanto* [1986, 1988] made use of the servo equations of *Rishbeth* [1967] and *Rishbeth et al.* [1978]. Rather than computing α by modeling the F region at a few wind speeds as was done by *Miller et al.* [1986], he has used the MSIS-86 model to determine α through its dependence on the diffusion coefficient and the neutral scale height.

Krishnamurthy et al. [1990] made use of the ionosondes available in the equatorial region of Indian sector to derive meridional winds. The ionosondes are located at Trivandrum (8.6°N, 77°E, geographic; 0.8°S dip), an equatorial station, and at

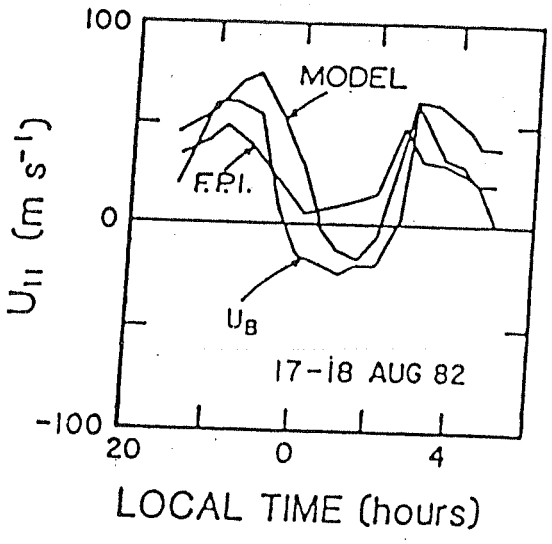

Fig. 5.2. Comparison of the derived wind using ionosonde data with the direct measurements of meridional wind over Arecibo using Fabry Perot Spectrometer and the inferred wind (U_B) made from ion diffusion velocities obtained by the incoherent scatter radar at Arecibo. (after *Miller et al.*, 1986)

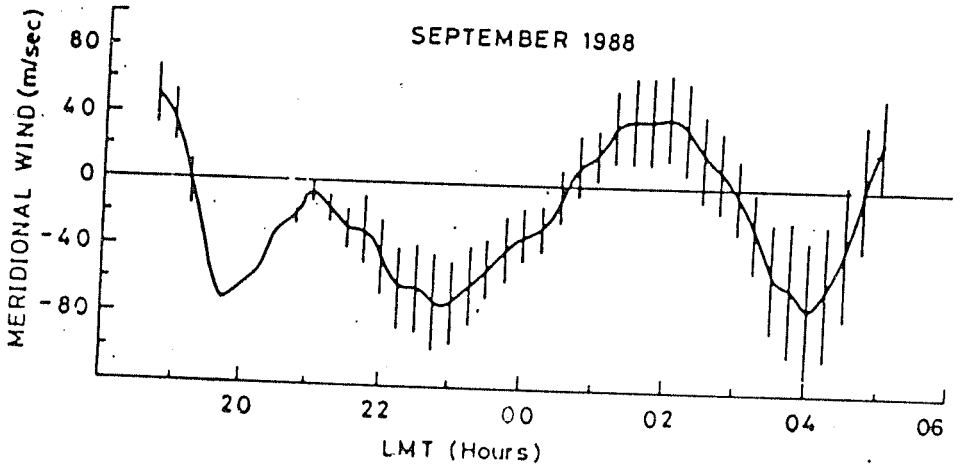

Fig. 5.3. Nocturnal variation of meridional wind obtained by *Krishnamurthy et al.* [1990] for the low latitude station, Sriharikota (SHAR) in the Indian sector. Ionosonde data from Trivandrum, a station situated at the magnetic equator and from SHAR ($I = 10°$N), slightly away from the equator, have been made use of for this purpose.

Sriharikota (SHAR) (13.7°N, 80.2°E, geographic; 10°N dip), a station slightly away from the dip equator. Assuming that $\mathbf{E} \times \mathbf{B}$ drift is the same at both stations, the vertical drift at SHAR is given by

$$v = v_D \cos I - U \cos I \sin I - w_D \sin^2 I \tag{5.1}$$

where U is the meridional wind, w_D is the plasma drift due to diffusion, v_D is the vertical drift over the magnetic equator and I is the dip angle. This is essentially subtraction of drifts due to electric field and diffusion from the observed drifts at a place where the meridional wind is to be estimated, to yield the drift due to wind. The rate of change of $h'F$, the virtual height of the F layer, at both stations is assumed to represent the drift velocity of the plasma. They have incorporated the effect of apparent drift due to chemical loss. Fig. 5.3 shows the average nocturnal variation of U (positive poleward) in the September month of 1988 as reported by *Krishnamurthy et al.* [1990]. Recently, *Sekar and Sridharan* [1992] validated the above method and showed that the existing ground-based ionograms can be effectively used for deriving meridional winds during nighttime at least in the Indian sector. They have utilized the bottomside ionograms available from SHAR and thermospheric and ionospheric data obtained from a rocket experiment conducted in 1982 at SHAR, wherein high altitude vapour clouds were released and the winds were estimated directly by ground photography [*Raghavarao et al.*, 1987].

Buonsanto et al. [1989] have discussed in detail the assumptions and uncertainties involved in obtaining meridional neutral winds from ionosonde data. The greatest uncertainty in the servo model derived winds is the uncertainty associated with ion-diffusion coefficient. How close is the ion-diffusion coefficient (ion-neutral collision cross-section, as some authors prefer) determined by the currently available methods to the actual value is a reigning controversy. At night, when there

are few collisions between ions and neutrals, the diffusion coefficient is larger, and the uncertainties in the MSIS model parameters translate into greater uncertainty in the diffusion coefficient, and therefore in the estimated wind. This effect becomes pronounced during geomagnetic storms, when there arise large changes in neutral composition and temperature [*Prolss*, 1987]. *Buonsanto et al.* [1989] found it necessary to tune the servo model by changing the empirical constant 'c' appearing in the servo equations, to obtain a better agreement between the winds derived from the servo model and those derived from incoherent scatter velocity measurements. They demonstrated possible deviations the derived winds can undergo from incoherent scatter measurements when the allowed composition changes during a severe magnetic storm are incorporated in the servo model.

Another source of uncertainty lies in the electric field whose effects are not included by any of the research workers. *Miller et al.* [1987] showed that for quiet or moderate geomagnetic conditions, the effect of electric fields on the neutral wind determination is generally small and usually smaller than the statistical uncertainties in the calculation. In the present work too, it is shown (Chapter 4, section (4.6)) that the effect of electric field in the low latitude thermosphere-ionosphere system is relatively unimportant considering the immediate response of the F layer to changes in neutral temperature and meridional winds. However, it was proved by *Buonsanto et al.* [1989] that during disturbed periods, the effects of electric fields must be included in calculations of neutral winds obtained by the servo model method.

Finally, the effects of neutral temperature changes on the F layer height are not incorporated by any of the workers who derive meridional winds from ionosonde and incoherent scatter line-of-sight ion velocity measurements. It is shown in Chapter 3 (section (3.5)) that the currently available neutral atmospheric models do not represent the variation of neutral temperature properly on many nights, especially in

the low latitude regions covered under the present study. This effect on the derived meridional winds is examined in one of the sections to follow. It is demonstrated that the changes in neutral temperature, in the wake of the well known geophysical processes such as equatorial ionization anomaly, equatorial spread F and thermospheric and F region storms, which at times act as sources of energy inputs, must be included in the servo model calculations to derive meridional winds.

5.5 Method adopted in the present study to derive meridional winds

As described in the previous section, all the methods, namely, those of *Miller et al.* [1986], *Buonsanto* [1988] and *Forbes et al.* [1988], employ the linear relationship between the F layer height displacement and the meridional wind which causes it, to determine the latter parameter.

In the absence of electric fields, the poleward meridional wind

$$U_p = \frac{h_o - h_{max}}{\alpha} = \frac{\Delta h_{max}}{\alpha} \tag{5.2}$$

where $\alpha = \frac{2H^2 \cos I}{(k+1) D_m \sin I}$. This follows from the linearization of the servo equation (4.17) and the elimination of rate of change of layer height, dh/dt, being a valid assumption in the F region.

The method adopted in the present work is similar to the one by *Buonsanto* [1988]. Use of MSIS-86 model to determine the balance height h_o, in the absence of U_p, and the constant of proportionality α at that height h_o, and the h_{max} determined by the true height reduction of ionograms, yields U_p, the neutral wind in the magnetic meridian.

The spectroscopically measured neutral temperature is adopted as a representation of T_∞, the exospheric temperature, in the MSIS-86 model, to deduce the neutral densities of O, O_2 and N_2, and obtain the relevant recombination and diffusion coefficients (β_m and D_m) at each height. The iteration method same as employed to estimate the F layer peak height in Chapter 4 (section (4.6)), is used to determine h_o from the servo expression (4.16). At this height, as already stated in Chapter 4, the diffusion and the loss due to recombination are of equal importance. The F layer peak height (h_{max}), at this instant, is found from the scaled ionograms obtained by the ground-based ionosonde. Equation (5.2) then yields the meridional wind U_p.

The uncertainty for the derived wind is given by

$$\frac{\delta U}{U} = \left[\left(\frac{\delta h_{max}}{h_o - h_{max}}\right)^2 + \left(\frac{\delta h_o}{h_o - h_{max}}\right)^2 + \left(\frac{\delta \alpha}{\alpha}\right)^2\right]^{1/2} \qquad (5.3)$$

similar to that derived for h_m in Chapter 4.

An h_{max} lower (higher) than h_o implies poleward (equatorward) wind since the result of the wind has been to move the plasma down (up) the magnetic field lines.

It is useful to analyze the extent of linearity that holds between U_p and Δh_{max} (in equation (5.2)) before any estimate of meridional wind is made. This can be done by solving the servo equation for the vertical drift of ionization, which in our case has been assumed to be due to the neutral wind in the magnetic meridian. The result is

$$-U_p \sin I \cos I = \frac{D_m \sin^2 I}{2H}\left[\exp\left[\frac{(h_{max} - h_o)}{H}\right] - \exp\left[\frac{-k(h_{max} - h_o)}{H}\right]\right] \qquad (5.4)$$

To illustrate the response of the F_2 peak to different wind speeds and to examine the nonlinearity in (5.4), the servo equation has been worked out for the solar geophysical conditions as on 10 April 1991, and the result is shown in Fig. 5.4. The FP measurement in the premidnight hours on this night, yielded a neutral temperature of 1071 K, which determines the balance height in the absence of wind to be at about

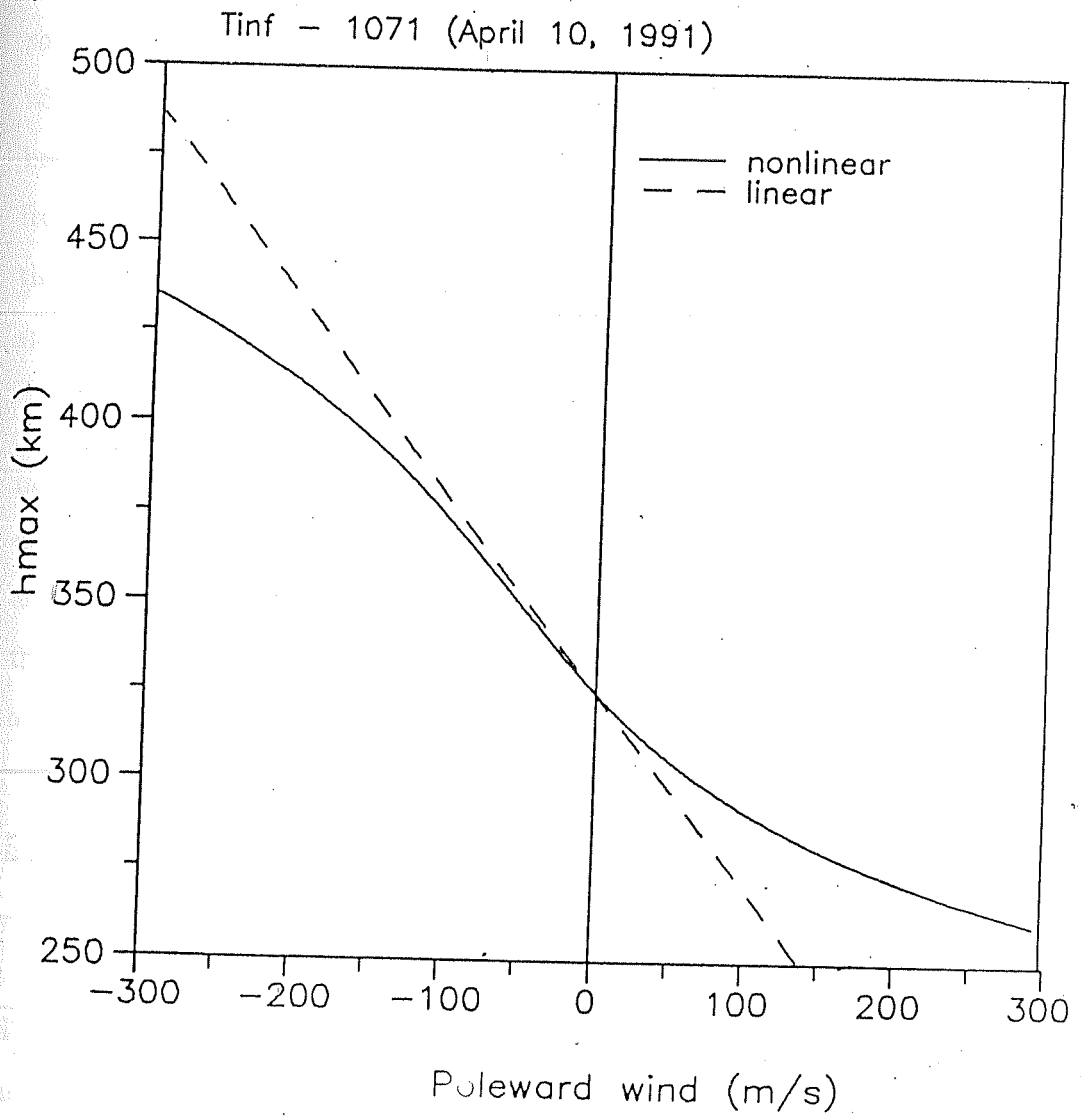

Fig. 5.4. The expected response of the F layer peak height, $h_{\max}$, to different wind speeds at the low latitude station, Mt. Abu. The servo equation (5.4) has been solved for different F layer peak heights and the result is the non-linear curve. The dashed line represents the linear relation between the layer displacement $\Delta h_{\max}$ and the meridional wind.

325 km. D_m and H in (5.4) are the parameters at this height h_o. Equation (5.4) is then solved for different F_2 peak heights to evaluate the corresponding meridional winds which cause the displacement. Also shown in the figure, is the result of calculations based on equation (5.2), i.e., the linear relation between Δh_{max} and U_p. It is evident from Fig. 5.4 that the response of the F layer is nearly linear (the deviation is less than 25 km) for equatorward wind speeds less than 200 m/s and for poleward wind speeds less than 125 m/s.

The assumption of linearity would then lead to an underestimate (overestimate) of equatorward (poleward) wind, which becomes significant if the layer gets displaced upward (downward) by more than 100 km (50 km). These numbers differ as the solar activity changes. For low solar activity period, it has been found that the slope of the linear curve decreases which implies the effect of nonlinearity on the derived winds is slightly reduced.

5.6 Results on derived meridional winds from low latitudes

The Fabry Perot Spectrometer which was commissioned at Mt. Abu (24.6°N, 72.7°E, geographic; 33°N dip) in 1985, has been yielding neutral temperatures since then and meridional wind measurements since the winter months of 1989. Since the required temperature stability of the etalon of about 0.1° C (which corresponds to an uncertainty in wind of about 10 m/s), was achieved only during December 1989, direct measurements of neutral winds are not available for earlier periods. Making use of the ionosonde data that are continuously being obtained from Ahmedabad ($\sim$ 2 degrees in latitude south of Mt. Abu) and the temperature measurements from Mt. Abu, meridional winds are derived for the period 1986–1989, using the method described in the previous section. Data belonging to quiet days only are taken up for the present

study.

Seven examples are depicted in Figs. 5.5a to 5.5g, to illustrate the results. Two cases were considered for all the examples, one using MSIS-86 model temperatures and the other using measured temperatures, and the differences between them have been investigated.

Figs. 5.5a to 5.5d show the winds derived for four nights of data during October 1986. The agreement between the winds derived using measured T_n and those derived with model T_n is overall good except at times when the measured T_n deviated considerably from the model T_n. These differences have been shown in Chapter 3 (section (3.5)). From equation (5.2), for a given h_{max}, the derived wind depends on h_o and α. Since the change in h_o is more than that in α with height, the meridional wind increases in magnitude (more poleward or less equatorward) if the balance height h_o determined by the measured T_n is greater than that determined by model T_n. A striking example has been the result on 27 October (Fig. 5.5d). The deviation between the curves of about 30–50 m/s is seen throughout the period for which T_n measurements are available. This implies an uniformly higher neutral temperature than what MSIS-86 model predicts for this night. Five out of seven T_n measurements on this night were atleast 125 K more than the model values (as can be seen in Chapter 4, section (4.5)).

On 23 and 24, October (Fig. 5.5a and 5.5b), apart from differences in the range 50-70 m/s at certain times, the trend appears to be the same in both the cases for these days. On 26 October (Fig. 5.5c), the direction of the wind was opposite to each other for the two cases in the time period 2000–2130 h. The deviation was as large as 150 m/s. There happened to be a cross-over on this day implying that the temperatures in the time period 2000–2130 h had been less than the model values while those after about 2130 h had been more than what were predicted by the MSIS

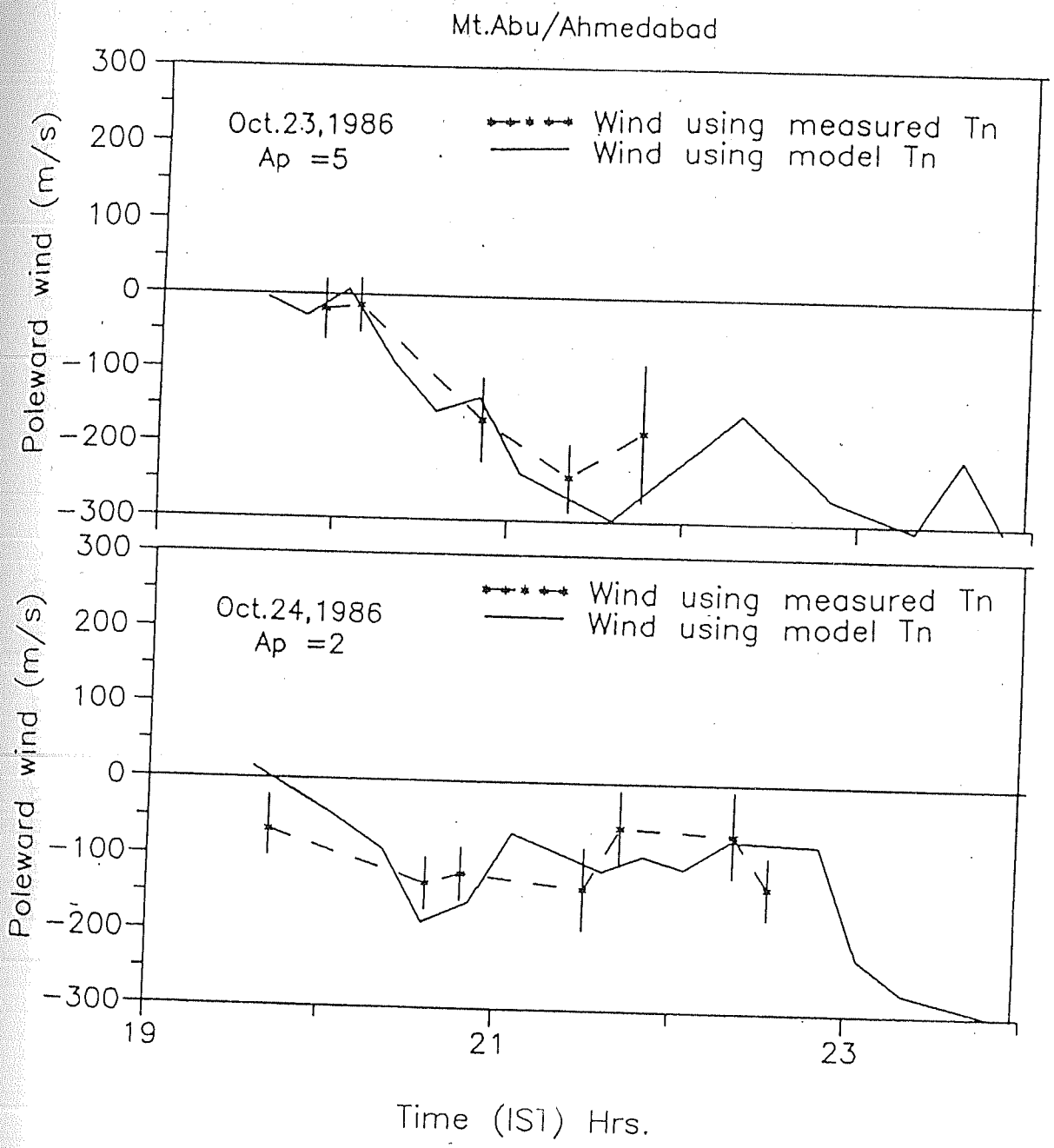

Figs. 5.5a,b. Comparison of derived meridional winds using spectroscopically measured temperatures and those derived using MSIS-86 model temperatures, for 23 (top panel) and 24 (bottom panel), October 1986. The method of deriving them is based on the servo model.

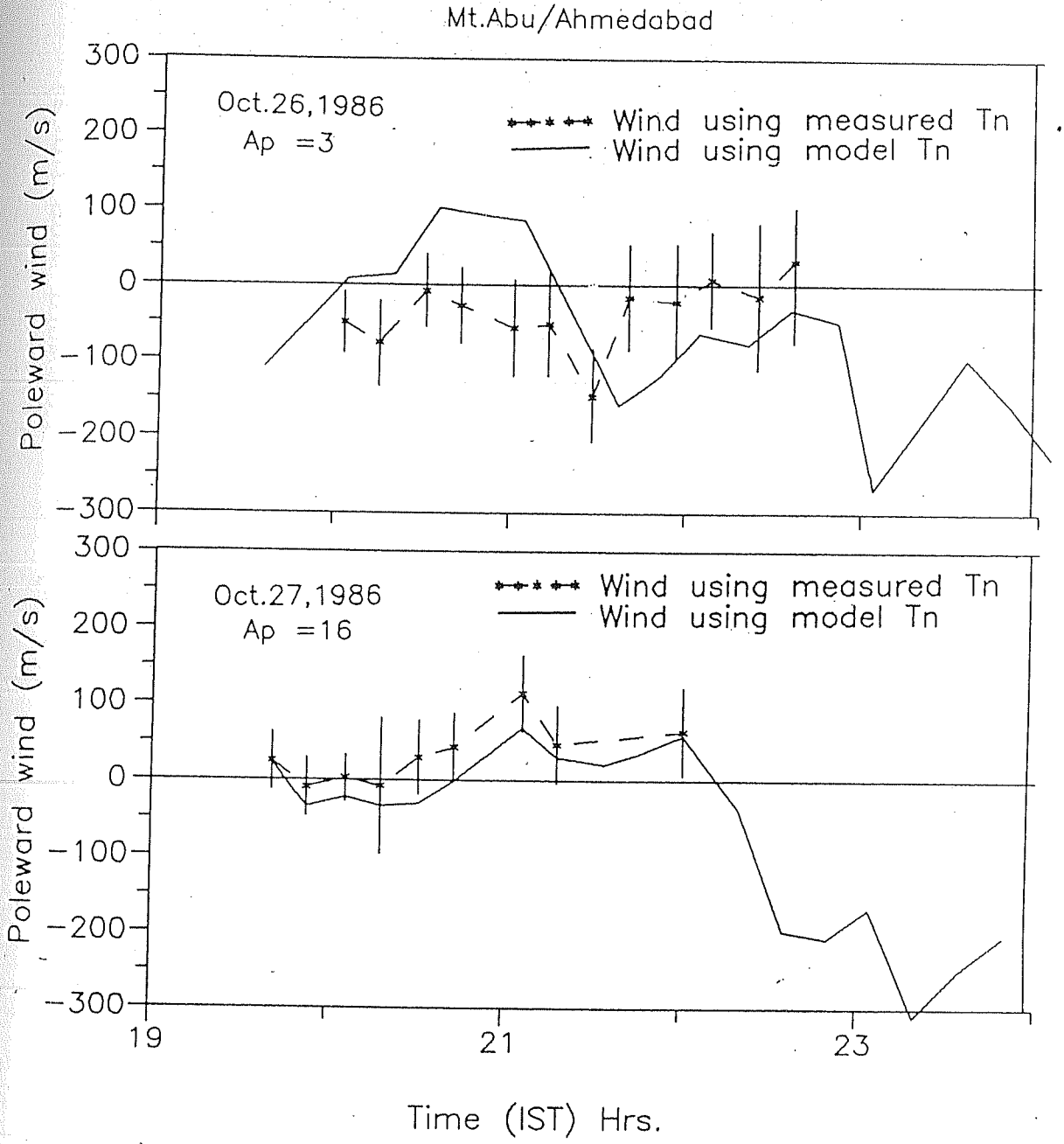

Figs. 5.5c,d. Same as Figs. 5.5a,b but for 26 October (top panel) and 27 October (bottom panel), 1986.

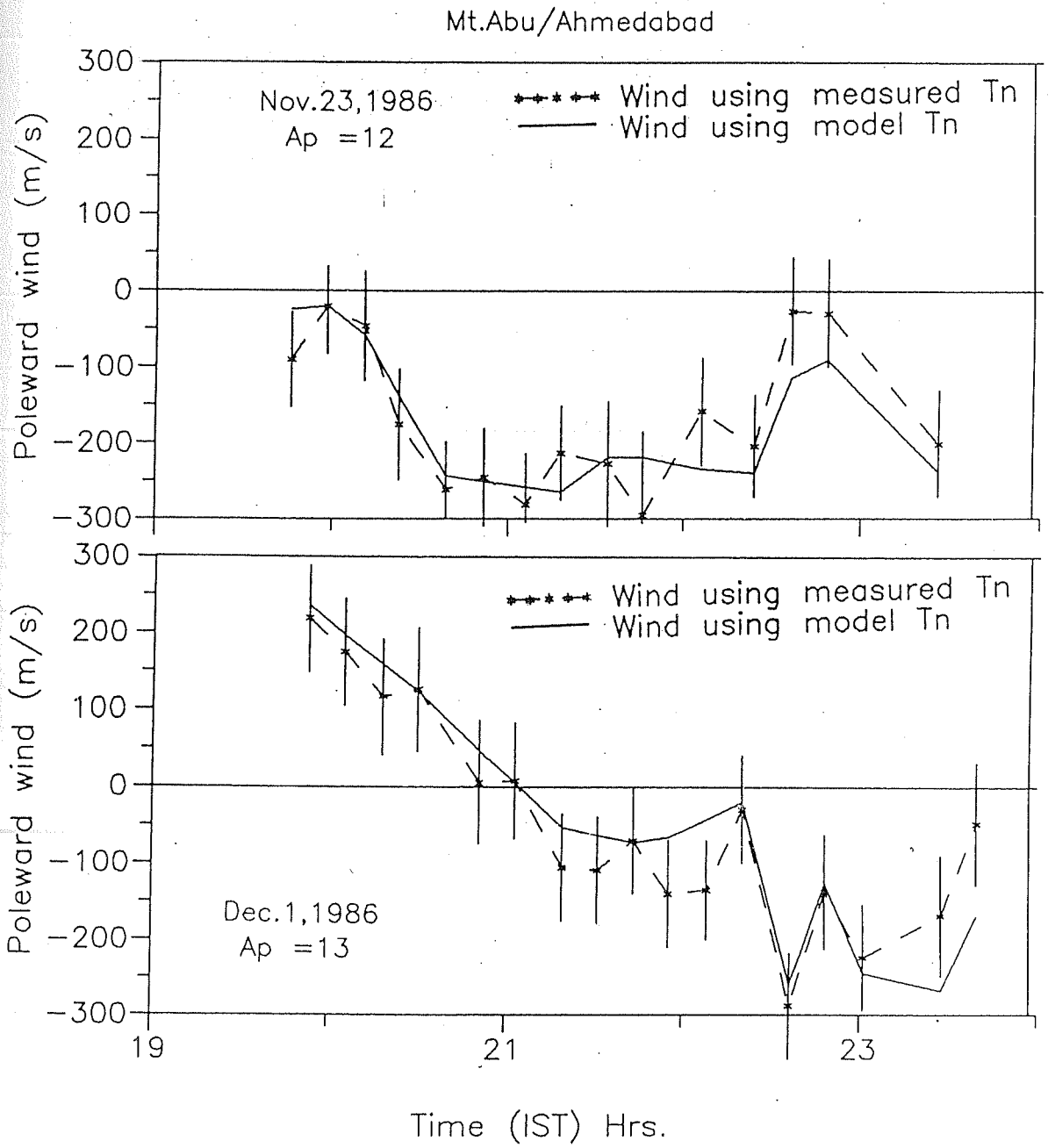

Figs. 5.5e,f. Same as Figs. 5.5a,b but for 23 November (top panel) and 1 December (bottom panel), 1986.

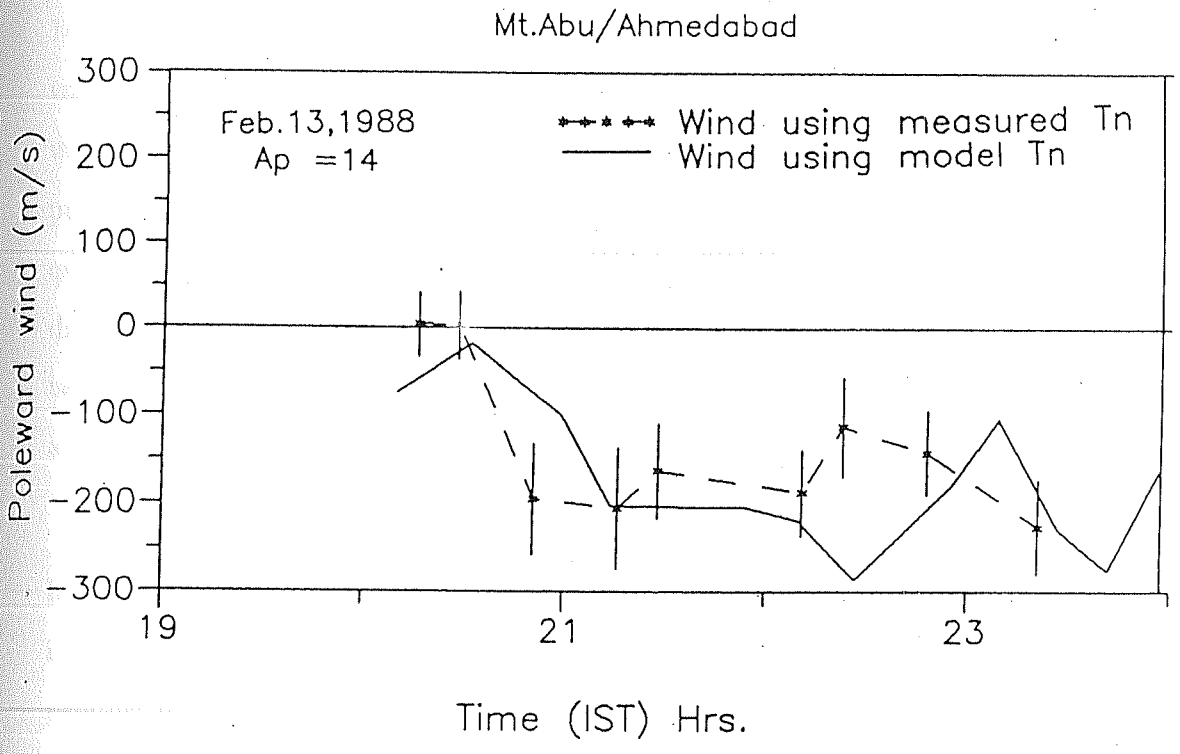

Figs. 5.5g. Same as Figs. 5.5a,b but for 13 February 1988.

model (Chapter 3, section (3.5)). Despite small differences, for days 23 November and 1 December, 1986, the agreement was good (Fig. 5.5e and Fig. 5.5f). The poleward wind on 1 December need not be as large as depicted in the figure, since the poleward wind is always overestimated depending on to what height ($h_{\mathbf{max}}$) the layer is pushed below the balance level (h_o). However, the equatorward wind is only slightly overestimated as explained in the last section. On 13 February 1988 (Fig. 5.5g), the differences between the two cases considered were significant ($\sim$ 150 m/s) at least at two different times (the differences in temperatures between the model predictions and the measurements can be seen in Chapter 4, section (4.5)).

The number of measurements on nights selected for this case study has been limited extending only upto midnight. This being a solar minimum period, the airglow intensity had decayed rapidly after about 2300 h leading to the rejection of emission profiles for the retrieval of Doppler information. With modifications to be made shortly in the optics that would enhance the flux gathered by the detector of the central-aperture scanned Fabry Perot, it is hoped that we would be able to retrieve the Doppler parameters even beyond midnight, even during periods of weak emission as one encounters during solar minimum.

The important results we arrive at, in the present study, are the following:

- The balance height (h_o) of the F_2 peak, in the absence of winds, is determined by neutral temperature.
- It has been shown that the measured temperatures need to be incorporated in all calculations associated with the derivation of meridional winds from ionosonde data.

5.7 Nocturnal and seasonal variabilities of meridional winds

In order to understand the nature of the forcings which establish the neutral wind patterns, it is necessary to study the variation of thermospheric winds over different periods ranging from a few hours on a given night to a solar cycle. The amount of available data in this regard for the low latitude and equatorial regions is very less. As reviewed in section (5.3), *Biondi et al.* [1990, 1991] and *Burnside and Tepley* [1989] have attempted to understand the behaviour of thermospheric winds over Arequipa, Peru and Arecibo, Puerto Rico, respectively over a long period. In their analysis, they have made use of the fact that the solar radiation acts as a principal driving force that sets up the wind patterns, and obtained overall agreement between the expected and the observed wind variations.

Though averaging individual measurements over a month or a season masks the day-to-day variations as well as features such as gravity waves occurring on a shorter time scale, say, a few hours on any particular night, it still yields fruitful results for variations on a longer time scale. The results we presented in Chapter 3 (section (3.5)) on neutral temperature measurements, suggested that only about 65 % of variations observed in them can be explained by the solar cycle dependence of thermospheric temperature and for the remaining, other physical processes must be operative which at certain times, control the temperature variations. In this section and the following chapter, we shall discuss these processes at large. Essentially, they compete with the solar forcing to establish the temperature and wind patterns, and the measurements reported herein probably are the result of this intimate competition within the solar-terrestrial environment.

As already mentioned in the last section, meridional winds have been derived

for the period 1986–1989 when both measurements in neutral temperature and ionospheric peak height ($h_{\max}$) are available, using the servo model concept described in Chapter 4. It has been shown earlier that the balance height of the F_2 layer peak is determined by the neutral atmospheric parameters, namely, temperature and densities and that the meridional winds act as a perturbation on the equilibrium state of the F region. In the last section, we have seen that winds derived from model temperatures differ significantly at certain times from those derived using measured temperatures. This has been the case when we adopted the case study approach. However, for an average picture over a long period, say, a month, it is suffice that we make use of the model temperatures to derive meridional winds.

We present an example in Fig. 5.6 wherein the average winds obtained from the two different methods for the month of October 1986 are depicted. The spectroscopically measured neutral temperature and the ionospheric peak height $h_{\max}$ determined by the true height reduction of ionograms obtained from the ground-based ionosonde located at Ahmedabad, are made use of, at each instant, to estimate meridional winds, using the servo principle. MSIS-86 model exospheric temperature is also used to derive atmospheric densities and hence winds. The estimated wind values are sorted out in bins of half an hour duration and are then averaged for all the nights. The vertical bars (given only for winds derived using measured temperature) associated with each point represent the 1σ deviation among the individual estimated values. It can be seen that the winds derived using the atmospheric parameters determined by the MSIS-86 model for the two cases, namely, the measured temperature and the model temperature are within 1σ except for the large deviations near midnight. It is to be noted that the results presented in Chapter 3 indicated a large deviation in average temperature from the model prediction for this month (October 1986) after 2200 h. Since both equatorward winds and increase in neutral temperature act together in raising the height of the F_2 peak, the role of equatorward winds is magnified if one

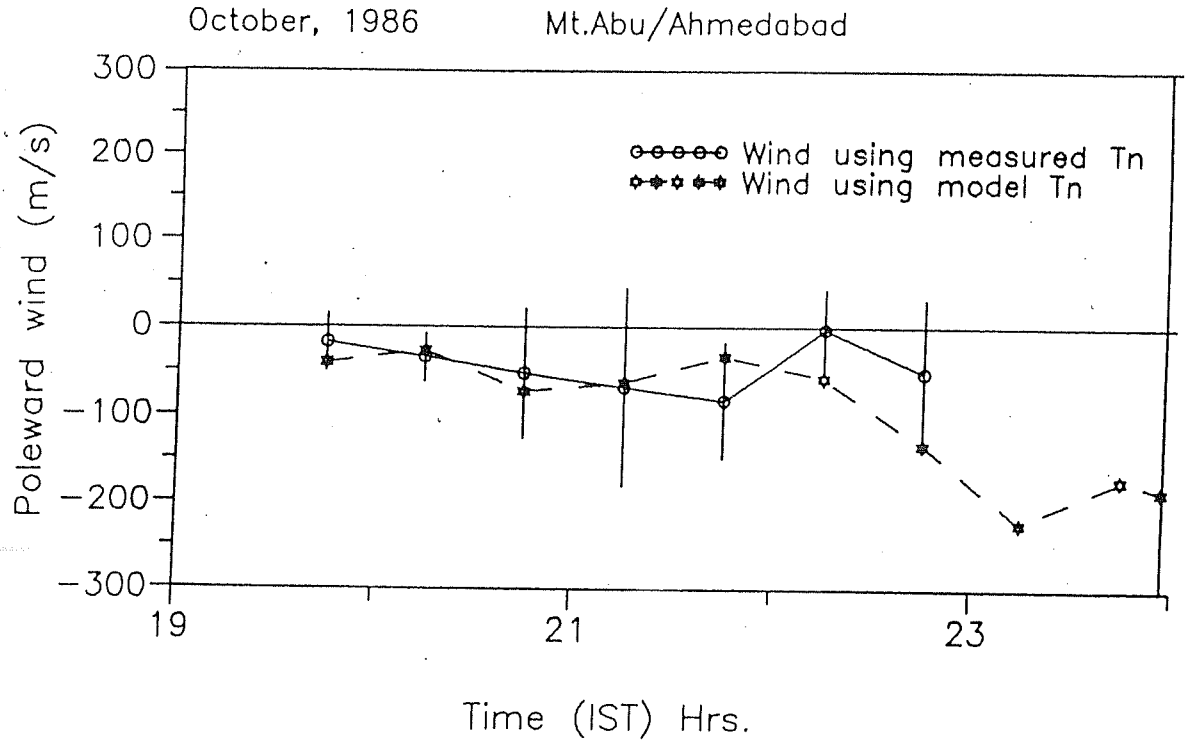

Fig. 5.6. Average derived meridional winds over Ahmedabad for October 1986, using the ionospheric data. Wind derived using measured T_n and those derived using model T_n are compared.

uses the model temperatures which slowly decrease throughout the night. This effect tends to get nullified if we consider the average picture since the increase in measured T_n is not observed on all nights and does not occur at the same time. Thus for gross, average, features, the winds derived using the atmospheric densities determined by the model temperature can be taken to represent the average nightly variations in thermospheric winds. However, for the individual case study approach, we stress the importance of observed neutral temperature and its variations which need to be incorporated in deriving meridional winds.

For the present study, we have also used the horizontal wind model (HWM) of *Hedin et al.* [1988] and the vector spherical harmonic model of *Killeen et al.* [1987]. The HWM is an empirical model based on wind data obtained from the AE-E and DE 2 satellites. A limited set of vector spherical harmonics has been used to describe the zonal and the meridional components of horizontal wind. A modified version of the model is now available [*Hedin et al.*, 1991]. The VSH model is based on the output from a set of runs of the NCAR Thermospheric-Ionospheric General Circulation Model (TIGCM) [*Dickinson et al.*, 1981] generated on the Cray supercomputer in Boulder, Colorado. An advantage of the VSH model is that the geophysical fields of interest can be obtained over a wide range of solar-geophysical conditions, even on a computer with modest storage requirements. These models are more commonly used nowadays among the upper atmospheric researchers, since they not only provide an understanding of the spatial and temporal variation of the geophysical parameters but also help in testing them against the direct measurements available and thereby aid further understanding.

The average derived winds and their variations for the seasons (post-equinox and winter) under study are depicted in Figs. 5.7a to 5.7d, the post-equinoctial months being October and November (belonging to years 1986 and 1988 respectively) and

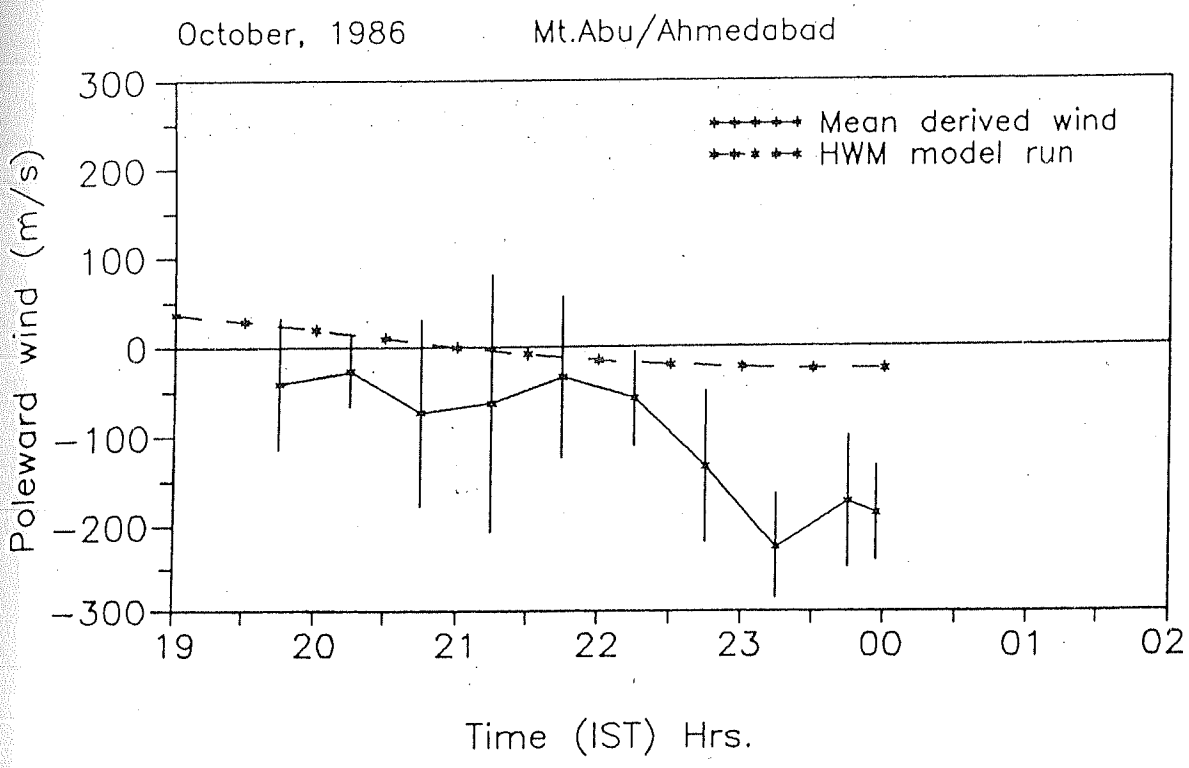

Fig. 5.7a. Nocturnal variation of derived meridional winds over Mt. Abu/Ahmedabad averaged for October 1986. The horizontal wind model (HWM) prediction is shown for comparison.

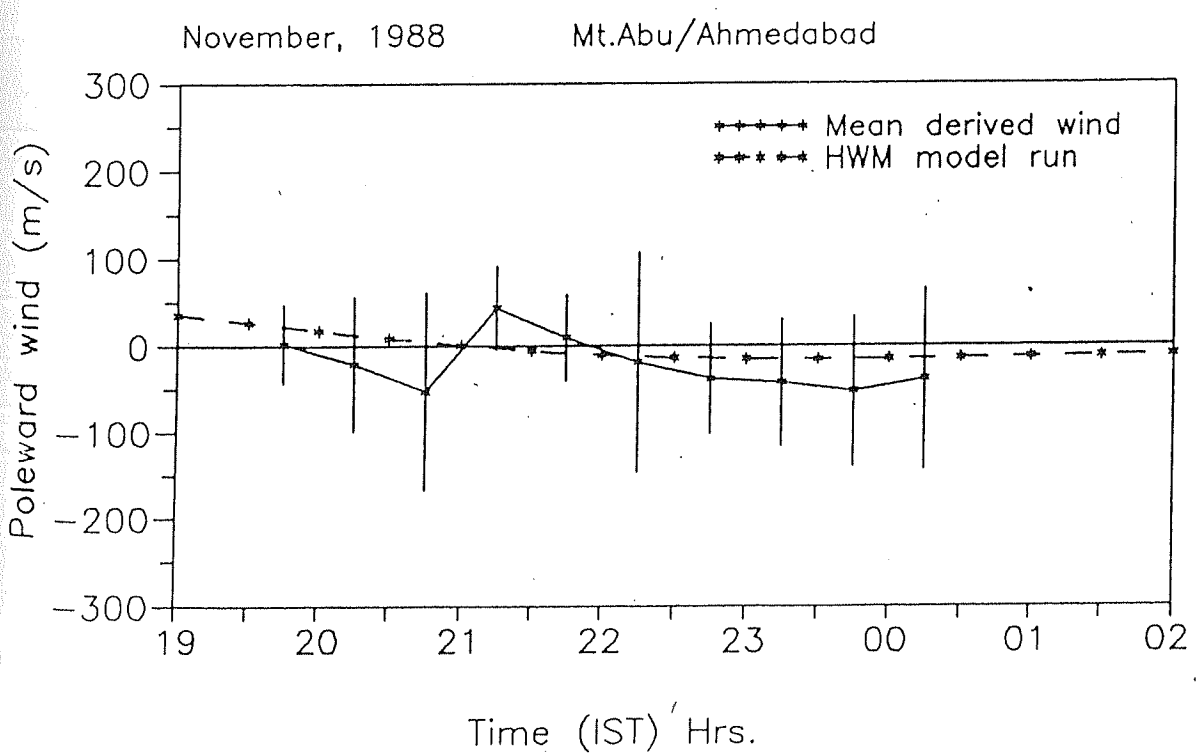

Fig. 5.7b. Same as above but for November 1988.

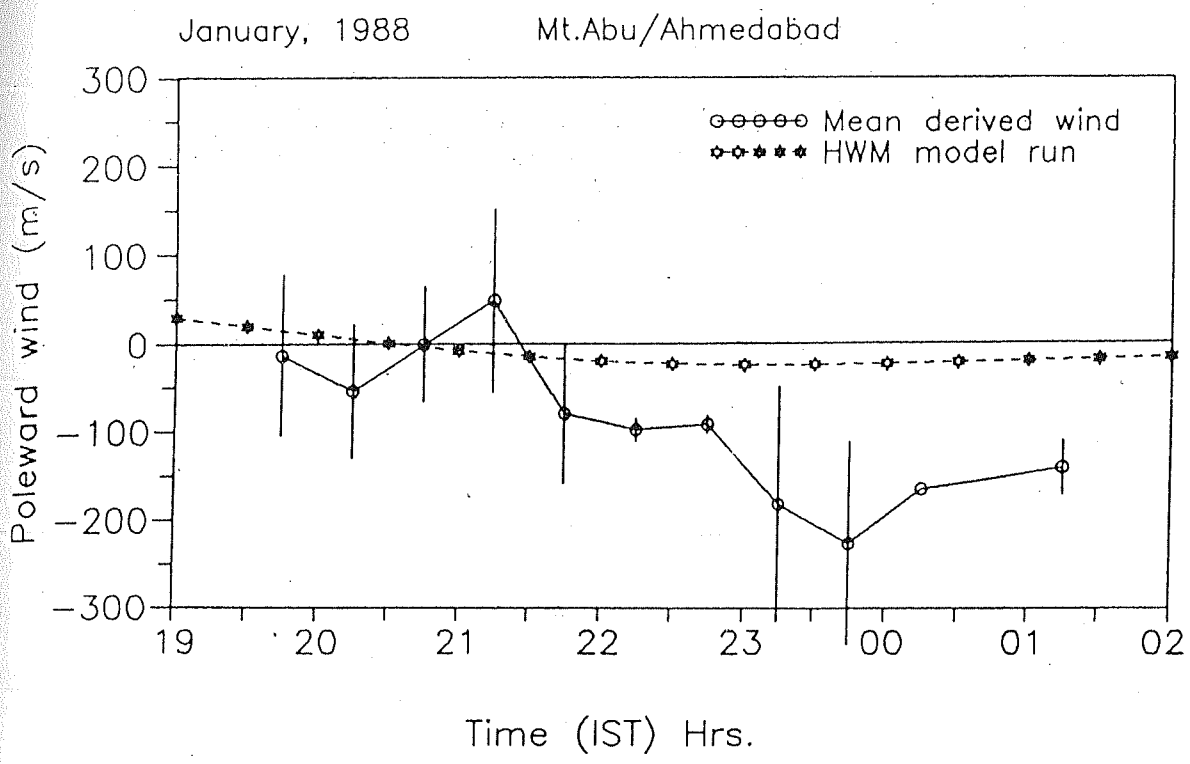

Fig. 5.7c. Same as Fig. 5.7a but for January 1988.

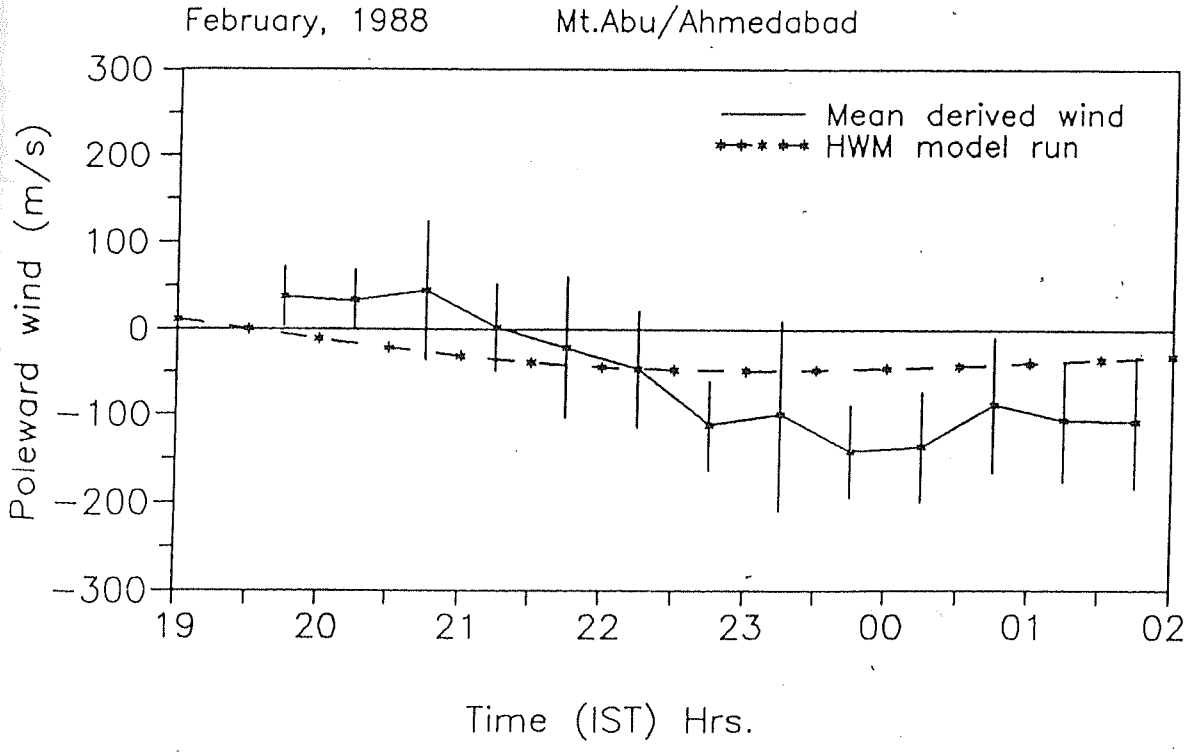

Fig. 5.7d. Same as Fig. 5.7a but for February 1988.

the winter months being January and February (1988). Due to the limitations in the availability of ionospheric data for this epoch, we have selected only four months for this exercise, the average number of nights for each month being only 6. The data belong to quiet geomagnetic conditions. For each of these months, the horizontal wind model is run, and the result is also depicted along with the average variation of estimated winds. The vertical bars represent the night-to-night variations in the derived winds.

Figs. 5.7a and 5.7b show the variation of average derived meridional winds for the months of October (1986) and November (1988). In the post-equinoctial period, the winds exhibit considerable deviations from the model predictions in October, 1986, while the agreement is reasonably good during November, 1988. During October, as discussed earlier, the equatorward wind becomes very large and shows maximum amplitude ($\sim$ 200 m/s) at about 2315 h. The wind shows a constant speed of $\sim$ 50 m/s near midnight in the month of November.

Similar variations are seen in the winter months of 1988. The HWM yields small equatorward wind speeds of less than 30 m/s throughout the night, in January. A strong transequatorial flow (from the southern hemisphere) is expected to get superposed over the normal equatorward wind and the net result is a weak equatorward wind. Though a transition is seen from the poleward to the equatorward flow, the estimated wind magnitudes are significantly higher than the model values, near and after midnight. The smallest vertical bars indicate the sparsity of ionograms available during the particular time slot, while the largest error bars indicate the large day-to-day variations in the derived wind at 1σ level. The average picture that emerges for these two seasons is that there exists a poleward or a small equatorward wind in the early part of the night which then becomes an equatorward wind of large magnitude (150 to 200 m/s) near midnight. There are not much differences in the wind variabilities between the two seasons, the overall features remaining similar.

Before we discuss about the seasonal variations exhibited by direct measurements of meridional winds, a few comments assume significance regarding the results presented above. They are only a few examples selected during the solar minimum years 1986–1988 to show the sort of variations the meridional winds undergo for the two seasons (post-equinox and winter). Though it had been demonstrated earlier that during this solar epoch, the use of model temperatures instead of the measured ones does reasonably represent the actual conditions, these would not be valid during the solar maximum period when the swings in the observed temperature variations are significantly larger as has been shown in Chapter 3 (section (3.5)). This is illustrated by examples shown in Figs. 5.8 and 5.9. In Fig. 5.8, the direct measurements for 17 February 1991 are compared with winds estimated for the two cases discussed earlier. The estimates using measured T_n are seen to follow closely the measured meridional winds than those using model T_n implying the importance of temperature variations in influencing the derived winds. There has been a systematic difference in wind magnitudes between the two estimates in the time sector 2000–2200 h. While the estimated wind with measured T_n determining the balance height h_o does show the transition to poleward as exhibited by the direct measurements, the wind with model T_n continues to blow equatorward. The large differences between both the estimates and the measurments in the late night hours are due to electric fields not being taken into account while deriving the meridional component of the neutral wind.

Fig. 5.9 depicts the average variations exhibited by direct measurements and the estimates based only on model temperatures for the month of December 1989. The vertical bars attached to each data point in the case of measured mean winds indicate the night-to-night deviations in the observations. On comparison between the two, significant differences are evident especially in the 2200–0000 h sector. The average observed wind had become poleward at about 2230 h whereas the derived wind remained equatorward with a magnitude of $\sim$ 100 m/s. There are differences

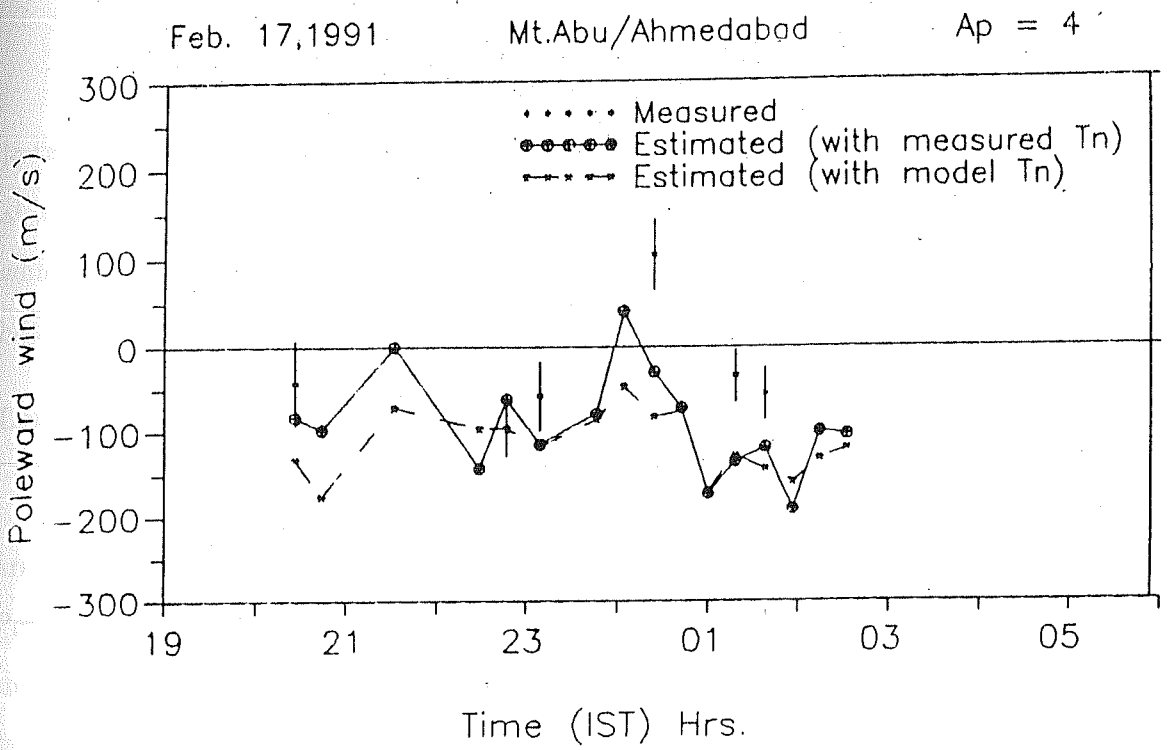

Fig. 5.8. Comparison of meridional winds derived using ionospheric data for the two cases, namely, those with measured T_n and those with model T_n, with spectroscopic measurements of meridional winds for 17 February 1991. The significant effect of measured neutral temperatures in influencing the derived winds may be noted.

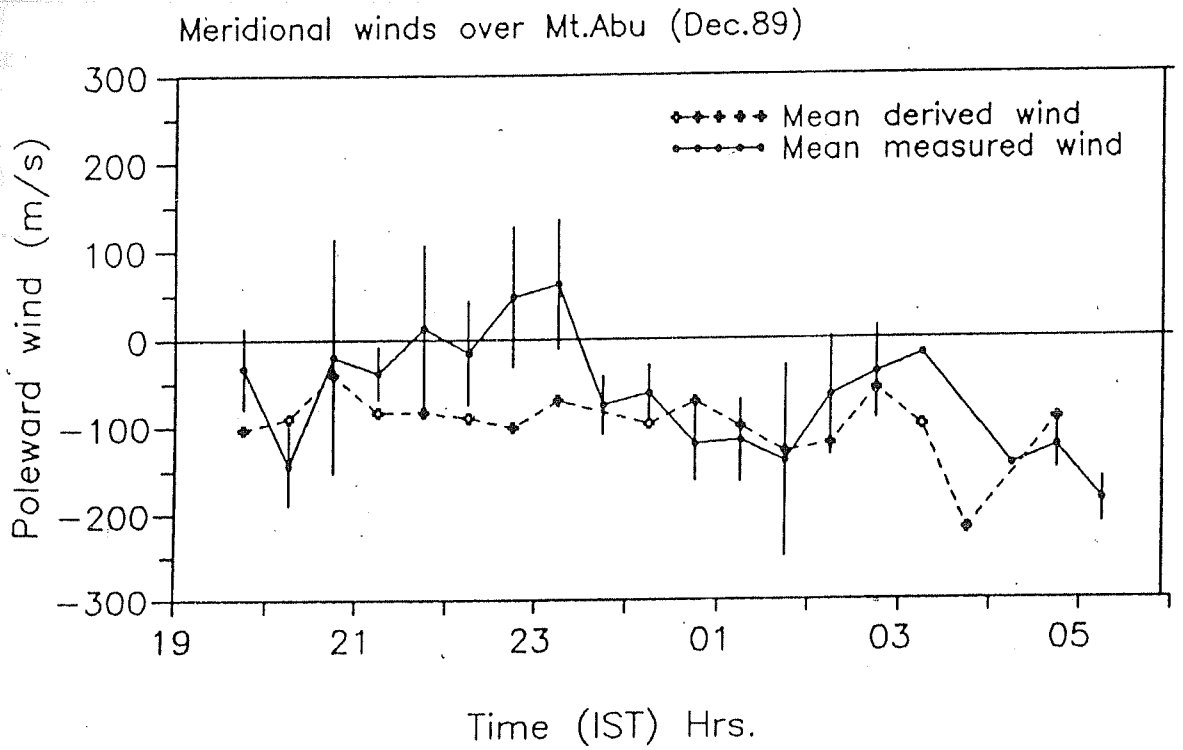

Fig. 5.9. Comparison of derived winds based only on model temperatures with direct measurements for December 1989.

in the early morning hours as well. These examples strengthen the conclusion arrived at in the last section that the effects of temperature variations need to be incorporated while deriving meridional winds from the ionosonde data at least during periods of high solar activity.

Long-term variability of measured meridional winds

As had been mentioned earlier, the direct measurements of meridional winds are being made since the winter months of 1989. The required stability of the Fabry Perot etalon is about 0.1° C for useful data on line-of-sight winds. Though the thermal stability of the etalon has been achieved upto this desired limit, during certain campaigns, the drifts observed have been very large and the data belonging to these measurements are not considered for analysis. Even on nights when we could maintain the required stability, the intensity of 6300 Å happened to be too low during the early night period and exhibited fast variations during subsequent times calling for extreme care in selecting the line profiles for analysis. Due to these various reasons, we have a limited data base on direct measurements of neutral winds. In spite of this limitation, important results and conclusions have still been arrived at, and these will be discussed shortly.

Fig. 5.10 shows an example in which the measurements of meridional wind made on 28 December, 1989, from Mt. Abu are compared with the VSH and the HWM model runs. The VSH model prediction for this night indicates a poleward wind all through the night implying a transequatorial flow of air originating in the southern (summer) hemisphere. The HWM model predicts a small equatorward velocity ($\sim$ 30 m/s) around midnight. The measurements show a wavy pattern of a periodicity of about 4 hours, the magnitude and the direction differing significantly from the models. The possibility of sources of such large deviations of the observed values from the model predictions will be discussed later.

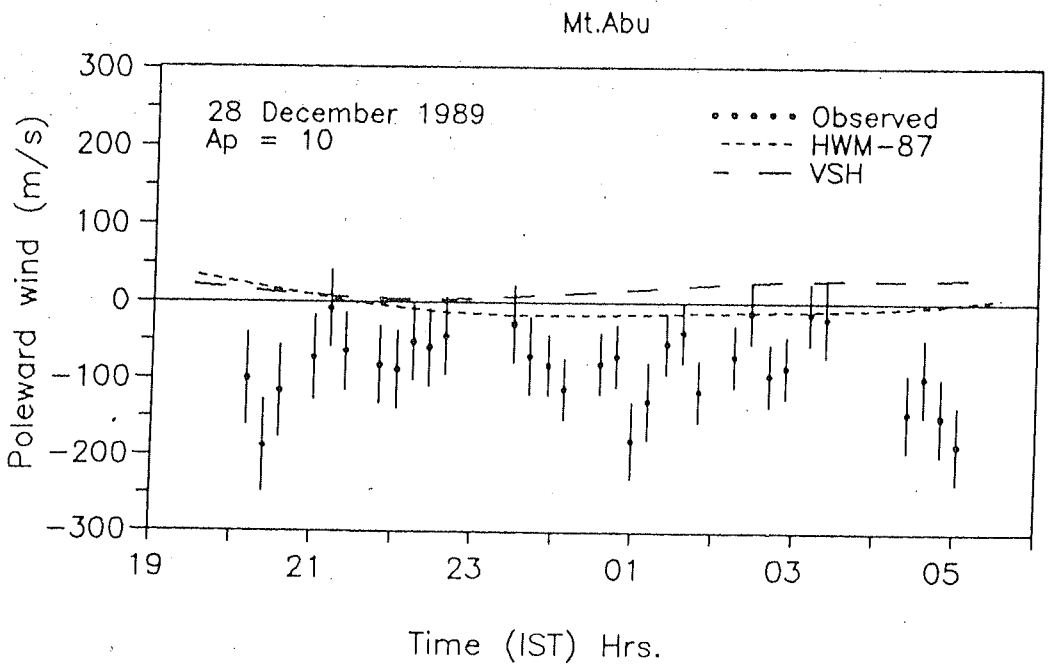

Fig. 5.10. Comparison of measured meridional wind with HWM and VSH model results for 28 December 1989.

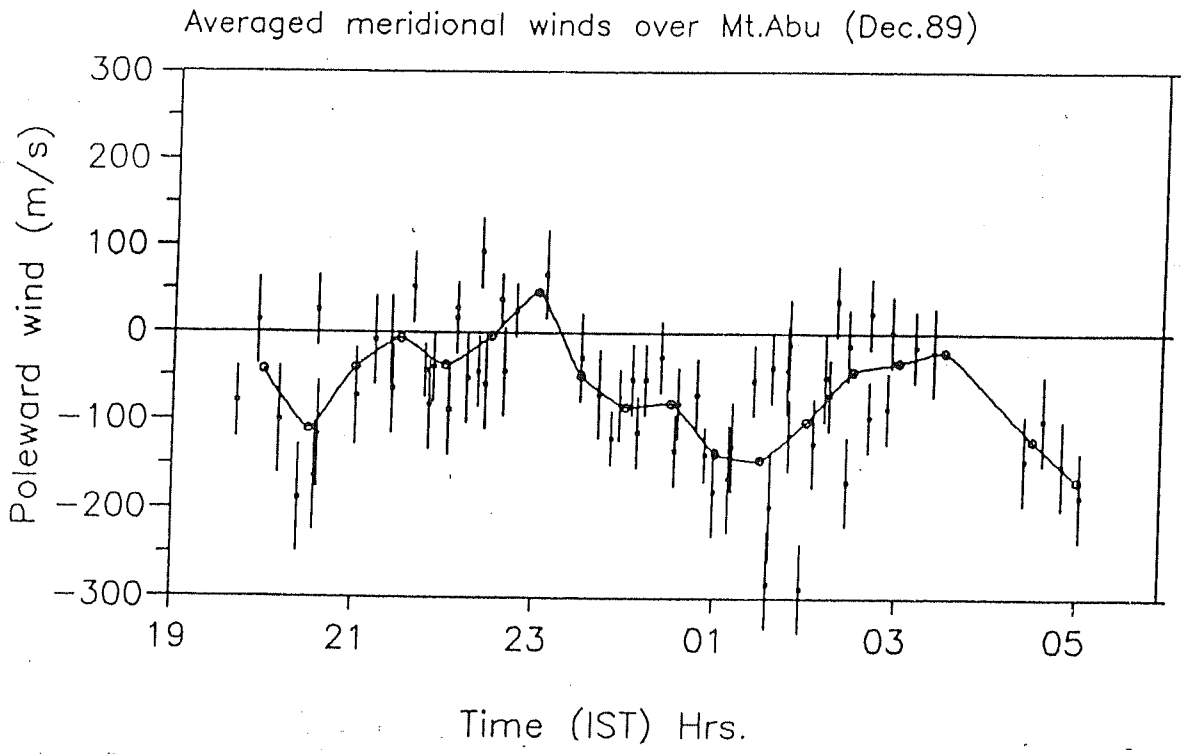

Fig.5.11a. Nocturnal variation of measured meridional winds from Mt. Abu for December 1989. Individual spectroscopic measurements are plotted here. The continuous curve depicts the average values of data points put in slots of half an hour duration.

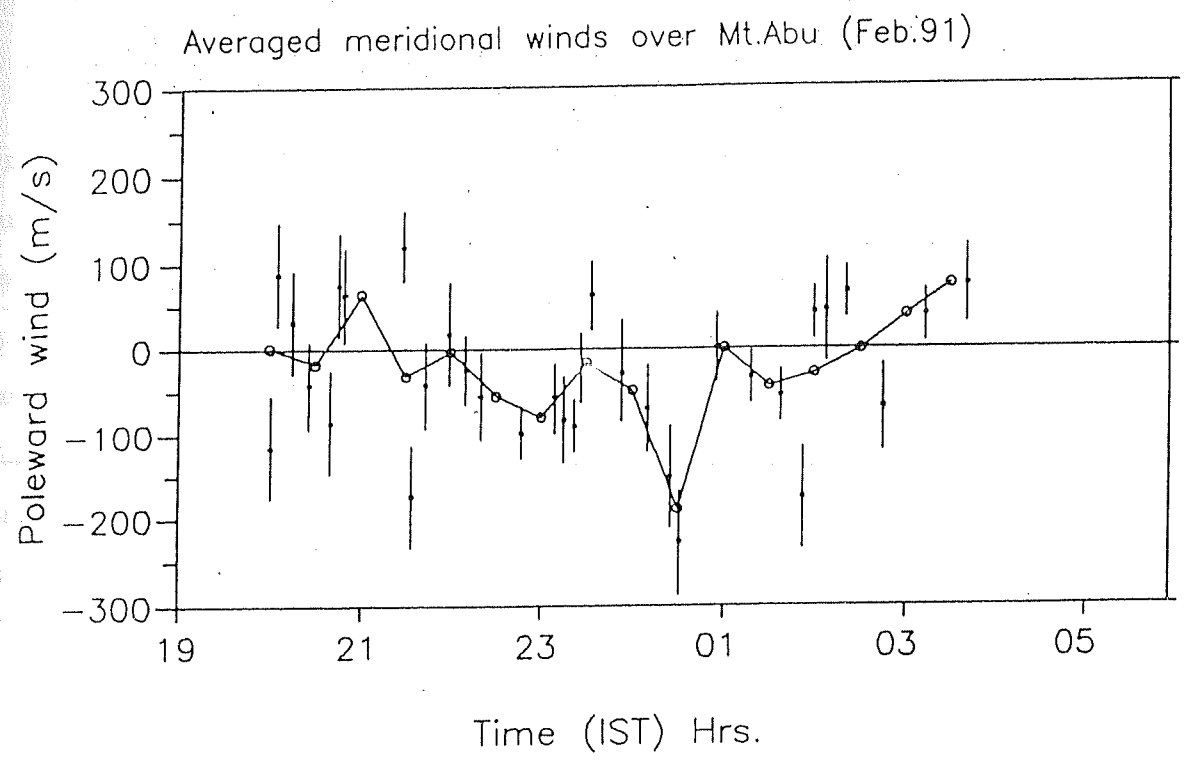

Fig. 5.11b. Same as Fig. 5.11a but for February 1991.

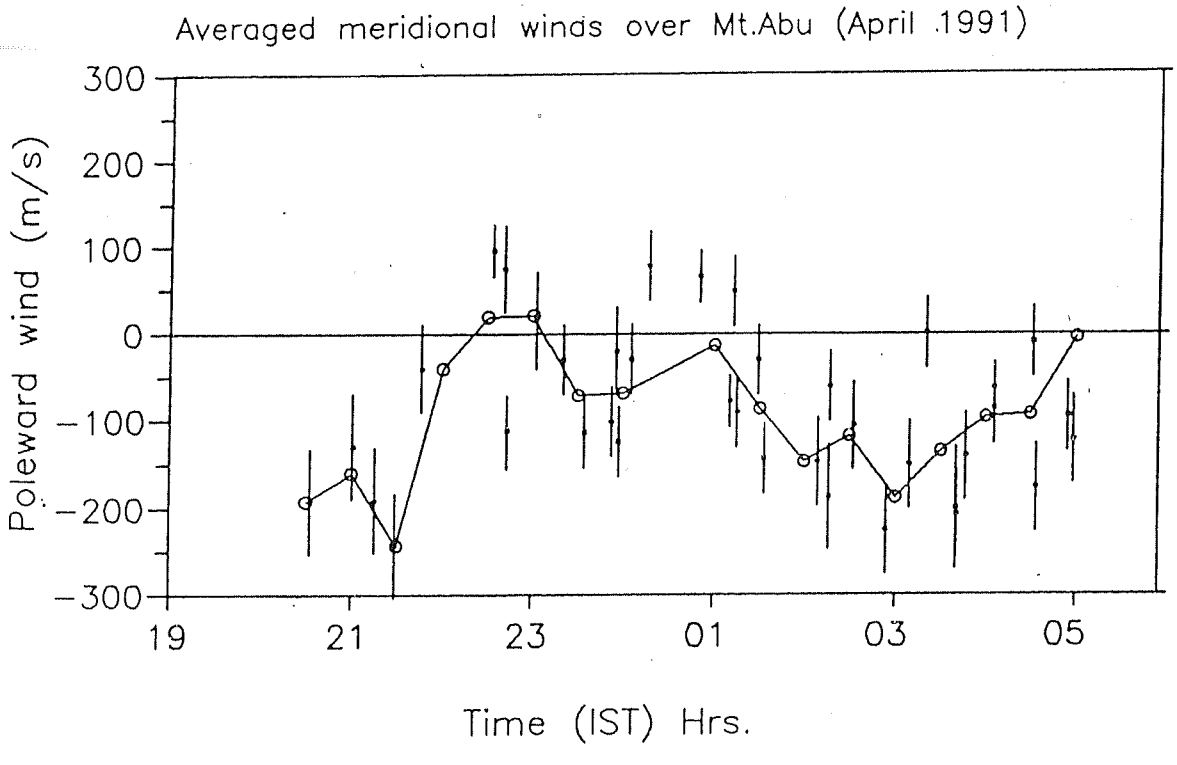

Fig. 5.11c. Same as Fig. 5.11a but for April 1991.

We shall be deviating from the case study approach we have adopted till now, and look at the gross features indicating the response of the thermosphere to the underlying forcings. For such a study, it is necessary that the number of measurements is large enough to draw any meaningful statistical inference. Adopting a criterion of at least 30 individual measurements needed from a campaign, we have selected three months, namely, December (1989) and February (1991), and the equinox month of April (1991). The total individual measurements (data points) run upto about 140, the largest of 65 being in the December month. The method of averaging is the same as described earlier. The results are shown in Figs. 5.11a, 5.11b and 5.11c for these three months. Individual measurements are also shown so that the day-to-day variabilities become evident. A first look at these figures indicates that the measured winds are largely in the equatorward direction. Though the day-to-day variations are significant, still a systematic pattern emerges for each of these months.

The results for December 1989, are depicted in Fig. 5.11a. The average A_p value during this moderately disturbed period had been 19, the lowest being 10 on 28 December and the highest being 26 on 22 December. There had occurred a geomagnetic storm on 29 December with A_p value of 50. We have not considered the data belonging to this day, which incidentally happened to be the last day of the campaign during this month. For the remaining period, we can safely assume the geomagnetic activity to be moderate to low.

With the exception of large variability following sunset hours, the winds fit into a pattern during December 1989. From a large equatorward wind (of about 100 m/s), the average wind either approaches small equatorward or turns poleward between 2100 to 2300. From 2300 h onwards, the equatorward wind gains in magnitude and reaches its highest amplitude of $\sim$ 150 m/s at about 0130 h. There is a tendency to become poleward at 0300 h after which the wind becomes equatorward once again.

Let us look into the wind pattern for the month of February (1991), depicted in Fig. 5.11b. This has been a geomagnetically quiet period (average A_p value for the period of observations during this month being 10). The day-to-day variability is large for this month when compared to other months. However, a closer look suggests that it is not much different from the average picture that has emerged for the month of December. The mean wind in February is poleward around 2100 h which then gradually becomes equatorward. Since the largest changes in intensity occur around midnight and immediately after, the number of measurements is less during this period. However, there is a clear transition to poleward at about 0300 h, the trend being similar to the one that occurred during December. These might be the characteristics of a winter season.

The variation for the month of April (1991) is depicted in Fig. 5.11c. This also has been a geomagnetically quiet period (average A_p value for the period of observations during this month being 9). In this month also, the winds tend to follow an established pattern. A large equatorward wind often occurs in the early night hours which then reduces in magnitude, sometimes becoming poleward at about 2300 h. At about 0300 h, the average wind reaches its highest amplitude of about 175 m/s after which the wind decelerates. An important point to be noted here is that the time at which the equatorward wind attains the maximum speed is $\sim$ 2 hours later when compared to December and February months.

Even with a limited data base representing winter and equinoctial periods, there emerges systematic behaviour of thermospheric winds in these two seasons. In both the seasons, the wind makes its transition to poleward for a brief period at about 2300 h. In the winter months, the equatorward wind reaches its highest value at about 0100 h while during the equinox period, the maximum equatorward wind occurs at about 0300 h exhibiting a shift in phase of about 2 hours.

It is worth comparing the seasonal behaviour of winds over Mt. Abu with that at other latitudes. At Cachoeira Paulista (22.7°S, 45°W, geographic; 16°S dip latitude), Brazil, during winter months, the wind velocities are poleward early in the night, reduce to zero around midnight and change to poleward again. During the spring-equinox period, the average winds are largely equatorward in the pre-midnight hours which then reduce in magnitude to zero around 0100–0200 h [*Sahai et al.*, 1992]. They report that the wind patterns are similar to those predicted by HWM-87 and HWM-90 and apart from some discrepancies in absolute magnitudes, the trends appear to agree. Considering that their observing location is situated within the purview of equatorial ionospheric and South Atlantic magnetic anomalies, their result that the wind patterns are in overall agreement with HWM models needs to be considered carefully. *Biondi et al.* [1991] have compared the winds over Arequipa (16.5°S, 71.5°W, geographic; 3.2°S dip latitude) with those observed at Arecibo (18.6°N, 66.8°W, geographic; 30°N dip latitude). The early night winds during winter at both the locations are weakly poleward, reversing direction in the later part of the night, conforming with the expected nocturnal pattern. At Arequipa, the data during equinox periods indicate a large equatorward wind in the early part of the night which then dies down to zero around midnight and again becomes weakly equatorward in the late night. *Biondi et al.* [1991] have compared the winds over Arequipa with the airglow data of *Burrage* et al. [1990] and the findings are in agreement with the sense of a general transequatorial flow at the solstices. From these results it is difficult to construct a coherent picture for all the low latitude stations located at different longitudes.

Biondi and Sipler [1985] observed some unusual features in the flow of thermospheric winds and the temperatures over Natal (5.9°S, 35.2°W, geographic; 6.4°S dip latitude) identical to those observed earlier in midlatitude studies [*Hernandez*, 1982c]. On a particular night of 26 August 1982, they have observed convergence in

meridional wind between 2100 to 2330 UT accompanied by a downward wind and an associated temperature increase. The geomagnetic activity had remained low and hence their effects can be ruled out. Owing to the renewed interest by the work of *Raghavarao et al.* [1991, 1993] wherein one of the first direct experimental evidence for the presence of Equatorial Temperature and Wind Anomaly (ETWA) colocated with the EIA, the EIA and its associated effects on thermospheric circulation have become relevant. The meridional wind measurements from Mt. Abu appear to provide credence to the hypothesized circulation cells associated with ETWA getting set up. We shall be discussing this process and the relevance of our measurements in detail in the next chapter.

To conclude,

- The predictions made by the wind models, namely, HWM and VSH, do not agree with the observations from low latitudes.
- The observed features are considerably different from those reported from other latitudes showing significant longitudinal difference.

Chapter 6

Large scale geophysical processes over low latitudes

The geophysical processes that have direct relevance to the low latitude thermosphere-ionosphere system are (1) the midnight temperature maximum and (2) the equatorial ionization anomaly (EIA) associated processes. The influence of each of these processes is only beginning to be understood now as more and more evidences like equatorial temperature and wind anomaly, the midnight abatement of equatorward wind observed at low latitudes, etc., that show the interactive dynamical coupling between the thermosphere and the ionosphere, are coming up. In this section, we do not intend to give a complete background to the basic phenomena listed above, rather we shall provide a brief review on the current understanding of these processes drawing examples from the present study whenever possible, and present some of the results we have obtained in this regard.

6.1 The midnight temperature maximum

The first manifestation of the midnight temperature maximum was brought out by the airglow observations carried out during an expedition along the Pacific coast of South

America [*Greenspan*, 1966]. The subsequent work by *Nelson and Cogger* [1971] who observed 6300 Å airglow enhancements at Arecibo, and *Behnke and Harper* [1973] who inferred an abatement of equatorward wind using the incoherent scatter radar at Arecibo, arrived at the same conclusion, that a single physical process, namely, the midnight temperature maximum (MTM), is responsible for these observed features. Using the Jicamarca incoherent scatter radar situated at 12 degrees south of the geographic equator, *Bamgboye and McClure* [1982] inferred from ion temperature measurements, the seasonal behaviour of the occurrence of the MTM. *Herrero and Spencer* [1982] confirming the earlier results, generated maps of thermospheric temperatures at four different altitudes and for four seasons that showed the horizontal distribution of the MTM within a latitudinal belt of $\pm$ 20° centered about the equator. They have used the AE-E measurements of gas kinetic temperature [*Spencer et al.*, 1973]. Optical observations using Fabry Perot Spectrometer by *Sobral et al.* [1978], *Herrero and Meriwether* [1980], *Friedman and Herrero* [1982], and *Burnside et al.* [1983] supported the inferences made earlier that the neutral temperature near the geographic equator shows a maximum at about midnight. Following the direct *in situ* measurements of this feature by the NATE experiment on board AE-E satellite [*Spencer et al.*, 1979], *Mayr et al.* [1979] formulated a theory based on tidal phenomena to explain the observations that holds till today. A brief account of their theory is given below.

The thermospheric tides at F region heights is basically diurnal in nature, driven *in situ* by the solar EUV radiation. The resulting meridional winds are generally poleward during the day and equatorward during the night (especially during the equinox). Near the equator, the zonal winds are responsible for transporting energy and momentum from the dayside toward the night side. The neutral air motions at thermospheric heights are slowed down by their frictional interactions with ions. This ion-neutral momentum coupling is responsible for the generation of semi-diurnal tides

and hence the midnight temperature maximum. As the physical reasoning goes, the larger ion density during the day impedes the wind motion and an increase in temperature is expected to develop since the energy does not get transported efficiently toward the nightside. A lower ion density during the night leads to greater speeds of neutral winds which leads to more efficient deposition of energy and momentum on the nightside and this gives rise to a larger temperature there than what normally is expected. The result is the generation of a semi-diurnal component in the variation of neutral temperature on a given day. Similarly, a semi-diurnal wind component, on its interaction with the diurnal variation of ion-drag, is expected to give rise to a terdiurnal component in the temperature variation and so on. The variability in the tidal modes accounts for the lability of the MTM.

Fig. 6.1 shows a block diagram illustrating these interactions that lead to the observed anomaly in the midnight temperature. The semi-diurnal tide of the upper atmosphere is due to the tidal waves originating in the lower atmosphere (for example, the semi-diurnal tides generated due to the ozone and water vapour absorption of solar UV radiation) and propagating upwards and also due to the momentum coupling associated with the diurnal variation in the wind field and ion density. *Mayr et al.* [1979], with the above conception of basic interactions between the neutral wind field and the large diurnal variations in ion density, obtained theoretical results that are in close agreement with the observed MTM. Fig. 6.2a shows an example of this observation from a particular orbit (6431, Day 77041) of the AE-E satellite which indicates that the magnitude of the MTM at a latitude of about 17°S in this example, can sometimes be as large as the principal daytime maximum. The behaviour of the meridional wind as revealed by the data from orbit 9261 (Day 77217) of the AE-E satellite is depicted in Fig. 6.2b. The equatorward wind (positive velocity) reached its maximum speed at about 2200 h local time and the reversal occurred at midnight and at about 16°N latitude.

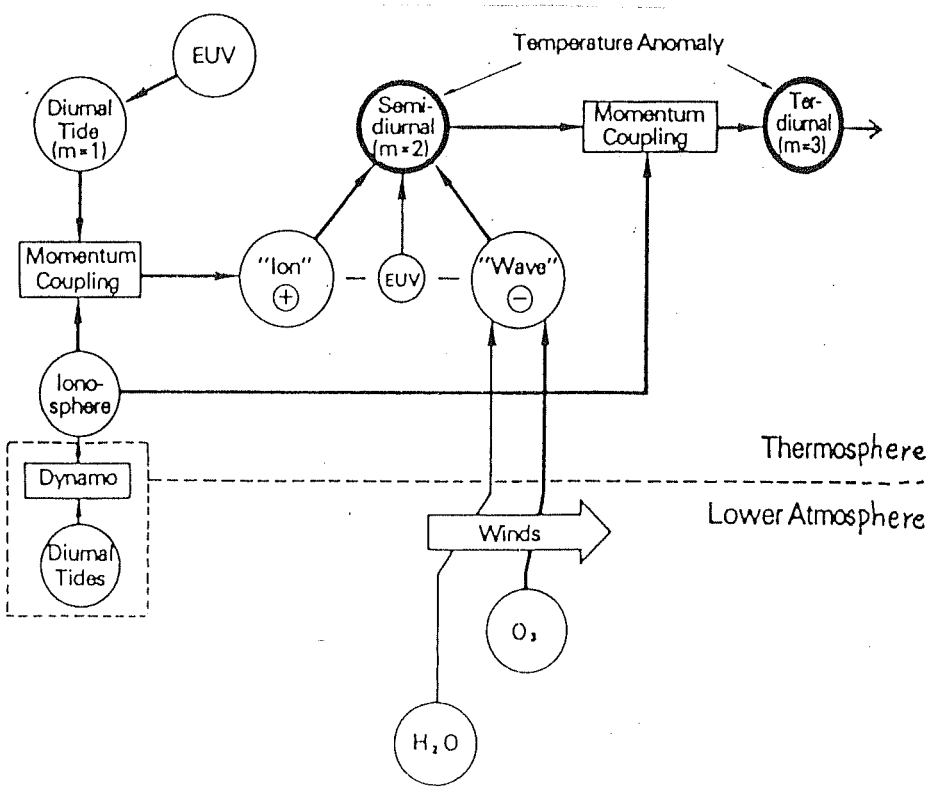

Fig. 6.1. Schematic of physical processes that lead to midnight temperature maximum (MTM) near the geographic equator. (after *Mayr et al.*, 1979)

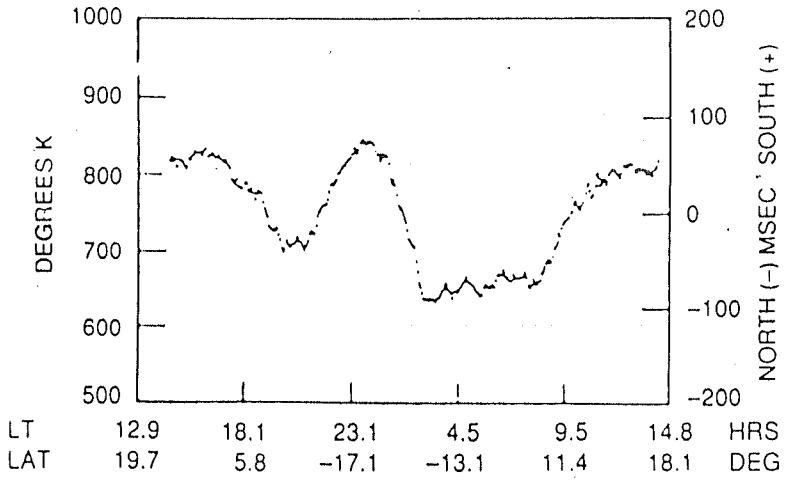

Fig. 6.2a. An example illustrating the observed midnight temperature maximum (MTM). The data belong to orbit 6431 (Day 77041) of the AE-E satellite pass. (after *Herrero et al.*, 1993)

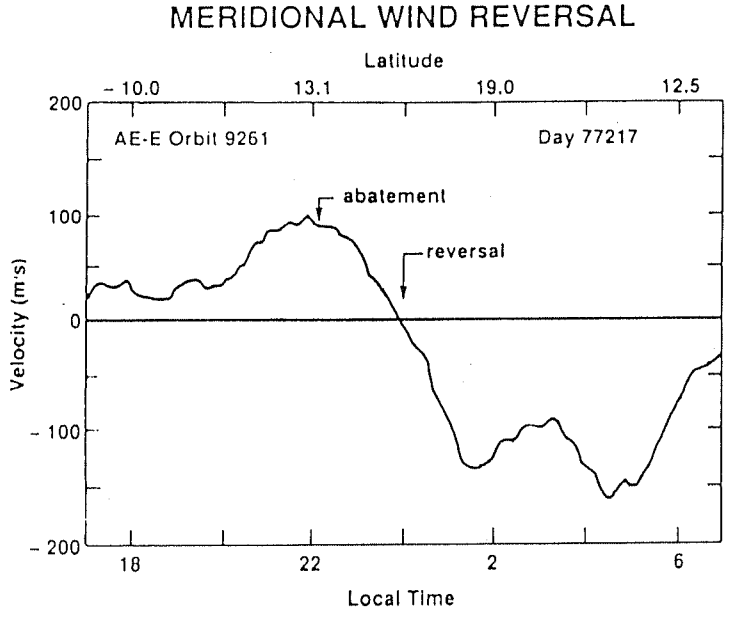

Fig. 6.2b. The meridional wind (positive southward) feature illustrating the occurrence of MTM. The data belong to orbit 9261 (Day 77217) of the AE-E satellite pass. (after *Herrero et al.*, 1993)

Two temperature maps of AE-E data obtained by *Herrero and Spencer* [1982] are depicted in Figs. 6.3a and 6.3b. The temperatures measured from 1700 to 0600 h LT in all the passes during the summer period in the northern hemisphere have been averaged to obtain the two dimensional horizontal distribution of the thermospheric nighttime temperature maximum (shown as shaded contours). These two maps correspond to two different heights, namely, 250 and 350 km respectively. The V-shaped feature in the MTM is represented well in the top panel of this figure. At 250 km altitude, there occurs a pronounced maximum near the equator, which then shifts to northern latitudes first. The maximum appears in the southern hemisphere too about 2 hours later. However, the bottom panel, which represents the distribution of temperatures at 350 km altitude does not reveal this feature clearly. The maximum at the equator is not well pronounced and there arise secondary maxima in the late night hours both in summer and winter hemispheres. The presence of the secondary maxima may be attributed to the dominance of higher order tidal modes. The absence of the MTM at the equator suggests that either the disturbance does not reach this altitude propagating from below or some other process (whose role is equivalent to a dominant term among the higher order modes) acts in opposition to the development of temperature anomaly. However, at equinoxes, the MTM is quite prominent at the equator at altitudes as high as 370 km and this is clearly seen in the temperature maps of *Herrero and Spencer* [1982].

The consequences of the MTM on the dynamics of the thermosphere-ionosphere system are many. The abatement of the equatorward wind and its reversal are regular features in the low latitude sector [*Behnke and Harper*, 1973; *Friedman and Herrero*, 1982; *Burnside et al.*, 1983; *Herrero et al.*, 1988]. The F layer responds to these changes in wind and moves downward as the equatorward wind abates. One of the means of inferring this vertical motion is the monitoring of 6300 Å airglow intensities [*Nelson and Cogger*, 1971; *Sobral et al.*, 1978; *Herrero and Meriwether*, 1980].

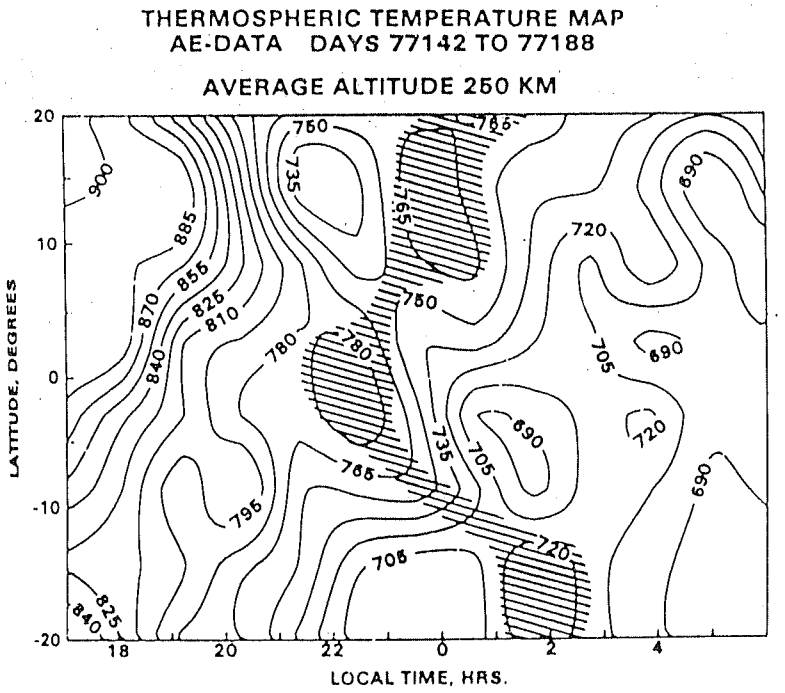

Fig. 6.3a. Thermospheric temperature map obtained by the AE-E satellite for the solstice period (summer in the northern hemisphere) of 1977 for an average altitude of 250 km. (after *Herrero et al.*, 1993)

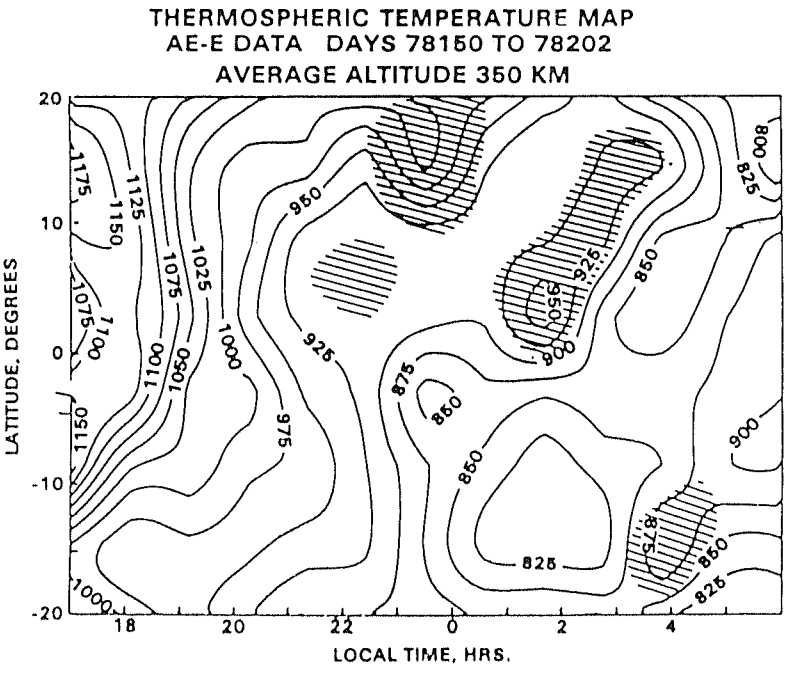

Fig. 6.3b. Same as above but for an altitude of 350 km.

A collapse of the F layer increases the recombination rate of molecular oxygen ions and electrons, and hence the emission rate of 6300 Å line increases. Another effect which becomes prominent during geomagnetic storms at midlatitudes, is the meridional intensity gradient (MIG) in the 6300 Å airglow intensity. An interaction of the winds associated with geomagnetic disturbances, with those of MTM leads to a zone where both the processes are equally important. In this region, sharp changes in F layer height are observed which gives rise to the observed intensity gradient in the magnetic meridian [*Herrero and Meriwether*, 1980].

The tidal theory of *Mayr et al.* [1979] is quite satisfactory in reproducing the observed phenomenon of MTM with respect to seasons. However, there are certain unexplained features like the absence of MTM over the equator at 350 km altitude, that need detailed investigation for a better understanding of thermospheric structure and dynamics during nighttime in the equatorial and low latitude regions.

Meridional winds from equatorial and low latitudes

In this context some of our results on the meridional winds from the region of EIA and as well as the winds derived from using two ionosondes one right over the dip equator and the other slightly away, are important. The movement of the F layer over the dip equator is purely due to electric fields while at locations away from the equator, the effect of meridional winds also is present. Under certain valid assumptions [*Krishnamurthy et al.*, 1990; *Sekar and Sridharan*, 1992], meridional winds were estimated for a few occasions when direct measurements were available from Mt. Abu, during the months of February and April, 1991 [Somayajulu, personal communication].

Figs. 6.4a to 6.4e show the comparison of the winds measured from Mt. Abu and those derived for the low latitude station Sriharikota (SHAR) (13.7°N, 80.2°E,

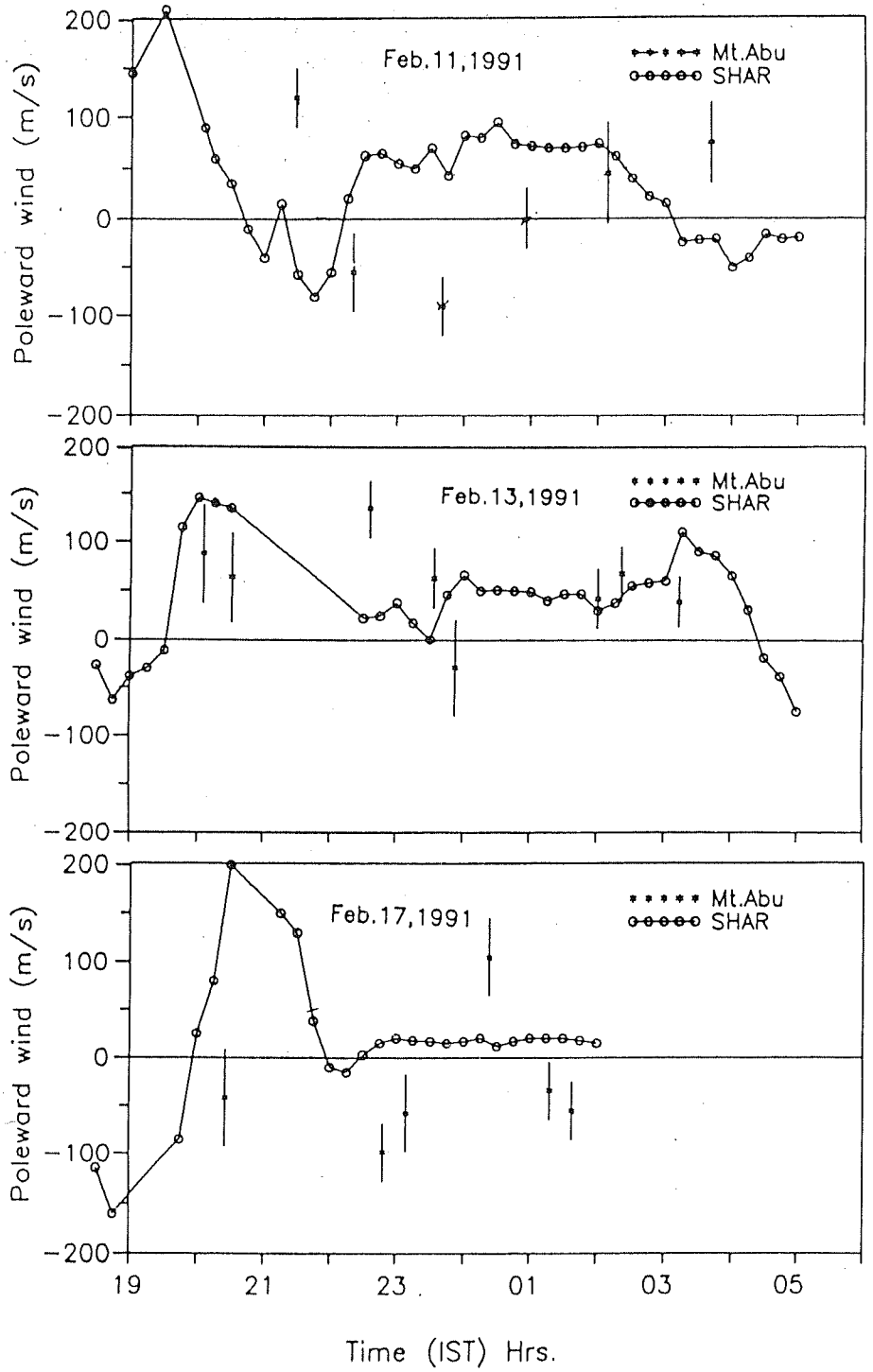

Figs. 6.4a,b,c. Comparison of the nocturnal variation of meridional winds from two latitudes: Mt. Abu (24.6°N geographic) and Sriharikota (SHAR) (13.7°N geographic) for 11 (top), 13 (middle) and 17 (bottom), February 1991. (*V. V. Somayajulu*, personal communication)

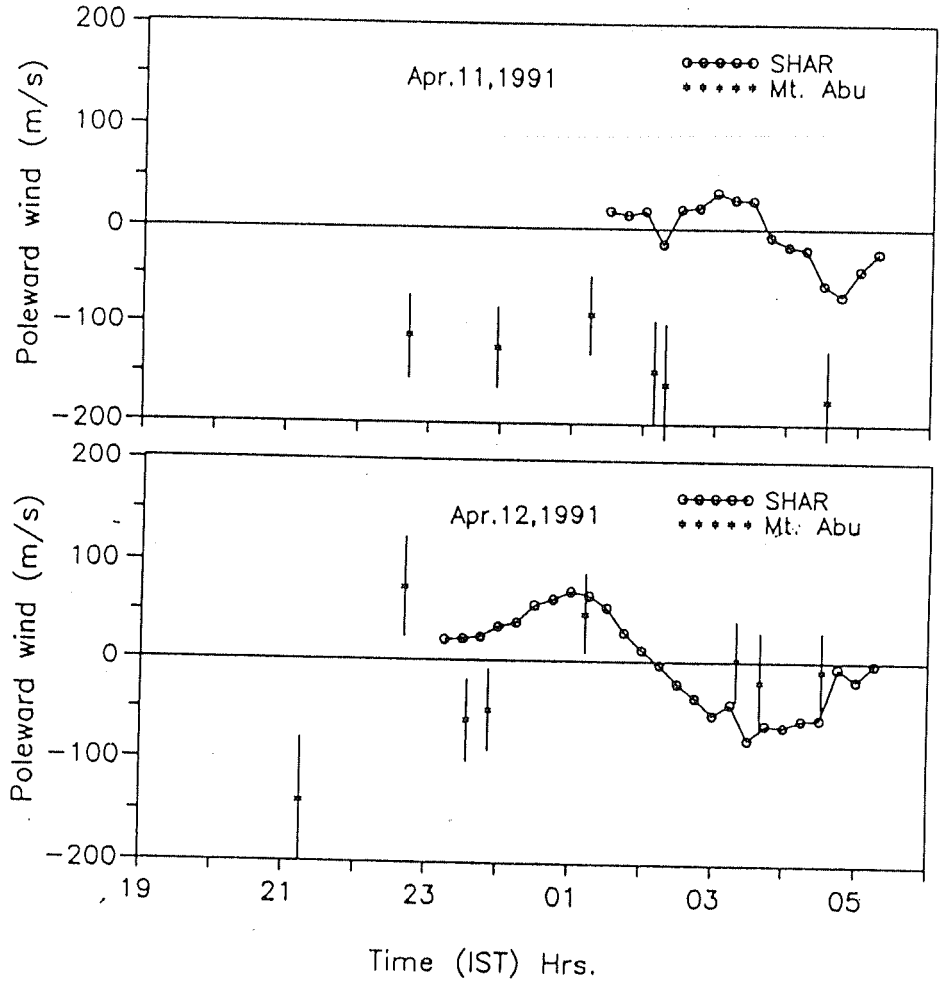

Figs. 6.4d,e. Same as Figs. 6.4a,b,c but for 11 (top) and 12 (bottom), April 1991.

geographic; 10°N dip). During February, there appears to be a systematic phase difference in the variabilities ranging from 2 to 4 hours and always the Mt. Abu measurements were lagging in phase. The preceding of the reversal to poleward wind over the equatorial zone indicates the source to lie over the equatorial zone. It is suggested to be due to the midnight pressure bulge and the temperature maximum prevalent near the equator. However, the situation is drastically different during April. The winds over Mt. Abu and SHAR show contrasting features on 11 April. The wind had been poleward over SHAR till about 0330 h when a reversal had occurred while equatorward winds of high velocities (100–150 m/s) have been observed over Mt. Abu on this day. On 12 April, the winds over both the places appear to be in phase. The comparison for the month of April does not reveal any clear phase difference between the wind velocities as had been noticed for the month of February, over two low locations separated by about 20 degrees dip angle. It is suggested here that during the equinoctial month of April, the EIA phenomenon might have had a dominant role to play in altering the wind patterns over the low latitude zone.

6.2 The EIA associated processes

The equatorial ionization anomaly manifests itself as the most persistent feature of thermosphere-ionosphere coupling. The F region of the ionosphere exhibits pronounced peaks of plasma density occurring on either side of the magnetic equator at dip latitudes between 10° and 20°. This feature is known to persist during most of the day often extending to nighttime. The interaction of plasma with horizontal electric and magnetic fields in conjunction with diffusion along magnetic field lines produces the crests of ionization at these latitudes and a resultant trough over the magnetic equator. The dynamo electric field of E region origin drives the F region plasma

vertically upward over the equator which then diffuses downward along the magnetic field lines [*Moffett*, 1979]. This action responsible for the equatorial ionization anomaly, produces significant effects on the ionosphere and the neutral thermosphere, and induces close interactions between them.

1. Behaviour of the post-sunset and nighttime F region at the crest location of EIA

The location of the ionospheric measurements made under the present sudy, i.e., Ahmedabad, is at a dip latitude of about 18°N and is situated very close to the northern crest of the EIA in the Indian zone. This presents an ideal situation for studying the close interaction between the crests of enhanced ionization and the neutral thermosphere which is believed to result in the anomaly in neutral temperature and zonal winds (ETWA), and to initiate additional meridional circulation. The diurnal development of the EIA and its dependence on season and the phase of the solar cycle have been well discussed in the literature [*Raghavarao et al.*, 1988; *Sastri*, 1990; and the references cited therein].

It has been observed by *Woodman* [1970] that the horizontal eastward electric field during sunset hours is often enhanced before its reversal. The causes of this enhanced horizontal electric field at the equator have been discussed and modeled by several workers [*Rishbeth*, 1971b; *Heelis et al.*, 1974; *Stening*, 1981; *Farley et al.*, 1986] based on the F region dynamo. The neutral winds at F region heights are now known to establish the F region dynamo action by its horizontal motion across the magnetic field over the equator [*Rishbeth*, 1971a; *Rishbeth*, 1981]. The horizontal F region winds drive net upward currents, which in the event of the decay of E region conductivity to very low values after sunset, produce vertical polarization fields that are responsible for the east-west plasma drifts. Recently, *Haerendel and Eccles* [1992] have pointed out the role of equatorial electrojet current near sunset in the post-sunset enhancement of the eastward electric field and the consequent vertical drift

over the magnetic equator.

The enhancement in the eastward electric field after sunset leads to large vertical plasma drifts at the equator thereby renewing the fountain action. When the electric fields are eastward, the ionization gets pumped upward that subsequently diffuses downward along the magnetic field lines to reach the crest locations of the equatorial ionization anomaly. Making use of the ionospheric data in the African zone, *Rao* [1963] first observed the occurrence of the strengthening of the anomaly in the time period 2000–2200 h, in the form of enhancements of ionization density near the crests. *Lyon and Thomas* [1963] studied the characteristics of the evening anomaly in the African, American and East Asian sectors. They showed that the enhancement of the anomaly during the evening hours is caused both by a reduction in $N_{\mathrm{m}}F_2$ at the equatorial trough and increases near the crests.

In a later study by *Sastri* [1982], the characteristics of the post-sunset feature of the EIA over the Indian sector have been brought out. Significant positive correlation has been obtained between the post-sunset rise of the F region and the depth of the anomaly (ratio of $f_{\mathrm{o}}F_2$ at the crest to that at the trough) on quiet days of summer and equinox periods. With a delay of 2 hours, the $f_{\mathrm{o}}F_2$ at the crest also shows a positive correlation with the evening rise of the F region at the trough (over equator). However, the comparison revealed a poor correlation during winter months. The presence of poleward winds which would not only strengthen the fountain action by bringing the ionization down along the magnetic field lines but also lead to increased loss of ionization at heights where recombination occurs at a faster rate, has been invoked to explain the poor correlation between the $f_{\mathrm{o}}F_2$ at the crest of the EIA and the rise of the F layer over the magnetic equator.

Before showing some of the results we obtained on the behaviour of the F region in the post-sunset hours over Ahmedabad, we reproduce the vector plots of

Hanson and Moffett [1966] in Figs. 6.5a and 6.5b that illustrate the fountain action. The results obtained by them from the solutions of the continuity equation for electrons in the F_2 region, were for vertical drifts of $\pm$ 10 m/s at the equator. The motion of the ionization flux at different heights with respect to the magnetic field lines is depicted in these figures. The eastward electric field during daytime leads to the upward $\mathbf{E} \times \mathbf{B}$ drift of the plasma (Fig. 6.5a). Since the collision frequencies of ions with neutrals decrease upwards, the plasma near the magnetic equator readily diffuses down along the magnetic field lines at higher heights. Computations of Hanson and Moffett show that the plasma at the F_2 peak height of 450 km altitude near 17° dip latitude is not transported from very great heights but instead, is transferred almost horizontally from lower latitudes.

An examination of Fig. 6.5b shows a clear development of inverted fountain when the drifts over the equator are downward. This typically happens during nighttime when the electric field at the equator reverses its polarity [*Fejer*, 1981]. During this period, the magnetic flux tubes containing the plasma ('frozen in' condition) are 'sucked' in towards the equator. These results further show that below 400 km, the plasma flux is increasingly directed vertically downward at low latitudes near the crest location and that above this altitude, a motion towards the equator results in this 'inverted' or 'reverse' fountain effect.

The effects of the inverted fountain on the local ionosphere at low latitudes are many. The density profile at the crest location gets narrowed as the peak height of the F region gets lowered and gets broadened when the motion is upward, and as a consequence, the shape factor Y_m has been shown to be positively correlated with the height of the F_2 peak [*Roy and Rastogi*, 1989]. Further, a downward drift of plasma

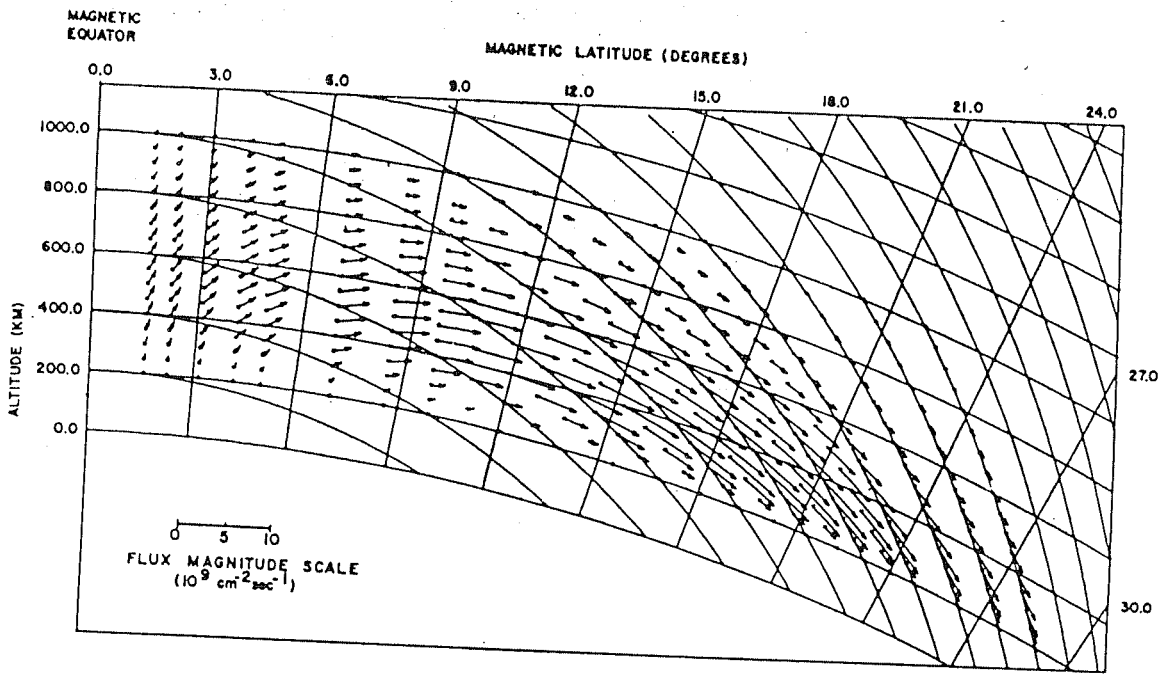

Fig. 6.5a. Vector plots of the ionization flux driven by an electric field at the magnetic equator. These theoretical simulations are for an upward vertical drift of 10 m/s at the equator. (after *Hanson and Moffett*, 1966)

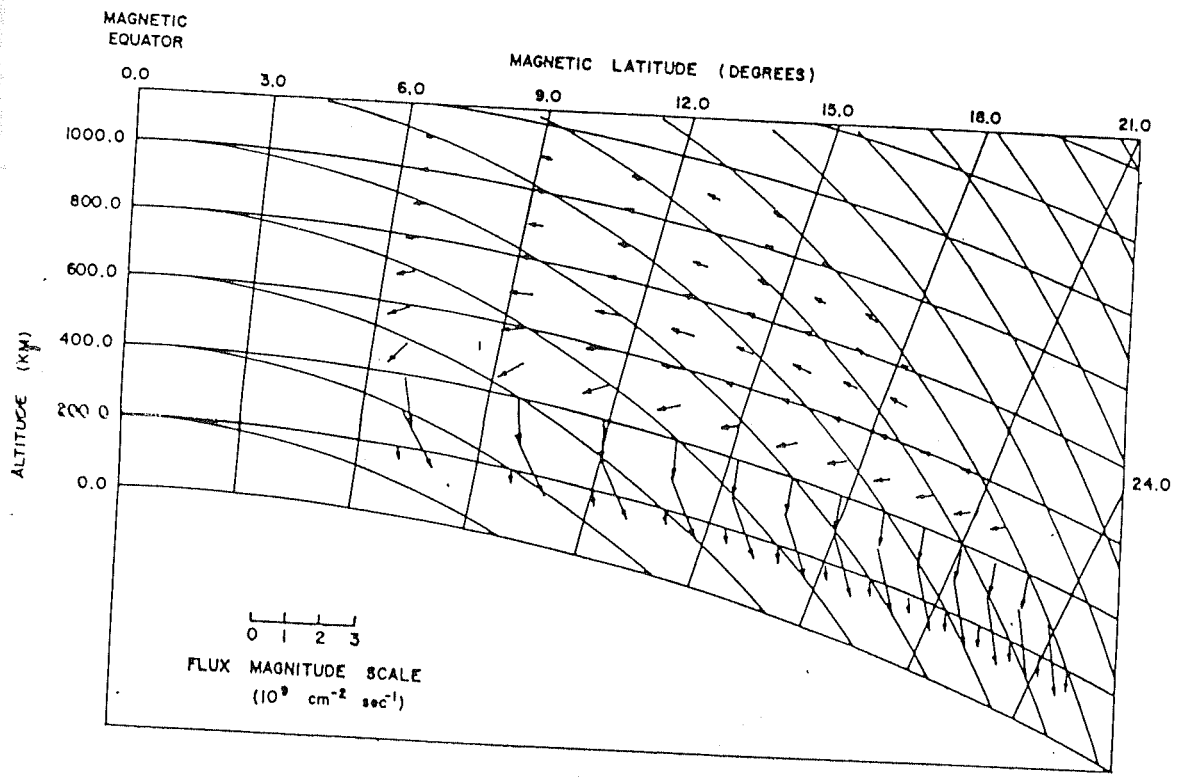

Fig. 6.5b. Same as above but for a downward drift of 10 m/s at the equator illustrating the 'inverted' or reverse fountain effect.

which moves the F layer down, would result in the enhancement of its density at any height below h_{max}. In other words, there would be an anti-correlation between the density and the height at a given time. During the late evening hours, when the drifts associated with the EIA are large, this anti-correlation between the height of the F layer below the peak and the local plasma density at any level close to this height prominently shows up. A close examination at the reduced ionograms obtained by the ground-based ionosonde at Ahmedabad indicates that this anti-correlation is present all through the night till about 0300 h local time beyond which the electron density starts decaying. The downward motion of the F layer is limited by the increased recombination at lower heights and this would result in the enhancement of 6300 Å airglow emission.

Figs. 6.6a and 6.6b illustrate these features observed in the months of February and April, 1991, during the high solar activity period. The top panel shows the base height of the F layer obtained from the reduced ionograms. An electron density of 1.2 $\times$ 10^5 cm^{-3} has been considered to represent the base of the F layer. The variation in electron density at 290 km is plotted in the middle panel. The peak intensity of the line profiles obtained by the Fabry Perot Spectrometer operating on O I 6300 Å from Mt. Abu is depicted in the bottom panel. It can be seen from these diagrams that as the base height of the F layer is lowered, the electron density below the F_2 peak increases accompanied by increases in the intensity of 6300 Å emission. The distinct difference in the pattern of variation of F layer height between the February and April months is to be noted. There is a double humped structure seen in the intensity and electron density variation of February that has not been observed in April. These results have some important repercussions with regard to the derivation of ionospheric parameters based on coordinated measurements.

As discussed in Chapter 4, the vertical velocity of the plasma at the F_2 peak

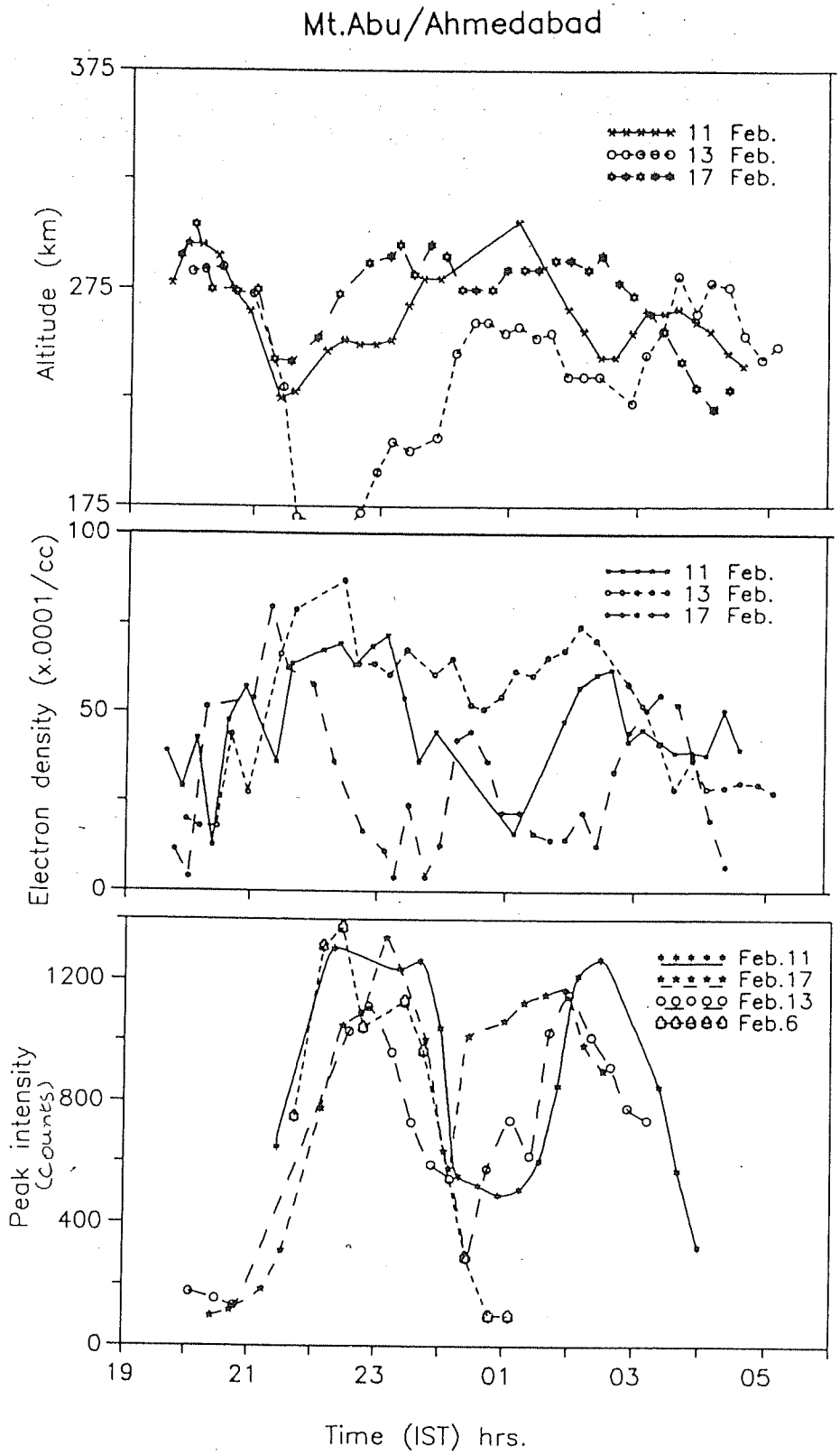

Fig. 6.6a. Motions of F layer (top) over Ahmedabad represented by the base height (corresponding to an electron density of $1.2 \times 10^5 cm^{-3}$) and the electron density at 290 km (middle) obtained by the true height analysis of ionograms. The bottom panel illustrates the peak emission intensities of 6300 Å nightglow over Mt. Abu at these times for the month of February 1991.

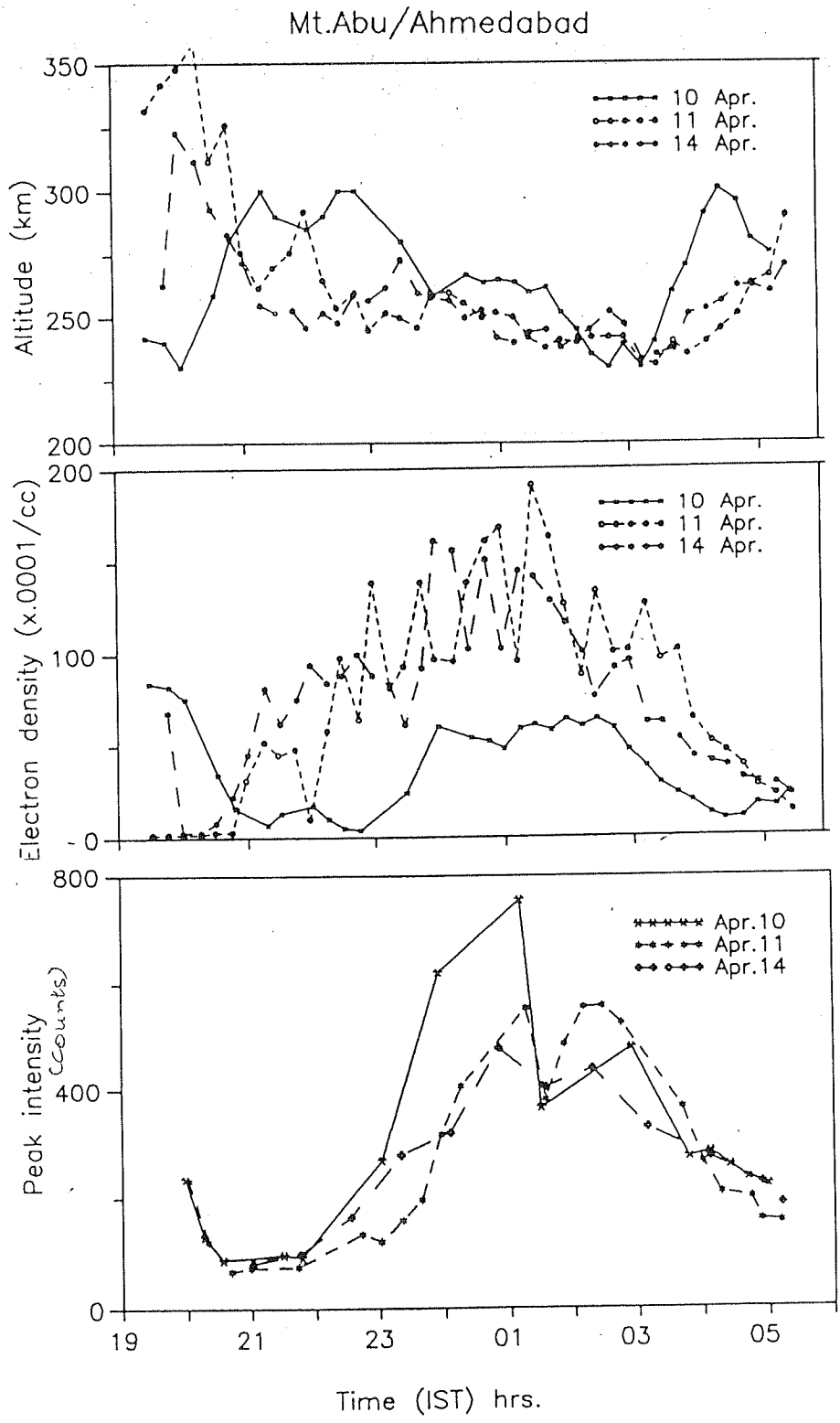

Fig. 6.6b. Same as Fig. 6.6a but for the month of April 1991.

is due to the drifts imposed by electric field, wind and diffusion. Since the diffusion is downward below the F_2 peak, according to the servo model, the balance height of the F_2 peak occurs at a level where the loss of plasma due to recombination, balances the supply due to diffusion and this is entirely determined by the neutral atmospheric parameters. This balance height gets altered in the presence of winds and electric fields. Based on this principle, the electric fields have been estimated and presented in Chapter 4.

Under normal circumstances, the polarity of the electric field is expected to remain westward all through the night. One would expect a similar behaviour at latitudes away from the equator as well. The inferred field over Ahmedabad changing its direction to eastward beyond midnight poses many questions. It could possibly be due to the assumptions made in the estimation using servo model. The changes in F layer height are assumed to be entirely determined by the thermospheric parameters, namely, temperature and meridional winds, and electric fields. It is not known whether changes in the plasma density and the F layer height due to the latitudinal sweeping motion of the EIA crest, contribute to the uncertainties associated with the magnitude and direction of the estimated electric fields. This aspect needs to be explored in detail considering the suggestion being made in the present study that there prevails a close coupling between the EIA associated processes, namely the ETWA and its associated neutral circulation, and the observed thermospheric parameters.

2. Effects of EIA on the neutral atmosphere

Hedin and Mayr [1973] analysed the neutral density data between 400 and 500 km obtained by the neutral mass spectrometer on OGO 6 satellite and showed that the latitudinal variations in density near the equator are more complex than those predicted by the static diffusive equilibrium models of *Jacchia* [1965,1971]. The major molecular gas, N_2, has been found to show density variations with a minimum

at the magnetic equator and maxima at ± 20° magnetic latitude, during daytime. The reverse has been observed in the early morning hours. They have tested the hypothesis suggested by earlier workers that ion-neutral collisions would significantly modify the behaviour of the thermosphere and would lead to geomagnetic control of neutral atoms and molecules. Making use of a two-dimensional theoretical model, they inferred that at latitudes of enhanced electron densities like those of crest locations of EIA, there would be a decrease in the diurnal amplitude of the zonal wind velocities. As a consequence of this, less energy would flow from the dayside to the nightside and thus temperature and density of the neutral atmosphere would show a maximum. Hedin and Mayr expected the time of maximum density variations to shift to later local times and to latitudes of enhanced electron density. Though their model could not lead to variations with respect to longitudes, it described the average behaviour quite well.

The experimental evidence for the neutral wind dynamics controlled by the geomagnetic field configuration was brought out by *Raghavarao et al.* [1991] through the revelation that the zonal wind magnitudes do indeed show a minima at magnetic latitudes ± 20° and maximum at the magnetic equator collocated with the crests and trough of EIA respectively. They have made use of the WATS (Wind And Temperature Spectrometer) data on DE 2 satellite flown during high solar activity periods.

Recently, *Raghavarao et al.* [1993] have shown that vertical winds of significant magnitudes, i.e., in the range of 10–40 m/s, were also collocated with the EIA/ETWA crests/trough at pre-midnight hours. The source of the vertical winds has been shown to lie in the ETWA. They have proposed that the temperature and the pressure ridges associated with the EIA, would drive a new wind system in the meridional plane and that the measured vertical winds form a part of this wind system. During the

evening hours of high solar activity period, when the fountain effect is renewed, the EIA crests get strengthened and the pressure ridges would prominently show up due to the increased ion-drag. This would give rise to an upward neutral wind at the crest locations with a sinking motion near the magnetic equator. The first experimental evidence for the presence of vertical winds of significant amplitudes over the equatorial zone was provided by *Anandarao et al.* [1978] and *Raghavarao et al.* [1987]. The work of *Biondi and Sipler* [1985] at Natal, Brazil, revealed vertical winds which were upward in the evening twilight that quickly changed to downward and reversed again to upward by local midnight revealing a periodicity of 4 to 5 hours. The wind model proposed by *Raghavarao et al.* [1993] seems to explain the converging meridional winds observed by *Biondi and Sipler* [1985] at 2100 LT near the magnetic equator.

With the data obtained from a single station, it is difficult to infer the wind systems associated with ETWA, as proposed by *Raghavarao et al.* [1993], especially so when there are no data on vertical winds. However, the results on meridional winds presented in Chapter 5 point toward the possibility of the effects of ETWA being present. It is to be noted that there has been a systematic shift in the occurrence of maximum equatorward winds from winter to equinox periods. At these times, the electron density at 290 km and the 6300 Å airglow intensity too showed maxima suggesting the possibility of pressure ridges getting generated. Though the wind results obtained as a part of the investigation provides a positive indication, more coordinated data on both vertical and horizontal components of the neutral winds are needed to confirm this possibility.

3. Effects on equatorial spread F

The wind system proposed by *Raghavarao et al.* [1993] has important consequences on the thermosphere-ionosphere system as a whole. The magnitude of the vertical winds would act as an indicator of the energy deposition associated with

EIA/ETWA. At locations equatorward of the anomaly crests, strong equatorward winds would occur that would, in the winter hemisphere, oppose the normal transequatorial wind, and in the summer hemisphere, add up to the interhemispheric wind, thus having significant influence on the occurrence of equatorial spread F (ESF) as has been addressed by *Maruyama* [1988]. It is well recognized now that the longitudinal gradient in the Pedersen conductivity of the conjugate E layers plays a major role in the determination of the onset time and amplitude of the prereversal enhancement at sunset hours, which is one of the prerequisites for the triggering of ESF [*Abdu et al.*, 1992]. This situation is most favourable during equinox periods when both the conjugate E regions are perfectly aligned for simultaneous sunset and a maximum longitudinal gradient in Pedersen conductivity is then bound to occur. On the other hand, if the E region Pedersen conductivity in one of the hemispheres is increased by some means, the growth rates of R-T instability will be proportionately reduced. A transequatorial wind, for example, on the downwind portion of the field line would bring the plasma downward thereby increasing the Pedersen conductivity more than the decrease in conductivity on the upwind portion of the flux tube. This could lead to an E region load at one end of the flux tube that would short-circuit the polarization field and possibly lower the instability growth rates [*Maruyama*, 1988].

Mendillo et al. [1992] have suggested that the transequatorial wind does provide a stabilizing effect on the irregularity growth rates. They have made use of the ALTAIR incoherent scatter radar observations and an all sky airglow imaging system to make a two-night case study on the occurrence of ESF. On one of the nights, they have observed an unusual meridional gradient in 6300 Å intensity when one of the intertropical arcs associated with EIA had been asymmetrical with respect to the magnetic equator. They have inferred a strong transequatorial wind ($\sim$ 130 m/s) that could have caused this feature and suppressed the occurrence of ESF as well on this night. In their concluding remark, they have made a suggestion that Fabry Perot

measurements of neutral winds near the crests of the EIA along a magnetic flux tube can be compared to irregularity onset and development patterns observed near the magnetic equator.

Coming to the vertical component of the circulatory cell, *Sekar and Raghavarao* [1987] have shown the importance of downward neutral winds over the equator that can have a destabilizing effect and enhance the growth rate of the R-T instability. Comparing the relative contributions due to gravity, zonal and vertical winds, they have shown that a downward wind of about 9 m/s at 270 km and 16 m/s at 300 km, have the same contribution as that of gravitational drift at respective altitudes. In fact, the eastward ion motion due to Hall effect imparted by the downward wind can add to that due to gravitational drift, thus enhancing the growth rate of the R-T instability.

Thus it becomes evident from the above assessment that the measurements of neutral winds (both meridional and vertical) are important to explain the enigmatic problem of the occurrence of equatorial spread F. In the light of the complexities of the phenomena discussed above, development/adaptation of newer methods for these investigations becomes necessary.

6.3 All sky imaging high resolution Fabry Perot Spectrometer

Though the central-aperture pressure-scanned Fabry Perot Spectrometer yields continuous data on temperature and winds, for a large spatial and simultaneous temporal information, the look angle of the instrument needs to be scanned both in azimuth and elevation. The desired spatial and temporal resolution would not be achieved

by such scanning. With the advent of two-dimensional detectors like the charge coupled devices and the imaging photon detectors, and by making use of the imaging property of the FP etalon, mapping of wind fields of any airglow emitting region in the sky has become possible. One such FP spectrometer has been built and commissioned for the studies of high latitude auroral phenomena [*Rees and Greenaway*, 1983]. Looking into the potential of this spectrometer and its possible application to the study of geophysical processes described in this chapter, an All Sky Imaging Fabry Perot Spectrometer (ASIFPS) has been designed and built under the auspices of the All India Coordinated Programme for Ionosphere-Thermosphere Studies (AICPITS) supported by the Department of Science and Technology, Government of India.

The schematic of the optical set-up of ASIFPS is depicted in Fig. 6.7. The design details are given elsewhere [*Sekar et al.*, 1993]. In brief, the ASIFPS consists of three essential subsystems, namely, (i) a high resolution FPS, the FP etalon being identical to that of the central-aperture scanned FPS described in Chapter 2, (ii) field-widening optics and (iii) a two-dimensional detector (imaging photon detector).

The Fabry Perot has a distinct property in that each point of the object field is mapped onto a corresponding point in the image plane. In a normal FPS, the flux is integrated over the central fringe which corresponds to a field of view of a fraction of a degree. An imaging system requires the flux to be distributed over an array in a two-dimensional detector in order to retrieve the spatial information. This requirement demands a field widening optics at the front end so that the flux from a large portion of the sky can be collected and distributed uniformly over the image plane. A suitable front end optics has been designed in order to compress the chosen field of view of 100° of the sky into 2.4° (the acceptance angle of the available etalon with 10 mm airgap to form 5 fringes is 1.2°) at the entrance port of the FP etalon. The field widening optics consists of a fish eye lens and field and collimating lenses.

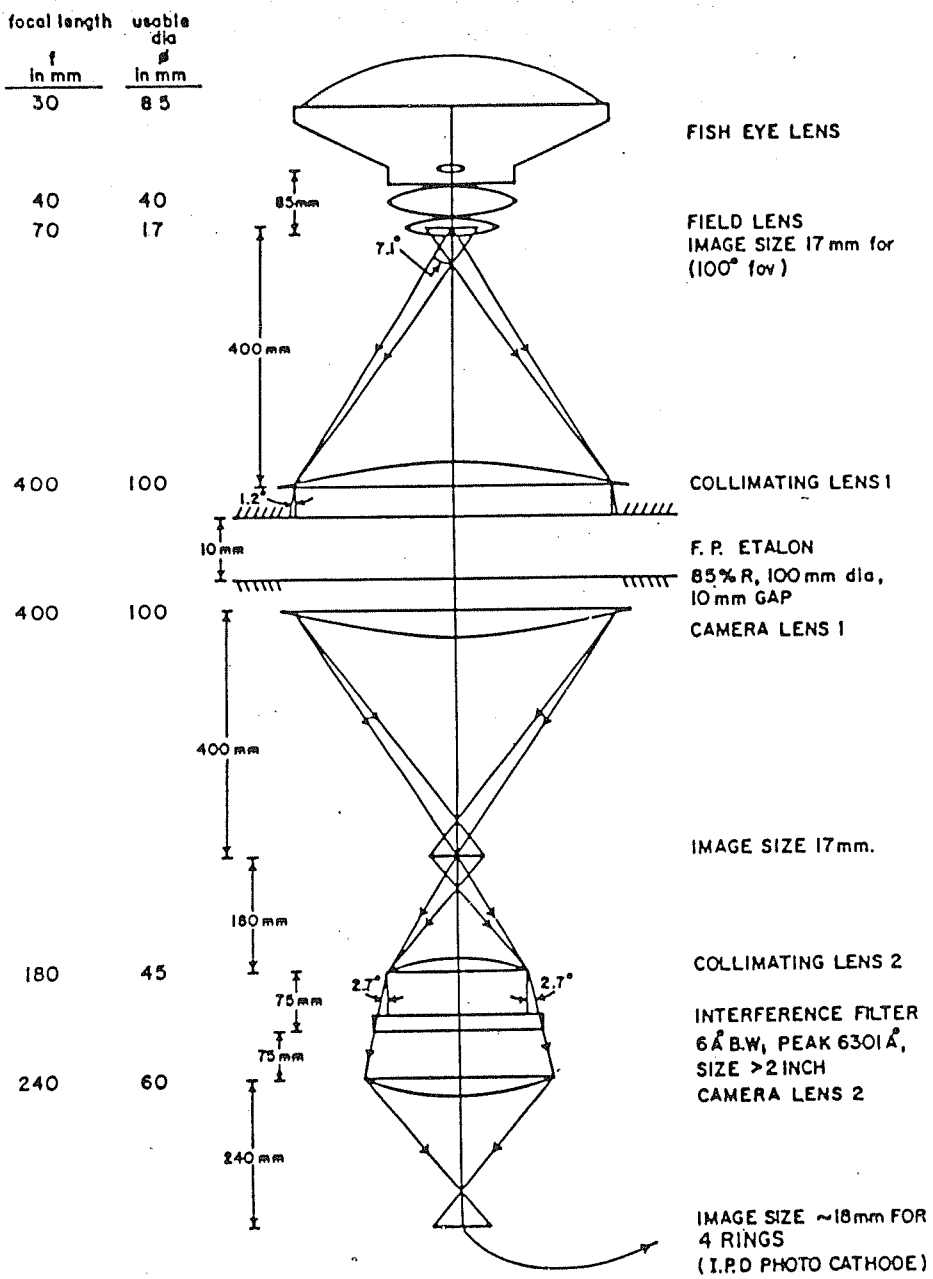

Fig. 6.7. Schematic diagram of the optical set-up of All Sky Imaging Fabry Perot Spectrometer (ASIFPS).

The details of the optics and the detector used are presented in a separate paper [*Sekar et al.*, 1993]. The preliminary results that pertain to the present investigation are as follows. Fig. 6.8 depicts a sequence of Doppler images obtained at different times on 5 January, 1992. In this figure, there are 12 frames of interferograms arranged in a sequence; with each one consisting of three orders of Fabry Perot fringes corresponding to different spatial positions on the sky. The sequence number and the time duration in IST are marked beneath each frame. Central fringes correspond to the zenith sky over Mt. Abu. The direction corresponding to magnetic north is depicted by an arrow while the line perpendicular to this arrow (not shown in the figure) corresponds to magnetic zonal direction. In each frame, the outermost fringe in the north-south direction corresponds to $\pm$ 2.6° latitude with respect to zenith, while the middle and inner fringes correspond to $\pm$ 2° and 1.2° respectively. The intensity scale in the figure increases with degree of whiteness and the dark areas correspond to minimum intensity. In the figure, the first frame corresponding to 1916–1946 h shows the northern part of the interferogram to be brighter than the rest of the frame. With time, in the subsequent frames (upto fourth) there is enhancement in intensity in other areas as well. Fourth, fifth and sixth frames reveal saturation in intensity in the scale adopted for representing the images. The present scale is chosen keeping in view of the least intensity levels as encountered in the case of twelfth frame. The development, brightening (frames 4 to 6) of the central fringe (corresponding to zenith) and its subsequent decay are clearly seen in the sequence of frames from 3 to 10. From the sixth frame onwards, one notices decrease in intensities in the northern sector, while in the southern sector, the intensities remain at a higher level. The tenth frame is nearly complementary to the first frame in terms of intensity distribution in the meridional plane. Frame 12 shows the near disappearance of fringes in the northern sector and a very low level of intensity in the southern sector.

As seen in Fig. 6.8, the EIA crest is located north of Mt. Abu upto $\sim$ 2130 h

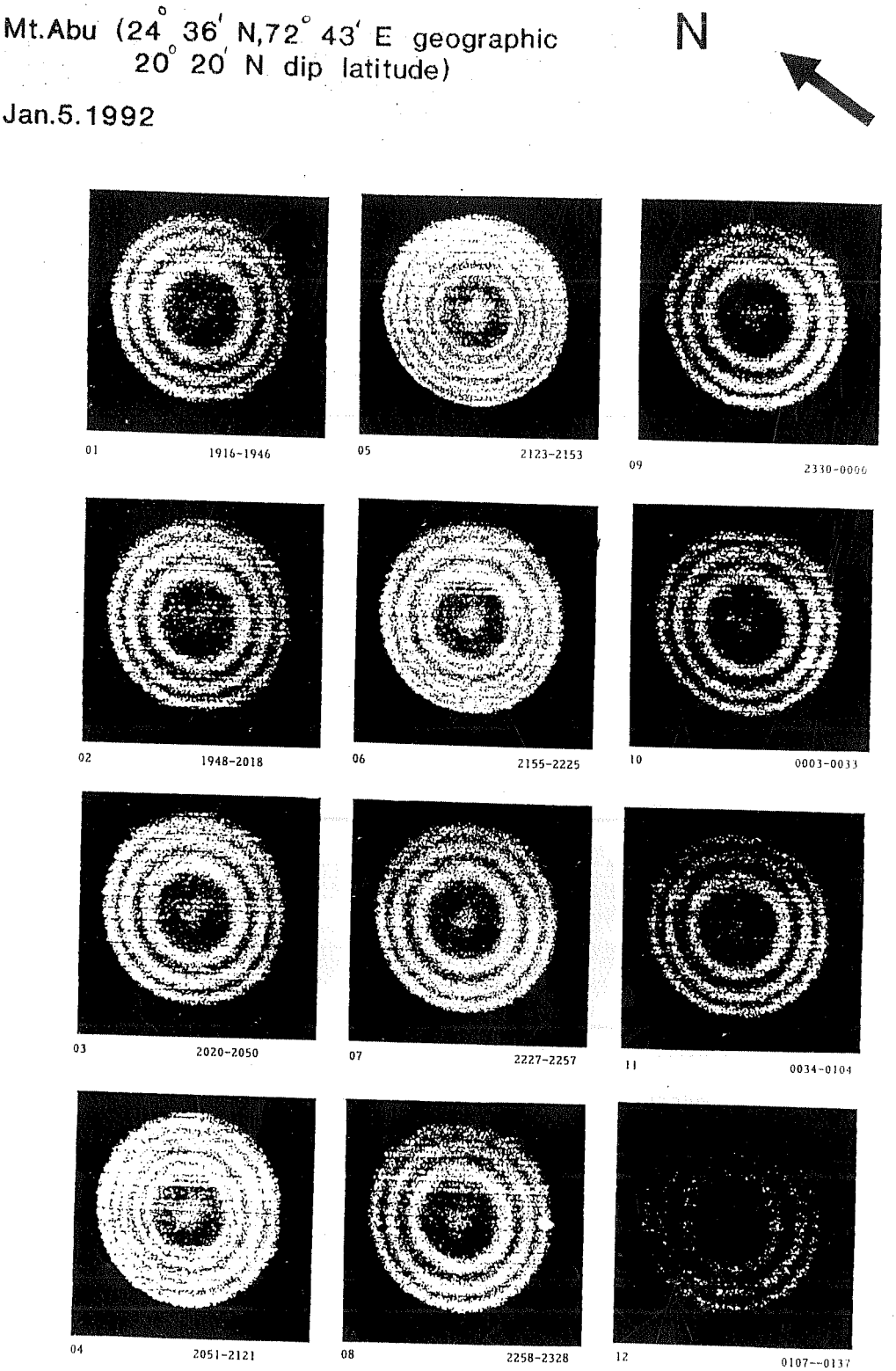

Fig. 6.8. Sequence of Doppler images obtained by the ASIFPS on the O I 6300 Å nightglow emission from Mt. Abu at different times on 5 January 1992

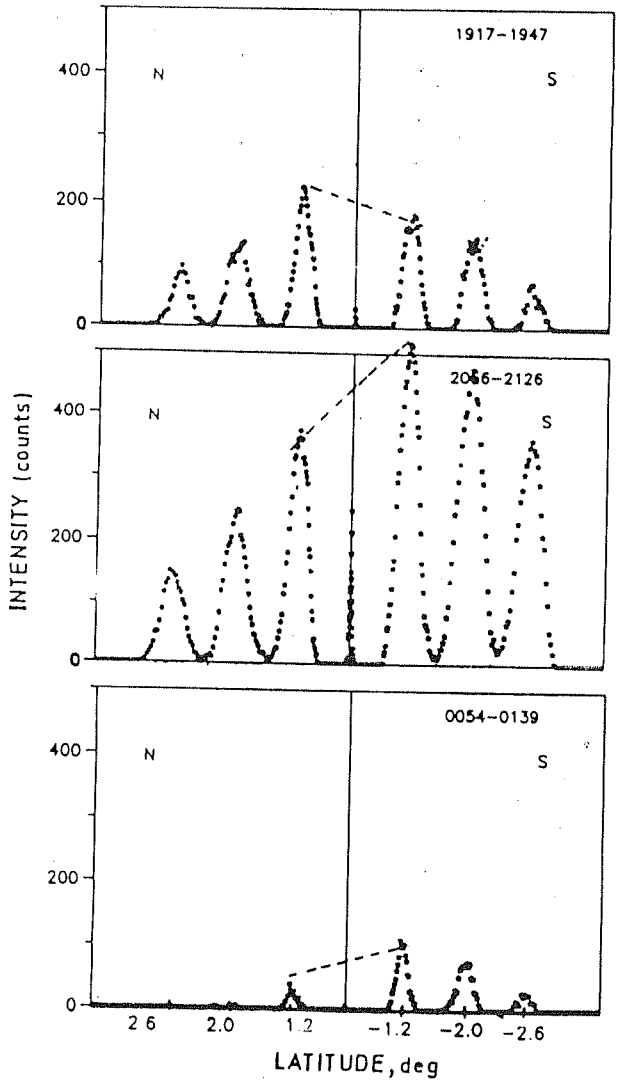

Fig. 6.9. Reduced line profiles of 6300 Å emission (spatially integrated to ± 15° angular segments on either side of the north-south axis) corresponding to a set of interferograms obtained on 8 January 1992 from Mt. Abu

and its retrieval southwards makes it to come overhead encompassing the complete field of view. This enables the development of a bright central fringe in frames 4 to 6. With time, the EIA crest moves southwards causing decrease in fringe intensity in the northern sector as well as overhead. The complete disappearance of EIA crest from the field of view of spectrometer is seen in the twelfth frame. This observaton is a clear visual representation of the 'inverted equatorial fountain'. Assuming a linear movement of EIA crest, the retrieval rate has been estimated to be 1.4° latitude per hour (i.e., with the velocity of $\sim$ 150 km/h) based on the crest positions overhead (fifth frame) and its total disappearance from the field of view of the spectrometer (twelfth frame). This estimate is one of the direct determination of the retrieval velocity and thus provides confirmation to the earlier estimates based on simple scanning photometer [*Kulkarni*, 1975; *Sridharan et al.*, 1993].

To study the gradients in the intensity levels along a particular direction, radial scans of the observed fringe systems are made. The line profiles at each spectral location are integrated to $\pm$ 15° angular segments on either side of the north-south axis. The results are depicted in Fig. 6.9 showing the reduced line profiles obtained in this manner. Each spectral location can be transformed into a latitude pertaining to a particular spatial location in the sky. The north-south intensity gradients with respect to zenith latitude are shown by means of a dashed line.

Another interesting result pertains to the latitudinal and longitudinal extent of the EIA crest. As mentioned earlier, the EIA shows a highly localized effect, being very strong in a certain longitude zone and totally absent in a zone just separated by 30° [*Sharma and Raghavarao*, 1989]. Though this may serve as an upper limit, the lower limit for the longitudinal extent is inferred from frames 4 to 6 in Fig. 6.8. The saturation in intensities all over the field of view in these frames indicates that the spatial extent of the crest is larger than the field of view. This observation indicates

that typically the longitudinal extent of the EIA crest is $\pm$ 6°. Same is true for the latitudinal extent also for which the confirmation from satellite data is available in literature [*Sharma and Raghavarao*, 1989].

The potential of the ASIFPS as a contender for mapping EIA features is well recognized now [*Sekar et al.*, 1993; *Sridharan et al.*, 1993]. It has become possible to visually track the crest of the EIA by continuous operation of this instrument. The most important use of this instrument is widely accepted to lie in the spatial mapping of wind and temperature fields in the vicinity of the emitting region. Especially in investigating phenomena like ETWA, such imaging spectrometers are expected to be very handy.

To conclude,

- we note that the low latitude thermosphere-ionosphere exhibits complex features that differ from season to season and attempts have been made to understand some of the underlying geophysical processes. Coordinated optical and radio probing measurements similar to the ones carried out during the course of the present investigation hold enough potential to provide answers to many of the enigmatic/unsolved problems.

Chapter 7

Summary and Scope for future work

This chapter contains the summary of the work contained in the thesis with emphasis on the important and new results that were obtained. The scope for future work, as an extension of and related to, the present studies is also indicated.

7.1 Summary of results obtained

The thesis is devoted to the study of low latitude thermosphere-ionosphere system based on coordinated thermospheric and F region measurements using a central-aperture pressure-scanned Fabry Perot Spectrometer operating on O I 6300 Å airglow, and a ground-based ionosonde located nearby. The focus has been on understanding the closed cycle of interactions that occur continuously between the neutral and the ionized species, in the presence of large scale geophysical processes in the low latitude region. Since the interaction mechanisms depend on the chemical, fluid dynamical and electrodynamical properties of the neutral-plasma medium, the behaviour of the thermosphere-ionosphere system as a whole is looked upon in terms of these properties. Earlier workers have employed the servo model of Rishbeth as a tool, in order

to understand and determine the nature and magnitude of the driving forces (like winds and electric fields) on the midlatitude F region, and the resulting interactions. According to the servo model, the peak of the F_2 region lies at a level determined by neutral atmospheric parameters where chemical equilibrium prevails; the external forces perturb this level and the F_2 peak approaches a new equilibrium level. At the equilibrium F_2 peak itself, diffusion and chemical recombination are of equal importance. Assuming that the time required for diffusion at the F_2 peak is shorter than times associated with the largest variations in applied drifts, it has been shown by many workers that the midlatitude F_2 layer does behave in accordance with the expectations of servo model. Making use of the servo principle, several workers have derived meridional winds from the existing ground-based ionosondes. In spite of inherent assumptions and limitations involved in the methodology they have adopted, the pattern of derived winds showed overall agreement with direct measurements and empirical model predictions. This ability to derive meridional winds using the basic physical principles in turn had demonstrated the fact that the behaviour of the midlatitude thermosphere-ionosphere system has been fairly understood.

The behaviour of the low latitude region is complicated by large scale processes such as equatorial ionization anomaly, equatorial temperature and wind anomaly, equatorial spread F and midnight temperature maximum, whose role in the energetics and dynamics of the upper atmosphere is largely unknown. Till recently, no attempts have been made to understand the basic interaction mechanisms that get significantly modified in the presence of these processes. As mentioned in Chapter 1, the reason for our limited knowledge on the behaviour of the low latitude thermosphere-ionosphere system had been the non-availability of a wider data base on both thermospheric and ionospheric parameters. In view of this fact, systematic coordinated measurements have been initiated and the results have formed a part of this thesis.

Line profile measurements of airglow emissions have been carried out from Mt. Abu (24.6°N, 72.7°E geographic; 33°N dip) for more than six years. Though the number of profiles that have been obtained by the central aperture-Fabry Perot Spectrometer was very large, there were severe limitations in retrieving useful information that led to the development of a comprehensive and more appropriate data analysis scheme described in Chapter 2.

The results were presented in four chapters in the following categories.

- Obtaining the variabilities of neutral temperature, which is important since the equilibrium height of the F_2 layer is determined by neutral temperature. The importance and applications of neutral temperature in understanding various physical processes have been illustrated in Chapter 3. The results from this chapter are as follows: Making use of the temperature measurements available during low and high solar activity periods, an exercise has been carried out to determine the effects of solar variability on the behaviour of the thermospheric temperatures over low latiutdes. The limitations of the MSIS-86 model, one of the most comprehensive models available as on this day, in representing low latitudes, has been demonstrated by means of individual case studies. These studies show that significant enhancements occur in measured neutral temperatures at certain times considerably deviating from the model predictions. Next the response of thermospheric temperatures to changes in solar flux over a longer period was examined. A plot of mean measured temperatures versus mean model temperatures over the years covering half the solar cycle suggests that only about 65 % of the variation in the measured temperatures can be accounted for and that most of the mean measured temperatures are higher than the mean model temperatures leading to the suggestion that there should be additional energy sources that significantly contribute to the energetics of

the low latitude neutral atmosphere.

Identification of these energy sources has been the next step in the presentation. The geophysical processes of relevance during quiet geomagnetic conditions are (1) the Joule heating associated with the fluctuating electric fields of equatorial spread F irregularities, (2) the equatorial temperature and wind anomaly (ETWA) associated with the equatorial ionization anomaly (EIA) and (3) the midnight temperature maximum (MTM).

The possibility of significant amount of energy that might be deposited along magnetic flux tubes in the presence of fluctuating electric fields and drift velocities associated with equatorial spread F, causing enhancement in neutral temperatures, has been cross-checked, and it has been concluded that the excess heating cannot be ascribed to the possibility of spread F associated heating alone. Owing to the renewed interest in EIA associated processes such as ETWA and the presence of vertical winds, the possibility of these processes acting as sources of energy has been explored. It has been shown that electrodynamic properties of the thermosphere-ionosphere system have the potential to be one of the controlling factors for the variabilities of thermospheric temperatures at the location of the crest of EIA.

- Having ascertained the variabilities of neutral temperatures and their possible sources, the next step has been to examine the validity of servo model for low latitude regions. It has been demonstrated in Chapter 4 that the servo model of Rishbeth is an ideal tool for investigating the behaviour of the thermosphere-ionosphere system since it incorporates the basic coupling mechanisms. Having given a description of servo principles, derivation of the servo equation and the earlier work done for midlatitudes, details of the simulation exercise that has been carried out in order to determine the latitude beyond which the servo model can be applied, were presented. Since the 'servo' response of the F reigon

varies as $\sin^2 I$ and the diffusion process becomes insignificant near the magnetic equator, the latitude from where on the servo model can be applied and tested against the actual behaviour of the F region, was determined to be beyond 20°. Several case studies have been made and the results presented in this chapter demonstrate the fact that the F region behaves according to the expectations of servo model at this low latitude station. The height of the F layer was shown to vary as 11 $\pm$ 2 km for every 100 K change in neutral temperature. Based on servo principles and making use of measured temperatures and meridional winds, estimates of F layer peak height were made and compared with the independently obtained peak height values from the ground-based ionosonde. The results obtained for a few days have indicated fairly good to very good agreement. The deviations between the estimated and the measured peak heights were ascribed to zonal electric fields. Estimates of electric fields for all the days under consideration made with certain valid assumptions show considerable variability from season to season, at times becoming eastward.

- The servo model reveals a direct relationship to exist between the F layer displacement and the wind vector. Using the servo model principles, the importance of neutral temperature that determines the F layer peak height, and its variabilities, in influencing the derived meridional winds were demonstrated in Chapter 5 through case studies. Variabilities of measured meridional winds have been studied for two seasons, namely, the winter and equinox periods. Comparisons of these measurements with those from other low and equatorial latitudes have been made and they were found to be significantly different. The present estimates differ from both horizontal wind model and the vector spherical harmonic model. It has been concluded that solar radiation does not seem to be the sole agent that sets and governs the observed wind patterns.

- The limitations of numerical models to describe the observed variation of thermospheric temperatures and winds over different time intervals ranging from a few hours on a given night to a solar cycle, over a low latitude station, demonstrates the need for incorporating the effects of geophysical processes into the models by means of a parameterization. Such an effort would need a thorough understanding of the processes themselves and coordinated measurements from a chain of stations in the near-equatorial zone are needed for this purpose. Work in this direction has been initiated and some of the results obtained were presented in Chapter 6.

The processes that were investigated in this regard are (1) the MTM and (2) the EIA. After reviewing the mechanisms that are responsible for MTM, the results on the comparison of the variation of meridional winds from two different latitudes, namely, Mt. Abu (24.6°N geographic) where direct measurements are available and Sriharikota (13.7°N geographic) for which winds were derived from the ionosonde data, were presented. In the winter month of February (1991), there appeared to be a systematic phase difference in the variation ranging from 2 to 4 hours and always the Mt. Abu measurements were lagging in phase. This has been suggested to be probably due to the MTM occurring near the equator and giving rise to an associated wind pattern. However, for the equinoctial month of April, no such feature was seen probably due to the dominant role played by electrodynamic processes during this season.

The EIA associated processes in the low latitude region were studied under three categories: (1) behaviour of the post-sunset and nighttime F region, (2) effects of EIA on the neutral atmosphere and (3) effects of thermospheric winds on equatorial spread F. Though we have results only for (1) and (2), the importance of (3) was highlighted in the text for the sake of completeness. The post-sunset behaviour of the F region at the crest location of EIA has been

shown to be controlled by the EIA. The passage of the crest of EIA across the low latitude observing site would alter the neutral and ionospheric parameters significantly.

Though it is difficult to infer the wind systems associated with ETWA especially when no data on vertical winds are available, the results that were presented in Chapter 5 provide a positive indication for the neutral air circulation associated with ETWA to be active over the low latitude station. This has been demonstrated utilizing electron densities available from the ground-based ionosonde and the airglow intensities.

Finally, the potential of the all sky imaging Fabry Perot Spectrometer that has been designed and fabricated for the purpose of mapping temperature and wind fields was highlighted and its importance in studying the geophysical processes was emphasized.

7.2 Scope for future work

There are several areas that need to be explored in detail and the following suggestions in this direction are meant to be an useful extension of the present thesis.

It is proposed that more coordinated measurements of both thermospheric and ionospheric parameters be made at least from two stations making use of the available resources. The spatial variabilities of thermospheric parameters need to be brought out since they are capable of providing clues to the relative roles played by all known physical processes. It is important to estimate quantitatively the effect of each of these processes for a full understanding of the thermosphere-ionosphere system.

The existing models of neutral upper atmosphere need to be improved upon to represent better the low latitude observed features. The measurements from these

locations may be utilized for a parameterization of numerical models in terms of the competing effects of dominant geophysical processes.

The effects of geomagnetic storms were not touched upon in the thesis owing to limited data available for these occasions. Only recently, reports have come on the observed effects of storms on the thermospheric densities, temperatures and winds from other latitudes. Continuous, systematic, ground-based measurements are necessary to infer information regarding geomagnetic activity effects at low and equatorial latitudes.

The present spectrometer has a limitation of not being able to measure vertical winds of small magitudes. Recent satellite measurements have revealed them to be present in significant amplitudes and the instrument could be improved upon to be able to make these measurements so that equatorial spread F associated investigations could be carried out.

Mapping of the dynamical features is an attractive proposition for a region like ours which has several geophysical features. Relation of the neutral thermospheric parameters with ETWA, processes associated with geomagnetic storms, etc., are considered extremely important from the dynamics and energetics point of view.

More detailed investigations are being planned for the coming years.

With the sanctioning of TIMED (Thermosphere - Ionosphere - Mesosphere - Energetics and Dynamics) satellite mission, a comprehensive set of complementary ground-based measurements are a must. The capabilities developed during the course of the present work and the proposed improvements and scientific investigation are expected to play a crucial role in the understanding of the complex system namely 'The thermosphere - ionosphere system'.

References

1. Abdu, M. A., I. S. Batista and J. H. A. Sobral, A new aspect of magnetic declination control of equatorial spread F and F region dynamo, *J. Geophys. Res.*, 97, 14897, 1992.

2. Anandarao, B. G., R. Raghavarao and J. N. Desai, G. Haerendel, Vertical winds and turbulence at 93 km over Thumba, *J. Atmos. Terr. Phys.*, 40, 157, 1978.

3. Anandarao, B. G. and R. Suhasini, A deconvolution method for astronomical photometric and spectroscopic observations, *Bull. Astr. Soc. India*, 14, 34, 1986.

4. Anderson, D. N. and R. G. Roble, The effect of vertical $\mathbf{E} \times \mathbf{B}$ ionospheric drifts on F region neutral winds in the low latitude thermosphere, *J. Geophys. Res.*, 79, 5231, 1974.

5. Anderson, D. N., Modeling ambient low latitude F region ionosphere - A review, *J. Atmos. Terr. Phys.*, 43, 753, 1981.

6. Anderson, D. N., M. Mendillo and B. Herniter, A semi-empirical low latitude ionospheric model, *Radio Sci.*, 22, 292, 1987.

7. Anderson, D. N., J. M. Forbes and M. Codrescu, A fully analytic low and middle latitude ionospheric model, *J. Geophys. Res.*, 94, 1520, 1989.

8. Armstrong, E. B., A note on the use of the Fabry Perot etalon for upper atmospheric temperature measurements, *J. Atmos. Terr. Phys.*, 3, 274, 1953.

9. Atherton, P. D., N. K. Reay, J. Ring and T. R. Hicks, Tunable Fabry Perot

filters, *Opt. Engg.*, 20, 806, 1981.

10. Babcock, H. D., A study of the green auroral line by the interference method, *Astrophys. J.*, 57, 209, 1923.

11. Balsley, B. B., G. Haerendel and R. A. Greenwald, Equatorial spread F: Recent observations and a new interpretation, *J. Geophys. Res.*, 77, 5625, 1972.

12. Bamgboye, D. K. and J. P. McClure, Seasonal variation in the occurrence time of the equatorial midnight temperature bulge, *Geophys. Res. Lett.*, 9, 457, 1982.

13. Banks, P. M. and G. Kockarts, Aeronomy, Academic Press, New York, 1973.

14. Bates, D. R., A suggestion regarding the use of rockets to vary the amount of atmospheric sodium, *J. Geophys. Res.*, 55, 347, 1950.

15. Bedinger, J. F., Thermospheric motions measured by chemical releases, *Space Res.*, XII, 919, 1972.

16. Behnke, R. and R. M. Harper, Vector measurements of F region ion transport at Arecibo, *J. Geophys. Res.*, 78, 8222, 1973.

17. Behnke, R. and H. Kohl, The effects of neutral winds and electric fields on the ionospheric F_2 layer over Arecibo, *J. Atmos. Terr. Phys.*, 36, 325, 1974.

18. Bens, A. R., L. L. Cogger and G. G. Shepherd, Upper atmospheric temperatures from Doppler line widths - III, *Planet. Space Sci.*, 13, 551, 1965.

19. Bevington, P. R., Data Reduction and Error Analysis for the Physical Sciences, McGraw-Hill Book Co., New York, 1969.

20. Bhavsar, P. D., M. S. Narayanan and K. Ramanuja Rao, Neutral atmosphere winds above 100 km, *Space Res.*, IX, 374, 1969.

21. Biondi, M. A. and W. A. Feibelman, Twilight and nightglow spectral line shapes of oxygen λ 6300 and λ 5577 radiation, *Planet. Space Sci.*,

16, 431, 1968.

22. Biondi, M. A. and J. W. Meriwether, Jr., Measured response of the equatorial thermospheric temperature to geomagnetic activity and solar flux changes, *Geophys. Res. Lett.*, 12, 267, 1985.

23. Biondi, M. A. and D. P. Sipler, Horizontal and vertical winds and temperatures in the equatorial thermosphere: Measurements from Natal, Brazil during August–September 1982, *Planet. Space Sci.*, 33, 817, 1985.

24. Biondi, M. A., J. W. Meriwether, Jr., B. G. Fejer and R. Woodman, Measurements of the dynamics and coupling of the equatorial thermosphere and F region ionosphere in Peru, *J. Atmos. Terr. Phys.*, 50, 937, 1988.

25. Biondi, M. A., J. W. Meriwether, Jr., B. G. Fejer and S. A. Gonzalez, Seasonal variations in the equatorial thermospheric wind measured at Arequipa, Peru, *J. Geophys. Res.*, 95, 12243, 1990.

26. Biondi, M. A., J. W. Meriwether, Jr., B. G. Fejer, S. A. Gonzalez and D. C. Hallenbeck, Equatorial thermospheric wind changes during the solar cycle: Measurements at Arequipa, Peru from 1983 to 1990, *J. Geophys. Res.*, 96, 15917, 1991.

27. Blamont, J. E. and J. M. Luton, Geomagnetic effect on the neutral temperature of the F region during the magnetic storm of September 1969, *J. Geophys. Res.*, 77, 3534, 1972.

28. Bittencourt, J. A., B. A. Tinsley, G. T. Hicks and E. I. Reed, Tropical F region winds from O I 1356 Å and O I 6300 Å emissions, 2, Analysis of OGO 4 data, *J. Geophys. Res.*, 81, 3786, 1976.

29. Bittencourt, J. A. and B. A. Tinsley, Nighttime thermospheric winds at low latitudes deduced from AE-C ionospheric measurements, *J. Geophys. Res.*, 82, 4694, 1977.

30. Bramley, E. N. and M. Young, Winds and electromagnetic drifts in the equatorial F_2 region, *J. Atmos. Terr. Phys.*, 30, 99, 1968.

31. Briggs, B. H. and H. Rishbeth, An analogue solution of the continuity equation of the ionospheric F region, *Proc. Phys. Soc.* (London), 78, 409, 1961.

32. Buonsanto, M. J., Seasonal variations of daytime ionization flows inferred from a comparison of calculated and observed $N_{\mathrm{m}}F_2$, *J. Atmos. Terr. Phys.*, 48, 365, 1986.

33. Buonsanto, M. J., Diurnal variations in F_2 peak density and ionization flux above Tahiti, *J. Atmos. Terr. Phys.*, 49, 237, 1987.

34. Buonsanto, M. J., Subsidiary maxima in late evening $N_{\mathrm{m}}F_2$ at a low latitude station at solar maximum, *J. Atmos. Terr. Phys.*, 50, 573, 1988.

35. Buonsanto et al., Observations of neutral circulation at midlatitudes during the equinox transition study, *J. Geophys. Res.*, 94, 16987, 1989.

36. Buonsanto, M. J., Observed and calculated F_2 peak heights and derived meridional winds at midlatitudes over a full solar cycle, *J. Atmos. Terr. Phys.*, 52, 223, 1990.

37. Burns, A. G. and T. L. Killeen, The equatorial neutral thermospheric response to geomagnetic forcing, *Geophys. Res. Lett.*, 19, 977, 1992.

38. Burnside, R. G., F. A. Herrero, J. W. Meriwether, Jr. and J. C. G. Walker, Optical observations of thermospheric dynamics at Arecibo, *J. Geophys. Res.*, 86, 5532, 1981.

39. Burnside, R. G., R. A. Behnke and J. C. G. Walker, Meridional neutral winds in the thermosphere at Arecibo: Simultaneous incoherent scatter and airglow observations, *J. Geophys. Res.*, 88, 3181, 1983.

40. Burnside, R. G., Dynamics of the low latitude thermosphere and ionosphere, Ph.D. Thesis, Univ. of Michigan, 1984.

41. Burnside, R. G. and C. A. Tepley, Optical obervations of thermospheric neutral winds at Arecibo between 1980 and 1987, *J. Geophys. Res.*, 94, 2711, 1989.

42. Burnside et al., The neutral thermosphere at Arecibo during geomagnetic storms, *J. Geophys. Res.*, 96, 1289, 1991.

43. Burrage, M. D., C. G. Fesen and V. J. Abreu, Low latitude thermospheric neutral winds determined from AE-E measurements of the 6300 Å nightglow at solar maximum, *J. Geophys. Res.*, 95, 10357, 1990.

44. Burrage, M. D., M. F. Storz, C. G. Fesen, R. G. Roble and V. J. Abreu, Solar tides in the upper equatorial thermosphere: A comparison between AE-E data and the NCAR TGCM for solstice, solar minimum conditions, *J. Geophys. Res.*, 96, 187, 1991.

45. Burrage, M. D., V. J. Abreu, N. Orsini, C. G. Fesen and R. G. Roble, Geomagnetic activity effects on the equatorial neutral thermosphere, *J. Geophys. Res.*, 97, 4177, 1992.

46. Chabbal, R., Recherche des meilleures conditions d'utilisation d'un spectrometre photoelectrique Fabry Perot, *J. Rech.* (CRNS), 24, 138, 1953.

47. Chamberlain, J. W., Physics of the Aurora and Airglow, Academic Press, New York, 1961.

48. Chandler et al., Comparison of measured and calculated low latitude ionospheric properties, *J. Geophys. Res.*, 88, 9187, 1983.

49. Chapman, S. and R. S. Lindzen, Atmospheric Tides, D. Reidel, Dordrecht, 1970.

50. Chen, F. F., Introduction to Plasma Physics, Plenum Press, New York, 1974.

51. Cogger, L. L., G. J. Nelson, M. A. Biondi, R. D. Hake, Jr. and D. P. Sipler, Coincident F region temperature determinations from incoherent backscatter and Doppler broadening of O I 6300 Å, *J. Geophys. Res.*, 75, 4887, 1970.

52. Cogger, L. L., J. S. Murphree, C. A. Tepley and J. W. Meriwether, Jr., Measurements of the E region neutral wind field, *Planet. Space Sci.*, 33, 373, 1985.

53. Cole, K. D., Energetics of and a source of energy for equatorial spread F events, *J. Atmos. Terr. Phys.*, 36, 1099, 1974.

54. Cole, K. D. and M. P. Hickey, Energy transfer by gravity wave dissipation, *Adv. Space Res.*, 1, (12)65, 1981.

55. Connes, P., Augmentation du produit luminosite × resolution des interferometres par l'emploi d'une difference de marche independante de l'incidence, *Rev. Opt.*, 35, 37, 1956.

56. Cooper, M. J., Deconvolution: If in doubt, don't do it, *Phys. Bullettin*, October issue, 463, 1977.

57. Crary, D. J. and J. M. Forbes, The dynamic ionosphere over Arecibo: A theoretical investigation, *J. Geophys. Res.*, 91, 249, 1986.

58. Crowley, G., Dynamics of the earth's thermosphere: A review, *Rev. Geophys.*, 29, 1143, 1991.

59. Dalgarno, A., Ambipolar diffusion in the F region, *J. Atmos. Terr. Phys.*, 26, 939, 1964.

60. Danilov ,A. D., U. A. Kalgin and A. A. Pokhunkov, Variation of the turbopause level in the polar regions, *Space Res.*, XIX, 173, 1979.

61. Danilov ,A. D., U. A. Kalgin and A. A. Pokhunkov, Variation of the turbopause level in the equatorial regions, *Space Res.*, XX, 83, 1980.

62. Desai, J. N. and M. S. Narayanan, Determination of upper atmospheric temperatures from diffusion of vapour clouds, *J. Atmos. Terr. Phys.*, 32, 1235, 1970.

63. Desai, J. N., P. D. Bhavsar, R. Raghavarao and M. S. Narayanan, Winds and diffusion in the upper atmosphere observed by a sodium vapour trail released over Thumba, *Space Res.*, XV, 267, 1975.

64. Desai, J. N., Fabry Perot Spectroscopy in space science, *Proc. Indian Acad. Sci.* (Earth and Planetary Sci.), 93, 189, 1984.

65. Dickinson, R.E. , R. G. Roble and E. C. Ridley, Response of the neutral thermosphere at F layer heights to interaction of a global wind with anomalies of ionization, *J. Atmos. Sci.*, 28, 1280, 1971.

66. Dickinson, R.E. , Meteorology of the upper atmosphere, *Rev. Geophys. Space Phys.*, 13, 771, 1975.

67. Dickinson, R.E. , E. C. Ridley and R. G. Roble, Meridional circulation in the thermosphere, 1, Equinox conditions, *J. Atmos. Sci.*, 32, 1737, 1975.

68. Dickinson, R.E. , E. C. Ridley and R. G. Roble, A three-dimensional general circulation model of the thermosphere, *J. Geophys. Res.*, 86, 1499, 1981.

69. Draper, N. R. and H. Smith, Applied Regression Analysis, John Wiley and Sons Inc., New York, 1966.

70. Duncan, R. A. , The behaviour of a Chapman layer in the night F_2 region of the ionosphere under the influence of gravity, diffusion and attachment, *Aust. J. Phys.*, 9, 436, 1956.

71. Farley, D. T., E. Bonelli, B. G. Fejer and M. F. Larsen, The prereversal enhancement of the zonal electric field in the equatorial ionosphere, *J. Geophys. Res.*, 91, 13723, 1986.

72. Fejer, B. G., The equatorial ionospheric electric fields: A review, *J. Atmos. Terr. Phys.*, 43, 377, 1981.

73. Fejer, B. G. and M. C. Kelley, Ionospheric irregularities, *Rev. Geophys. Space Phys.*, 18, 401, 1980.

74. Fesen, C. G., R. E. Dickinson and R. G. Roble, Simulation of the thermospheric tides at equinox with the NCAR TGCM, *J. Geophys. Res.*, 91, 4471, 1986.

75. Fesen, C. G., R. G. Roble and E. C. Ridley, Thermospheric tides at equinox: Simulations with coupled composition and auroral forcings, 1, Diurnal component, *J. Geophys. Res.*, 96, 3647, 1991a.

76. Fesen, C. G., R. G. Roble and E. C. Ridley, Thermospheric tides at equinox: Simulations with coupled composition and auroral forcings, 2, Semi-diurnal component, *J. Geophys. Res.*, 96, 3663, 1991b.

77. Forbes, J. M., Atmospheric tides, 1, Model description and results for the solar diurnal component, *J. Geophys. Res.*, 87, 5222, 1982.

78. Forbes, J. M. and M. E. Hagan, Diurnal propagating tide in the presence of mean winds and dissipation: a numerical investigation, *Planet. Space Sci.*, 36, 579, 1988.

79. Forbes, J. M., M. Codrescu and T. J. Hall, On the utilization of ionosonde data to analyze the latitudinal penetration of ionospheric storm effects, *Geophys. Res. Lett.*, 15, 249, 1988.

80. Forbes, J. M. and R. G. Roble, Thermosphere - Ionosphere Coupling: An experiment in interactive modeling, *J. Geophys. Res.*, 95, 201, 1990.

81. Francis, S. H., Global propagation of atmospheric gravity waves: A review, *J. Atmos. Terr. Phys.*, 37, 1011, 1975.

82. Friedman, J. F. and F. A. Herrero, Fabry Perot interferometer measurements of thermospheric neutral wind gradients and reversals at Arecibo, *Geophys. Res. Lett.*, 9, 785, 1982.

83. Fuller-Rowell, T. J. and D. Rees, A three-dimensional time-dependent global model of the thermosphere, *J. Atmos. Sci.*, 37, 2545, 1980.

84. Fuller-Rowell, T. J., D. Rees, S. Quegan, R. J. Moffett and G. J. Bailey, Interactions between neutral thermospheric composition and the polar ionosphere using a coupled ionosphere - thermosphere model, *J. Geophys. Res.*, 92, 7744, 1987.

85. Ganguly, S., J. C. G. Walker and H. Rishbeth, The dynamic F_2 layer over Arecibo, *J. Atmos. Terr. Phys.*, 42, 553, 1980.

86. Garriott, O. K. and H. Rishbeth, Effects of temperature changes on the electron density profile in the F_2 layer, *Planet. Space Sci.*, 11, 587, 1963.

87. Geisler, J. E., Atmospheric winds in the middle latitude F region, *J. Atmos. Terr. Phys.*, 28, 703, 1966.

88. Geisler, J. E., A numerical study of the wind system in the middle thermosphere, *J. Atmos. Terr. Phys.*, 29, 1469, 1967.

89. Golomb, D., F. P. DelGreco, O. Harang, R. H. Johnson and M. A. MacLeod, Neutral diffusion coefficients, temperatures and densities in the lower thermosphere, *Space Res.*, VIII, 705, 1968.

90. Greenspan, J. A., Synoptic description of the 6300 Å nightglow near 78°W longitude, *J. Atmos. Terr. Phys.*, 28, 739, 1966.

91. Guest, P. G., Numerical methods of curve fitting, Cambridge Univ. Press, London, 1961.

92. Gurubaran, S. and R. Sridharan, Effect of neutral temperatures and meridional winds on F layer height, To appear in *J. Geophys. Res.*, 1993.

93. Haerendel, G. and J. V. Eccles, The role of the equatorial electrojet in the evening ionosphere, *J. Geophys. Res.*, 97, 1181, 1992.

94. Hanson, W. B. and J. N. Patterson, The maintenance of the nighttime F layer, *Planet. Space Sci.*, 12, 979, 1964.

95. Hanson, W. B. and R. J. Moffett, Ionization transport effects in the equatorial F region, *J. Geophys. Res.*, 71, 5559, 1966.

96. Hanson, W. B., B. L. Cragin and A. Dennis, The effect of vertical drift on the equatorial F region stability, *J. Atmos. Terr. Phys.*, 48, 205, 1986.

97. Harper, R. M., Nighttime meridional neutral winds near 350 km at low to midlatitudes, *J. Atmos. Terr. Phys.*, 35, 2023, 1973.

98. Harper, R. M., A semi-diurnal tide in the meridional wind at F region heights at low latitudes, *J. Geophys. Res.*, 84, 411, 1979.

99. Hays, P. B., A. F. Nagy, K. D. McWatters and J. V. Evans, Comparison of radar and optical temperature measurements in the F region, *J. Geophys. Res.*, 75, 4881, 1970.

100. Hays, P. B. and R. G. Roble, A technique for recovering Doppler line profiles from Fabry Perot interferometer fringes of very low intensity, *Appl. Opt.*, 10, 193, 1971.

101. Hays, P. B., T. L. Killeen and B. C. Kennedy, The Fabry Perot Interferometer on Dynamics Explorer, *Space Sci. Instrum.*, 5, 395, 1981.

102. Hedin, A. E. and H. G. Mayr, Magnetic control of the near equatorial neutral thermosphere, *J. Geophys. Res.*, 78, 1688, 1973.

103. Hedin, A. E., H. G. Mayr, C. A. Reber, N. W. Spencer and G. R. Carignan, Empirical model of global thermospheric temperature and composition based on data from OGO 6 quadrupole mass spectrometer, *J. Geophys. Res.*, 79, 215, 1974.

104. Hedin et al., A global thermosphere model based on mass spectrometer and incoherent scatter data, MSIS 1, N_2 density and temperature, *J. Geophys. Res.*, 82, 2139, 1977a.

105. Hedin et al., A global thermosphere model based on mass spectrometer and incoherent scatter data, MSIS 2, Composition, *J. Geophys. Res.*, 82, 2148, 1977b.

106. Hedin, A. E., A revised thermospheric model based on mass spectrometer and incoherent scatter data: MSIS-83, *J. Geophys. Res.*, 88, 10170, 1983.

107. Hedin, A. E., MSIS-86 thermospheric model, *J. Geophys. Res.*, 92, 4649, 1987.

108. Hedin, A. E., N. W. Spencer and T. L. Killeen, Empirical global model of upper thermosphere winds based on Atmosphere and Dynamics Explorer satellite data, *J. Geophys. Res.*, 93, 9959, 1988.

109. Hedin et al., Revised global model of thermospheric winds using satellite and ground-based observations, *J. Geophys. Res.*, 96, 7657, 1991.

110. Heelis, R. A., P. C. Kendall, R. J. Moffett, D. W. Windle and H. Rishbeth, Electrical coupling of the E and F regions and its effect on F region drifts and winds, *Planet. Space Sci.*, 22, 743, 1974.

111. Hernandez, G., Spectroscopic studies of the arc of March 8–9, 1970, *Planet. Space Sci.*, 20, 1309, 1972.

112. Hernandez, G. and O. A. Mills, Feedback stabilized Fabry Perot interferometer, *Appl. Opt.*, 12, 126, 1973.

113. Hernandez, G., T. E. VanZandt, V. L. Paterson and J. P. Turtle, Comparison of optical, incoherent scatter and Jacchia model neutral temperatures in the nighttime equatorial F_2 region, *EOS Trans.* (AGU), 54, 1160, 1973.

114. Hernandez, G., Contamination of the O I ($^3P_2 - {}^1D_2$) emission line by the (9–3) band of OH $X^2\Pi$ in high resolution measurements of the night sky, *J. Geophys. Res.*, 79, 1119, 1974.

115. Hernandez, G., T. E. VanZandt, V. L. Paterson and J. P. Turtle, Comparison of optical and incoherent scatter measurements of nighttime exospheric temperature at the magnetic equator, *J. Geophys. Res.*, 80, 3271, 1975.

116. Hernandez, G. and R. G. Roble, Direct measurements of thermospheric winds and temperatures, 1, Seasonal variations during geomagnetically quiet periods, *J. Geophys. Res.*, 81, 2065, 1976.

117. Hernandez, G., Lower thermospheric temperatures determined from the line profiles of the O I 17924 K (5577 Å) emission in the night sky, 2, Interaction with the lower atmosphere during stratospheric warmings, *J. Geophys. Res.*, 82, 2127, 1977.

118. Hernandez, G., Analytical description of a Fabry Perot Spectrometer, 4, Signal noise limitations in data retrieval; winds, temperature and emission rate, *Appl. Opt.*, 17, 2967, 1978.

119. Hernandez, G., Analytical description of a Fabry Perot Spectrometer, 5, Optimization for minimum uncertainties in the determination of Doppler widths and shifts, *Appl. Opt.*, 18, 3826, 1979.

120. Hernandez, G. and R. G. Roble, Thermospheric dynamics investigations with very high resolution spectrometers, *Appl. Opt.*, 18, 3376, 1979.

121. Hernandez, G., Analytical description of a Fabry Perot Spectrometer, 6, Minimum number of samples required for the determination of Doppler widths and shifts, *Appl. Opt.*, 21, 1695, 1982a.

122. Hernandez, G., Midlatitude neutral kinetic temperatures, 1, Solar, geomagnetic and long-term effects, *J. Geophys. Res.*, 87, 1623, 1982b.

123. Hernandez, G., Vertical motions of the neutral thermosphere at midlatitudes, *Geophys. Res. Lett.*, 9, 555, 1982c.

124. Hernandez, G., R. J. Sica and G. J. Romick, Equal-noise spectroscopic measurement method, *Appl. Opt.*, 23, 915, 1984.

125. Hernandez, G., Analytical description of a Fabry Perot Spectrometer, 8, Optimum operation with equidistant equal-noise sampling, *Appl. Opt.*, 24, 2442, 1985.

126. Hernandez, G., Fabry Perot Interferometers, Cambridge Univ. Press, Cambridge, 1986.

127. Hernandez, G. and T. L. Killeen, Optical measurements of winds and kinetic temperatures in the upper atmosphere, *Adv. Space Res.*, 8, (5)149, 1988.

128. Herrero, F. A. and J. W. Meriwether, Jr., 6300 Å airglow meridional intensity gradients, *J. Geophys. Res.*, 85, 4191, 1980.

129. Herrero, F. A. and N. W. Spencer, On the horizontal distribution of the equatorial thermospheric midnight temperature maximum and its seasonal variation, *Geophys. Res. Lett.*, 9, 1179, 1982.

130. Herrero, F. A., H. G. Mayr and N. W. Spencer, Low latitude thermospheric meridional winds between 250 and 450 km altitude: AE-E satellite data, *J. Atmos. Terr. Phys.*, 50, 1001, 1988.

131. Herrero, F. A., N. W. Spencer and H. G. Mayr, Thermosphere and F region plasma dynamics in the equatorial region, *Adv. Space Res.*, 13, (1)201, 1993.

132. Hines, C. O., Internal atmospheric gravity waves at ionospheric heights, *Can. J. Phys.*, 38, 1441, 1960.

133. Hines, C. O., Dynamical heating of the upper atmosphere, *J. Geophys. Res.*, 70, 177, 1965.

134. Hooke, W. H., Ionospheric irregularities produced by internal atmospheric gravity waves, *J. Atmos. Terr. Phys.*, 30, 795, 1968.

135. Huang, Y. N., K. Cheng and W. T. Huang, Seasonal and solar cycle variations of spread F at the equatorial anomaly crest zone, *J. Geomag. Geoelectr.*, 39, 639, 1987.

136. Hunsucker, R. D., Atmospheric gravity waves generated in the high latitude ionosphere: A review, *Rev. Geophys. Space Phys.*, 20, 293, 1982.

137. Jacchia, L. G., Copuscular radiation and the acceleration of artificial satellites, *Nature*, 183, 1662, 1959.

138. Jacchia, L. G., Static diffusion models of the upper atmosphere with empirical temperature profiles, *Smithson. Contrib. Astrophys.*, 8, 215, 1965.

139. Jacchia, L. G., Revised static models of the thermosphere and exosphere with empirical temperature profiles, *Smithson. Astropys. Obs. Spec. Rept. No.* 332, 1971.

140. Jacchia, L. G., Thermospheric temperature, density and composition: new models, *Smithson. Astropys. Obs. Spec. Rept. No.* 375, 1977.

141. Jacquinot, P. and Ch. Dufour, Conditions optiques d'emploi des cellules photo-electriques dans les spectrographes et les interferometres, *J. Res.*

(CRNS), 6, 91, 1948.

142. Jacquinot, P., The luminosity of spectrometers with prisms, gratings or Fabry Perot etalons, *J. Opt. Soc. Am.*, 44, 761, 1954.

143. Jarrett, A. H., G. J. McGrattan and F. J. Smith, The measurement of high altitude wind velocities from vapour releases - III, *Planet. Space Sci.*, 11, 1319, 1963.

144. Kelley, M. C., Relationship between electrostatic turbulence and spread *F*, *J. Geophys. Res.*, 77, 1327, 1972.

145. Killeen, T. L. and P. B. Hays, Doppler line profile analysis for a multichannel Fabry Perot interferometer, *Appl. Opt.*, 23, 612, 1984.

146. Killeen, T. L., Energetics and dynamics of the earth's thermosphere, *Rev. Geophys.*, 25, 433, 1987.

147. Killeen, T. L., R. G. Roble and N. W. Spencer, A computer model of global thermospheric winds and temperatures, *Adv. Space Res.*, 7, 207, 1987.

148. Killeen, T. L. and R. G. Roble, Thermosphere dynamics contributions from the first 5 years of the Dynamics Explorer program, *Rev. Geophys.*, 26, 329, 1988.

149. King, G. A. M., The dissociation of oxygen and high level circulation in the atmosphere, *J. Atmos. Sci.*, 21, 231, 1964.

150. King, J. W. and H. Kohl, *Nature*, 206, 699, 1965.

151. Kohl, H. and J. W. King, Atmospheric winds between 100 and 700 km and their effects on the ionosphere, *J. Atmos. Terr. Phys.*, 29, 1045, 1967.

152. Krishnamurthy, B. V., S. S. Hari and V. V. Somayajulu, Nighttime equatorial thermospheric meridional winds from $h'F$ data, *J. Geophys. Res.*, 95, 4307, 1990.

153. Kulkarni, P. V., 6300 Å night airglow and the geomagnetic control of the equatorial anomaly, *Proc. Indian Acad. Sci.* (Earth and Planetary Sci., 82, 46, 1975.

154. Liu, C. H., Acoustic gravity waves in ionosphere/thermosphere system, *Adv. Space Res.*, 12, (6)187, 1992.

155. Lyon, A. J. and L. Thomas, The F_2 region equatorial anomaly in the African, American and East Asian sectors during sunspot maximum, *J. Atmos. Terr. Phys.*, 25, 373, 1963.

156. McClure, J. P. and R. F. Woodman, Radar observations of equatorial spread F in a region of electrostatic turbulence, *J. Geophys. Res.*, 77, 5617, 1972.

157. McCormac, F. G., T. L. Killeen, B. Nardi and R. W. Smith, How close are ground-based Fabry Perot thermospheric wind and temperature measurements to exospheric values ? - A simulation study, *Planet. Space Sci.*, 35, 1255, 1987.

158. Martyn, D. F., Processes controlling ionization distribution in the F_2 region of the ionosphere, *Aust. J. Phys.*, 9, 161, 1956.

159. Maruyama, T., A diagnostic model for equatorial spread F, 1, Model description and application to electric field and neutral wind effects, *J. Geophys. Res.*, 93, 14611, 1988.

160. Mayr, H. G., I. Harris and N. W. Spencer, Some properties of upper atmosphere dynamics, *Rev. Geophys. Space Phys.*, 16, 539, 1978.

161. Mayr et al., Tides and the midnight temperature anomaly in the thermosphere, *Geophys. Res. Lett.*, 6, 447, 1979.

162. Meaburn, J., Detection and spectrometry of faint light, D. Reidel Publ. Co., Dordrecht, 1976.

163. Mendillo, M., J. Baumgardner, P. Xiaoqing, P. J. Sultan and R. Tsunoda, *J. Geophys. Res.*, 97, 13865, 1992.

164. Meriwether, J. W., Jr., C. A. Tepley, S. A. Price, P. B. Hays and L. L. Cogger, Remote ground-based observations of terrestrial airglow emission and thermospheric dynamics at Calgary, Alberta, Canada, *Opt. Eng.*, 22, 128, 1983.

165. Meriwether, J. W., Jr., M. A. Biondi and D. N. Anderson, Equatorial airglow depletions induced by thermospheric winds, *Geophys. Res. Lett.*, 12, 487, 1985.

166. Meriwether, J. W., Jr., J. W. Moody, M. A. Biondi and R. G. Roble, Optical interferometric measurements of nighttime equatorial thermospheric winds at Arequipa, Peru, *J. Geophys. Res.*, 91, 5557, 1986.

167. Miller, K. L., D. G. Torr and P. G. Richards, Meridional winds in the thermosphere derived from measurement of F_2 layer height, *J. Geophys. Res.*, 91, 4531, 1986.

168. Miller, K. L., J. E. Salah and D. G. Torr, The effect of electric fields on measurements of meridional winds in the thermosphere, *Ann. Geophys.*, 5A, 337, 1987.

169. Miller, K. L., P. G. Richards and D. G. Torr, The derivation of meridional neutral winds in the thermosphere from F_2 layer height, *WITS handbook*, Vol. 2, 439, 1989.

170. Mitra, S. K., Geomagnetic control of region F_2 of the ionosphere, *Nature*, 158, 668, 1946.

171. Miyahara, S., Zonal mean winds induced by vertically propagating atmospheric tidal waves in the lower thermosphere, *J. Meteorol. Soc. Jpn.*, 56, 548, 1978.

172. Moffett, R. J., The equatorial anomaly in the electron distribution of the terrestrial F region, *Fund. Cosmic Phys.*, 4, 313, 1979.

173. Namboothiri, S. P., N. Balan and P. B. Rao, Vertical plasma drifts in the F region at the magnetic equator, *J. Geophys. Res.*, 94, 12055, 1989.

174. Nelson, G. J. and L. L. Cogger, Dynamical behaviour of the nighttime ionosphere at Arecibo, *J. Atmos. Terr. Phys.*, 33, 1711, 1971.

175. Nisbet, J. S., Neutral atmospheric temperatures from incoherent scatter observations, *J. Atmos. Sci.*, 24, 586, 1967.

176. Okano, S. and J. S. Kim, Thermospheric temperatures during geomagnetically disturbed periods, *J. Geomag. Geoelectr.*, 38, 173, 1986.

177. Oliver, W. L. and J. E. Salah, The global thermospheric mapping study, *J. Geophys. Res.*, 93, 4039, 1988.

178. Oliver, W. L., D. Alcayde and P. Bauer, Incoherent scatter radar contributions, *Adv. Space Res.*, 8, (5)119, 1988.

179. Pokhunkov, A. A., Yu. A. Kalgin and A. D. Danilov, The variability of the turbopause altitude in middle latitudes, *Geomag. Aeron.*, 25, 579, 1985.

180. Prölss, G. W., Magnetic storm associated perturbations of the upper atmosphere: Recent results obtained by satellite-borne gas analyzers, *Rev. Geophys. Space Phys.*, 18, 183, 1980.

181. Prölss, G. W., Solar wind energy dissipation in the upper atmosphere, *Adv. Space Res.*, 3, (1)55, 1983.

182. Prölss, G. W., M. Roemer and J. W. Slowey, Dissipation of solar wind energy in the earth's upper atmosphere: The geomagnetic effect, *Adv. Space Res.*, 8, (5)215, 1988.

183. Raghavarao et al., Evidence for a large scale electric field gradient at the onset of equatorial spread *F*, *J. Atmos. Terr. Phys.*, 46, 355, 1984.

184. Raghavarao et al., *In situ* measurements of winds, electric fields and electron densities at the onset of equatorial spread *F*, *J. Atmos. Terr. Phys.*, 49, 485, 1987.

185. Raghavarao et al., The equatorial ionosphere, *WITS handbook*, 48, 1989.

186. Raghavarao, R., L. E. Wharton, N. W. Spencer, H. G. Mayr and L. H. Brace, An Equatorial Temperature and Wind Anomaly (ETWA), *Geophys. Res. Lett.*, 18, 1193, 1991.

187. Raghavarao, R., R. Sekar and R. Suhasini, Non-linear numerical simulation of equatorial spread F - Effects of winds and electric fields, *Adv. Space Res.*, 12, (6)227, 1992.

188. Raghavarao, R., W. R. Hoegy, N. W. Spencer and L. E. Wharton, Neutral temperature anomaly in the equatorial thermosphere - A source of vertical winds, *Geophys. Res. Lett.*, 20, 1023, 1993.

189. Rajaraman, T. N., J. N. Desai and S. S. Degaonkar, Variation of F region nighttime neutral temperatures with equatorial spread F activity, *Proc. Indian Acad. Sci.* (Earth and Plan. Sci.), 88, 69, 1979.

190. Rajaraman, T. N., Optical studies in the upper atmosphere, Ph. D. Thesis, Gujarat Univ., 1982.

191. Ranjan Gupta et al., Excess heating over the equatorial latitudes during storm sudden commencement, *Geophys. Res. Lett.*, 13, 1055, 1986.

192. Rao, B. C. N., The post-sunset rise of f_oF_2 in the transition region and its dependence on the post-sunset rise of $h'F$ in the equatorial region, *J. Geophys. Res.*, 68, 2551, 1963.

193. Rastogi, R. G., The diurnal development of the anomalous equatorial belt in the F_2 region of the ionosphere, *J. Geophys. Res.*, 64, 727, 1959.

194. Rawer, K. and D. Bilitza, Electron density profile description in the international reference ionosphere, *J. Atmos. Terr. Phys.*, 51, 781, 1989.

195. Rees, D., R. G. Koper, K. H. Lloyd and C. H. Low, Determination of the structure of the atmosphere between 90 and 250 km by means of contaminant releases at Woomera, May 1968, *Phil. Trans. Roy. Soc. London*, 271, 631, 1972.

196. Rees, D. and A. H. Greenaway, Doppler imaging system; an optical device for measuring vector winds, 1, General principles, *Appl. Opt.*, 22, 1078, 1983.

197. Rees, D., in introduction to CIRA models, *Adv. Space Res.*, 8, (5)5, 1988.

198. Richmond, A. D., Gravity wave generation, propagation and dissipation in the thermosphere, *J. Geophys. Res.*, 83, 4131, 1978.

199. Richmond, A. D., Large-amplitude gravity wave energy production and dissipation in the thermosphere, *J. Geophys. Res.*, 84, 1880, 1979.

200. Rishbeth, H. and D. W. Barron, Equilibrium electron distributions in the ionospheric F_2 layer, *J. Atmos. Terr. Phys.*, 18, 234, 1960.

201. Rishbeth, H., Further analogue studies of the ionospheric F layer, *Proc. Phys. Soc.*, 81, 65, 1963.

202. Rishbeth, H., A time-varying model of the ionospheric F_2 layer, *J. Atmos. Terr. Phys.*, 26, 657, 1964.

203. Rishbeth, H., F_2 layer rates at sunspot minimum, *J. Atmos. Terr. Phys.*, 28, 94, 1966.

204. Rishbeth, H., The effect of winds on the ionospheric F_2 peak, *J. Atmos. Terr. Phys.*, 29, 225, 1967.

205. Rishbeth, H. and O. K. Garriott, Introduction to Ionospheric Physics, Academic Press, New York, 1969.

206. Rishbeth, H., The F layer dynamo, *Planet. Space Sci.*, 19, 263, 1971a.

207. Rishbeth, H., Polarization fields produced by winds in the equatorial F region, *Planet. Space Sci.*, 19, 357, 1971b.

208. Rishbeth, H., Thermospheric winds and the F region: A review, *J. Atmos. Terr. Phys.*, 34, 1, 1972.

209. Rishbeth, H., F region storms and thermospheric circulation, *J. Atmos. Terr. Phys.*, 37, 1055, 1975.

210. Rishbeth, H., S. Ganguly and J. C. G. Walker, Field-aligned and field-perpendicular velocities in the ionospheric F_2 layer, *J. Atmos. Terr. Phys.*, 40, 767, 1978.

211. Rishbeth, H., Ion-drag effects in the thermosphere, *J. Atmos. Terr. Phys.*, 41, 885, 1979.

212. Rishbeth, H., The F region dynamo, *J. Atmos. Terr. Phys.*, 43, 387, 1981.

213. Rishbeth, H., On the F_2 layer continuity equation, *J. Atmos. Terr. Phys.*, 48, 511, 1986.

214. Rishbeth, H., T. J. Fuller-Rowell and A. S. Rodger, F layer storms and thermospheric composition, *Physica Scripta*, 36, 327, 1987.

215. Rishbeth, H. and R. Edwards, The isobaric F_2 layer, *J. Atmos. Terr. Phys.*, 51, 321, 1989.

216. Roble, R. G. and R. E. Dickinson, Is there enough solar EUV radiation to maintain the global mean thermospheric temperature ? *J. Geophys. Res.*, 78, 249, 1973.

217. Roble, R. G., E. C. Ridley, A. D. Richmond and R. E. Dickinson, A coupled thermosphere/ionosphere general circulation model, *Geophys. Res. Lett.*, 15, 1325, 1988.

218. Roy, M. and R. G. Rastogi, A semi-analytic method for studying plasma properties near the F_2 peak of the low latitude ionosphere, *J. Atmos. Terr. Phys.*, 51, 477, 1989.

219. Sahai et al., Observations of thermospheric neutral winds at 23°S, *Planet. Space Sci.*, 40, 767, 1992a.

220. Sahai et al., Observations of thermospheric temperatures at 23°S, *Planet. Space Sci.*, 40, 1545, 1992b.

221. Sastri, J. H., Post-sunset behaviour of the equatorial anomaly in the Indian sector, *Indian J. Radio Space Phys.*, 11, 33, 1982.

222. Sastri, J. H., Equatorial anomaly in F region - A review, *Indian J. Radio Space Phys.*, 19, 225, 1990.

223. Schunk, R. W. and J. J. Sojka, Approaches to ionospheric modeling, simulation and prediction, *Adv. Space Res.*, 12, (6)317, 1992.

224. Sekar, R. and R. Raghavarao, Role of vertical winds on the Rayleigh - Taylor mode instabilities of the nighttime equatorial ionosphere, *J. Atmos. Terr. Phys.*, 49, 981, 1987.

225. Sekar, R. and R. Sridharan, Validity of the estimates of nighttime meridional winds made from bottomside ionograms, *J. Atmos. Terr. Phys.*, 54, 1197, 1992.

226. Sekar, R., S. Gurubaran and R. Sridharan, All sky imaging Fabry Perot Spectrometer for optical investigation of the upper atmosphere, *Indian J. Radio and Space Phys.*, 22, 197, 1993.

227. Sharma, P. and R. Raghavarao, Simultaneous occurrence of ionization ledge and counter-electrojet in the equatorial ionosphere: observational evidence and its implications, *Can. J. Phys.*, 67, 166, 1989.

228. Shepherd, G. G., Spectroscopic measurements of auroral and airglow temperatures, *Ann. Geophys.*, 25, 841, 1969.

229. Shimazaki, T., Dynamical structure of the ionospheric F_2 layer, *J. Radio Res. Labs. Japan*, 4, 309, 1957.

230. Shimazaki, T., Effects of vertical mass motions on the composition structure in the thermosphere, *Space Res.*, XII, 1039, 1972.

231. Sipler, D. P. and M. A. Biondi, Equatorial F region neutral winds from nightglow O I 630.0 nm Doppler shifts, *Geophys. Res. Lett.*, 5, 373, 1978.

232. Sipler, D. P., M. A. Biondi and R. G. Roble, F region neutral winds and temperatures at equatorial latitudes: Measured and predicted behaviour during geomagnetically quiet conditions, *Planet. Space Sci.*, 31, 53, 1983.

233. Sobral, J. H. A., H. C. Carlson, D. T. Farley and W. E. Swartz, Nighttime dynamics of the F region near Arecibo as mapped by airglow features, *J. Geophys. Res.*, 83, 2561, 1978.

234. Sojka, J. J. and R. W. Schunk, A theoretical study of the global F region for June solstice, solar maximum and low magnetic activity, *J. Geophys. Res.*, 90, 5285, 1985.

235. Spencer, N. W., H. B. Niemann and G. R. Carignan, The neutral atmosphere temperature instrument, *Radio Sci.*, 8, 287, 1973.

236. Spencer et al., The midnight temperature maximum in the earth's equatorial thermosphere, *Geophys. Res. Lett.*, 6, 444, 1979.

237. Spencer et al., The Dynamics Explorer wind and temperature spectrometer, *Space Sci. Instrum.*, 5, 417, 1981.

238. Spencer, N. W. and G. R. Carignan, *In situ* measurements of thermospheric composition, temperature and winds by mass spectrometry, *Adv. Space Res.*, 8, (5)107, 1988.

239. Sridharan, R. and R. Raghavarao, Evidence for turbopause control on neutral density variations in the lower thermosphere, *J. Atmos. Terr. Phys.*, 46, 851, 1984.

240. Sridharan et al., Winds, wind-shears and plasma densities during the initial phase of a magnetic storm from equatorial latitudes, *J. Atmos. Terr. Phys.*, 51, 169, 1989.

241. Sridharan, R., S. Gurubaran, R. Raghavarao and R. Suhasini, Coordinated thermospheric and F region measurements from low latitudes, *J. Atmos. Terr. Phys.*, 53, 515, 1991.

242. Sridharan, R., R. Sekar and S. Gurubaran, Two dimensional high resolution imaging of the retrieval of the equatorial plasma fountain, To appear

in *J. Atmos. Terr. Phys.*, 1993.

243. Stening, R. J., A two-layer ionospheric dynamo calculation, *J. Geophys. Res.*, 86, 3543, 1981.

244. Stening, R. J., Modeling the low latitude F region: A review, *J. Atmos. Terr. Phys.*, 54, 1387, 1992.

245. Stolarski, R. S., P. B. Hays and R. G. Roble, Atmospheric heating by solar EUV radiation, *J. Geophys. Res.*, 80, 2266, 1975.

246. Thuillier, G., J. L. Falin and F. Barlier, Global experimental model of the exospheric temperature using optical and incoherent scatter measurements, *J. Atmos. Terr. Phys.*, 39, 1195, 1977.

247. Tinsley, B. A., Neutral atom precipitation - A review, *J. Atmos. Terr. Phys.*, 43, 617, 1981.

248. Torr, M. R., D. G. Torr and P. G. Richards, The solar UV heating efficiency of the midlatitude thermosphere, *Geophys. Res. Lett.*, 7, 373, 1980a.

249. Torr, M. R., P. G. Richards and D. G. Torr, A new determination of the UV heating efficiency of the thermosphere, *J. Geophys. Res.*, 85, 6819, 1980b.

250. Vasseur, G., Vents daus la thermosphere deduits des mesures par diffusion de Thomson, *Ann. Geophys.*, 25, 517, 1969.

251. Vial, F., Numerical simulations of atmospheric tides for solstice conditions, *J. Geophys. Res.*, 91, 8955, 1986.

252. Walker, J. C. G., The midlatitude thermosphere, *Planet. Space Sci.*, 36, 1, 1988.

253. Weber, E. J., J. Aarons and A. L. Johnson, Conjugate studies of an isolated equatorial irregularity region, *J. Geophys. Res.*, 88, 3175, 1983.

254. Woodman, R. F., Vertical drift velocities and east-west electric fields at the magnetic equator, *J. Geophys. Res.*, 75, 6249, 1970.

255. Yagi, T. and P. L. Dyson, The influence of neutral temperatures and winds on the F layer height, *J. Atmos. Terr. Phys.*, 47, 575, 1985.

256. Yeh, K. C. and C. H. Liu, Acoustic gravity waves in the upper atmosphere, *Rev. Geophys. Space Phys.*, 12, 193, 1974.

257. Yeh, K. C., C. H. Liu and A. L. Hearn, Propagation of gravity wave spectra in the thermosphere, *J. Geophys. Res.*, 84, 834, 1979.

258. Yonezawa, T., On the influence of electron-ion diffusion exerted upon the formation of the F_2 layer, *J. Radio Res. Labs. Japan*, 5, 165, 1958.

List of Publications

1. Coordinated thermospheric and F region measurements from low latitudes, Sridharan R., **S. Gurubaran**, R. Raghavarao and R. Suhasini, *J. Atmos. Terr. Phys., 53*, 515, 1991.

2. First results of O I 630.0 nm dayglow measurements from equatorial latitudes, Sridharan R., R. Raghavarao, **S. Gurubaran** and R. Narayanan, *J. Atmos. Terr. Phys., 53*, 521, 1991.

3. O I 630.0 nm dayglow in the region of equatorial ionization anomaly: Temporal variability and its causative mechanism, Sridharan R., S. A. Haider, **S. Gurubaran**, R. Sekar and R. Narayanan, *J. Geophys. Res., 97*, 13715, 1992.

4. Effect of meridional winds and neutral temperatures on the F layer heights over low latitudes, **Gurubaran, S.** and R. Sridharan, To appear in *J. Geophys. Res.*, 1993.

5. Two dimensional high resolution imaging of the equatorial plasma fountain, Sridharan R., R. Sekar and **S. Gurubaran**, To appear in *J. Atmos. Terr. Phys.*, 1993.

6. All sky imaging Fabry-Perot Spectrometer for the optical investigation of the upper atmosphere, Sekar R., **S. Gurubaran** and R. Sridharan, *Indian J. Radio and Space Phys.*, 22, 197, 1993.

7. Variabilities in the thermospheric temperature in the region of equatorial ionization anomaly - A case study, **Gurubaran, S.**, R. Sridharan and K. G. Jani, Paper in preparation.

8. Meridional winds and their variabilities over low latitudes, **Gurubaran, S.** and R. Sridharan, Paper in preparation.

9. An improved data reduction scheme for the determination of Doppler parameters from Fabry Perot interferometer fringes, **Gurubaran, S.** and R. Suhasini, Paper in preparation.

Papers presented at Symposia/Conferences

1. On the response of the F region to the variations in the thermospheric temperature over low latitudes, **Gurubaran, S.**, R. Narayanan, R. Sekar, R. Sridharan and R. Raghavarao, IAGA symposium, Exeter, U. K., 1989.

2. (a) Nighttime thermospheric temperatures and associated F region dynamics from low latitudes, **Gurubaran S.**, R. Sridharan, R. Suhasini and R. Raghavarao.
(b) Pre-dusk enhancements of OI 630.0 nm dayglow intensities from low latitudes, Sridharan R., R. Raghavarao, **S. Gurubaran** and R. Narayanan.

These papers were presented in the National Space Science Symposium, Nagpur, India, 1990 and the XXVIII COSPAR Symposium and Associated meetings at The Hague, The Netherlands, 1990.

3. Dayglow photometry - Promise and Future, Sridharan, R., **S. Gurubaran** and A. K. Tewari, International Symposium on Optical and Radio Remote Sensing of the Atmospheric Environment, New Delhi, India 1990.

4. (a) The low latitude thermosphere/ionosphere system, **Gurubaran, S.**, R. Sridharan, R. Narayanan, R. Sekar and N. K. Modi.
(b) First results from a high resolution doppler imaging spectrometer from Ahmedabad located under equatorial ionization anomaly, Sridharan R., R. Sekar, **S. Gurubaran**, R. Naryanan and N. K. Modi.
(c) Determination of emission line profiles of dayglow - an innovative approach, Sridharan R., R. Narayanan, N. K. Modi, D. P. Raju and **S. Gurubaran.**

These papers were presented in the National Space Science Symposium, Ahmedabad, India, 1992.

5. First results from a Doppler Imaging Spectrometer from the region of equatorial ionization anomaly (Mt. Abu), Sridharan, R., R. Sekar and **S. Gurubaran**, COSPAR (World Space Congress), Washington D.C., 1992.